HARVARD
Kenneth C. Griffin

GRADUATE SCHOOL
OF ARTS AND SCIENCES

THESIS ACCEPTANCE CERTIFICATE

The undersigned, appointed by the

Department of Physics

have examined a dissertation entitled

Photonic Interfaces for Neutral Atom Quantum Computers

presented by Brandon Grinkemeyer

candidate for the degree of Doctor of Philosophy and hereby certify that it is worthy of acceptance.

Signature _____

Typed name: Prof. Mikhail Lukin

Signature _____

Typed name: Prof. Susanne Yelin

Signature _____

Typed name: Prof. Federico Capasso

Signature _____

Typed name: Prof. Vladan Vuletić (MIT)

Date: May 5, 2025

Photonic Interfaces for Neutral Atom Quantum Computers

A DISSERTATION PRESENTED
BY
BRANDON GRINKEMEYER
TO
THE DEPARTMENT OF PHYSICS

IN PARTIAL FULFILLMENT OF THE REQUIREMENTS
FOR THE DEGREE OF
DOCTOR OF PHILOSOPHY
IN THE SUBJECT OF
PHYSICS

HARVARD UNIVERSITY
CAMBRIDGE, MASSACHUSETTS
MAY 2025

©2025 – Brandon Grinkemeyer
all rights reserved.

Photonic Interfaces for Neutral Atom Quantum Computers

Abstract

As quantum computers advance toward larger, more powerful systems, scaling beyond a single quantum processing unit (QPU) will require the development of fast, high-fidelity interconnections between QPUs. One of the most promising strategies for achieving this is coupling qubits to optical cavities. Strong atom-cavity interactions enable the generation of atom-photon entanglement at rates orders of magnitude faster than alternative approaches, offering a critical advantage for scalable architectures. This thesis investigates the use of nanophotonic and microscale cavities to achieve exceptional atom-photon coupling while maintaining compatibility with state-of-the-art neutral atom QPUs.

The experiments presented in this thesis demonstrate coherent transport between a free-space atom array and an optical cavity, coherent Rydberg excitations and interactions in the presence of the cavity interface, fast high-fidelity readout and cavity-mediated operations, and novel fabrication techniques for improved microcavities that further enhance system performance. Together, these advances outline a pathway toward utility-scale quantum computing.

Contents

Title i
Copyright ii
Abstract iii
Table of Contents iv
List of Figures xxiv
Dedication xxv
Citations to Previous Work xxxii

1 Introduction 1
1.1 Neutral Atoms for Quantum Information Science 3
1.2 Ultracold Neutral Atoms 4
1.3 Neutral Atom Qubits 6
1.4 Quantum Networking with Neutral Atoms 6
1.5 Quantum Computing with Neutral Atoms 7
1.6 Overview of Thesis 9

2 Cavity Quantum Electrodynamics 12
2.1 Quantization of the Electric Field 13
2.2 Excited Atom in Free Space 14
2.3 Single Atom Coupled to an Optical Cavity 16
2.4 Purcell Effect 19
2.5 Strong Coupling Regime 21
2.6 Cavity-Mediated Gates 23
2.7 Optical Cavities for Quantum Sciences 26
2.8 Cavity Transmission and Reflection 26
2.9 Atom–Cavity Spectrum 31
2.10 One-Dimensional Photonic Crystal Cavities 34
2.11 Fabry-Perot Cavities 36
2.12 Fabry-Perot Cavity Modes 40
2.13 Optimal Cavities for Quantum Networking 45

3 Rydberg Atoms 49

3.1 Rydberg Blockade . . . 53
3.2 Rydberg Mediated Two-Qubit Gates . . . 55
3.3 Rydberg Atom Electric Field Sensitivity . . . 58
3.4 Rydberg Atom Interaction with Electric Field Gradients . . . 59

4 Construction of the Fiber Cavity Apparatus **66**
4.1 High Finesse Optical Cavities in Ultrahigh Vacuum . . . 68
4.2 Alignment of the Fiber Cavity . . . 68
4.3 Vacuum Chamber Assembly . . . 72
4.4 Fiber Cavity Mount . . . 74

5 Entanglement Transport **77**
5.1 Experimental Setup . . . 78
5.2 Atoms Coupled to Photonic Crystal Cavity . . . 80
5.3 Cavity Carving . . . 81
5.4 Entanglement Transport . . . 84
5.5 Outlook . . . 85

6 Rydberg Atoms near Nanophotonics **87**
6.1 Experimental Setup . . . 90
6.2 Coherence Properties of Rydberg Atoms near Nanophotonics . . . 91
6.3 Rydberg Mediated Entanglement . . . 93
6.4 Entanglement Enhanced Sensing . . . 93
6.5 Outlook . . . 98

7 Error Detected Quantum Operations **99**
7.1 Experimental Setup . . . 101
7.2 Photon-Mediated Entanglement Through Dark States . . . 104
7.3 Cavity Carving with Integrated Error Detection . . . 106
7.4 Quantum Phase Gate with Integrated Error Detection . . . 108
7.5 Outlook . . . 110

8 High Finesse Optical Microcavities **112**
8.1 CO_2 Laser Ablated Micromirrors . . . 113
8.2 Silicon Micromirrors . . . 115
8.3 Buckled Micromirrors . . . 118
8.4 Buckled Micromirror Fabrication . . . 120
8.5 Buckled Micromirror Cavity Characterization . . . 123
8.6 Buckled Micromirror Cavity Integrability and Scalability . . . 127
8.7 Outlook . . . 127

9 Next Generation Experiments and Conclusions 129
9.1 Atom Arrays Coupled to Fiber Cavities . . . 130
9.2 Multiplexed Atom Photon Entanglement . . . 132
9.3 Many-Qubit State Carving . . . 134
9.4 Atom-telecom Photon Entanglement . . . 142
9.5 Conclusion . . . 149

Appendix A Supplement of Chapter 5 150
A.1 Cooperativity estimate . . . 150
A.2 Experimental sequence . . . 152
A.3 State preparation . . . 154
A.4 Two-atom readout in free space . . . 156
A.5 Readout through the cavity . . . 157
A.6 Fidelity extraction from parity . . . 158
A.7 Concurrence bound . . . 159
A.8 Entanglement scheme using the interferometer . . . 160
A.9 Theoretical models for the entanglement protocol . . . 162
A.10 Coherence properties of atoms next to the photonic crystal cavity . . . 166
A.11 Phase accumulation while moving . . . 170
A.12 Modeling losses upon loading into the cavity near-field . . . 175

Appendix B Supplement of Chapter 6 178
B.1 Setup details . . . 178
B.2 Electric field from the device . . . 181
B.3 Stabilizing the Rydberg spectral shift . . . 184
B.4 Single-atom coherence . . . 188
B.5 Two-atom coherence . . . 198
B.6 Electric field gradient . . . 205
B.7 Optimizing the Rydberg quantum number n . . . 214

Appendix C Supplement of Chapter 7 216
C.1 Fiber Cavity Mounting and Parameters . . . 216
C.2 Experimental Methods . . . 218
C.3 Readout . . . 224
C.4 Cavity Spectra . . . 231
C.5 Experimental Characterization of the Entanglement Fidelity . . . 237
C.6 Theoretical Models . . . 240
C.7 Theoretical Modelling for Rb-87 . . . 248

Appendix D Supplement of Chapter 8 258
D.1 Properties of the dielectric coating . . . 258

D.2 Cavity finesse measurement setup and method 260
D.3 FEM simulation of the buckling mode 263
D.4 Simulation of the diffractive loss of the mirror 263
D.5 Fabrication pitfall 264

References **282**

Listing of figures

1.1 (**A**) Atoms in optical tweezers are transported from an atom array into the mode of a microcavity. (**B**) Resonant transmission spectra for a bare cavity (gray), one atom (blue), and two atoms (red) coupled to the microcavity, demonstrating strong coupling with a cooperativity of $C = 101(2)$. (**C**) Histograms showing photon counts collected in 10 μs for an atom in the $F = 1$ state (gray) and an atom in the $F = 2$ state (blue), yielding a qubit state readout fidelity of $99.960^{+14}_{-24}\%$. (**D**) A Rydberg atom array operating in free space near a nanophotonic optical link. (**E**) Measurements of Rydberg atom coherence near the nanophotonic cavity at a distance of 130 μm. For a Ramsey measurement, $T_2^* = 200(40)$ ns (blue line); for spin-echo, $T_2 = 4.1(2)$ μs (red line). With a Carr-Purcell decoupling sequence, no decay is observed within the measurement time. (**F**) Rydberg coherence for different decoupling sequences as a function of distance from the nanophotonic cavity, showing retention of coherence even in proximity to the device. . . 9

2.1 An atom cavity system showing the coherent coupling between the atom and the cavity, g, the atomic free space decay rate, γ, cavity decay rate, κ, and a coherent drive on the input, η 17

2.2 The time dynamics of an initially excited atom coupled to an optical cavity showing two different regimes, $\kappa = \gamma$, where we see coherent oscillation between the atom and the cavity at a frequency of $2g$ with a damping given by $\frac{\kappa+\gamma}{2}$, and $\kappa = 10\gamma$ where we see a quick exponential decay of the atomic excitation that goes as the purcell enhanced decay rate of $C\gamma = \frac{4g^2}{\kappa}$ 21

2.3 A level diagram depicting the different excitation manifolds of the Jaynes–Cummings Hamiltonian. (Left): States with the same number of excitations, n, are coupled with a strength of $\sqrt{n}\,g$. (Right): The eigenstates of a given excitation manifold are given by $|n, \pm\rangle = |g, n\rangle \pm |e, n-1\rangle$, with an energy splitting of $\sqrt{n}g$. 23

2.4 An optical cavity system driven by an external source, η, with a circulating electric field, a. The cavity experiences three types of loss: transmission through the input mirror, κ_{in}, transmission through the output mirror, κ_{out}, and scattering losses, κ_{sc}, which together yield a total loss rate κ. 27

2.5 Reflectivity $|r(\Delta)|^2$ and phase $\arg[r(\Delta)]$ versus detuning Δ for three coupling regimes: undercoupled ($\kappa_{in} = 0.1\kappa$), critically coupled ($\kappa_{in} = 0.5\kappa$), and overcoupled ($\kappa_{in} = 0.9\kappa$). 28
2.6 Reflectivity spectra of two atom-cavity systems with identical cooperativity, $C = \frac{4g^2}{\kappa\gamma} = 25$, but with different κ/γ ratios. In the first regime, where $g > \kappa = \gamma$, the system operates in the strong-coupling regime, allowing coherent exchange of excitations between the atom and the cavity. This is spectroscopically observable as two resolvable dressed states split by $2g$ (black line between peaks), with linewidths of $\frac{\kappa+\gamma}{2}$. In the second regime, known as the "bad cavity" regime ($\kappa > g > \gamma$), the cavity decay rate is dominant, suppressing coherent oscillations and causing a rapid decay of the atomic excitation through the cavity at a rate of $\frac{4g^2}{\kappa} = C\gamma$. This manifests as a Purcell-enhanced atomic linewidth, seen spectroscopically as a hole burned into the bare cavity resonance. 30
2.7 Reflectivity $|r(\Delta)|^2$ and phase $\arg[r(\Delta)]$ versus detuning Δ for an atom coupled to a cavity with cavity parameters $(g, \kappa, \gamma) = (2, 1, 1)$ with three different coupling regimes: undercoupled ($\kappa_{in} = 0.1\kappa$), critically coupled ($\kappa_{in} = 0.5\kappa$), and overcoupled ($\kappa_{in} = 0.9\kappa$). 34
2.8 A plot showing the stability condition of an optical cavity along with various cavity configurations. Three key regions are highlighted: the plano-plano region, where the mirrors are flat (i.e., the radii of curvature approach infinity); the confocal region, where the cavity length is equal to the radii of curvature, R_1 and R_2; and the concentric region, where the cavity length is equal to twice the mirror radius of curvature. 39
2.9 Transverse electromagnetic (TEM_{mn}) modes of a Hermite-Gaussian beam, where m and n represent the number of nodes in the horizontal and vertical directions, respectively. The color indicates the electric field amplitude and phase. 41
2.10 Cavity transmission spectrum showing resonances of different Hermite-Gaussian transverse electromagnetic modes TEM_{mn} as a function of detuning, expressed in units of the free spectral range ν_{FSR}. In this example, multiple higher-order modes are populated due to cavity misalignment, which results in imperfect mode matching. The modelled cavity has mirror radii of curvature of 200 μm. Multiple lengths ($65\mu m$, $70\mu m$, and $75\mu m$) are shown to demonstrate how different modes will behave differently. We also note that higher order transverse modes of the lower longitudenal mode can even be higher in frequency that the upper longitudenal mode. 43

2.11 The total collection efficiency CE_{max} and optimal cooperativity C_{opt} are plotted as a function of the intrinsic cooperativity, C_{int}. Several points are included that are representative for specific cavity geometries, including macroscopic cavities[204], photonic crystal Cavities (PCC)[170], Fiber cavities[70], and silicon micromirror cavities[202]. The values used are extracted from existing atom cavity experiments: $(g, \kappa_{sc}, \gamma) = 2\pi \times (7.8, 0.4, 6)$ MHz[204], $2\pi \times (624, 2.77, 6)$ MHz[170], $2\pi \times (100, 7.5, 6)$ MHz[61,70], $2\pi \times (100, 1.5, 6)$ MHz[61,46,202] 45

3.1 (A) A characteristic neutral atom quantum system for Rubidium-87, showing optical tweezers projected into a vacuum chamber through a microscope objective using an SLM for static traps of arbitrary geometry and AODs for dynamic, moving traps. Fluorescence from the atoms is collected on an EMCCD for atom readout through a secondary microscope objective. Counter-propagating beams of 420 nm and 1013 nm lasers are used to excite atoms to Rydberg states for performing two-qubit gates. A microwave horn is used to drive single-qubit rotations with a 6.8 GHz field. These rotations can also be driven by an optical field sent along the same path as the beams used for Rydberg excitation. This figure was adapted from Ref.[50] with permission from the author. (B) Qubit information is encoded in the ground states of the atom, $|0\rangle$ and $|1\rangle$, where single-qubit rotations are applied via a microwave drive, $\Omega_{\mu w}$, which can be applied by microwave fields or a modulated laser. The two-photon transition to the Rydberg state $|r\rangle$ is excited using a 420 nm drive, Ω_{420}, and a 1013 nm drive, Ω_{1013}, both far detuned from the intermediate state $|t\rangle$, but on two-photon resonance with the Rydberg state $|r\rangle$. 51

3.2 The energy level structure showing the Rydberg blockade in a two-atom system. The energy of the two atom pair states are shown as a function of interatomic distance R. The lowest energy level corresponds to the ground state $|gg\rangle$. A laser excitation couples the ground state to a symmetric singly excited state $(|rg\rangle + |gr\rangle)$ with an effective coupling strength of $\sqrt{2}\,\Omega$. The coupling to the doubly excited Rydberg state $|rr\rangle$, which is shifted upward by strong van der waals interactions is "blockaded" when the interatomic distance is within the blockade radius R_b where the $|rr\rangle$ state shift exceeds the rabi frequency Ω. 54

3.3 (A) A level diagram illustrating the $\pi - 2\pi - \pi$ gate. ① A π-pulse is applied to atom 1. ② A 2π-pulse is applied to atom 2. ③ A final π-pulse is applied to atom 1, completing the sequence and resulting in a controlled phase gate. (B) The pulse sequence used to perform the $\pi - 2\pi - \pi$ gate. (C) A level diagram showing the time-optimal gate, where a global drive is applied to both atoms with a phase and intensity profile defined by $\varphi(t)$ and $\Omega(t)$. (D) The temporal profile of the phase $\varphi(t)$ and intensity $\Omega(t)$ used to implement the time-optimal gate. This figure was adapted from ref[54] with permission from the author. 57

3.4 (Left) Full Stark map of the $70S_{1/2}$ manifold in rubidium as a function of external electric field. The color scale indicates the dipole transition strength $\left|\langle 70S_{1/2}|\mu|r\rangle\right|^2$. (Right) A magnified view of the stark map, showing how electric fields in combination with strong dipole coupling severely modifies the energy levels as well as mixing rydberg states. 58
3.5 (Left) Displacement Δr of the Rydberg state as a function of the number of charges Q on a point charge source, for various initial distances r_0. The vertical dashed line indicates 50 nm, the typical wavepacket width. (Right) Corresponding wavefunction overlap at $r_0 = 120\ \mu$m, showing rapid decoherence for $Q > 200e$. . 60
3.6 Simulated ground state population after a Carr-Purcell sequence ($N = 2$), as a function of total sequence time T, at distance $r_0 = 70\ \mu$m. 64
3.7 Averaged ground state population over a point charge distribution $q = 200 \pm 10\ e$, for varying sequence times and distances. 65

4.1 A pictorial representation of the fiber cavity experiment, rendered in the style of Studio Ghibli, illustrates an array of atoms trapped above the cavity where entangling operations are performed using Rydberg interactions. Coherent transport is used to shuttle atoms between the quantum processor and the photonic interface. The photonic interface, a fiber-based Fabry–Perot cavity, enables fast readout as well as quantum networking. 67
4.2 (a) An image showing the alignment setup for the fiber cavity when being loaded into the mount. (b) Po aligning the fiber cavity using the x and y plane images. . . 69
4.3 (a) shows a top view of our vacuum chamber with ports (1-3) labeled for the glass cell, ion pump, and turbo pump ports. (b) shows a bottom view of our chamber with ports (4-6) labeled for the fiber feedthrough, back viewport, and electrical feedthrough 72
4.4 (a) Vacuum parts for the chamber are baked in a large oven provided by QuEra Computing, held at 450 °C for two days to reduce outgassing. This process also imparts a brown hue to the parts due to oxidation. (b) The glass cell is carefully placed over the cavity-mount structure. The chamber is tilted upward so that the copper gasket can rest on the "razor blade" of the vacuum chamber. (c) The glass cell is protected by a vacuum-foil wrapping and then wrapped with heater cables. The temperature is monitored at multiple points along the chamber to ensure even heating, which is especially important at the glass–metal interface. For these bakes, we typically go to a temperature of 150 °C for one or two weeks. During the bake, we continuously monitor the fiber cavity to ensure its alignment is not severely shifted. The oscilloscope trace shows the cavity resonance, as well as a sideband used to measure the linewidth. 73

4.5 (a) We receive our fiber cavities from QLibri in a Tupperware container, in which the fibers are mounted on a machined metal structure. (b) The fiber-cavity mount is shown. The piezos, which modulate the cavity length, are attached to a microscope slide. On top of the piezos is a monolithic V-groove that holds the fiber. Part of this V-groove was deliberately broken to allow the piezos to move freely. The fiber cavity is visible in the V-groove, with a single-mode fiber on the left and a multimode fiber on the right; the latter is bent and redirected down the mount. For strain relief, both the piezo wires and fibers are secured to an additional glass slide. 75

4.6 (a) The rod structure used to mount the fiber cavity onto the vacuum chamber. (b) A side view of the chamber, looking along the axis of the fiber cavity. The tilt of the cavity mount permits an imaging beam to enter from the bottom of the chamber and pass through the center of the fiber cavity without clipping. Additionally, the high-NA optical tweezers can be introduced from the side without intersecting the cavity or its mount. 76

5.1 **Nanophotonic interface for atoms in tweezers. (A)** A nanophotonic cavity could act as a photonic link for atom arrays serving as quantum information processors. Our system consists of two atoms in optical tweezers coupled to a fiber-linked cavity capable of a coherent one-way transport. (Inset) Atomic qubit states coupled by a microwave drive Ω_{MW}, with one coupled by the cavity field g to an excited state. **(B)** Cavity reflection spectrum for an atom in a strongly coupled state (blue) and an uncoupled state (gray), described by $(2g, \gamma, \kappa) = 2\pi\times$ (786, 6, 3800) MHz. **(C)** Readout of different two-qubit basis states by using the reflected photon counts. State $|00\rangle$ is distinguished from the others with fidelity $\mathcal{F} = 0.95(3)$. The atoms, cavity, and probe are on resonance. **(D)** Single-qubit Rabi oscillations in the cavity near-field showing preparation and coherent rotation with a π pulse fidelity $\mathcal{F}_\pi = 0.946(3)$. 79

5.2 **Qubit coherence during the transport between the cavity and free space. (A)** Measurement of the echo T_2' for stationary traps at the PCC (red) and in free space (blue). **(B)** Changes in the trapping potential configuration during transport cause differences in the light shift and therefore qubit frequency, which can lead to additional dephasing. The gray line indicates fit to the programmed ramp. **(C)** Single-atom coherence for atoms in each trap (labeled "A" and "B") after transport measured in a Ramsey-type sequence. A four-pulse Carr-Purcell sequence symmetric with respect to the qubit frequency profile during transport was used to echo out the light shift variations. 82

5.3 **Heralded entanglement at the cavity. (A)** Protocol description. Post-selection on a photon reflection from a superposition state carves out the $|00\rangle$ component, leaving the atoms predominantly in $|\Psi^+\rangle$. **(B)** Populations of the resulting state in different basis states. A $\pi/2$ pulse was applied before the measurement converting the Bell state $|\Psi^+\rangle$ into $|\Phi^+\rangle$. $\{P_{11}, P_{00}\}$ is extracted {with, without} an additional global π pulse before cavity reflection reflection. P_{01} and P_{10} cannot be distinguished. **(C)** Parity oscillations of the $|\Phi^+\rangle$ state after rotating over a varied axis φ, showing non-classical correlations between the qubits in all bases. The coherence $\rho_{11,00}$ is extracted from the amplitude. The combined coherence and populations gives a Bell state fidelity of $\mathcal{F} = 0.72(3)$. 83

5.4 **Coherent transport of entangled atoms from the cavity to free space.** After entangling the atoms at the cavity, the tweezers are moved away while applying dynamical decoupling. Free space readout in different bases after transport shows the remaining entanglement fidelity of $\mathcal{F} = 0.65(6)$, which is larger than the classical limit of 0.5. 85

6.1 Rydberg spectral shift. (a) Experimental setup. (b) Two-photon excitation to the Rydberg state which is shifted by electric fields (yellow shade). (c) Ground state population P_g as a function of the two-photon detuning Δ at 150 μm from the device, where the spectrum center (dashed line) is determined via a Lorentzian fit (black line). (d) Measured spectral shift as a function of distance from the device fitted to a point-charge model (yellow line, Supplement B, Section 2.1). The shift only exceeds the Rabi-broadened linewidth (shaded gray region) for distances less than 250 μm. (Inset) Spectral shift dependence on UV power at 160 μm. 89

6.2 Ground-Rydberg qubit coherence. Ground state population P_g as measured after a Ramsey (a), spin-echo (b), and Carr-Purcell (CP) $N = 2$ (c) pulse sequences at 130 μm (dotted line in (d)). A decaying sinusoid fit (blue line) gives $T_2^* = 200(40)$ ns and a Gaussian decay function (red line) gives $T_2 = 4.1(2)$ μs. The CP $N = 2$ data exhibits no decay within the measurement time. (d) Measured T_2 (red circles) and T_2^* (blue circles) as a function of distance from the device. The solid lines are fits to the data given our decoherence model (Supplement B, Section 4). The shaded green region is a lower bound on the CP $N = 2$ coherence time. 92

6.3 Two-atom entangled state. (a) The Rydberg interaction U shifts the $|rr\rangle$ state and allows the preparation of the $|W\rangle = \frac{1}{\sqrt{2}}(|gr\rangle + |rg\rangle)$ state. (b) Tomography of the $|W\rangle$ state (purple) at 170 μm. We measure population $\rho_{rg,rg} + \rho_{gr,gr} = 0.87(5)$ and coherence $2|\rho_{gr,rg}| = 0.78(7)$ with correction for preparation error and loss (light purple). (c) Comparison between the two-atom $|W\rangle$ state lifetime T_W (purple circles) and the single-atom ground-Rydberg coherence time T_2^* (gray circles, data and fit from (Fig. 6.2(d))). The dotted purple line is a theoretical prediction (Supplement B, Section 5.4). 94

6.4 Entanglement-assisted sensing of electric field gradients. (a) The orientation of an entangled atom pair is varied with respect to the device. (b) The $|W\rangle$ state lifetime measurement (blue circles) reveals gradient-induced oscillations by fitting to a decaying sinusoid (blue lines) for different θ (offset for clarity). (c) Angular dependence of the fitted oscillation frequency at different x (circles) with solid curves being simultaneous fit (Supplement B, Section 6) to extract background field orientation. (d) A 200 nW UV-power reduction from its optimized value causes a rotation (53 degrees) of the gradient. (e) Reconstructed electric field magnitude $|\vec{E}|$ (contour scale) and direction (white arrows) given the measurements in (c) at the positions of the black circles. (f) Electric field contour plot reconstructed from (d) showing direction at the optimal UV value (gray arrow) and shifted UV value (orange arrow). 95

7.1 **Experimental setup and qubit readout. (A)** Atoms in optical tweezers are loaded above a Fabry-Perot Fiber Cavity (FPFC) and transported into the cavity mode. The FPFC has a single-mode input port and a multi-mode output port, over which we collect transmitted light. The FPFC length is stabilized using an 810 nm laser and the atoms are trapped in a 850 nm mode of the cavity. The 780 nm mode couples to the D2 line in Rubidium. The magnetic field is aligned along the cavity axis. **(B)** Atomic level diagram of Rubidium-87. Readout is performed with the cavity on resonance with the $2 \leftrightarrow 3'$ transition, while for entanglement generation the cavity is tuned to the $1 \leftrightarrow 1'$ transition. **(C)** Resonant transmission spectra of a bare cavity (gray), one atom (blue), and two atoms (red) coupled to the cavity. The lines are a simultaneous fit yielding parameters $g = 2\pi \times 100.0(8)$ MHz and $\kappa = 2\pi \times 65(1)$ MHz, resulting in a cooperativity of $C = 101(2)$. **(D)** Histograms showing photon counts collected in 10 μs with an atom in the F=1 state (grey) and an atom in the F=2 state (blue), yielding a qubit state readout fidelity of $99.960^{+14}_{-24}\%$. 102

7.2 **Photonic dark state spectroscopy. (A-B)** Side drive spectroscopy of one (A) and two (B) atoms coupled to the cavity as a function of cavity and probe laser detuning (Δ_C and Δ_P, respectively). With two atoms coupled to the cavity, the spectrum reveals a feature on resonance with the atomic transition, corresponding to a photonic dark state. **(C)** Energy level diagram of the first excitation manifold for one and two atoms coupled to a single cavity mode, which correspond to the states probed in the spectra plotted against the cavity detuning, Δ_c (*S4.1*C). **(D)** Probe spectroscopy at $\Delta_C = \Delta_A$ for one (blue circles) and two (red circles) atoms coupled to the cavity while probed with a side beam. Lines are simultaneous fits to a numerical model (*S4.2*C). 103

7.3 **Bell state preparation with cavity carving. (A)** For entanglement generation, the cavity is tuned to the $1 \leftrightarrow 1'$ transition and a single side drive on the $2 \leftrightarrow 1'$ transition is applied to atom A only. **(B)** (top) Quantum circuit for preparing two-qubit states and measuring the $|err\rangle_A$ population. (bottom) Decay rates into the error states after preparing each of the four two-qubit states. The resonant coupling to the dark state $|D_0\rangle$ results in much faster decay of $|10\rangle$ compared to the off-resonant coupling in $|11\rangle$. $|00\rangle$ and $|01\rangle$ do not couple to the driving beam. **(C)** (top) Quantum circuit of a Carr-Purcell cavity carving scheme which prepares a $|\Phi^-\rangle$ Bell state. (bottom) Measured correlations in the ZZ (blue), XX (red), and YY (green) bases verify that $|\Phi^-\rangle$ is prepared with a Bell state fidelity of $\mathcal{F} = 91(4)\,\%$ and a success probability of $32(1)\,\%$. Direction of histograms denote the expected sign of parity for $|\Phi^-\rangle$ in each bases. **(D)** Bell state fidelity (blue circles) and success probability (red circles) as a function of carving pulse length τ. Stars mark the data presented in (C). Lines are a fit to a semi-classical numerical model, and the gray line is the expected Bell state fidelity without SPAM errors (*S7.1*C). Dotted line denotes the fidelity limit for verifiable entanglement. 107

7.4 **Deterministic quantum gate with error detection. (A)** Conditional blockade mechanism. A resonant 2π Rabi oscillation can be realized only between the $|10\rangle$ state and the dark state $|D_0\rangle$, causing a phase of π on state $|10\rangle$, while the excitation from the $|11\rangle$ state is blockaded. Unwanted atomic scattering results in mainly detectable $|err\rangle_A$ states. **(B)** Quantum gate flow chart showing the two possible outcomes: "Success" is a conditional phase on atom B and "Failure" is a detectable scattering event **(C)** Quantum circuit of the gate: Following the gate, we apply a local Z_π pulse on atom B and a global microwave $X_{\pi/4}$ pulse to generate the $|\Phi^+\rangle$ Bell state. **(D)** Measured correlations in the ZZ (blue), XX (red), and YY (green) bases verify that $|\Phi^+\rangle$ is prepared. (dark) Without error detection, we measure a deterministic Bell state fidelity of $\mathcal{F} = 52.5(1.8)\%$. (light) Error detection improves the fidelity to $\mathcal{F}' = 76(2)\,\%$ with a success probability of $69(1)\,\%$. Direction of histograms denote the expected sign of parity for $|\Phi^+\rangle$ in each bases. 109

8.1 Four types of mirrors are shown. The first is the traditional diamond-milled mirror, capable of a radius of curvature (ROC) and diameters greater than 5 mm[44]. The second, a buckled micromirror (discussed further in this chapter), achieves smaller dimensions, with diameters exceeding 300 μm and ROCs above 900 μm[46]. The third type is the CO_2 laser-ablated fiber mirror, with achievable ROCs between 30 and 300 μm[70] (up to 1 mm using special techniques[137]) and a fixed fiber diameter of 125 μm. Lastly, the silicon micromirror offers ROCs ranging from 30 to 900 μm and can have a diameter as small as 40 μm[202]. 113
8.2 (a) Schematic of the CO_2 laser ablation setup. (b) Optical-microscope image of the ablated silica substrate. (c) Scanning stylus profilometer measurement of the ablated surface, showing its overall Gaussian-like shape. 114
8.3 (a) Atomic force microscope (AFM) surface profile of the ablation. (b) Residual of a 4th-order polynomial fit to the surface, revealing an RMS roughness (R_q) of 1.8 Å. 114
8.4 (a) Array of CO_2 laser ablation sites measured with a scanning stylus profilometer. (b) Parabolic fits to the bases of the micromirror ablations, indicating the variation in radius of curvature and depth across different ablation sites. 115
8.5 Two cavity geometries and their mode matching. The first geometry is a fiber cavity formed by two 150 μm ROC fiber mirrors. The red represents the single-mode fiber output $|\psi_{\text{fiber}}\rangle$ and the blue the cavity mode $|\psi_{\text{cavity}}\rangle$. Their limited overlap results in a low mode matching efficiency (orange curve), $\eta = \left|\langle\psi_{\text{fiber}}|\psi_{\text{cavity}}\rangle\right|^2$. The second geometry is a hybrid cavity employing a 200 μm ROC fiber mirror and a 110 μm ROC silicon micromirror, which enhances mode matching (blue curve). The adjacent plot shows the mode matching as a function of cavity length, highlighting the superior performance of the hybrid configuration. 116
8.6 Silicon Micromirror Fabrication and Profile Characterization: (a) A diagram illustrating the fabrication flow. (b) A microscope image of a 15×15 array of 60μm-diameter silicon micromirrors, demonstrating the reproducibility and high density achievable with this technique. (c) An SEM image of a Bosch-etched silicon micromirror structure, providing large optical access. (d) The cross-section of a silicon micromirror fit, showing excellent agreement with a spherical model. (e) An AFM image of the silicon micromirror substrate prior to film deposition; the residual from a spherical fit is displayed and used to calculate an RMS surface roughness (R_q) of 0.5 Å. 117
8.7 Compact micromirror array and device (a) a photo of the fabricated micromirror array and a singular micromirror next to a penny and a half inch diameter Thorlab mirror used in a commercial Fabry Perot cavity. (b) Finesse and quality factors as figures of merit for FP cavities. 119

8.8 Micromirror fabrication and profile characterization (a) The diagram for the fabrication flow. (b) The fabricated micromirrors of d =600 μm. The left two are microscope images. The top right image is an SEM image. The bottom right image is an AFM image of the Si substrate before the film deposition, representing the lower bound of the mirror surface roughness. (c) The simulated mirror shape, assuming a uniform strain of .3% in the film, compared to the measurement, shows almost perfect agreement. (d) The depth and ROC of the fabricated mirrors as a function of the diameter defined by lithography. (e) The fabricated mirror's X and Y cross-section profile shows perfect rotational symmetry. The inset is a contour plot of the mirror profile. The profile data shown in (c) and (e) are taken by PL on a d =600 μm mirror. 121

8.9 Microcavity characterization (a) A diagram for the measurement setup. CAM: camera; PD: photodetector; Scope: oscilloscope. The data is the transmission signal of the cavity while scanning the cavity distance with a piezoelectric transducer. (b) The FSR of the cavity at a cavity length of 58.7 μm is 2.5 THz. There are three modes visible in the range. The modes are confirmed by corresponding the shape of the transmitted light on the camera to the Hermite polynomials. (c) The Q and finesse vs. cavity length data. (d) The data point that corresponds to the highest finesse of 0.9 million. (e) The data point that corresponds to the narrowest linewidth of $\kappa = 2\pi \times 124 \pm 0.5$ kHz. (f) The F survey to show the yield on a 3-by-3 chip of d= 600 μm mirrors. They are measured against another d= 600 μm buckled micromirror. Most of them show high finesse at L=175 μm, that are consistent with the data points from (c). 124

8.10 Microcavity assembly (a) A photo of the measurement setup and the actual measured cavity device. The fiber is a visible fiber that has been cleaved. The inset shows the cavities with two different lengths (45 μm and 1 mm). The tip is inserted into the cavity mirror slot from the back. (b) The measured ringdown of the cavity for the cavity assembly at different lengths. The laser frequency is swept in this case. 126

9.1 (A) Two Neutral atom quantum processor nodes connected by an optical link allowing for distribution of entanglement through photons. (B) The architecture of a single modular quantum processor, which includes an entangling zone for two qubit gates mediated by Rydberg excitation, a storage zone for holding many qubits, and a networking zone where atoms can be entangled with photons, enabling fast high fidelity quantum networking. (C) A scanning electron microscope (SEM) image showing a fabricated microcavity optical interconnect. 131

9.2 Multiplexed atom photon entanglement can be generated by utilizing coherent transport through the cavity while simultaneously emitted photons through the cavity as they travel through the cavity mode, enabling faster entanglement attempt rates. 132

9.3 **(A)** Two modules containing arrays of atoms coupled to arrays of optical cavities are used for multiplexed REG. **(B)** Each module will consist of a chip integrated microcavity array coupling to an array of atoms. **(C)** A cross-section showing the material stack of the proposed device. This device will provide fast tuning of the cavity resonance and directed emission into the photonic interface through grating couplers. 133

9.4 (A) An array of atoms coupled to an optical cavity, with one atom designated as an ancilla and the others serving as qubits. The ancilla is locally addressable via a tightly focused beam used for gate operations. (B) Level structure: the ancilla atom has three relevant states—an initial state $|i\rangle_a$, an excited state $|e\rangle_a$, and an error state $|err\rangle_a$. The transition $|i\rangle_a \leftrightarrow |e\rangle_a$ is driven via a two-photon process, with one leg provided by a local optical drive Ω_{opt} and the other by a microwave drive $\Omega_{\mu w}$. This approach enables the use of states in which all gate-induced errors are, in principle, detectable, owing to the suppressed direct coupling between $|e\rangle_a$ and $|i\rangle_a$. The $|e\rangle_a \leftrightarrow |\text{err}\rangle_a$ transition is strongly coupled to the cavity with detuning Δ. Qubit atoms are coupled to the cavity through the $|1\rangle \leftrightarrow |e\rangle$ transition with a detuning of δ, such that the $|1\rangle$ state induces a dispersive shift of the cavity resonance, while the $|0\rangle$ state remains uncoupled. 136

9.5 (A) An atom in a fiber mirror–silicon micromirror cavity driven from the side by 1033 nm and 780 nm laser fields. These drives produce 1529 nm telecom photons can be entangled with the atomic qubit states.(B) Energy level diagram illustrating the two-photon process used for atom–photon entanglement: a 1033 nm excitation, Ω_{1033}, couples the $|5P_{3/2}\rangle$ and $|5S_{1/2}, F = 1\rangle$ states, resulting in the emission of a 1529 nm photon via strong coupling to the cavity with strength g_{1529}. An additional 780 nm, drive, Ω_{780}, on the $|5S_{1/2}\rangle \leftrightarrow |5P_{3/2}\rangle$ transition coherently maps the system back to the qubit manifold, thereby generating an entangled pair between the telecom photon and the atomic qubit. 142

9.6 (A) An image of the fiber mirror-silicon micromirror device shows the fiber cavity mounted in the v-groove structure, with the micromirror cavity glued to the side of the v-groove. The v-groove is then mounted on two shear plate piezos, as seen in the lower left and right. (B) A zoomed-in image of the fiber mirror-silicon micromirror device demonstrates that the micromirror design offers ample optical access. (C-D) The linewidths of the 1530 nm and 780 nm resonances of the cavity were measured using sideband spectroscopy with sidebands of 200Mhz and 500MHz, respectively. The 1530 nm line exhibits a linewidth of $2\pi \times 65$ MHz, corresponding to a finesse of 30,000, while the 780 nm line has a linewidth of $2\pi \times 23$ MHz, corresponding to a finesse of 81,000. 144

9.7 (Left) The low passed reflection signal showing sidebands on the laser. This reflection signal is plotted for a variety of mode matching values showing that the depth of the signal increases and then begins to decrease again, making it challenging to determine the mode matching. (Right) the PDH error signal generated when demodulating the laser light from the cavity . This is plotted as a function of mode matching to show that as the mode matching increases this signal increases. 146

A.1 Experimental sequence. **(A)** Time breakdown of a typical two-atom entanglement sequence between atom-A and atom-B. **(B)** An experimental sequence for the coherent transport of the atomic states that incorporates phases both at the cavity (red and green) and in free space (blue). 152

A.2 An illustration of the Raman-assisted state preparation. Cycling between repumping the atom into $F = 1$ (green) and depleting the population in $m_F = \{-1, 1\}$ (blue) leaves the atom in $|1, 0\rangle$. 156

A.3 Sketch of the interferometer in the detection path used to improve the reflection contrast between a cavity with and without coupled atoms. 161

A.4 Parameters that determine the entanglement fidelity. (Left) Dependence of the maximal Bell state fidelity (solid lines, left y axis) and protocol success probability (dotted lines, right y axis) on the initial angle and interferometer contrast. Not using the interferometer would limit the maximal fidelity to $\sim$ 0.6. With our measured interferometer contrast of 0.96, the fidelity is limited to 0.76 (black dot). (Right) Keeping the interferometer contrast the same, the protocol maximal fidelity can be improved by using a cavity with a smaller reflectivity R_{00}. 162

A.5 Comparison of the experimental measurements (blue), mixed model predictions (red), and coherent model predictions (green) for the parity measurement (left panel) and the ZZ basis populations (right panel). 164

A.6 Temperature-limited Ramsey decay. **(A)** Ramsey decay of an atom next to the PCC fitted using the model described in [92], giving $T_2 = 0.35(4)$ ms. **(B)** Linear dependence of the Ramsey dephasing rate on the temperature. 168

A.7 Measured lifetime of 180(7) ms at a trap depth of 2.7 mK next to the PCC. . . . 169

A.8 Sketches of how variations in detuning can cause dephasing. **(A)** Variations in the overall qubit frequency offset (vertical variations), caused by atom's finite temperature, can be echoed out with an even number of CP pulses. **(B)** Variations in the moving trajectory (horizontal variations), caused by trap pointing instabilities, cannot be echoed out exactly and contribute to extra dephasing. 173

A.9 Optimizing the number of pulses in the CP sequence for a moving atom. **(A)** CP sequences of $N = (1, 2, 4)$ pulses that begin with an atom at the cavity and end with an atom in free space. Decoupling pulses are applied in parallel with the transport. **(B)** Fitted contrast of the CP sequences versus the number of CP pulses. 174

A.10 The effects of temperature and trap depth on the survival probability of an atom loading into the cavity near-field. The theoretical curves are generated by averaging over classical trajectories weighted by the Boltzmann factor with no free parameters. Our experimental observations (yellow circles) are taken at a trap depth of 1.6 mK. Previous work on our platform with Raman sideband cooling before transport observed 0.94(6) survival probability (yellow star)[193]. 176

B.1 Single-atom Rabi oscillations near (130 μm) and far (1300 μm) from the device. The decay time τ decreases close to the device with $\tau_{130} = 1.6(1)$ μs and $\tau_{1300} = 4.9(2)$ μs. 180

B.2 SiN device attached to a silica fiber. **(a)** Diagram showing the dimensions and angles of the device with respect to the $x-$axis. **(b)** Measured spectral shift (green circles) as a function of distance from both the device and the fiber surface. We fit the measured shifts to a point-charge (blue) and a line-charge (pink) model, finding good agreement with charges on the SiN device and not on the fiber. . . . 182

B.3 UV power tuning. **(a)** Rydberg spectral shift settling after changing the UV power at 160 μm. **(b)** Settled shift at different distances as a function of the UV power. The 160 μm curve is generated from the averages of white-faced points in (a). For Fig. 4(D) in the main text the UV power is changed from the optimal value (star) to the shifted value (square). 184

B.4 Effect of large UV power. **(a)** Measured spectral shift as a function of UV power at a distance of 1 mm from the device. A single parameter linear fit is included as a guide to the eye. **(b)** Spectral shift as a function of distance from the device at a UV power of 29 mW. The line is a fit to a point-charge model with $Q = 3.4(3) \times 10^4$e charges and $E_x = 0.08(4)$ V/cm. The points marked by in a star are the same data point. 185

B.5 Rydberg production studied at 130μm. **(a)** After the initial settling of the Rydberg spectral shift over the first hour, the experiment is run without an atom in the tweezer. When the single atom is again loaded, the spectral shift settles. The dashed blue line and shaded region is the average settled value and standard deviation from (b). **(b)** The Rydberg spectral shift monitored between periods of running the experiment with no Rydberg excitation by not sending the 420nm or 1013nm light. The dashed blue line and shaded region is the average settled value and standard deviation respectively. 187

B.6 Rydberg spectral shift stability in time. **(a)** Stability shown over 8 hours at several distances after the initial settling of the spectral shift. The shaded area here is the Rabi-broadened linewidth of 3MHz. **(b)** Reproducibility over 6 days at 160μm where many settling periods can be seen, each after a period of either not running the experiment or not exciting Rydberg atoms. The shaded area is one standard deviation ($\pm$ 0.9 MHz) around the average settled value (7.2 MHz) of all curves. . 187

B.7 Variance of the Rydberg shift detuning as a function of distance. Plotted are different distance scalings, suggesting that the measured variance scales as $1/|r|^4$. . 193
B.8 Model comparison of Ramsey decay time. We compare a model taking into account only charge fluctuations and constant baseline T_2^* (red) to the model that incorporates both charge and **E** fluctuations (blue). 194
B.9 Pulse sequence that cancels polynomial phase noise up to t^2 contribution. 198
B.10 $|W\rangle$-state coherence measurement embedded in a Ramsey-type sequence (blue) $\pi - \delta \cdot t - \pi$ and embedded in an echo-type sequence (red) $\pi - \delta \cdot t - 2\pi - t - \pi$. The fitted decays are $\tau_{\text{in Ramsey}} = 570 \pm 10$ ns, $\tau_{\text{in echo}} = 930 \pm 10$ ns. 200
B.11 Preparation fidelity of the $|W\rangle$-state at two distances from the device. Both the SPAM corrected (blue) and the uncorrected (red) fidelities are shown. We observe little dependence of the fidelity on distance from the device. 201
B.12 $|W\rangle$ state fidelity for three different orientations with inter-atomic distance 3.15 μm. The energy differences between the atoms for $\theta = 45^o, 90^o, 135^o$ are 0.11 MHz, 0.63 MHz, 0.84 MHz respectively. 201
B.13 Uncorrected Rydberg-blockaded Rabi Oscillation. This data corresponds to the corrected data for the diagonal elements shown in Fig. 3(B) of the main text. We observe a blockaded Rabi frequency of $\Omega_{Blockade} = 2\pi \times 4.46(3)$ MHz between the $P_{|gg\rangle}$ (red) and $P_{|gr\rangle} + P_{|rg\rangle}$ (blue) populations. Additionally, the $P_{|rr\rangle}$ population oscillates at $\Omega = 2\pi \times 3.2(1)$ MHz agreeing with the expected non-blockaded Rabi frequency and therefore expected behavior given uncorrected single-atom loss. 204
B.14 Gradient scaling with distance from the device. **(a)** The oscillation frequency at two angular orientations of the atom pair. **(b)** Extracting the power law scaling a/r^n of the gradient magnitude for each angular orientation measured. For $\theta = 0^o$: $n = 4.6 \pm 0.6$ where we expect $n = 5$. For $\theta = 90^o$: $n = 3.4 \pm 0.2$ where we expect $n = 3$. 209
B.15 Rydberg spectral shift as a function of distance from the device. Comparing data used in Fig. 1 in the main text (blue) where the UV value was optimized for each point, and data from Fig. 4 (pink) where the UV value was kept at the value that minimized the shift at 160μm for each point. The two datasets were taken 6 months apart but a similar electric field environment could be stabilized. 210
B.16 Rydberg blockade softening at an inter-atomic distance of 6.3 μm. Polar plot of measured (pink) and calculated (blue) Rydberg-Rydberg interaction strength. We find reasonable agreement between data and theory when using the electric fields found by fitting the measured gradient as shown in Fig. 4(C) of the main text. . . 214

C.1 **FPFC Mounting and Characterization.** (A) Photo of the mounting structure for the Fabry-Perot Fiber Cavity. (B) Cavity transmission *vs.* piezo voltage (blue circles) when probed with resonant light using 300 MHz sidebands. A fit to 3 Lorentzians (blue line) reveals the cavity linewidth $\kappa = 2\pi\times 57.9$ MHz and finesse $\mathcal{F}_{cav} = 25904$ assuming a 100 μm length. (C) The mounting structure for the Fabry-Perot Fiber Cavity in vacuum 217

C.2 Experimental Sequence for: A) the experiments presented in Figs. 1-2 in the main text; B) cavity carving and the data in Fig. 3 in the main text; and C) Bell state preparation using an error-detected gate and the data in Fig. 4 in the main text. . . 219

C.3 Atom positioning in the cavity mode. **A** Single-shot spectra (averaged) of single atoms placed at different positions along the cavity. **B** and **C** Two such spectra at positions of minimum (2.64 um) and maximum (4.95 um) coupling. The solid lines are fits of the form $T(\delta)$ in (C.5). **D** Fitted atom-cavity coupling strength g as a function of position along the cavity. The solid line is a fit of the form $g(x) = a\cos(2\pi(x - x_0)/P) + c$. Note that we use the fitted period P to calibrate the distance along the cavity. 220

C.4 Atom Positioning in the 810 nm Cavity Mode: We present single-shot spectra (averaged) of single atoms placed at various positions along the cavity using the 810 nm lattice. The cooperativity as a function of position is fit to a model based on the intensity profile of a standing-wave Gaussian beam. From this fit, we extract a Rayleigh range of 62(10) μm, consistent with a cavity waist of 3.9(3) μm. Additionally, the beat note between the 810 nm trap and the 780 nm mode yields a spatial period of approximately 11 μm. 222

C.5 **FPFC laser system.** Diagram of the lasers coupled to the FPFC and the different locking systems for the cavity and each laser. Waveplates and fiber couplings have been ommitted. 224

C.6 **Readout Characterization.** (A) Measured count-rate C_M *vs.* probe count-rate C_P (gray circles) of our detection system with a fit (gray line) to model in Eqn. C.1 used to extract detector dead time. (B) Degenerate cavity allows for fast pumping into stretched state for enhanced coupling during readout. (C) Photon count-rate when with coupled atom C_{Atom} *vs.* probe count-rate C_P showing the breakdown of the linear weak-probe regime. (D) 2D histogram of readout pulse characterization, showing the counts of subsequent state- and atom-readout pulses for atoms in the coupled (green) and uncoupled (orange) ground state manifolds, as well as for an empty cavity (gray). Transparency is proportional to occurrence, normalized to the highest of each case. Dotted lines are optimal threshold to minimize infidelity. (E) Measured infidelity for atom (pink) and state (purple) readout *vs.* probing time for two different probe powers. Black dotted curves are the theoretical expected infidelity from the known count-rates. Gray dotted lines are the measured best probing time in each case to find minimum fastest infidelity. (F) Lowest measured infidelity for atom (pink) and state (purple) readout *vs* probe count-rate, which is proportional to the probe power. 229

C.7 Readout sequences for one (A) and two (B) atoms. The tables show the corresponding readout labels for each group of distinguishable states. 231

C.8 Side spectrum of the ^{87}Rb D_2 line showing the avoided crossings and the hyperfine structure. 235

C.9 (A) Quantum circuit for preparing two-qubit states and measuring the $|err\rangle_A$ population. (B) With the cavity tuned to the $2 \leftrightarrow 1'$ transition, we measure the probability of transferring population to the $|err\rangle_A$ state as a function of probe detuning for the $|11\rangle$ state (blue) and the $|10\rangle$ state (red). The solid line shows theoretical simulations of the system with characteristic parameters. This curve shows relative agreement of the numerical model with experimental data, and is not used to extract any specific parameters. (C-D) Measurements of the probability of transferring population to the $|err\rangle_A$ as a function of both probe detuning and cavity detuning for the $|11\rangle$ state (C) and the $|10\rangle$ state (D) 237

C.10 (A) The level structure for both the carving and CZ gate protocols. The cavity is coupled to the $|err\rangle_A \leftrightarrow |e\rangle_A$ transition and the $|0\rangle_B \leftrightarrow |e\rangle_B$ transition. Atom A is driven from the side by a drive Ω_A that couples $|1\rangle_A$ and $|e\rangle_A$. (B) Upon diagonalization of the states coupled to the cavity, we show the effective level structure for a weak drive Ω_A. Here, the $|11\rangle$ state experiences a suppressed excitation due to the avoided crossing formed by the splitting of the states $|\pm\rangle = |e\rangle_A|0\rangle_{ph} \pm |err\rangle_A|1\rangle_{ph}$. The $|10\rangle$ state couples resonantly to the dark state $|D\rangle = \frac{1}{\sqrt{2}}\left(|e\rangle_A|0\rangle_B - |err\rangle_A|e\rangle_B\right)|0\rangle_{ph}$ while being detuned from the bright states $|B_\pm\rangle = \frac{1}{\sqrt{2}}|err\rangle_A|0\rangle_B|1\rangle_{ph} \pm \frac{1}{2}\left(|e\rangle_A|0\rangle_B + |err\rangle_A|e\rangle_B\right)|0\rangle_{ph}$. 242

C.11 Hyperfine structure of the D_2 line in ^{87}Rb. The laser driving and cavity field couples only a small subset of the hyperfine states marked in red under the assumptions mentioned in the main text. 250

D.1 (a) Reflectivity spectrum of the coating from FiveNine Optics (b) The reflectivity spectrum for the high reflectivity region of the coating from 750nm to 820nm showing a minimum transmission of 1.33ppm 259
D.2 Comsol simulations of the profile of the buckled mirror 264

To my Family

Acknowledgments

The work presented in this thesis represents the culmination of nearly a decade of research in this field. I would like to thank not only those with whom I worked during my Ph.D. but also the many people who have supported and guided me along the way.

First, I must express my gratitude to my advisor, Misha Lukin, who gave me the freedom to explore the scientific questions I found intriguing while gently steering me toward projects that could "benefit humanity". He has cultivated a fantastic environment for delving into quantum science. I am also deeply grateful to Vladan Vuletic, the co-PI of my experiment, whose extensive knowledge of atomic physics and quantum optics was invaluable in overcoming technical challenges. In addition, I would like to thank Susanne Yelin for serving on my committee and for being an excellent sounding board for both scientific and career-related questions. My thanks also go to Federico Capasso, whose perspective beyond quantum physics and engaging conversations over the past six years enriched my journey. I also thank Kiyoul Yang, who I have had the privilege of working with throughout the later years of my Ph.D. and was willing to stand in as a back-up committee member.

Even before beginning my Ph.D. at Harvard, I had already started exploring atomic physics and quantum optics. This began in high school when I interned at the National Institute of Standards

and Technology, working with Trey Porto, Elizabeth Goldschmidt, and Roger Brown, each of whom I still see frequently at conferences and I thank for introducing me to the field. I remember when Elizabeth first handed me a Griffiths textbook; that experience marked my first real exposure to physics, setting me off on this lifelong journey.

After high school, I continued working in Trey's lab at the University of Maryland, where I became acquainted with James Maslek, Eric Magnan, Pierre Bataille, Carlos Bracamontes Palma, Thomas Boulier, and AJ Hachtel. I thank them all for teaching me many fundamentals of laser cooling and neutral atoms. On Eric's recommendation, I spent a semester abroad at L'Institut d'optique in Paris.

In Paris, I had the opportunity to work with Antoine Browaeys and Yvan Sortais. Yvan immersed me in the optics of trapping single atoms and taught me proper alignment techniques. I am grateful to all the members of the Browaeys group at that time, including Ludovic Brossand, Sylvain de Léséleuc, Vincent Lienhard, Thierry Lahaye, Daniel Barredo, and Florence Nogrette.

After returning from Paris, I graduated from the University of Maryland and spent the summer working at Princeton with Jeff Thompson. I am thankful to Jeff for inviting me to join his lab, even though I was a somewhat random student who had emailed him. Jeff's exceptional motivation, capability, and inspirational approach to science made working with him a fantastic experience, and the first time I felt that I could contribute meaningfully, applying all I had learned. I also had a wonderful time with the rest of the Thompson lab, including Sam Saskin, Jack Wilson, Rohit Dilip, Alan Dibos, Chris Phenicie, and Mouktik Raha. This group not only produced outstanding science, but also created many memorable moments in the lab.

I then spent a gap year before graduate school at the University of Wisconsin, Madison, working with Mark Saffman. I am grateful to Mark for the opportunity to join his lab. His review paper on neutral-atom quantum computing was a major inspiration for my pursuit of this field, which made the experience in his lab extremely special. There, I met a fantastic group of people, including

Trent Graham, Zac Alphonse Marra, Minho Kwon, Chris Yip, Chris Young, Xiaoyu Jiang, Juan Bohorquez, Preston Huft, and Cody Poole, as well as colleagues outside the Saffman lab, such as Shimon Kolkowitz. I will never forget the late nights in the lab with Trent and I continue to admire his dedication, and I still encounter Alphonse in various settings, a trend I hope continues.

Finally, after several years of working in various laboratories, I began my Ph.D. at Harvard, joining the lab of Misha Lukin. There, I met a truly remarkable group of people who foster an atmosphere of scientific creativity, technical rigor, and camaraderie. When I joined the atom-cavity subgroup -also known by our lab number B01 - the team comprised Po Samutpraphoot, Tamara Djordevic, and Paloma Ocola, all of whom were much ahead of me in their PhD work. I am immensely grateful to Po for encouraging me to explore bold new directions and for teaching me to approach problems more scientifically. Our time together in our two-person COVID pod made the pandemic bearable, especially during the DOTA sessions afterward with Harry, David, and Maddie. I am equally grateful to Tamara for instilling in me a critical perspective on science and imparting essential technical quantum optics skills. Whenever I presented a hand-waving argument, she was always able to demonstrate its flaws with rigorous mathematics. I am also grateful to Paloma for teaching me to continually question our scientific methods and for introducing me to the musical styling of Carly Rae Jepsen and Dad Rock, genres that are still appreciated in B01 today. All of these mentors have been instrumental during my PhD and have become lifelong friends. I look forward to our paths crossing again in the future.

Along the way, we were joined by two post-docs, Ivana Dimitrova and Elmer Guardado-Sanchez. The synergy between Ivana, Elmer, and me was crucial for the later stages of my Ph.D. Together, we created a unique experiment at an exceptionally rapid pace. I am grateful to Ivana not only for her deep knowledge of atomic physics but, even more so, for her persistence in pushing the experiment forward when I might have given up. I am equally grateful to Elmer for his superb technical lab skills. Although I consider my own experimental abilities to be strong, I must concede that Elmer

often outpaces me. Many aspects of our experiment rely on his innovative contributions. Both have been wonderful lab mates and friends.

In the past year, although Elmer and Ivana have departed, we have welcomed many new faces, including Danilo Shchepanovich, Eirini Mandopoulou, Andrei Ruskuc, Matthew Bilotta, Offek Tziperman, and Michel Tao. Danilo and Eirini have already begun to advance the next generation of experiments. Danilo, who joined as a new G1, has contributed valuable technical skills that have helped upgrade the system. Eirini, who joined as a master's student, brought a fearless enthusiasm to explore new projects and challenges, taking on tasks that I often found tedious, which has been a driving force for the lab's progress.

Andrei joined as a new postdoc and has spearheaded the initiation of a new experiment. He brings both extensive technical knowledge of quantum optics and a strong drive, which complement the lab remarkably well. I am still amazed by how quickly he mastered atomic physics, as evidenced by his innovative work with a five-daisy-chained AWG setup. I eagerly await the scientific discoveries that will emerge from this new endeavor. To further enhance this new experiment, Matthew Bilotta has joined the team, bringing with him a strong drive and a fresh perspective that promises to propel our research capabilities even further.

In addition to the atom-cavity team, I would like to thank the many other members of the Lukin group, which has now grown to the point where there are almost too many to list, and I am sure I will leave out many.

I am especially grateful to Eric Peterson for being a constant presence throughout my PhD. Somehow, wherever I go, you've always been there to hang out, and I truly appreciate that. I also thank Maddie Cain for being a wonderful companion throughout my PhD—and now, my academic twin (same defense date!).

I would like to thank the atom subgroups of the Lukin group, including Atom Array 1 and Atom Array 2. It has been great to share equipment, knowledge, and laughter with you all. I thank

the Atom Array 1 team—Harry, Alex, Sepehr, Dolev, Simon, Giulia, Marcin, Tout, Sasha, Sophie, Harry, and Tom—for being such excellent collaborators and labmates.

I'm also grateful to the Atom Array 2 team. Watching such a challenging experiment take shape during my PhD has been truly inspiring. I thank Elias Trapp for insightful discussions, Mohammed Abobeih for his essential presence on the volleyball team, and Tim Guo for welcoming me into the Qiao gang for hot pot. I also acknowledge the rest of the team, including Tout, Allen, Simon, Pavel, and Luke, for their camaraderie.

To the SiV team: thank you for countless enjoyable cavity lunches, through which I learned a great deal about quantum networking and your atom-like systems. Special thanks to Can Knaut for supporting Lukin group poker night, and to Pieter-Jan Constant Stas for being a driving force in maintaining group culture with pub crawls, Secret Santas, and Lukin group merch. I thank Yan-Cheng Wei simply for being cool. I'm also grateful to the rest of the SiV team: Yan-Qi, Aziza, Maddie, Daniel Assumpcao, Umut, Francisca, Maxim, Mihir, David, Bart, and Denis.

I owe a special debt to the nanomechanics team for their support during many late nights in the lab. I am particularly grateful to DaLi Schaeffer and Frankie Fung, who taught me invaluable experimental techniques that deeply shaped my Ph.D. I also thank Trisha and Yiqi, who later joined the team and have continued to enrich the Lukin group with their warm and welcoming presence. This trend continues with the addition of Addison and Binhan.

I also thank the theorists in the group including Nishad, Maddie, Nathan, Gefen, Pablo, Varun, Nazli, Shayan, Leo, Emil, Katherine, and Simone.

I also thank Luis Orozco, who came to visit Harvard for only a few months but has been a great inspiration for me to continue pursuing science.

My family has supported me through all these experiences and their unwavering support has helped me throughout my career. I would like to thank my father Douglas Grinkemeyer for teaching me to be an engineer, scientist, and comedian since the day I was born; I still use many of the

skills he has taught me on a daily basis (comedy included). I would like to thank my mother Gina Grinkemeyer, who has been an excellent role model for perseverance and has instilled in me an acceptable level of social skills. I would like to thank my brothers Austin and Nathaniel Grinkemeyer. Thank you for putting up with me and listening to me talk about science over the last few decades, and thank you for making my time outside the lab enjoyable as well.

I would like to thank my long-term friends, I am happy to always know that they are there for me, and when we see each other it is like nothing has changed since we met more than a decade ago. Thanks, Yuchao Dave, Krishna, Prajwal, Andrew, Rodrigo, Elan, Ingyum, Corey, JShih, Jeffrey, Yogith, Glenn Ren and Conor.

Lastly, I would like to thank Sophie Weiyi Ding. Throughout my Ph.D., she has served as a peer, a mentor, a collaborator, and, above all, an incredible companion both in and out of the lab. I am deeply grateful for her support. None of this would have been possible without you.

Citations to previously published work

The chapters of this thesis cover research reported in the following articles:

Chapter 5 and Appendix A have been published as:

> **Entanglement transport and a nanophotonic interface for atoms in optical tweezers**
> T. Đorđević*, P. Samutpraphoot*, P.L. Ocola*, H. Bernien, B. Grinkemeyer, I. Dimitrova, V. Vuletić, M.D. Lukin, Science, Vol 373, Issue 6562, pp. 1511-1514 (2021)

Chapter 6 and Appendix B have been published as:

> **Control and entanglement of individual Rydberg atoms near a nanoscale device**
> P.L. Ocola*, I. Dimitrova*, B. Grinkemeyer*, E. Guardado-Sanchez*, T Đorđević, P. Samutpraphoot, V. Vuletić, and M. D. Lukin, Physical Review Letters, Vol 132, Issue 11, pp. 113601 (2024)

Chapter 7 and Appendix C have been published as:

> **Error-detected quantum operations with neutral atoms mediated by an optical cavity**
> B. Grinkemeyer*, E. Guardado-Sanchez*, I. Dimitrova*, D. Shchepanovich, G.E. Mandopoulou, J. Borregaard, V. Vuletić, M. D. Lukin, Science, Vol 387, Issue 6740, pp. 1301-1305 (2025).

Chapter 8 and Appendix D are in preparation to be submitted for publication as:

> **Near a Million Finesse Near-Infrared Microcavity**
> S.W. Ding*, B. Grinkemeyer*, R. Jiang, G.E. Mandopoulou, A.S. Zibrov, K.Y. Yang, M.D. Lukin, M. Lončar, in preparation (2025)

* These authors contributed equally to this work.

Let's go make the world a better place.

Mikhail Lukin

1 Introduction

Quantum mechanics is a cornerstone of modern physics that governs the behavior of physical systems at microscopic scales. As a field, it has revolutionized our understanding of nature and allowed the development of much of the modern technology that we rely on today. As opposed to our classical intuition, quantum mechanics allows particles to exist in two distinct states simultaneously, also known as superpositions of states. Additionally, particles can exist in non-local correlated states that can only be described by the collective state of both particles, known as entanglement. The

combination of superposition and entanglement results in dynamics that are exponentially challenging to classically simulate. By creating well-controlled quantum systems, we can simulate these intrinsically quantum effects. Further control of these systems can even allow for solving classically intractable problems. This idea is the basis of quantum information science.

Quantum information science leverages the principles of quantum mechanics to process information in ways that classical systems cannot efficiently emulate. The basic unit of quantum information, the quantum bit or qubit, can exist not only in logical states $|0\rangle$ and $|1\rangle$, but in any coherent superposition $\alpha|0\rangle + \beta|1\rangle$. Furthermore, entanglement between qubits enables correlations between two qubits. Together, entanglement and superposition can enable exponential speed-ups in certain computational tasks. As a result, the development of utility-scale quantum computers has emerged as a central goal of both academic and industrial research.

However, despite rapid advances, the realization of large-scale, fault-tolerant quantum computers remains an outstanding challenge. Quantum systems are inherently fragile: interactions with the environment lead to decoherence, and measurement collapses the quantum state. To address these issues, quantum error correction encodes logical qubits into entangled states of many physical qubits, enabling errors to be detected and corrected without disturbing the stored quantum information. Performing error-corrected quantum computation requires a substantial number of physical qubits per logical qubit. Consequently, developing scalable quantum architectures has become a central focus of quantum information science.

Several hardware platforms are currently being pursued for quantum computing, including trapped ions, superconducting circuits, photonics, and neutral atoms. Each offers distinct advantages in terms of coherence time, scalability, and gate fidelity. This thesis focuses on quantum computing with neutral atoms, a platform in which atoms are confined in arrays using optical tweezers.

In particular, this thesis explores the use of optical cavities to enable quantum networking and Rydberg interactions to mediate entanglement for quantum computing. Together, these tools open

the door to building modular quantum processors capable of scaling to larger system sizes by interconnecting multiple units and providing a clear path toward fault-tolerant quantum architectures.

1.1 Neutral Atoms for Quantum Information Science

The leading architectures for neutral atom quantum processors utilize optical tweezers to trap and manipulate single atoms as qubits. Each atom encodes quantum information using internal degrees of freedom, such as electron and nuclear spin. These states interact weakly with the environment, allowing for long coherence times. This capability enables the preparation and control of large arrays of high-fidelity qubits.

These qubits can interact with optical photons to generate atom-photon entanglement for quantum networking and can also be made to interact with each other to perform two-qubit gates for quantum computation. To achieve strong atom-photon coupling, atoms can be placed inside optical resonators. These cavities enhance the interaction between an atom and a photon, allowing high-fidelity atom-photon entanglement and enabling long-distance quantum communication between distant processors.

o mediate interactions between qubits for gate operations, atoms are excited from the ground state to highly excited Rydberg states. These states exhibit large dipole moments, resulting in strong dipole-dipole interactions between nearby atoms. The concept of building a quantum computer using this architecture has been around for almost two decades, but only recently have experimental groups succeeded in achieving high-fidelity quantum operations [168]. These advances have paved the way for the demonstration of a logical quantum processing [16].

1.2 Ultracold Neutral Atoms

The field of ultracold neutral atoms originated with the development of laser cooling techniques, recognized by the 1997 Nobel Prize in Physics[144]. This innovation made it possible to trap and cool millions of neutral atoms to microkelvin temperatures. Because these atoms are electrically neutral, they interact only weakly with their environment and with each other, resulting in long coherence times and enabling high atomic densities. These features quickly led to applications in precision timekeeping using hyperfine transitions in alkali atoms such as rubidium and cesium, transitions that now define the SI unit of the second[171]. More recently, optical transitions in alkaline-earth-like (AEL) atoms, such as strontium and ytterbium, have been used to create the most accurate atomic clocks to date[1,109]. These attributes have also made neutral atoms a promising platform for quantum computing, where long coherence times and large numbers of qubits are essential. However, to harness neutral atoms for quantum computation, it was first necessary to isolate and control individual qubits.

1.2.1 Single Atoms Trapped in Optical Tweezers

Methods for isolating single atoms were developed by the Grangier group in the 2000s[173]. This was achieved by creating tightly focused optical dipole traps, commonly referred to as optical tweezers, to confine single neutral atoms. These traps are generated using high numerical aperture (NA) optics to achieve micron-sized confinement[187]. A spatial light modulator (SLM) is used to project arbitrary static light patterns, while acousto-optic deflectors (AODs) enable the creation of trap arrays that can be repositioned on sub-microsecond timescales[51,5,50]. The combination of arbitrarily shaped static traps and dynamically adjustable traps has been crucial in advancing the field of neutral-atom quantum computing as well as quantum simulation.

Early experiments trapping single atoms in optical tweezers encountered the phenomenon of

light-assisted collisions, where pairs of atoms would expel each other from the trap [173]. This process results in "parity projection," where a trap with an even number of atoms becomes empty, while a trap with an odd number of atoms retains a single atom. This allows for the high-fidelity preparation of single trapped atoms. Once a single atom is trapped in the optical tweezer, its presence can be confirmed by imaging it with the same optics used to generate the optical tweezers. The trapping lifetime of the atom is limited by collisions with background gases, causing the atoms to leave the trap. For a standard system, this time is on the order of tens of seconds. However, with improved vacuum pressure or cryogenic chambers, this can be extended to minutes [115,176].

Another consequence of parity projection is stochastic loading, where only approximately half of the optical tweezers will be occupied with atoms. Despite this limitation, significant progress was made using stochastic loading techniques, enabling demonstrations of single-qubit rotations [81,210], two-qubit gates [71,206,114,77], coherent transport [15], and ground-state cooling [192,83]. With a better understanding of light-assisted collisions, many groups have been able to perform enhanced loading of single atoms to achieve higher filling fractions [24,78,179]. Even with enhanced loading, it is challenging to achieve defect-free arrays. In order to perform more complex quantum computations, one requires methods to deterministically create defect-free atom arrays.

To achieve fully defect-free arrays, atom rearrangement techniques were developed. By imaging the traps to determine the atom occupancy, atoms could be repositioned into any desired configuration. This was first demonstrated by the Lukin group and the Browaeys group in one-dimensional [51] and two-dimensional [5] arrays, and later extended to three-dimensional arrays [8]. These advances made it possible to create large, defect-free arrays of neutral atoms, paving the way for quantum computation with thousands of qubits in a single system.

1.3 Neutral Atom Qubits

Quantum information can be encoded in the internal degrees of freedom of the atom that interact weakly with the environment. This will typically be the electron or nuclear spins. The weak interactions between neutral atoms and the environment provide long coherence times and allow for high-fidelity single-qubit gates.

Neutral atom single-qubit gates are implemented using either laser or microwave drives. For alkali atoms such as Rubidium and Cesium, quantum information is typically stored in magnetically insensitive "clock states," which are hyperfine states in the ground state manifold, separated by gigahertz frequencies. Coherent rotations between qubit states can be performed using a microwave drive, resulting in single-qubit gate times of tens of microseconds. Alternatively, using optical Raman transitions allow for fast ($\approx 100ns$) local single-qubit rotations with high fidelity[97]. After manipulating the qubit states, they can be measured via fluorescence readout by applying a laser that selectively ejects one of the two qubit states from the tweezer, effectively mapping the qubit state to atom presence. Atom imaging is then used to determine the qubit state based on whether the atom remains in the trap. Overall, the coherence and single-qubit operations in neutral atoms are among the attributes that have made the platform promising. The more challenging aspect for neutral atoms has been having them interact with photons for quantum networking, or with neighboring qubits to realize two-qubit operations for quantum computing[180].

1.4 Quantum Networking with Neutral Atoms

Quantum networking with nuetral atoms is enabled by entangling the single-atom qubits with single photons. Atom-photon entanglement can be generated by optically exciting an atom and collecting the emission into a high numerical aperture lens. The excitation and collection can then be engineered to produce entanglement between the atom and the polarization[201,200], or the time-

bin [102] state of the photon. These methods are limited to success rates of .1-2% depending on the efficiency of the objective collection. This efficiency becomes more pronounced when we consider that most remote entanglement generation protocols will have a success probability that scales as the square of the collection efficiency. These rates can be improved by several orders of magnitude by increasing this collection efficiency. This can be achieved by introducing an optical cavity to enhance the interaction between a single atom and a single photon, bringing the collection efficiency to nearly 100 %. [158] This topic will be explored in more depth in a later chapter 2. The coupling of atoms to optical cavities has played a crucial role in my PhD and will be discussed in chapters 5, 7, and 8

1.5 Quantum Computing with Neutral Atoms

For most quantum computing systems, performing two-qubit gates requires access to highly coherent interactions. In the case of neutral atoms, the ground states exhibit long coherence times but weak interactions, making it challenging to perform entangling gates between qubits. To induce interactions between neutral atoms, they are excited to Rydberg states, atoms with a high principal quantum number n. These Rydberg atoms exhibit exaggerated properties, such as significantly larger dipole moments that scale with n, allowing them to interact strongly with each other through dipole-dipole interactions. Another property of Rydberg atoms is that their lifetime also increases with n. The combination of increasing interaction rate and decreasing lifetime or decoherence rate results in a highly coherent interaction that can be utilized to perform high-fidelity two-qubit gates. This topic will be explored in chapter 3 and discussed in more detail in chapter 6.

1.5.1 Modular Quantum Computing with Neutral Atoms

To achieve large-scale, fault-tolerant quantum computing, neutral-atom quantum systems will need to improve both the fidelity of quantum operations and the size of their systems. Scaling neutral-atom quantum systems has long been recognized as one of their key strengths. The number of qubits in a neutral-atom system is determined by the number of optical tweezers that can be generated, which is constrained by the available laser power for optical traps and the field of view of the microscope objective used to project the tweezers. The Endres group at Caltech demonstrated the ability to trap up to 6,100 atoms using a custom objective designed for large fields of view and by combining three high-power laser sources. They also achieved exceptional coherence times and atom trapping lifetimes in a room-temperature system [115]. This progress highlights the significant power requirements and advanced optics needed to create such large tweezer arrays. Scaling these arrays to even larger system sizes remains an engineering challenge, but there is a clear path toward neutral-atom quantum processors with tens of thousands of qubits.

Another promising approach, currently under exploration in many academic labs, is the development of modular quantum computers, where quantum computation is distributed across distant quantum processors. This requires efficient quantum interconnects, and neutral atoms offer strong optical transitions that can generate atom-photon entanglement, allowing quantum information to be transmitted over long distances via optical fibers [153,38,35]. However, these interconnects must produce remote entanglement at rates high enough to keep pace with quantum computation.

Currently, remote entanglement generation rates are on the order of hertz, which is insufficient to provide an efficient link between quantum processors [38,157]. Increasing these rates is an active area of research. One promising approach involves coupling neutral atoms to optical cavities, which enhances both photon collection efficiency and the rate of entanglement generation [213,103,182,67,188]. Pursuing an optimal optical interface that would allow neutral atom quantum computers to scale

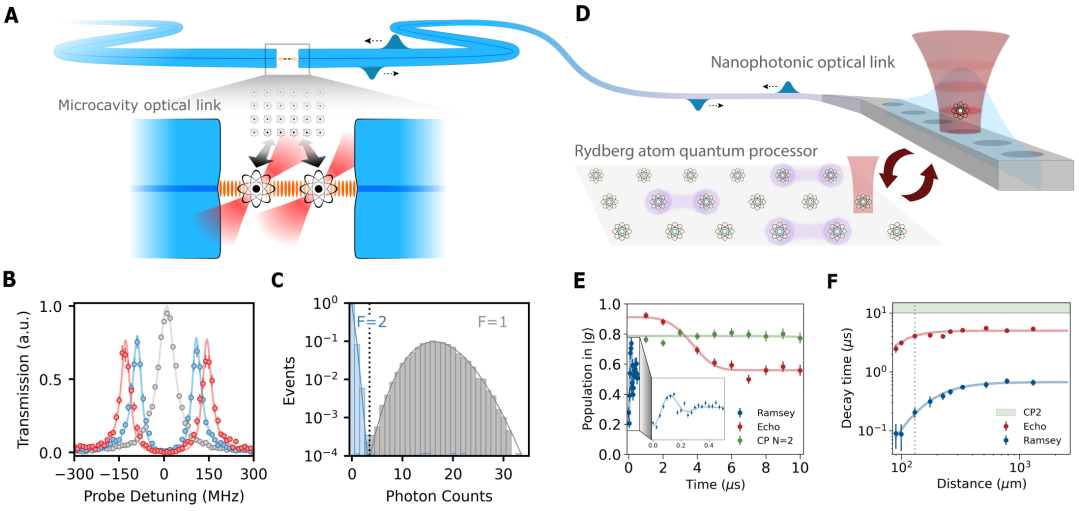


Figure 1.1: (**A**) Atoms in optical tweezers are transported from an atom array into the mode of a microcavity. (**B**) Resonant transmission spectra for a bare cavity (gray), one atom (blue), and two atoms (red) coupled to the microcavity, demonstrating strong coupling with a cooperativity of $C = 101(2)$. (**C**) Histograms showing photon counts collected in 10 μs for an atom in the $F = 1$ state (gray) and an atom in the $F = 2$ state (blue), yielding a qubit state readout fidelity of $99.960^{+14}_{-24}\%$. (**D**) A Rydberg atom array operating in free space near a nanophotonic optical link. (**E**) Measurements of Rydberg atom coherence near the nanophotonic cavity at a distance of 130 μm. For a Ramsey measurement, $T_2^* = 200(40)$ ns (blue line); for spin-echo, $T_2 = 4.1(2)$ μs (red line). With a Carr-Purcell decoupling sequence, no decay is observed within the measurement time. (**F**) Rydberg coherence for different decoupling sequences as a function of distance from the nanophotonic cavity, showing retention of coherence even in proximity to the device.

indefinitely in system size is the goal of my PhD and throughout the last six years I have explored several of the key components required to build a modular quantum computer.

1.6 Overview of Thesis

In this thesis, I present progress towards developing an optical interfaces that will enable neutral-atom quantum processors to perform both quantum computation and quantum networking in a single system, paving the way towards distributed quantum computation and providing a clear path towards large-scale quantum computation.

Chapters 2 and 3 provide a background on two of the important fields of physics used in this thesis. The first being Cavity Quantum Eletrodynamics (QED), which governs how light interacts

with matter at the quantum level. This chapter will review how the concepts of Cavity QED can be utilized for quantum networking. The second chapter then provides a brief overview of Rydberg atoms, their properties, and how they can be utilized for quantum computing.

Chapter 4 will discuss the construction of the system used in chapter 7 and shown in 1.1A.

Chapter 5 presents work demonstrating qubit coherence, entanglement, and coherent transport in a nanophotonic one-dimensional photonic crystal cavity as shown in figure 1.1D. In this work, entanglement is generated via a cavity-carving protocol, and we show that this entanglement can be preserved while moving from the nanophotonic cavity into free space. These results motivate the integration of nanophotonic cavities with free-space atom arrays for quantum computation, thereby combining quantum computing and quantum networking.

Chapter 6 discusses experiments that demonstrate coherent Rydberg excitation near the nanophotonic cavity as shown in figure 1.1E,F. Accessing these Rydberg states enables quantum computation, while still benefiting from the nanophotonic cavity for quantum networking. We measure the coherence properties of Rydberg atoms in the presence of the nanophotonic cavity, which exhibits surface charging that degrades Rydberg coherence. Despite this surface charging, we successfully generate Rydberg-mediated entanglement and additionally leverage this entanglement for quantum-enhanced electric-field sensing.

Chapter 7 explores fiber Fabry–Perot cavities as an optical interface as shown in figure 1.1A. These cavities allow atoms to be trapped and transported in a free space without requiring them to be placed on a device, as is the case with nanophotonic cavities. Furthermore, they offer stronger light–matter interactions through direct coupling to the optical mode, rather than relying on evanescent coupling. Leveraging this strong coupling enables fast, nondestructive qubit-state readout, as well as novel entangling gates mediated by the optical cavity. A key finding in this work is that the cavity can not only mediate interactions but also bias errors in a way that renders them detectable. Identifying these errors, we improve the fidelity of our cavity-mediated quantum oper-

ations. Overall, these results motivate further exploration of microcavity platforms for integration with atom arrays and additional investigations into cavity-mediated entanglement.

Chapter 8 explores strategies to improve the microcavity platform through the fabrication of micromirror devices. We demonstrate several methods for producing micromirrors, including CO_2 laser ablation, silicon isotropic etching, and thin film buckling. This chapter highlights the thin-film buckling approach we developed, showcasing a flexible and scalable technique for fabricating state-of-the-art optical cavities with applications in both quantum systems and classical photonics.

Raise your hand if you've never seen this in your life.

Mikhail Lukin

2

Cavity Quantum Electrodynamics

Cavity Quantum Electrodynamics (cQED) is the study of the interaction between strongly confined light and matter. The most natural system for which cavity QED arises is the atom in a cavity. In this system, we treat a single mode of light that strongly interacts with a dipole transition in a two-level atom.

2.1 Quantization of the Electric Field

The first step to defining the Hamiltonian of this system is quantizing the electric field of a single photon. To do this, we can start with Maxwell's equations for a free field. By treating the free field with wave equations for the electric and magnetic fields, we can describe these classical harmonic oscillators with quantum harmonic oscillators. Following this procedure, one can then find the electric field of a single photon. Another more simple procedure is to define the classical energy density of an electric field:

$$\frac{1}{2}\int dV\left(\varepsilon_0 E^2 + \frac{B^2}{\mu_0}\right) \approx VE^2\varepsilon_0 \tag{2.1}$$

$$\hbar\omega = VE_0^2\varepsilon_0 \tag{2.2}$$

Then solving for the electric field we find:

$$E_0 = \sqrt{\frac{\hbar\omega}{\varepsilon_0 V}} \tag{2.3}$$

We then divide this electric field into its positive and negative frequency components corresponding to running waves of light:

$$E_\alpha = \hat{\varepsilon}_\alpha + \hat{\varepsilon}_\alpha^\dagger \tag{2.4}$$

$$\hat{\varepsilon}_\alpha = \varepsilon_\alpha \sum \sqrt{\frac{\hbar\omega}{2\varepsilon_0 V}}\hat{a}_j e^{ik_j\cdot r} \tag{2.5}$$

From quantizing the electric field we can understand many quantum optics phenomena. For example, we can define the decay rate of a single atom in vacuum. In the next section we will solve

for this and then use it later.

2.2 Excited Atom in Free Space

We know that a single atom in free space will decay through spontaneous emission. One way of understanding this decay rate is that the atom is coupling to the vacuum modes of the universe. Using our result from the previous section we can find an equation for the decay rate of a single atom in an excited state. To do this we define a Hamiltonian:

$$H = -\hat{E} \cdot \hat{d} = -\sum_{\alpha} (\hat{\varepsilon}_{\alpha} + \hat{\varepsilon}_{\alpha}^{\dagger}) \cdot (\mu_{\alpha} |e\rangle \langle g| + \mu_{\alpha}^{*} |g\rangle \langle e|) \tag{2.6}$$

Each of the electric field terms corresponds to a photon creation or annihilation operator. When we multiply the electric field terms by the atom terms we will find that some terms do not conserve energy. For example, the $\hat{a}^{\dagger} |e\rangle \langle g|$ term would correspond to the atom being excited and emitting a photon. If we neglect these terms that do not conserve energy, we will be left with two energy-conserving terms that correspond to the atom absorbing a photon and being excited and the atom decaying and emitting a photon. This Hamiltonian can be written:

$$H = -\hat{E} \cdot \hat{d} = -\sum_{\alpha} \hat{\varepsilon}_{\alpha}^{\dagger} \mu_{\alpha} |e\rangle \langle g| + \hat{\varepsilon}_{\alpha} \mu_{\alpha}^{*} |g\rangle \langle e|) \tag{2.7}$$

$$H = -\hbar \sum_{\alpha} \frac{\mu_{\alpha}}{\hbar} \sqrt{\frac{\hbar \omega_{\alpha}}{2\varepsilon_0 V}} \hat{a}_{\alpha}^{\dagger} |e\rangle \langle g| + \frac{\mu_{\alpha}^{*}}{\hbar} \sqrt{\frac{\hbar \omega_{\alpha}}{2\varepsilon_0 V}} \hat{a}_{\alpha} |g\rangle \langle e|) \tag{2.8}$$

Here we can define a coupling strength to the electric field, also known as the single-photon Rabi frequency, as:

$$g_{\alpha} = \sqrt{\frac{\omega_{\alpha}}{2\hbar\varepsilon_0 V}} \cdot \mu_{\alpha} \tag{2.9}$$

From this we can now define a full Hamiltonian to describe an atom coupled to many vacuum modes:

$$H = \hbar\omega \left|e\right\rangle \left\langle e\right| + \sum_j \hbar\omega_j(\hat{a}^\dagger \hat{a} + \frac{1}{2}) - \sum_j (\hbar g_j \left|e\right\rangle \left\langle g\right| \hat{a} + \hbar g_j^* \left|g\right\rangle \left\langle e\right| \hat{a}^\dagger) \tag{2.10}$$

If we start in the initial state with the atom in the excited state and zero photons in the photonic modes, we can simplify our Hamiltonion to only span the states $|e, 0\rangle$ and $|g, 1_j\rangle$:

$$H = \hbar\omega \left|e, 0\right\rangle \left\langle e, 0\right| + \sum_j \hbar\omega_j \left|g, 1_j\right\rangle \left\langle g, 1_j\right| - \sum_j (\hbar g_j \left|e, 0\right\rangle \left\langle g, 1_j\right| \hat{a} + \hbar g_j^* \left|g, 1_j\right\rangle \left\langle e, 0\right| \hat{a}^\dagger) \tag{2.11}$$

This coupling to the vacuum modes gives the well-known Lamb shift. We can incorporate this into our definition of ω and then derive the decay rate. This rate will be given by:

$$\gamma = 2\pi \sum_{j,\alpha} |g_{j,\alpha}|^2 \delta(\omega_{j,\alpha} - \omega) \tag{2.12}$$

Because the mode spacing of the universe is infinitesimally small, the summation can be approximated by an integral, resulting in:

$$\gamma = \frac{V}{(2\pi)^2} \sum_\alpha \int_k \int_\varphi \int_\theta k^2 sin(\theta) |g_{j,\alpha}|^2 \delta(\omega_{j,\alpha} - \omega) d\theta d\varphi dk \tag{2.13}$$

We can sum over the two polarizations by only allowing the polarizations to exist in the x-y plane. Doing this, we can simplify the dot product of the dipole moment and the electric field:

$$\sum_\alpha |g_{k,\alpha}|^2 = \frac{\omega_j}{2\hbar\varepsilon_0 V} \sum_\alpha |\mu_\alpha \cdot \varepsilon_\alpha|^2 \tag{2.14}$$

$$= \frac{\omega_j}{2\hbar\varepsilon_0 V}(|\mu sin(\theta)cos(\varphi)|^2 + |\mu sin(\theta)sin(\varphi)|^2) \tag{2.15}$$

$$= \frac{\omega_j}{2\hbar\varepsilon_0 V}|\mu sin(\theta)|^2 = |g|^2 sin^2(\theta) \tag{2.16}$$

Solving for gamma we find:

$$\gamma = \frac{V}{(2\pi)^2}\int_k\int_\varphi\int_\theta k^2 sin^3(\theta)|g_j|^2\delta(\omega_j - \omega)d\theta d\varphi dk \tag{2.17}$$

$$\gamma = \frac{2V}{3\pi}\int_0^\infty k^2|g_j|^2\delta(\omega_j - \omega)dk \tag{2.18}$$

$$\gamma = \frac{2V\omega^2}{3\pi c^3}|g_{k=\omega/c}|^2 = \frac{\omega_{eg}^3\mu_{eg}^2}{3\pi\varepsilon_0\hbar c^3} \tag{2.19}$$

This yields an important result for future sections:

$$\gamma = \frac{\omega_{eg}^3\mu_{eg}^2}{3\pi\varepsilon_0\hbar c^3} \tag{2.20}$$

Notably we find that the free space decay rate is quadratic with the dipole moment of the transition and cubic with the transition frequency of the transition.

2.3 Single Atom Coupled to an Optical Cavity

In the previous section, we treated a single-atom coupling to many modes of light. Now, let us imagine a system in which one mode of light is much more strongly confined than others and enhanced through an optical cavity that allows the light to circulate many times before leaving the system. We can think about these systems in multiple ways, and each of them is equally valid and yields similar results, which we will discuss in this section.

This is an open quantum system with a two-level atom coupled to a bosonic mode of a cavity. From an intuitive perspective, we will have some exchange between the optical cavity and the atom,

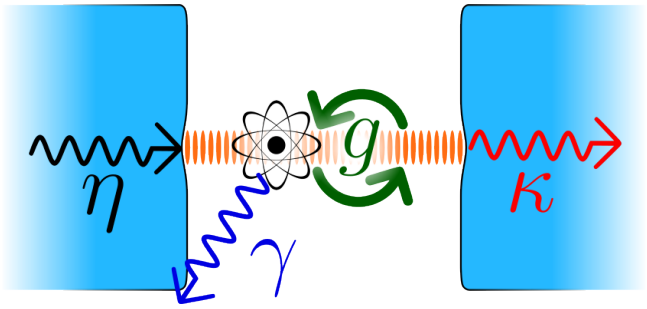


Figure 2.1: An atom cavity system showing the coherent coupling between the atom and the cavity, g, the atomic free space decay rate, γ, cavity decay rate, κ, and a coherent drive on the input, η

while these oscillations are damped by photon emissions out of the optical cavity and into free space. From this intuition, we have three important numbers to define and understand. The first of which is g_0, which we have somewhat defined in the previous section. This parameter defines our coherent exchange rate between the atom and the cavity mode.

$$g_0 = -\frac{\hat{d} \cdot \hat{E}_\alpha}{\hbar} = \sqrt{\frac{\omega_{eg}}{2\hbar\varepsilon_0 V}} \cdot \mu_{eg} \tag{2.21}$$

The next two parameters are the dephasing mechanisms. These are ways in which excitation can leave the system. The first of which is κ, which corresponds to the leakage rate of photons from our cavity. Previously, we treated modes of light that are not confined to a cavity. Now, we can imagine having a mode of light that is confined between two mirrors. This light will circulate between the mirrors for an amount of time that depends on the parameters of the cavity. There are many different types of cavities, and we will review different types of cavities in depth in future sections. The number κ defines the decay rate of the intensity inside the cavity. This can be measured spectroscopically as the full-width half-maximum (FWHM) of the optical cavity.

$$\kappa = \frac{\omega_{eg}}{Q} = 2\pi\frac{\nu_{FSR}}{F} \tag{2.22}$$

The final parameter is the atomic free-space decay rate γ, previously calculated in Eq. 2.20. This decay rate remains unchanged in the case of an open cavity, which is typically used in optical cavity QED experiments. In contrast, closed cavities, commonly used in superconducting qubit systems or in experiments that couple Rydberg atoms to microwave cavities, can exhibit modified decay dynamics. With these parameters defined, we can now express the effective Hamiltonian as:

$$H/\hbar = \omega_a \left|e\right\rangle \left\langle e\right| + \omega_c \hat{a}^\dagger \hat{a} + g(\left|e\right\rangle \left\langle g\right| \hat{a} + \left|g\right\rangle \left\langle e\right| \hat{a}^\dagger) \tag{2.23}$$

With Lindblad operators given by:

$$\sqrt{\kappa}a, \sqrt{\gamma} \left|g\right\rangle \left\langle e\right| \tag{2.24}$$

Now we define a dimensionless parameter called the cooperativity, which will be featured in many subsequent calculations. The cooperativity is given by the ratio of the coherent coupling between the atom and the cavity g to the decoherence rates of the atom and the cavity κ and γ, where κ and γ are the intensity and population decay rates of the cavity and the atom, respectively. In our notation, we define C with an overall factor of 4. This parameter describes how coherently a single atom can interact with a single photon. We will find that achieving $C > 1$ is necessary for many of the applications in quantum information. This regime is known as the strong-coupling regime:

$$C = \frac{4g_0^2}{\kappa\Gamma} = \frac{3\lambda^3}{4\pi^2}\frac{Q}{V} \tag{2.25}$$

Here we list several ways of rewriting the cooperativity using different parameters. We use the definition of the single photon Rabi frequency g_0 from equation 2.9 and the atomic decay rate γ from equation 2.20. The cavity decay rate κ will be determined by the cavity parameters and can be expressed in terms of various quantities, such as the quality factor Q. We then find that the cooper-

ativity is proportional to $\frac{Q}{V}$ where V is the mode volume of the cavity. This indicates that to achieve strong coupling, one requires a high Q resonator with a small mode volume. Another way of deriving the cooperativity can be understood from the perspective of light scattering off of a single atom. We can calculate the interaction probability of a single atom interacting with a single photon in free space by taking the ratio of the atomic absorption cross section $\sigma_a = \frac{3\lambda^2}{2\pi}$ to the photonic mode cross section $\sigma_{ph} = \frac{\pi}{4}w^2$. Now by implementing an optical cavity we can effectively increase the number of times that the single photon can interact with the atom. This number of times can be characterized by the finesse of the optical cavity, F. The finesse is proportional to the average number of round trips that the photon will make in the resonator, such that $N = \frac{F}{\pi}$

$$C = \frac{\sigma_a}{\sigma_{ph}}\frac{F}{\pi} = \frac{6\lambda^2 F}{\pi^3 w_0^2} = \frac{24F}{\pi k^2 w_0^2} \tag{2.26}$$

2.4 Purcell Effect

One of the first results that can be derived from a single atom coupled to an optical cavity is the Purcell effect. Essentially, now that the atom is more strongly coupled to this mode of light, we will find that it preferentially emits into that mode and at an enhanced rate. First, we can write our Hamiltonian:

$$H/\hbar = \omega_a \left|e\right\rangle \left\langle e\right| + \omega_c \hat{a}^\dagger \hat{a} + g(\left|e\right\rangle \left\langle g\right| \hat{a} + \left|g\right\rangle \left\langle e\right| \hat{a}^\dagger) \tag{2.27}$$

Here, ω_a and ω_c refer to the resonance frequencies of the atom and the cavity, respectively. For simplicity we can work with a non-hermition Hamiltonian and add terms for cavity decay and atomic decay. We can also move into the rotating frame of the cavity field and treat a system in which the atom and the cavity are on resonance $\omega_c = \omega_a$:

$$H/\hbar = i\frac{\gamma}{2}\left|e\right\rangle\left\langle e\right| + i\frac{\kappa}{2}\hat{a}^{\dagger}\hat{a} + g(\left|e\right\rangle\left\langle g\right|\hat{a} + \left|g\right\rangle\left\langle e\right|\hat{a}^{\dagger}) \tag{2.28}$$

We then solve for the dynamics using the Heisenberg picture:

$$\dot{C}_e(t) = -\frac{\gamma}{2}C_e(t) + igC_g(t) \tag{2.29}$$

$$\dot{C}_g(t) = -\frac{\kappa}{2}C_g(t) + igC_e(t) \tag{2.30}$$

Now we make an important assumption about the system in order to see Purcell enhancement. This assumption is that the cavity decay rate κ dominates over g and γ. This regime of cavity QED parameters is often referred to as the "bad cavity" regime where $\kappa > g > \gamma$. It is also important to note that the bad cavity regime does not prohibit being in the strong coupling regime where $\frac{4g^2}{\kappa\gamma} > 1$. With this assumption, we find that as soon as the excitation enters the cavity, it is immediately dissipated $\dot{C}_g(t) = 0$.

$$\dot{C}_e(t) = -(\frac{\gamma}{2} + \frac{2g^2}{\kappa})C_e(t) = -(1+C)\frac{\gamma}{2}C_e(t) \tag{2.31}$$

We find that the atom population decays at a rate of $(1+C)\gamma \approx C\gamma = \frac{4g^2}{\kappa}$ for large C, which is approximately $C\gamma$. This can be clearly seen in figure 2.2. With this result, we find that we can broaden an atom with a strongly coupled cavity. This is important for enhancing the bandwidth of an optical transition. Additionally, we can find the ratio of emission into the cavity versus outside of the cavity:

$$\frac{\gamma}{(1+C)\gamma} = \frac{1}{1+C} \approx \frac{1}{C} \tag{2.32}$$

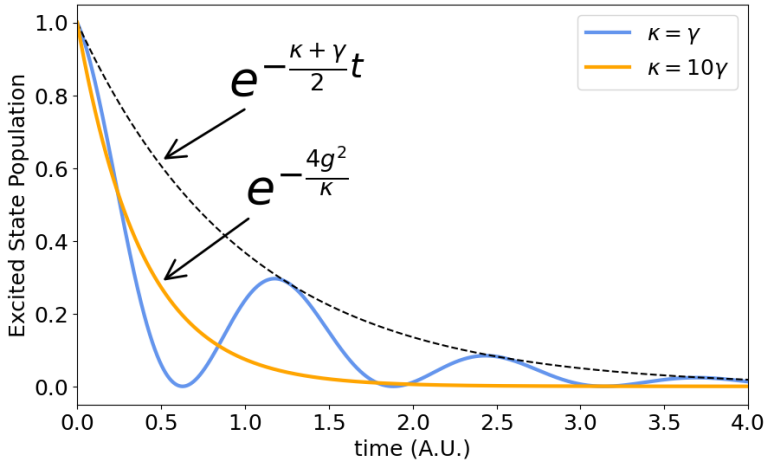


Figure 2.2: The time dynamics of an initially excited atom coupled to an optical cavity showing two different regimes, $\kappa = \gamma$, where we see coherent oscillation between the atom and the cavity at a frequency of $2g$ with a damping given by $\frac{\kappa+\gamma}{2}$, and $\kappa = 10\gamma$ where we see a quick exponential decay of the atomic excitation that goes as the purcell enhanced decay rate of $C\gamma = \frac{4g^2}{\kappa}$

Here we see that 1 in C photons will be emitted into free space. For a large C, we can collect almost every photon that the atom emits. This can be utilized for enhanced readout and quantum networking of atoms for two reasons. First, preferential emission increases the collection efficiency to near unity. Secondly, the broadened line width allows for much faster photon emission. [18]

2.5 Strong Coupling Regime

In the previous section, we have made the assumption that κ is dominant over g and γ, resulting in what we see as Purcell-enhanced emission from an atom coupled to the cavity. The more traditional view of the strong coupling regime is where $g > \kappa, \gamma$. In this regime, the oscillation rate between the atom and the cavity dominates over the decay rates, resulting in a damped coherent exchange between that atom and the cavity, as shown in Figure 2.2. If we solve for the dynamics of the equations of motion from equation 2.30 without any assumptions:

$$\ddot{C}_e(t) \;+\; \left(\tfrac{\gamma+\kappa}{2}\right)\dot{C}_e(t) \;+\; \left(\tfrac{\gamma\kappa}{4}+g^2\right)C_e(t) \;=\; 0$$

we will find that the atomic excitation and the cavity excitation will exchange at a rate of g with a decay rate set by $\frac{\kappa+\gamma}{2}$. An alternative way of viewing these dynamics is by diagonalizing the Jaynes-Cummings Hamiltonian in the single excitation manifold, where we only consider the states that have a single excitation $|e,0\rangle$ and $|g,1\rangle$.

$$|\pm\rangle = |g,1\rangle \pm |e,0\rangle \tag{2.33}$$

$$\lambda_\pm = \pm g \tag{2.34}$$

This results in two eigenstates $|+\rangle$ and $|-\rangle$ that are equal superpositions of atomic excitation and cavity excitation with the energies given by $\pm g$. The dynamics of the system will then be given by oscillations between these two dressed states at a frequency of $2g$. The Jaynes-Cummings Hamiltonian also exhibits higher excitation manifolds where more excitations exist in the system, because of this bosonic nature of the cavity mode, this results in the Jaynes-Cummings ladder as shown in figure 2.3. We can generalize the eigenstates of the Jaynes-Cummings Hamiltonian to different excitation manifolds with eigenstates and eigenenergies given by:

$$|\pm\rangle = |g,n\rangle \pm |e,n-1\rangle \tag{2.35}$$

$$\lambda_\pm = \pm\sqrt{n}g \tag{2.36}$$

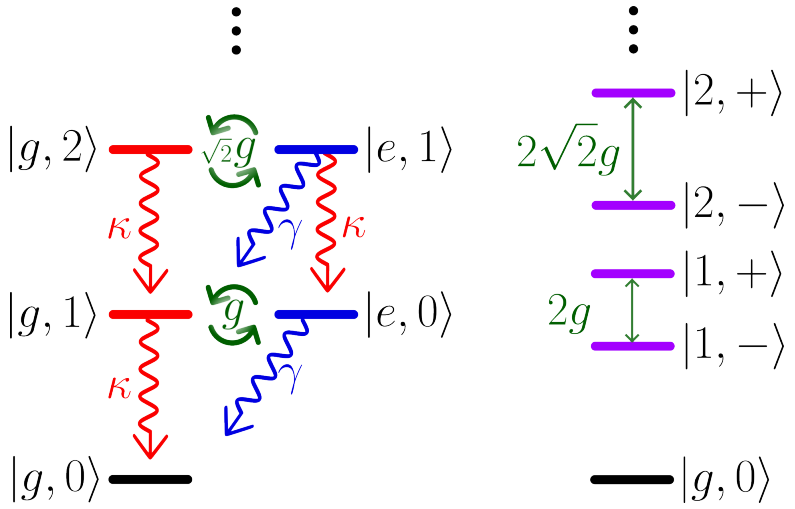


Figure 2.3: A level diagram depicting the different excitation manifolds of the Jaynes–Cummings Hamiltonian. (Left): States with the same number of excitations, n, are coupled with a strength of $\sqrt{n}\,g$. (Right): The eigenstates of a given excitation manifold are given by $|n,\pm\rangle = |g,n\rangle \pm |e,n-1\rangle$, with an energy splitting of $\sqrt{n}g$.

2.6 Cavity-Mediated Gates

In addition to mediating higher rate atom photon entanglement, optical cavities can be utilized to mediate interactions between atoms coupled to the same cavity. In this section, we will explore several examples of gates that can be realized using an optical cavity and how their fidelity will scale with cooperativity.

The simplest gate that can be performed with a cavity is simply exchanging an excitation from one atom to another. This is a good problem that will give us an idea for the general scaling of how the fidelity is set by the cooperativity. First, we can take two atoms coupled to an optical cavity, where we encode quantum information in hyperfine ground states ($|0\rangle$ and $|1\rangle$). The atom has an additional excited state, $|e\rangle$. We then couple the $|1\rangle \rightarrow |e\rangle$ transition to an optical cavity. This is a typical setup for atoms coupled to optical cavities in which one of the two qubit states is coupled to the cavity, where the other state is not coupled. This will also allow for state-selective readout, as we will see in Chapters 1 and 3. We can mediate an exchange interaction between the atoms through

the cavity by exchange of a photon. One intuition for this is that we can have one atom emit a photon and then the other atom absorb the photon. Here we can easily treat this case by adding a laser that excites the $|0\rangle$ state to the $|e\rangle$ state on both atoms and then applying the sequence, excite atom 1, wait, deexcite atom 2.

$$|01\rangle \xrightarrow[\text{Excite 1}]{} |e1\rangle \underset{\mathcal{H}}{\Rightarrow} \alpha\,|1e\rangle \xrightarrow[\text{Deexcite 2}]{} \alpha\,|10\rangle \tag{2.37}$$

$$\mathcal{H}/\hbar = \sum_{i=1,2} g(|e\rangle_i \langle 1|\,\hat{a} + |1\rangle_i \langle e|\,\hat{a}^\dagger) \tag{2.38}$$

We assume that the excitation occurs with high fidelity and significantly faster than the dynamics set by g. We will then find that the state $|e1\rangle$ will evolve by exchanging a photon into the cavity and then into atom 2. We can solve for the dynamics by diagonalizing the Hamiltonian and finding that the eigenstates.

The eigenstates of this hamiltonian are given by:

$$|B_+\rangle = \frac{1}{2}(|e1,0\rangle + |1e,0\rangle) + \frac{1}{\sqrt{2}}\,|11,1\rangle \tag{2.39}$$

$$|D_0\rangle = \frac{1}{\sqrt{2}}(|e1,0\rangle - |1e,0\rangle) \tag{2.40}$$

$$|B_-\rangle = \frac{1}{2}(|e1,0\rangle + |1e,0\rangle) - \frac{1}{\sqrt{2}}\,|11,1\rangle \tag{2.41}$$

with energies given by:

$$\lambda_{B_+}, \lambda_{D_0}, \lambda_{B_-} = \sqrt{2}g, 0, -\sqrt{2}g \tag{2.42}$$

We then time-evolution the initial state $|e1\rangle$ and find the equations of motion given by:

$$|\psi(t)\rangle = \frac{1}{2}(e^{i\sqrt{2}gt}|B_+\rangle + e^{-i\sqrt{2}gt}|B_-\rangle) + \frac{1}{\sqrt{2}}|D_0\rangle \tag{2.43}$$

$$= |\psi(t)\rangle = Cos^2(\frac{\sqrt{2}}{2}gt)|e1,0\rangle + Sin^2(\frac{\sqrt{2}}{2}gt)|1e,0\rangle + \frac{Sin(\sqrt{2}gt)}{2}|11,1\rangle \tag{2.44}$$

After evolving for a time of $\tau = \frac{2\pi}{\sqrt{2}g}$ we find $|\psi(t)\rangle = |1e,0\rangle$ and the excitation will have successfully transferred to the other atom. We can then account for decoherence by multiplying the decoherence rates by the time required to fully transfer the excitation.

$$\varepsilon = 1 - e^{-\tau(\kappa+\gamma)/2} \approx \frac{\pi(\kappa+\gamma)}{\sqrt{2}g} \tag{2.45}$$

From this result it is clear that one will always be limited by the ratio of the coherent exchange rate g compared to the dephasing rates κ and γ. If we set κ and γ equal to each other, then we can recover an important scaling that is almost universal for cavity-mediated gates.

$$\varepsilon = \frac{\pi(\kappa+\gamma)}{\sqrt{2}g} = \frac{\pi\sqrt{\kappa\gamma}}{\sqrt{2}g} = \frac{2\pi}{\sqrt{2C}} \tag{2.46}$$

We find that the error of this operation will scale as $\propto \frac{1}{\sqrt{C}}$. This scaling sets a fundamental limit on how high-fidelity cavity-mediated gates can be. For cooperativities that are achievable in optical cavities (≈ 100) this makes deterministic cavity-mediated gates infeasible for quantum computation.

However, many schemes have been developed to circumvent this limitation by performing non-deterministic, heralded, or post-selected gates[20,61,151,204,30]. These types of gates are demonstrated in both chapter 5 and chapter 7.

2.7 Optical Cavities for Quantum Sciences

In this thesis, we will explore many different types of cavities, including the one-dimensional photonic crystal cavity, optical fiber Fabry-Perot cavity, suspended membrane micromirror, and isotropically etched silicon micromirrors. The main differentiation between these cavities is the difference between the one-dimensional photonic crystal cavity and the fabry perot cavities. In this section, I will briefly describe the two.

In order to understand what the requirements for a good optical interface are, we need to think about the parameters that are important for an efficient light-matter interface. An important number that has been mentioned in several contexts is cooperativity. This number dictates things like the purcell enhancement and the fidelity of cavity-mediated gates. From this perspective, we find it is important to make this number large. However, depending upon the parameters of one cavity, a higher cooperativity could be detrimental.

2.8 Cavity Transmission and Reflection

Consider a two-mirror optical cavity with a photon decay rate κ. This total loss rate consists of several contributions as shown in 2.4:

$$\kappa = \kappa_{\text{in}} + \kappa_{\text{out}} + \kappa_{\text{sc}}$$

where κ_{in} and κ_{out} are the transmission losses through the input and output mirrors, respectively (determined by mirror coatings or photonic crystal cavity design), and κ_{sc} accounts for absorption or scattering out of the cavity mode.

A convenient way to analyze the cavity reflectivity and transmissivity is to use a non-Hermitian Hamiltonian for a driven optical cavity along with the input–output relations. In the lab frame, the

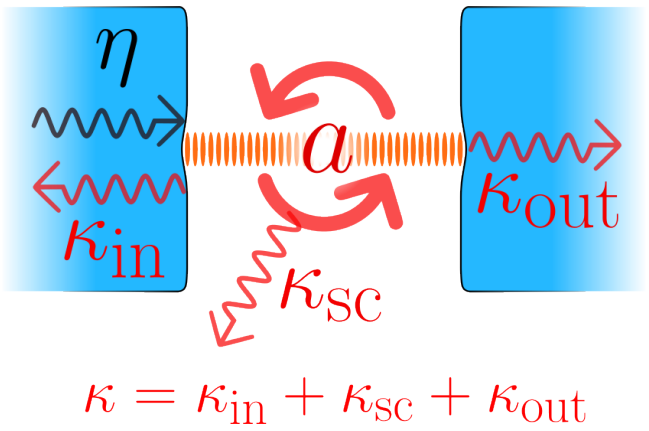


Figure 2.4: An optical cavity system driven by an external source, η, with a circulating electric field, a. The cavity experiences three types of loss: transmission through the input mirror, κ_{in}, transmission through the output mirror, κ_{out}, and scattering losses, κ_{sc}, which together yield a total loss rate κ.

Hamiltonian reads:

$$H = \left(\omega_c - i\tfrac{\kappa}{2}\right)a^\dagger a + \eta\sqrt{\kappa_{\text{in}}}\left(a\,e^{-i\omega_l t} + a^\dagger\, e^{i\omega_l t}\right) \tag{2.47}$$

where ω_c is the cavity resonance, ω_l is the driving-laser frequency, a ($a^\dagger$) is the annihilation (creation) operator for the cavity mode, κ is the total cavity decay rate, and η represents the drive amplitude. Moving into the rotating frame of the laser frequency ω_l gives

$$H = \left(\Delta - i\tfrac{\kappa}{2}\right)a^\dagger a + \eta\sqrt{\kappa_{\text{in}}}\left(a + a^\dagger\right) \tag{2.48}$$

where $\Delta = \omega_c - \omega_l$. The steady-state field satisfies

$$\frac{d}{dt}a^\dagger = \left(i\Delta + \tfrac{\kappa}{2}\right)a^\dagger + i\eta\sqrt{\kappa_{\text{in}}} = 0 \tag{2.49}$$

Solving for $a^\dagger$ yields

$$a^\dagger = \frac{2\eta\sqrt{\kappa_{\text{in}}}}{\kappa - 2i\Delta} \tag{2.50}$$

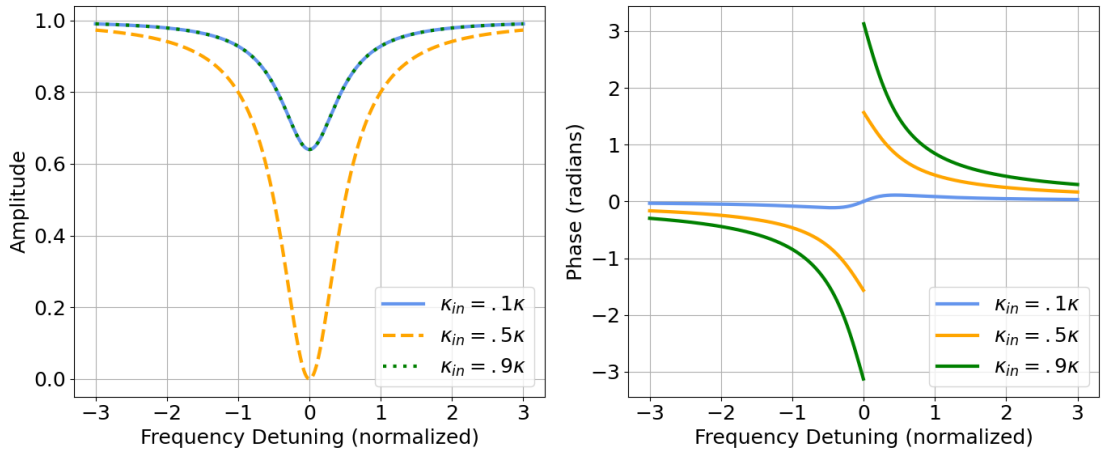


Figure 2.5: Reflectivity $|r(\Delta)|^2$ and phase $\arg[r(\Delta)]$ versus detuning Δ for three coupling regimes: undercoupled ($\kappa_{in} = 0.1\kappa$), critically coupled ($\kappa_{in} = 0.5\kappa$), and overcoupled ($\kappa_{in} = 0.9\kappa$).

The transmitted field amplitude is given by the leakage of the intracavity field through the output mirror:

$$\sqrt{\kappa_{\text{out}}}\, a^\dagger$$

Hence, the dimensionless transmission coefficient is

$$t(\Delta) \;=\; -\frac{\sqrt{\kappa_{\text{out}}}\, a^\dagger}{\eta} \;=\; -\frac{2\sqrt{\kappa_{\text{in}}\,\kappa_{\text{out}}}}{\kappa \;-\; 2\,i\,\Delta} \tag{2.51}$$

Determining the reflection coefficient $r(\Delta)$ requires accounting for the interference between the field directly reflected from the input mirror and the field leaking out of the cavity through that same mirror. Assuming the mirror's reflection is nearly 100%, one obtains

$$r(\Delta) \;=\; 1 \;-\; \frac{\sqrt{\kappa_{\text{in}}}\, a^\dagger}{\eta} \;=\; 1 \;-\; \frac{2\,\kappa_{\text{in}}}{\kappa - 2\,i\,\Delta} \tag{2.52}$$

2.8.1 Coupling Regimes

An important concept in cavity design is the ratio of the different decay channels $\kappa_{\text{in}}, \kappa_{\text{out}}, \kappa_{\text{sc}}$. The three primary *coupling regimes* are:

(1) Critical Coupling: $\kappa_{\text{in}} = \kappa_{\text{out}} = \frac{\kappa}{2}$.

$$t(\Delta) = -\frac{\kappa}{\kappa - 2i\Delta}, \quad r(\Delta) = 1 - \frac{\kappa}{\kappa - 2i\Delta}$$

On resonance ($\Delta = 0$), the reflection goes to zero and transmission reaches unity. This is a famously counterintuitive result, where two highly reflective mirrors become transparent when placed at the proper distance from eachother. This critical coupling regime is useful for high-contrast, transmission-based systems. In Chapter 7, a system that operates near critical coupling is used.

(2) Overcoupling: $\kappa_{\text{in}} \approx \kappa \gg \kappa_{\text{sc}}, \kappa_{\text{out}}$. By making the input mirror very "leaky," nearly all photons exit back through the input port, yielding

$$t(\Delta) = 0, \quad r(\Delta) = 1 - \frac{2\kappa}{\kappa - 2i\Delta}, \quad R(\Delta) = \left|r(\Delta)\right|^2 = 1$$

Here, the on-resonance reflection flips phase by π. This feature is used in phase-gate schemes between atoms and photons [196,152,47]. In addition, all photons predominantly emit into a single mode (the input port), which is desirable for certain emission-based protocols. Although the reflection intensity does not show variation on the resonance (leading one to think there is no signal), the information is actually imprinted on the phase of the reflected field, requiring an interferometric measurement.

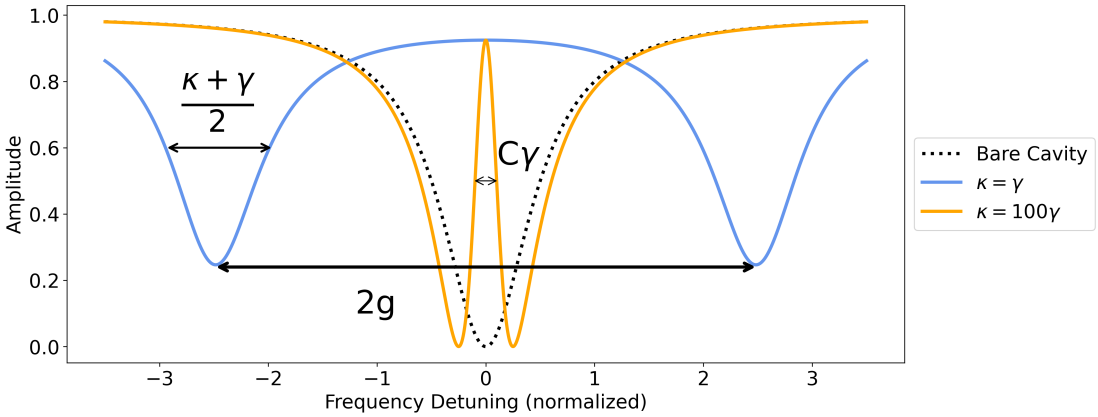


Figure 2.6: Reflectivity spectra of two atom-cavity systems with identical cooperativity, $C = \frac{4g^2}{\kappa\gamma} = 25$, but with different κ/γ ratios. In the first regime, where $g > \kappa = \gamma$, the system operates in the strong-coupling regime, allowing coherent exchange of excitations between the atom and the cavity. This is spectroscopically observable as two resolvable dressed states split by $2g$ (black line between peaks), with linewidths of $\frac{\kappa+\gamma}{2}$. In the second regime, known as the "bad cavity" regime ($\kappa > g > \gamma$), the cavity decay rate is dominant, suppressing coherent oscillations and causing a rapid decay of the atomic excitation through the cavity at a rate of $\frac{4g^2}{\kappa} = C\gamma$. This manifests as a Purcell-enhanced atomic linewidth, seen spectroscopically as a hole burned into the bare cavity resonance.

(3) UNDERCOUPLING: $\kappa_{\text{out}} \approx \kappa \gg \kappa_{\text{in}}, \kappa_{\text{sc}}$.

$$t(\Delta) = -\frac{\sqrt{\kappa_{\text{in}}\,\kappa}}{\kappa - 2i\Delta}, \quad r(\Delta) = 1 - \frac{\kappa_{\text{in}}}{\kappa - 2i\Delta}$$

In this regime, overall signals are reduced. It is generally the least favorable regime, though some systems may unintentionally fall into it (e.g., the cavity in Chapter 5).

Each of these coupling regimes has distinct advantages and applications, from high-contrast transmission in critically coupled systems to single-mode emission and phase gates in overcoupled designs. The choice of regime will depend on the specific goals of the experiment or device.

2.9 Atom–Cavity Spectrum

Having understood the reflectivity spectrum of the bare cavity, we now introduce the coupling of a two-level atom to the system. The full Hamiltonian is

$$H = \left(\Delta_c - i\,\tfrac{\kappa}{2}\right)a^\dagger a \;+\; \left(\Delta_a - i\,\tfrac{\gamma}{2}\right)|e\rangle\langle e| \;+\; g\left(a\,|e\rangle\langle g| \;+\; a^\dagger\,|g\rangle\langle e|\right) \;+\; \eta\sqrt{\kappa_{\text{in}}}\left(a + a^\dagger\right) \tag{2.53}$$

We can once again solve for the steady-state intracavity field while also considering the dynamics of the two-level atom. The relevant Heisenberg equations (or equivalently the expectation-value equations in the mean-field limit) are

$$\frac{d}{dt}a^\dagger = \left(i\,\Delta_c + \tfrac{\kappa}{2}\right)a^\dagger \;+\; i\,\eta\sqrt{\kappa_{\text{in}}} \;-\; i\,g\,|e\rangle\langle g| \;=\; 0 \tag{2.54a}$$

$$\frac{d}{dt}|e\rangle\langle g| = \left(i\,\Delta_a + \tfrac{\gamma}{2}\right)|e\rangle\langle g| \;+\; i\,g\,a^\dagger\Big(|g\rangle\langle g| - |e\rangle\langle e|\Big) \;=\; 0 \tag{2.54b}$$

$$\frac{d}{dt}|e\rangle\langle e| = \left(i\,\Delta_a + \tfrac{\gamma}{2}\right)|e\rangle\langle e| \;-\; i\,g\Big(|e\rangle\langle g|\,a \;-\; |e\rangle\langle g|\,a^\dagger\Big) \;=\; 0 \tag{2.54c}$$

We assume the weak-excitation regime, where the atom is predominantly in the ground state ($|e\rangle\langle e| \approx 0$ and $|g\rangle\langle g| \approx 1$). Under this approximation, one finds

$$a^\dagger = \frac{-\,\eta\sqrt{\kappa_{\text{in}}}}{\left(\frac{\kappa}{2} - i\,\Delta_c\right) + \frac{g^2}{\frac{\gamma}{2} - i\,\Delta_a}} = \frac{-\,\eta\sqrt{\kappa_{\text{in}}}}{\left(\frac{\kappa}{2} - i\,\Delta_c\right)}\left(1 + \frac{g^2}{\left(\frac{\gamma}{2} - i\,\Delta_a\right)\left(\frac{\kappa}{2} - i\,\Delta_c\right)}\right)^{-1} \tag{2.55}$$

We find that the bare-cavity circulating field is suppressed by a factor related to the coupling strength g. From this result we can calculate the reflectivity (r) and the transmitivity (t), and an additional channel that is the scattering of photons from the atom outside of the cavity (s). These are given by:

$$r = 1 - \frac{\kappa_{in}}{\tilde{\kappa}\left(1+\tilde{C}\right)},$$

$$t = -\frac{\sqrt{\kappa_{in}\kappa_{out}}}{\tilde{\kappa}(1+\tilde{C})}$$

$$s = \frac{i\,g\sqrt{\gamma\,\kappa_{\text{in}}}}{\tilde{\gamma}\,\tilde{\kappa}\left(1+\tilde{C}\right)}$$

where $\tilde{\kappa} = \kappa/2 + i\Delta_C$ and $\tilde{\gamma} = \gamma/2 + i\Delta_a$. We also define $\tilde{C} = \frac{g^2}{\tilde{\kappa}\tilde{\gamma}}$.

We probe the spectrum of the atom–cavity system by driving the cavity with a laser while measuring the reflectivity under the condition $\Delta = \Delta_a = \Delta_c$. In Figure 2.6 we see two features separated by $2g$ with line widths of $\frac{\gamma+\kappa}{2}$. These features correspond to the eigenstates of the Jaynes–Cummings Hamiltonian

$$|\pm\rangle = |e,0\rangle \pm |g,1\rangle$$

which are equal superpositions of an atomic excitation and a cavity excitation. It is important to note that, depending on the ratios of the cavity QED parameters (g, κ, γ), the spectrum can appear markedly different, as illustrated in Figure 2.6. In the traditional strong-coupling regime, where $g > \kappa, \gamma$, coherent oscillations between the atom and the cavity give rise to two resolvable spectral features corresponding to the eigenstates of the Jaynes–Cummings Hamiltonian. This is the regime utilized in Chapter 7. In contrast, in the "bad cavity" regime, the cavity decay rate dominates, where $\kappa > g > \gamma$. As a result, coherent oscillations are suppressed, leading to a rapid decay of atomic excitation through the cavity at a rate of

$$\frac{4g^2}{\kappa} = C\gamma$$

This rapid decay corresponds to a Purcell-enhanced atomic linewidth, observed spectroscopically

as a hole burned into the bare-cavity resonance. The system described in Chapter 5 operates in this regime. It is also important to note that the resonant reflection is only dependent on the cooperativity as shown by the coupled reflectivity in figure 2.6. We find that at resonance ($\Delta_c = \Delta_a = 0$),

$$a^\dagger = \frac{-2\eta\sqrt{\kappa_{\text{in}}}}{\kappa\left(1+\frac{4g^2}{\gamma\kappa}\right)} = \frac{-2\eta\sqrt{\kappa_{\text{in}}}}{\kappa\,(1+C)} \tag{2.56}$$

where we define $C = \frac{4g^2}{\gamma\kappa}$. In the strong-coupling regime ($C > 1$), a single atom strongly suppresses the resonant field entering the cavity. Resulting in reflectivity, transmitivity, and scattering given by:

The reflectivity phase and amplitude of the cavity, as functions of detuning, for different cavity coupling regimes are shown in Figure 2.7. If we examine how this suppression impacts transmission and reflection in different cavity regimes, we find that in the critically coupled case, on resonance,

$$t(0) = \frac{1}{1+C}, \quad r(0) = 1 - \frac{1}{1+C} \tag{2.57}$$

Here, a normally transmissive cavity becomes reflective when an atom is strongly coupled, yielding a high-contrast indicator of atomic coupling. In the overcoupled regime, on resonance,

$$r(0) = 1 - \frac{2}{1+C} = \frac{1-C}{1+C} \tag{2.58}$$

which can even flip the sign of the reflection for large C. This phenomenon underpins several proposals for atom–photon phase gates and can be extended to realize deterministic photon–photon gates[47].

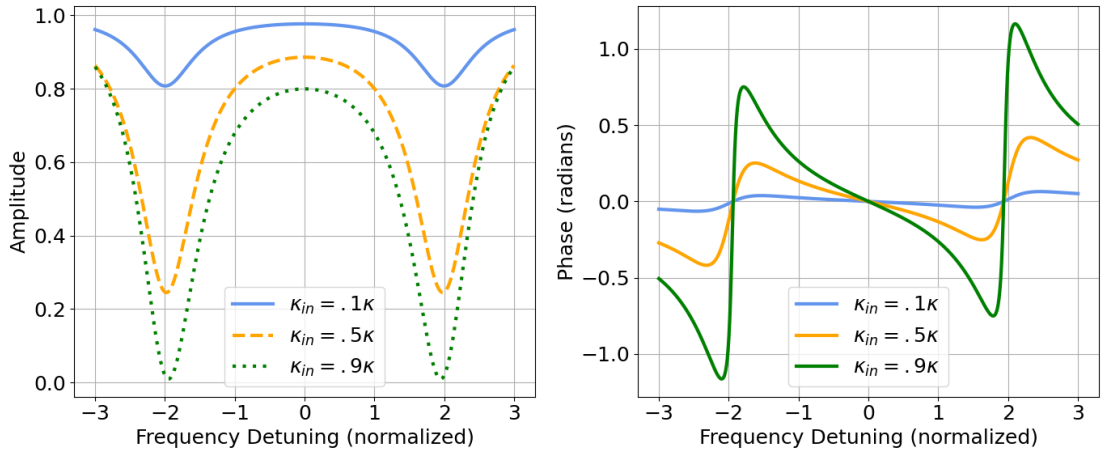


Figure 2.7: Reflectivity $|r(\Delta)|^2$ and phase $\arg[r(\Delta)]$ versus detuning Δ for an atom coupled to a cavity with cavity parameters $(g, \kappa, \gamma) = (2, 1, 1)$ with three different coupling regimes: undercoupled ($\kappa_{in} = 0.1\kappa$), critically coupled ($\kappa_{in} = 0.5\kappa$), and overcoupled ($\kappa_{in} = 0.9\kappa$).

2.10 One-Dimensional Photonic Crystal Cavities

One-dimensional photonic crystal cavities are nanofabricated waveguides that incorporate a periodic index of refraction introduced by patterning holes into the waveguide. These holes effectively act as Bragg reflectors. For a more thorough explanation of photonic crystals, I recommend the textbook in Ref. [119]. Here, we provide a brief overview, focusing on their relevance to quantum information.

The physical mechanism behind these photonic crystals can be understood by analogy to a $\lambda/4$ (quarter-wave) dielectric mirror. This mirror is constructed from a multilayer stack of two dielectrics with refractive indices n_1 and n_2, each layer having a thickness of $\frac{\lambda}{4n_i}$. This thickness ensures that reflections of light at wavelength λ from the interfaces between the two dielectrics interfere constructively, while transmissions interfere destructively, resulting in a high overall reflectivity. This structure is commonly called a Bragg reflector. Another way to view this is through the concept of a photonic band structure, where electromagnetic modes in the periodic dielectric are described by

Bloch states, analogous to electrons in a crystal lattice. In this interpretation, the high reflectivity at λ arises from a photonic band gap, meaning that no light of that frequency can propagate within the stack.

Extending these principles to nanophotonics involves patterning a waveguide. Typically, a waveguide is a suspended slab of dielectric that confines light to a single mode, much like an optical fiber. By etching periodic nanoscale holes into the waveguide, one locally reduces the effective refractive index (closer to that of air), thus forming a photonic crystal.

To understand the photonic crystal cavity, one can imagine two Bragg reflectors facing each other with a small gap between. This setup produces an optical cavity whose resonance is determined by the size of that gap. A more precise understanding comes from an analogy with solid-state crystals, where defects in the lattice produce localized electronic states. Similarly, by modulating the hole spacing in a photonic crystal (creating a "defect" in the otherwise periodic structure), one creates a localized photonic mode that can be narrow in frequency (high quality factor) and confined in space (small mode volume). These two key properties are precisely what make photonic crystal cavities ideal for efficient atom-photon interfaces in quantum information applications. This is evident when we look at the equation for the Cooperativity:

$$C = \frac{4g_0^2}{\kappa\Gamma} = \frac{3\lambda^3}{4\pi^2}\frac{Q}{V} \tag{2.59}$$

For most atomic systems, near-infrared or visible wavelengths are required, which makes silicon nitride (Si_3N_4) a natural choice due to its transparency in these regions and the ease of fabricating this material. Silicon nitride also has a moderate index of refraction of approximately 2, allowing it to effectively confine light when suspended in air and be fabricated into photonic crystals.

To illustrate typical coupling strengths, we consider a standard Si_3N_4 photonic crystal cavity at 780 nm. Such cavities can achieve quality factors of about 2×10^5 and mode volumes as small

as $0.4\,\lambda^3$, resulting in theoretical maximum cooperativities on the order of 40,000. In practice, however, atoms cannot be trapped at the electric field maxima, so only a fraction of this coupling strength is realized, resulting in cooperativities on the order of 100 [170,215]. This near-surface trapping is typically achieved by transporting an atom trapped in an optical tweezer in free space to the nanophotonic cavity, where the reflection of the tweezer forms a standing wave where the first pancake of this standing wave can localize the atom $\approx 250nm$ above the surface [193]. These cavities are also utilized in the solid-state community where spin defects can be placed directly into the mode maximum allowing for strong coupling to the mode [184]. Other approaches also utilize the evanescent field in which the host material contains defects, while a material with more promising optical properties is placed on top of the emitters [45].

In addition to these features, light from the nanophotonic cavity can be efficiently coupled out of the waveguide and into an optical fiber through a tapered fiber connection or through lensed fiber coupling [195,29,121]

2.11 Fabry-Perot Cavities

Fabry–Pérot cavities are widely utilized in optics as narrow filters, stable references, and, in our case, as elements for quantum networking. The simplest type is the two-mirror cavity. In this configuration, light can circulate between the mirrors many times.

For light to build up in the cavity, it must be resonant. This means that upon each round trip, the light acquires a phase shift that is an integer multiple of 2π. This resonance condition is expressed as

$$2nL = m\lambda,$$

where n is the refractive index of the medium inside the cavity, L is the cavity length, m is an integer, and λ is the wavelength of light. Because the resonance length corresponds to a specific resonance

frequency, a precisely stabilized cavity can serve as a stable frequency reference.

A deviation from resonance results in destructive interference and a reduction in the circulating power, leading to a Lorentzian lineshape. The linewidth of the resonance depends on the average number of round trips that light makes inside the cavity, which is determined by the mirror reflectivity. More precisely, the average number of round trips is set by the round-trip loss, $\mathcal{L}$. For small losses ($\mathcal{L} \ll 1$), this number is approximated as

$$N_{\mathrm{rt}} \approx \frac{2}{\mathcal{L}}$$

This same factor governs the power buildup; that is, the circulating power is enhanced by approximately

$$\beta \approx \frac{2}{\mathcal{L}}$$

A commonly used parameter to characterize the cavity is the finesse, defined as

$$F = \frac{2\pi}{\mathcal{L}} = \pi N_{rt}$$

In addition to the average number of round trips, it is important to consider the rate of photon leakage, κ. The round-trip time is given by

$$\tau_{\mathrm{rt}} = \frac{2nL}{c}$$

and the corresponding free spectral range is

$$\nu_{\mathrm{FSR}} = \frac{c}{2nL}$$

The ringdown time of the cavity and the photon leakage rate can then be expressed as:

$$\tau = F\tau_{\mathrm{rt}}, \kappa = \frac{\nu_{\mathrm{FSR}}}{F} \tag{2.60}$$

In order to create a high-finesse optical cavity it is necessary to create mirrors that are highly reflective with low scattering loss. These mirrors are typically made by coating a substrate with an ion beam sputtered (IBS) dielectric coating, where reflectivities of 99.999% can be achieved. In addition to high reflectivities, in order to form a stable cavity, one must add curvature to the mirrors in order to make the cavity mode image back onto itself. The two mirror cavities can then be defined by two radius of curvatures and a cavity length. From these parameters, one can extract the stability conditions using ABCD matrices. These conditions are given by:

$$0 \leq g_1 g_2 \leq 1 \tag{2.61}$$

Where $g_i = 1 - \frac{L}{R_i}$ is the stability parameter for the mirrors of the cavity and L and R_i are the length of the cavity and the radius of curvature of the given mirror. These stability parameters yield a range of stable cavity configurations shown in 2.8.

In addition to yielding the stability regimes, the ABCD matrices will also yield the stable solution for a given cavity geometry. An important result from this is the waist at the center of the cavity mode, w_0, and the waists at mirrors 1 and 2, $w_{1,2}$, are given by:

$$w_0 = \sqrt{\frac{\lambda\, d}{\pi}}\left[\frac{g_1 g_2\left(1 - g_1 g_2\right)}{\left(g_1 + g_2 - 2\, g_1 g_2\right)^2}\right]^{\frac{1}{4}} = \sqrt{\frac{\lambda}{\pi}}\left[\frac{d\left(R_1 + R_2 - L\right)\left(R_1 - L\right)\left(R_2 - L\right)}{(R_1 + R_2 - 2L)^2}\right]^{\frac{1}{4}} \tag{2.62}$$

$$w_1 = \sqrt{\frac{\lambda R_1}{\pi}\sqrt{\frac{L\left(R_2 - L\right)}{\left(R_1 - L\right)\left(R_1 + R_2 - L\right)}}} \quad ; \quad w_2 = \sqrt{\frac{\lambda R_2}{\pi}\sqrt{\frac{L\left(R_1 - L\right)}{\left(R_2 - L\right)\left(R_1 + R_2 - L\right)}}} \tag{2.63}$$

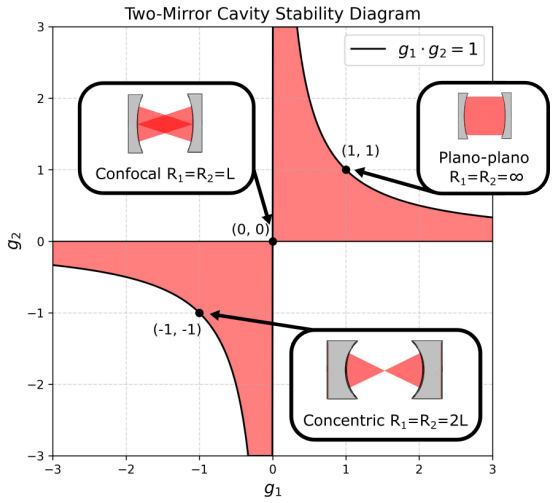


Figure 2.8: A plot showing the stability condition of an optical cavity along with various cavity configurations. Three key regions are highlighted: the plano-plano region, where the mirrors are flat (i.e., the radii of curvature approach infinity); the confocal region, where the cavity length is equal to the radii of curvature, R_1 and R_2; and the concentric region, where the cavity length is equal to twice the mirror radius of curvature.

We can further simplify this equation for a symmetric cavity where $R = R_1 = R_2$. In this case:

$$w_0 = \sqrt{\frac{\lambda}{2\pi}} \left[L\left(2R - L\right)\right]^{\frac{1}{4}} \tag{2.64}$$

$$w_{1,2} = \sqrt{\frac{\lambda R}{\pi} \sqrt{\frac{L}{\left(2R - L\right)}}} \tag{2.65}$$

Here we find an important result that as the length of the cavity approaches $L = 2R$, the cavity waist shrinks significantly, however the size of the waist on the mirrors becomes significantly larger as well. This is known as the concentric cavity regime. Many groups work with near concentric cavities due to the small waist[44,141]. Another important regime is the confocal cavity regime where the $L = R$. This is the cavity length where the mode waist will be the largest, with a size of $w_0 = \sqrt{\frac{\lambda L}{2\pi}}$ and a waist of $w_0 = \sqrt{\frac{\lambda L}{\pi}}$ on the mirror surface. Additionally at this length all of the even modes become degenerate, and similarly all the odd modes become degenerate, which present many

interesting scientific directions[89].

2.12 Fabry-Perot Cavity Modes

More generally, stable cavity modes are Hermite-Gaussian modes, where higher-order transverse modes introduce additional stable configurations within the cavity. We denote these modes as TEM_{mnq}, where q indicates the longitudinal mode number, and m and n indicate the orthogonal transverse mode numbers.

For cavities that are sufficiently long, the longitudinal mode number becomes exceedingly large and difficult to determine exactly. Therefore, we often omit it and denote different transverse modes as TEM_{mn}. The electric field of a Hermite-Gaussian mode in two dimensions, plotted in figure 2.9, is given by:

$$E_{n,m}(x,y,z) = \frac{A_0}{w(z)} H_n\left(\frac{\sqrt{2}x}{w(z)}\right) H_m\left(\frac{\sqrt{2}y}{w(z)}\right) \exp\left(-\frac{x^2+y^2}{w^2(z)}\right) \times \exp\left[-ikz - i(m+n+1)\zeta(z) + i\frac{k(x^2+y^2)}{2R(z)}\right] \tag{2.66}$$

where:

$$w(z) = w_0\sqrt{1+\left(\frac{z}{z_R}\right)^2}$$

$$R(z) = z\left[1+\left(\frac{z_R}{z}\right)^2\right]$$

$$\zeta(z) = \arctan\left(\frac{z}{z_R}\right)$$

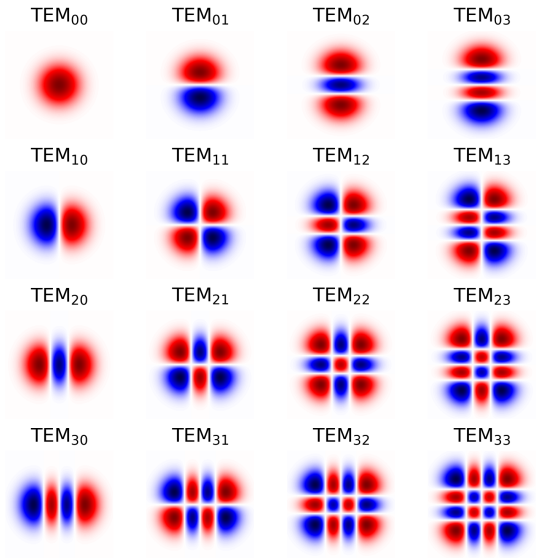


Figure 2.9: Transverse electromagnetic (TEM$_{mn}$) modes of a Hermite-Gaussian beam, where m and n represent the number of nodes in the horizontal and vertical directions, respectively. The color indicates the electric field amplitude and phase.

$$z_R = \frac{\pi w_0^2}{\lambda}, \quad k = \frac{2\pi}{\lambda}$$

H_n, H_m are Hermite polynomials of order n and m, respectively. Importantly, we find that the degeneracy between different transverse modes is lifted by a transverse mode dependent Gouy phase, $\zeta(z)$. The Gouy phase is an additional phase acquired by light as it propagates through a focus. This phase shift differs among Hermite-Gaussian modes, effectively resulting in a transverse-mode-dependent optical length of the cavity. The guoy phase is given by:

$$\zeta(z) = \tan^{-1}\left(\frac{\lambda z}{\pi w_0^2}\right) = \tan^{-1}\left(\frac{z}{z_r}\right) \tag{2.67}$$

where z_r denotes the Rayleigh range of the mode. For a two-mirror cavity, this leads to a round-trip phase shift given by:

$$\Delta\varphi = 2\left(\tan^{-1}\left(\frac{z_1}{z_r}\right) - \tan^{-1}\left(\frac{z_2}{z_r}\right)\right) \tag{2.68}$$

Here, $z_{1,2}$ represent the distances from the cavity waist to mirror 1 and mirror 2, respectively. We can then include this phase shift in the resonance condition, resulting in a mode frequency given by:

$$\nu_q = \frac{c}{2d}\left[q + \frac{1}{\pi}\cos^{-1}\left(\pm\sqrt{g_1 g_2}\right)\right] \tag{2.69}$$

Higher-order Hermite–Gaussian modes acquire an additional Gouy phase that is linear in the transverse mode numbers, resulting in a spectrum shown in figure 2.10, where we see resonance frequencies given by:

$$\nu_{mnq} = \frac{c}{2d}\left[q + \frac{1}{\pi}(m+n+1)\arccos\left(\pm\sqrt{g_1 g_2}\right)\right] \tag{2.70}$$

Furthermore, the Gouy phase depends on the waist size of the mode; thus, variations in the radius of curvature between the two transverse axes of the cavity can lift the degeneracy between the m and n indices in higher-order modes.

The size of the waist on a given mirror will set the minimum size of the mirror required to maintain high finesse; this can be understood as a clipping-loss limitation. If we assume that the mirrors are perfectly shaped and have no scattering or absorption loss, and that the only loss will be the result of clipping of the Gaussian mode, we can find an equation for the loss per round trip given by:

$$\mathcal{L}_{clipping} = 1 - \int_0^{2\pi}\int_0^{D/2}\frac{2}{\pi w_1^2} r e^{-\frac{2r^2}{w_1^2}} dr d\theta = e^{-\frac{D^2}{2w_1^2}} \tag{2.71}$$

Now we find a clipping limited finesse, F_c, given by:

$$F_c = \pi e^{\frac{D^2}{2w_1^2}} \tag{2.72}$$

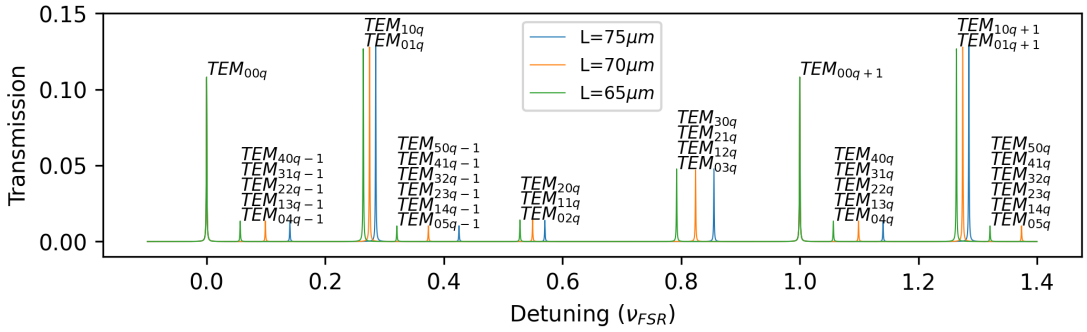


Figure 2.10: Cavity transmission spectrum showing resonances of different Hermite-Gaussian transverse electromagnetic modes TEM_{mn} as a function of detuning, expressed in units of the free spectral range ν_{FSR}. In this example, multiple higher-order modes are populated due to cavity misalignment, which results in imperfect mode matching. The modelled cavity has mirror radii of curvature of 200 μm. Multiple lengths (65μm, 70μm, and 75μm) are shown to demonstrate how different modes will behave differently. We also note that higher order transverse modes of the lower longitudenal mode can even be higher in frequency that the upper longitudenal mode.

The diameter of a mirror required to maintain a finesse of F is then given by:

$$D = w_1 \sqrt{2 \ln\left(\frac{F}{\pi}\right)} \tag{2.73}$$

To give an idea of the requirements this places on the size of the mirror, if we require a finesse of 100k, the diameter of the mirror will have to be $D = 5w_1$. This requirement makes near concentric cavity mirrors have relatively large size requirements compared to their length as opposed to near confocal cavities, which have lower size requirements, especially for smaller cavities.

With this understanding of Fabry-Perot Cavities, we can now extract information about which types of cavities will be the most efficient for coupling to atoms. First, we can redefine cooperativity in terms of parameters that are more natural to Fabry-Perot cavities. The mode volume of the TEM00 mode of an optical cavity is given by:

$$V = \frac{\pi}{4} w^2 L \tag{2.74}$$

In addition, Fabry-Perot cavities are typically characterized by their finesse. This is a metric that corresponds to the average number of round trips a photon will perform inside of the cavity. The finesse is inversely proportional to the loss on the mirror surfaces, thus a finesse can be defined as:

$$F = \frac{2\pi}{\mathcal{L}_{tot}} = \frac{\nu_{FSR}}{\kappa} = \frac{\pi\lambda}{2L}Q \tag{2.75}$$

Where $\mathcal{L}_{tot}$ is the total round trip loss, λ is the wavelength of the light, L is the length of the cavity, and Q is the quality factor. We can now reexpress cooperativity to give a better understanding of what the optimal parameters for a fabry perot cavity are.

$$C = \frac{3\lambda^3}{4\pi^2}\frac{Q}{V} = \frac{24F}{\pi k^2 w_0^2} \tag{2.76}$$

Where F is the finesse of the cavity, k is $\frac{2\pi}{\lambda}$, and w_0 is the waist at the center of the cavity. Here we clearly see that smaller cavity waists will correspond to larger cooperativities. For this reason, concentric cavities are an exciting regime in which to attain strong coupling. If we assume that we stay in the confocal regime then the waist will be given by $w_0 = \sqrt{\frac{\lambda L}{2\pi}} = \sqrt{\frac{L}{k}}$. We then find:

$$C = \frac{24F}{\pi k L} = \frac{24F}{\pi k R} \tag{2.77}$$

From this we find that the cooperativity will decrease with a longer length. We can then increase the cooperativity by making shorter cavities. As a result Microcavities are particularly useful because of their small mode volumes that are enabled by the small radius of curvatures. Another important consideration is that, in order to maintain strong coupling, one will typically require high-finesse cavities. This results in narrow linewidth cavities with long ring-down times that can limit the emission rate of photons from the system. Here, the ringdown time is given by $\tau = \frac{1}{\kappa} = \frac{c}{2LF}$. For this reason shorter and lower finesse cavities are preferred for quantum networking. Microcavities allow

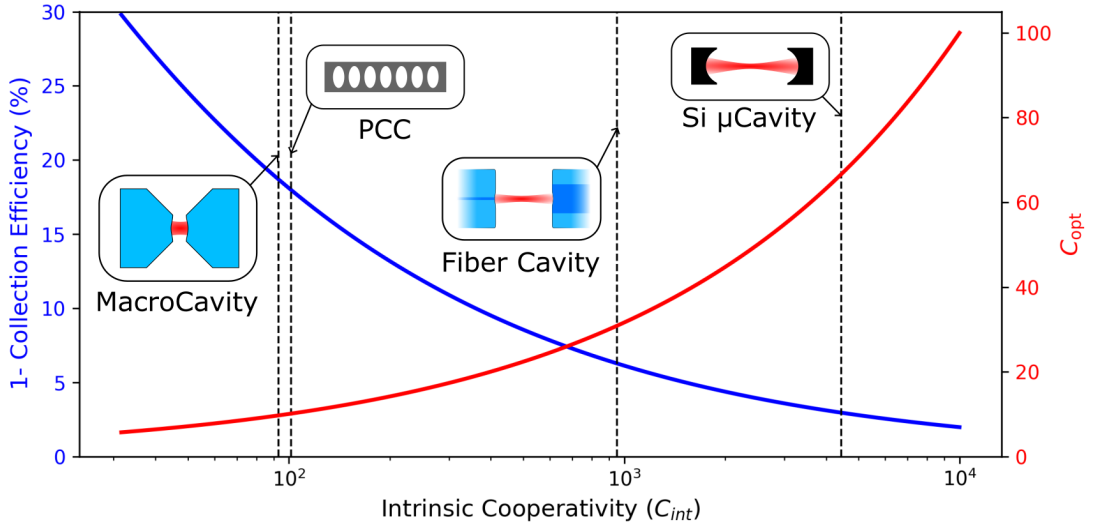


Figure 2.11: The total collection efficiency CE_{max} and optimal cooperativity C_{opt} are plotted as a function of the intrinsic cooperativity, C_{int}. Several points are included that are representative for specific cavity geometries, including macroscopic cavities[204], photonic crystal Cavities (PCC)[170], Fiber cavities[70], and silicon micromirror cavities[202]. The values used are extracted from existing atom cavity experiments: $(g, \kappa_{sc}, \gamma) = 2\pi \times (7.8, 0.4, 6)$ MHz[204], $2\pi \times (624, 2.77, 6)$ MHz[170], $2\pi \times (100, 7.5, 6)$ MHz[61,70], $2\pi \times (100, 1.5, 6)$ MHz[61,46,202]

one to maintain strong coupling without a large finesse while also maintaining a short length to increase the photon emission rate. As a result, microcavities are a promising direction for quantum networking.

2.13 Optimal Cavities for Quantum Networking

To compare which of these cavities is optimal for quantum networking, it is instructive to consider the total collection efficiency, that is the probability for an excited atom to emit a photon into the cavity mode and for it to be collected out of the cavity. If we assume that light is only collected from the front mirror this will be given by

$$CE = \eta \frac{\kappa_{in}}{\kappa} \frac{C}{C+1}, \tag{2.78}$$

Because we are only collecting light from the front mirror κ_{sc} and κ_{out} will both be loss into channels we do not collect as a result we can redefine κ_{sc} to include both scattering loss and loss out of the back mirror. Thus we can rewrite the collection efficiency as:

$$CE = \frac{\kappa_{in}}{\kappa_{in} + \kappa_{sc}} \frac{\frac{4g^2}{(\kappa_{in} + \kappa_{sc})\gamma}}{1 + \frac{4g^2}{(\kappa_{in} + \kappa_{sc})\gamma}}. \tag{2.79}$$

This expression is composed of three factors:

1. **Mode Matching (η)**: This parameter quantifies the efficiency with which the cavity mode can be coupled to a single mode.

2. **Output Coupling** $\left(\frac{\kappa_{in}}{\kappa}\right)$: This term represents the probability that a photon leaks out through the input mirror rather than through other loss channels.

3. **Purcell-Enhanced Emission** $\left(\frac{C}{C+1}\right)$: This factor accounts for the emission probability enhanced by the Purcell effect.

Note that the mode-matching parameter η is independent of the other two factors; it must be optimized by carefully evaluating the geometry of the cavity. In contrast, the second and third factors are interdependent. For example, to maximize κ_{in}/κ one would make the input mirror extremely lossy. However, increasing κ_{in} in this way increases the total decay rate κ, which in turn reduces the cooperativity C and thus lowers the Purcell-enhanced emission probability $\frac{C}{C+1}$. To analyze this trade-off more precisely, we can show that the optimal cooperativity, C_{opt}, and the corresponding optimal total decay rate, κ_{opt}, are given by

$$C_{\text{opt}} = \frac{C_{\text{int}}}{1 + \sqrt{1 + C_{\text{int}}}} \approx \sqrt{C_{\text{int}}} \tag{2.80}$$

$$\kappa_{\text{opt}} = \kappa_{sc}\left(1 + \sqrt{1 + C_{\text{int}}}\right) \tag{2.81}$$

where we have define the intrinsic cooperativity, C_{int} as

$$C_{\text{int}} = \frac{4g^2}{\kappa_{sc}\gamma} \tag{2.82}$$

which represents the highest possible cooperativity of the system when limited solely by scattering loss. The resulting maximum collection efficiency is then:

$$\eta_{\text{max}} = \frac{\sqrt{1+C_{\text{int}}}-1}{\sqrt{1+C_{\text{int}}}+1} \approx 1 - \frac{2}{1+\sqrt{C_{\text{int}}}} \tag{2.83}$$

Here it becomes clear that, in order to maximize the collection efficiency, one must increase the intrinsic cooperativity. This can be achieved by increasing the coupling rate g (by creating optical cavities with smaller mode volumes) or by decreasing κ_{sc} (by reducing scattering losses through improved fabrication). With this understanding, we can identify the most optimal cavities to improve collection efficiency.

1. **Macroscopic cavities**[204]**:** These cavities can be fabricated with exceedingly low surface roughness and absorption loss, resulting in the highest finesses. Unfortunately, the achievable radius of curvature is large, resulting in large waists (typically $\sim$ 30 μm) for the cavity mode and small g. Consequently, their maximum efficiency is lower than that of other cavity types.

2. **Photonic crystal cavities (PCC)**[170]**:** Explored in Chapter 5, these cavities feature an exceedingly large g due to their small mode volume. However, fabrication imperfections and material losses result in significant scattering loss. Furthermore, because atoms can only couple to the evanescent field of the cavity, the effective g is only a fraction of its maximum potential. If atoms could be placed closer to the device, these cavities would significantly outperform the others, but this remains experimentally challenging.

3. **Fiber cavities**[70]**:** Explored in Chapter 7, these cavities represent a middle ground. Their small radius of curvature allows for waists of around $\sim 4\,\mu$m, leading to a large g, while the low scattering roughness, achieved via CO_2 laser ablation, minimizes losses. This combination results in a cavity that outperforms both macroscopic and photonic crystal cavities.

4. **Silicon micromirror cavities**[202]**:** Explored in Chapter 8, these cavities have a radius of curvature similar to that of fiber cavities. However, improvements in fabrication have led to reduced surface roughness and scattering losses, placing these cavities above even the fiber cavities in terms of collection efficiency.

In this way, nature is kind.

Mikhail Lukin

3

Rydberg Atoms

To mediate interactions between qubits encoded in the ground states of atoms, laser excitation is used to couple these qubit states to high-lying Rydberg states. Direct excitation to high Rydberg states typically requires ultraviolet (UV) lasers[62,19]. However, working with UV light presents experimental challenges such as increased sensitivity to temperature via Doppler dephasing. Moreover, direct UV excitation couples the S ground state to a Rydberg P state, which exhibits additional structure, anisotropic interactions, and a higher sensitivity to external fields.

A more common and experimentally practical approach employs two-photon transitions via an intermediate P state, as illustrated in Fig. 3.1 [98,59]. This allows for excitation to S rydberg states. Additionally, in this scheme, the two lasers operate at wavelengths where high laser power is more readily available. Doppler dephasing can be minimized by exciting with counter-propagating beams.

In alkali atoms there are two primary schemes for two-photon excitation to Rydberg states. In the first scheme, an IR laser is used to drive the strongest optical transition in the atom, $|nS_{1/2}\rangle \leftrightarrow |nP_{1/2}\rangle$, for the first excitation leg. For rubidium and cesium, these transitions occur at 780 nm and 852 nm. The second leg requires significantly more energy to reach the Rydberg state; for rubidium and cesium, the required wavelengths are approximately 480 nm and 509 nm. However, because of the small optical dipole moment between states of largely different principal quantum numbers, this scheme demands much more power for the visible transition, which becomes a major limitation given the limited availability of high-power lasers in that spectral region.

As a result, the more commonly used "upside-down" scheme as shown in figure 3.1 replaces the first leg with a transition from the ground state $|nS_{1/2}\rangle \rightarrow |n+1P_{1/2}\rangle$, which typically lies in the blue region of the spectrum. For rubidium and cesium, these transitions occur at 420 nm and 459 nm. Although the dipole strength of the $|nS_{1/2}\rangle \leftrightarrow |n+1P_{1/2}\rangle$ transition is smaller than that of the $|nS_{1/2}\rangle \leftrightarrow |nP_{1/2}\rangle$ transition, this "upside down" approach overall requires less visible power. The second excitation leg is then driven by an IR laser operating at approximately 1013 nm for rubidium or 1033 nm for cesium, wavelengths at which high-power laser sources are more readily available.

When performing coherent two-qubit interactions, one must consider the interaction rates relative to the decoherence rate, as this ratio ultimately sets the limit on two-qubit gate fidelity. For Rydberg atoms, the coherent dipole-dipole interaction scales as $\sim n^4$, while the decay rate of the Rydberg state scales as $\sim n^{-3}$. Consequently, the ratio of coherent interaction to decoherence improves to $\sim n^7$, making high$n$ Rydberg states extremely promising. Furthermore, the interaction

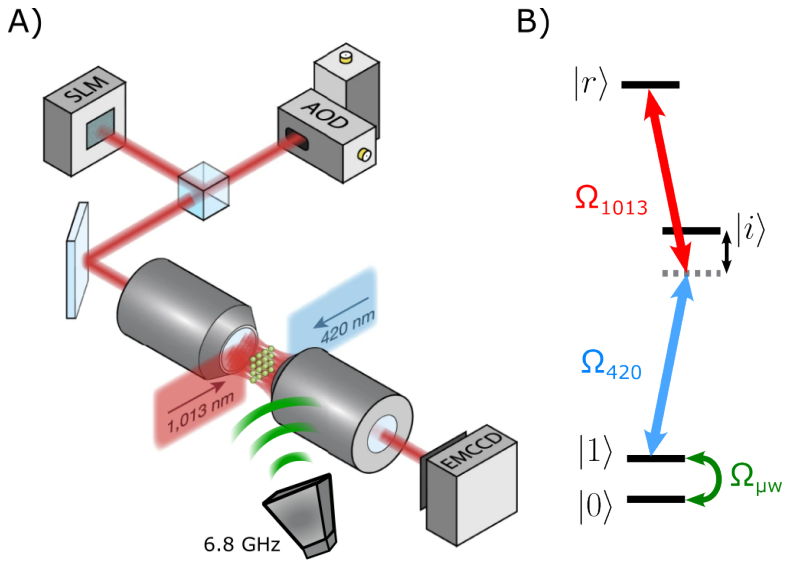


Figure 3.1: (A) A characteristic neutral atom quantum system for Rubidium-87, showing optical tweezers projected into a vacuum chamber through a microscope objective using an SLM for static traps of arbitrary geometry and AODs for dynamic, moving traps. Fluorescence from the atoms is collected on an EMCCD for atom readout through a secondary microscope objective. Counter-propagating beams of 420 nm and 1013 nm lasers are used to excite atoms to Rydberg states for performing two-qubit gates. A microwave horn is used to drive single-qubit rotations with a 6.8 GHz field. These rotations can also be driven by an optical field sent along the same path as the beams used for Rydberg excitation. This figure was adapted from Ref.[50] with permission from the author. (B) Qubit information is encoded in the ground states of the atom, $|0\rangle$ and $|1\rangle$, where single-qubit rotations are applied via a microwave drive, $\Omega_{\mu w}$, which can be applied by microwave fields or a modulated laser. The two-photon transition to the Rydberg state $|r\rangle$ is excited using a 420 nm drive, Ω_{420}, and a 1013 nm drive, Ω_{1013}, both far detuned from the intermediate state $|i\rangle$, but on two-photon resonance with the Rydberg state $|r\rangle$.

strengths can be on the order of gigahertz, allowing two-qubit gates to be executed on nanosecond timescales[55]. These Rydberg–Rydberg interactions manifest themselves through resonant dipole-dipole interactions, Förster resonances, or Van der Waals couplings[22].

Property	**Symbol**	n **scaling**	**For** $\lvert 70S_{1/2}, m_j = 1/2\rangle$
Binding energy	E_n	n^{-2}	~ -728 GHz
Energy spacing	$E_n - E_{n-1}$	n^{-3}	~ 22 GHz
Size of wavefunction	$\langle r \rangle$	n^2	$\sim 3200\, a_0$
Radiative lifetime	τ	n^3	~ 410 µs (147µs (at 25°C))
Dipole moment	$\langle r_1 \lvert e\,\mathbf{r} \rvert r_2 \rangle$	n^2	$\sim 1693\, e\, a_0$
Polarizability	α	n^7	~ 534 MHz/(V/cm)^2)
Dipole-Dipole coefficient	C_3	n^4	~ 17 GHz µm^3
Van der Waals coefficient	C_6	n^{11}	~ 874 GHz µm^6

Table 3.1: Example of Rydberg-atom properties and their dependencies on the principal quantum number n.[55] The fourth column gives approximate average values for the $\lvert r_1 \rangle = \lvert 70S_{1/2}, m_j = 1/2 \rangle$ state calculated using the Alkali Rydberg Calculator (ARC)[216]. For calculations involving a second rydberg state the $\lvert r_2 \rangle = \lvert 70P_{3/2}, m_j = -1/2 \rangle$ is used.

To illustrate how Rydberg atoms can enable highly coherent interactions, consider the exchange of a single excitation between two Rydberg states $\lvert r_1 \rangle$ and $\lvert r_2 \rangle$. Let the initial two-atom state be $\lvert r_1 \rangle \lvert r_2 \rangle$. Atoms interact via a dipole–dipole coupling of strength $\frac{C_3}{r^3}$, where C_3 scales as $\sim n^4$ (with n being the principal quantum number). Both Rydberg states decay with a lifetime τ_r, which scales approximately as $\sim n^3$. The effective Hamiltonian then takes the form:

$$H_{dd} = \frac{C_3}{r^3}\Big(\lvert r_2 r_1 \rangle \langle r_1 r_2 \rvert + \lvert r_1 r_2 \rangle \langle r_2 r_1 \rvert\Big). \tag{3.1}$$

This Hamiltonian describes an exchange interaction that requires an evolution time

$$\tau = \pi \frac{r^3}{C_3}$$

to rotate from $|r_1 r_2\rangle$ to $|r_2 r_1\rangle$. Over this duration, the total decay (or error) is

$$\varepsilon = 1 - e^{-\frac{\pi r^3}{C_3 \tau_r}} \approx \frac{\pi r^3}{C_3 \tau_r} \propto \frac{r^3}{n^7}, \tag{3.2}$$

indicating that the error decreases very rapidly with increasing n and decreasing distance.

As a concrete example, we consider the system in[7], which uses the $|62D_{3/2}, m_j = 3/2\rangle$ and $|63P_{1/2}, m_j = 1/2\rangle$ Rydberg states in ^{87}Rb. Atoms are spaced by $R = 30\,\mu$m, and the dipole–dipole coefficient is $C_3 = 7965\,\text{MHz}\,\mu\text{m}^3$. At this spacing, $\frac{C_3}{R^3} \approx 0.52\,\text{MHz}$. Both states have lifetimes on the order of $100\,\mu$s, yielding an expected exchange error of about 2.5%. By reducing the spacing to $3\,\mu$m, in principle one would achieve errors of $2.5 \times 10^{-3}\%$, corresponding to fidelity that exceeds 99.99%. This is challenging to achieve in practice, but gives an idea of how promising Rydberg interactions can be for performing quantum gates.

3.1 Rydberg Blockade

While the previous section focused on dipole-dipole interactions, the most commonly used interaction for Rydberg-mediated two-qubit gates in neutral-atom quantum computing is the strong van der Waals interaction. This interaction produces an energy shift in the Rydberg state of one atom as a result of the presence of another nearby Rydberg atom in the same state. Although two Rydberg atoms in the same state do not directly couple via dipolar interactions, they experience a second-order dipole-dipole interaction that results in this shift. To calculate the shift for the pair state $|r_1 r_1\rangle$, we use the nondegenerate perturbation theory:

$$\Delta E_{r_1 r_1} = \sum_{n,m} \frac{\left|\langle r_1 r_1 |\, H_{\text{dd}}\, | r_n r_m\rangle\right|^2}{E_{r_1 r_1} - E_{r_n r_m}}. \tag{3.3}$$

Here, r_n and r_m denote all Rydberg states that are dipole coupled to r_1. From the dipole-dipole

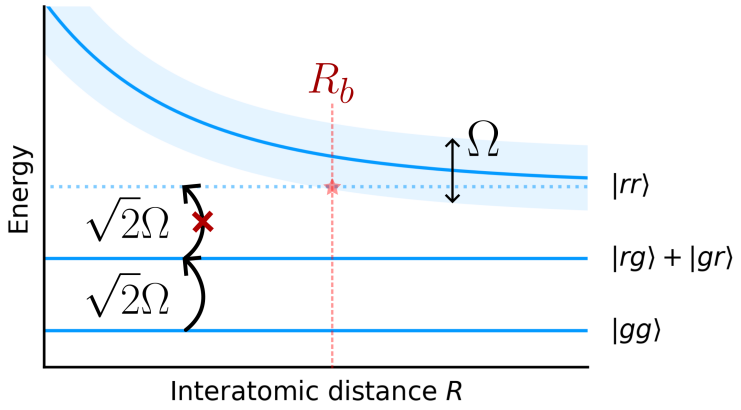


Figure 3.2: The energy level structure showing the Rydberg blockade in a two-atom system. The energy of the two atom pair states are shown as a function of interatomic distance R. The lowest energy level corresponds to the ground state $|gg\rangle$. A laser excitation couples the ground state to a symmetric singly excited state $(|rg\rangle + |gr\rangle)$ with an effective coupling strength of $\sqrt{2}\,\Omega$. The coupling to the doubly excited Rydberg state $|rr\rangle$, which is shifted upward by strong van der waals interactions is "blockaded" when the interatomic distance is within the blockade radius R_b where the $|rr\rangle$ state shift exceeds the rabi frequency Ω.

interaction, we know that the dipole matrix elements coupling Rydberg pair states scale as $\sim n^4/r^3$, whereas the energy spacing $\left(E_{r_1 r_1} - E_{r_n r_m}\right)$ scales as $\sim 1/n^3$. Consequently, the van der Waals shift scales as n^{11} and exhibits a $1/r^6$ distance dependence, the shift is typically written as C_6/r^6, where the C_6 coefficient is a state-dependent constant that typically scales as $\sim n^{11}$. For principal quantum numbers $n > 50$ and atom spacings of a few microns, these shifts can reach tens of megahertz.

Such large energy shifts give rise to the "Rydberg blockade effect", where the presence of one atom in a Rydberg state prevents nearby atoms from being excited to the same Rydberg state due to the van der waals shift. This can be seen by considering two atoms in their ground states, $|gg\rangle$, under a drive that excites both to $|r\rangle$, as shown in figure 3.2. The relevant Hamiltonian is

$$H = \frac{C_6}{r^6} |rr\rangle \langle rr| + \sum_{n=1,2} \left(\Omega \, |g\rangle_n \langle r| + \Omega^* \, |r\rangle_n \langle g| \right). \tag{3.4}$$

For $\Omega \ll \frac{C_6}{r^6}$, the energy shift prevents both atoms from being excited simultaneously to $|rr\rangle$.

Instead, the system undergoes Rabi oscillations between $|gg\rangle$ and an entangled state,

$$|gg\rangle \longleftrightarrow \frac{1}{\sqrt{2}}\big(|rg\rangle + |gr\rangle\big),$$

The presence of a large van der Waals shift leads to an enhanced Rabi frequency of $\sqrt{2}\,\Omega$. This effect is exploited in Chapter 6 to prepare entangled states between two atoms. To observe this behavior, the condition

$$\Omega \ll \frac{C_6}{r^6}$$

must be satisfied. From this inequality, one can derive a minimum spacing beyond which the blockade remains effective. This spacing, known as the blockade radius, is given by

$$r_b = \left(\frac{C_6}{\Omega}\right)^{\frac{1}{6}}.$$

3.2 Rydberg Mediated Two-Qubit Gates

The first proposal for a two-qubit gate mediated by the Rydberg blockade interaction was introduced in 2000[73]. These gates are implemented by bringing two single atoms within the blockage radius of each other, then applying a drive that couples states in the qubit manifold to a Rydberg state to mediate interactions. One of the proposed gates, now known as the "$\pi - 2\pi - \pi$ gate," provides an intuitive framework for how the Rydberg blockade effect can be used to perform two-qubit gates, shown in 3.3.

In this protocol, we consider three atomic states: two qubit levels, $|0\rangle$ and $|1\rangle$, and a Rydberg state, $|r\rangle$ as shown in fig 3.3. Local drives couple the $|1\rangle$ state to $|r\rangle$ in each atom. The gate is performed in three steps as shown in 3.3: (1) Apply a π-pulse to atom 1, exciting it to $|r\rangle$ if it is in $|1\rangle$. (2) Apply a 2π-pulse to atom 2. If atom 1 is in the $|r\rangle$ state, atom 2 will experience a Rydberg block-

ade, and no excitation to $|r\rangle$ will occur. If atom 1 is not in the Rydberg state, atom 2 will perform a rotation through $|r\rangle$ and return to $|1\rangle$, resulting in a conditional π-phase shift. (3) A final π-pulse is applied to return atom 1 back to the qubit manifold. This sequence results in a conditional phase gate. When combined with two Hadamard gates, the protocol implements a CNOT gate.

Leveraging advances in single-atom trapping, Rydberg-mediated entanglement was realized in 2010 by both the Saffman and Browaeys groups[71,206]. In particular, the Saffman group implemented the $\pi - 2\pi - \pi$ gate with fidelity of approximately 73%. At the time, these gate fidelities were far from those of more established platforms, such as trapped ions and superconducting qubits, which achieved fidelities closer to 99%. This remained a primary criticism of the neutral-atom quantum computing platform until recently.

Now, after several advances in both theoretical[100,74,76] and experimental[43,98,54] understanding, neutral atom quantum systems can consistently achieve fidelities that are competitive with other quantum systems. The current state-of-the-art method is the optimal time gate[74], shown in 3.3. These gates perform a controlled phase operation using a global drive between one of the qubit states and the Rydberg states of the atoms, with an optimized phase and intensity profile. These gates are optimized to minimize the amount of time spent in the Rydberg states during the gate, leading to less decay from the Rydberg states and higher gate fidelities. Gates of this type have been implemented across various atomic species, with fidelities exceeding 99.5% for two-qubit gates in a few hundred nanoseconds[54,197,111,25]. The understanding of these gates continues to evolve, and there is a clear path toward achieving 99.9% fidelity with improved laser power and pulse shaping[76,197,140]. An additional capability that neutral atoms possess is the ability to perform gates between arbitrary qubits. Rydberg-mediated gates are intrinsically nearest-neighbor interactions. However, by moving atoms, one can change the connectivity of the platform. Importantly, this transport does not cause any loss of quantum information and allows two-qubit gates to be performed between any two qubits[15,134,17,16]. The speed of this transport is limited by the trap fre-

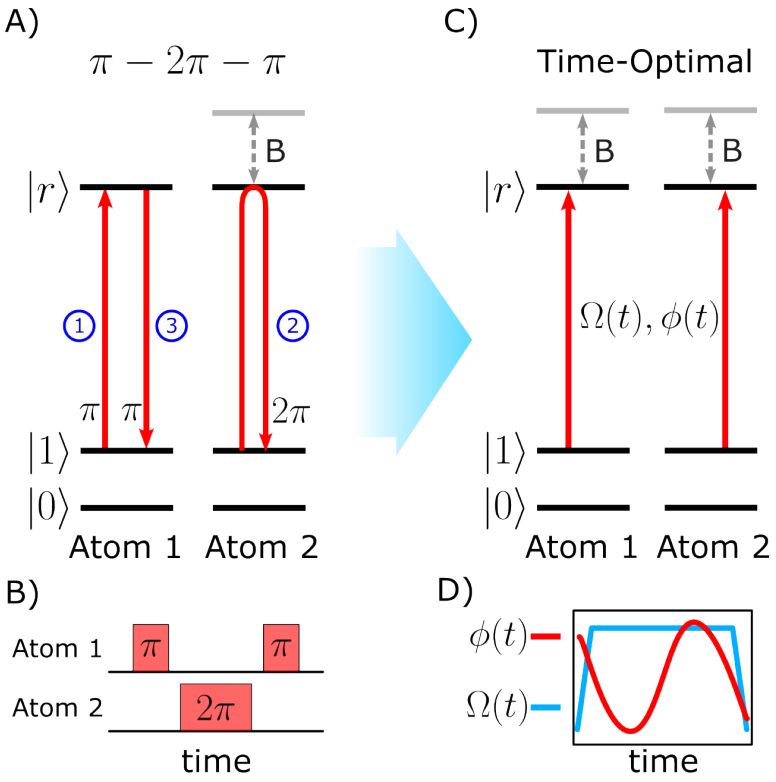


Figure 3.3: (A) A level diagram illustrating the $\pi - 2\pi - \pi$ gate. ① A π-pulse is applied to atom 1. ② A 2π-pulse is applied to atom 2. ③ A final π-pulse is applied to atom 1, completing the sequence and resulting in a controlled phase gate. (B) The pulse sequence used to perform the $\pi - 2\pi - \pi$ gate. (C) A level diagram showing the time-optimal gate, where a global drive is applied to both atoms with a phase and intensity profile defined by $\varphi(t)$ and $\Omega(t)$. (D) The temporal profile of the phase $\varphi(t)$ and intensity $\Omega(t)$ used to implement the time-optimal gate. This figure was adapted from ref [54] with permission from the author.

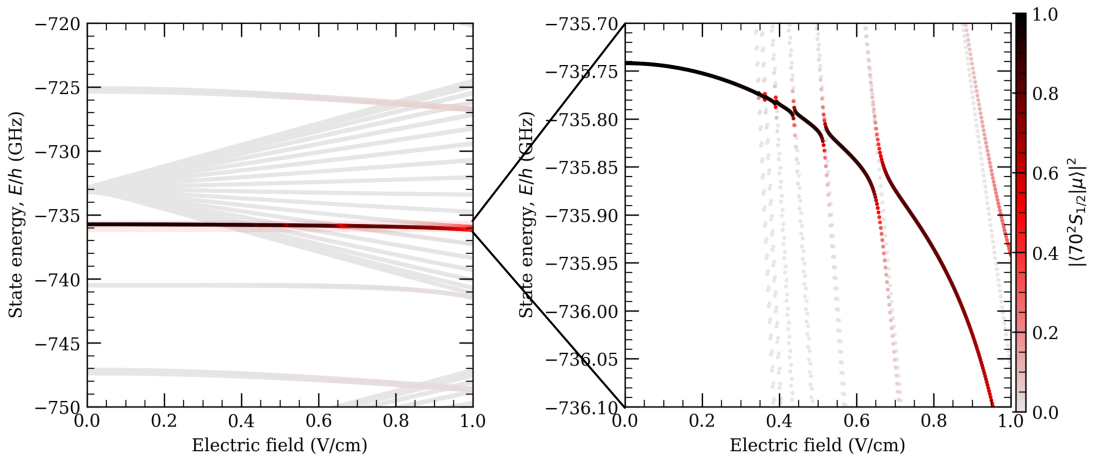


Figure 3.4: (Left) Full Stark map of the $70S_{1/2}$ manifold in rubidium as a function of external electric field. The color scale indicates the dipole transition strength $\left|\langle 70S_{1/2}|\mu|r\rangle\right|^2$. (Right) A magnified view of the stark map, showing how electric fields in combination with strong dipole coupling severely modifies the energy levels as well as mixing rydberg states.

quency, which sets a transport time of a few hundred microseconds.

3.3 Rydberg Atom Electric Field Sensitivity

Although going to higher principal quantum numbers n can theoretically increase gate fidelities, it also increases the atom's sensitivity to electric-field fluctuations. This sensitivity arises from second-order perturbations caused by the mixing of a Rydberg state with nearby Rydberg states of opposite parity. Consequently, the energy shift in the presence of an electric field E can be written as

$$\Delta\omega = \sum_n \frac{\left|\langle r_1 | \, e\mathbf{E} \, | r_n\rangle\right|^2}{E_{r_1} - E_{r_{n'}}} \tag{3.5}$$

where $\mathbf{E}$ is the electric field applied to the atom and r_n is all Rydberg states dipole-coupled to the state $|r_1\rangle$, and E_{r_n} is their corresponding energy

From the scaling of the dipole matrix elements ($\sim n^2$) and the energy spacing between neighbor-

ing Rydberg states ($\sim n^{-3}$), we find that the polarizability of the Rydberg state scales approximately as n^7. In most treatments, this is expressed using a polarizability α such that

$$\Delta\omega = \frac{1}{2}\alpha |\mathbf{E}|^2 \tag{3.6}$$

This polarizability can be displayed using a stark map as shown in figure 3.4. In this figure it can also be seen that the presence of nearby Rydberg states will introduce additional sensativity to fields, where avoided crossing with other states result in sharp increases in the polarizability at specific electric fields.

Fluctuation electric fields would then introduce a detuning noise to the ground-Rydberg excitation, resulting in a reduction in gate fidelities. In order to combat this, it is possible to design more robust gates. However, even in the best case, it is not possible to find a gate fully robust to this detuning noise[76]. As a result, it is necessary to understand how we can mitigate these charge fluctuations in order to maintain high-fidelity quantum gates, which is the focus of chapter 6.

3.4 Rydberg Atom Interaction with Electric Field Gradients

An intriguing effect, partially explored in Chapter 6, is the interaction of Rydberg atoms with electric field gradients, which arise naturally from point sources of charge. Such gradients exert a force on Rydberg atoms, and with coherent control, this effect can be harnessed to manipulate the atomic motional state. Effectively, electric field gradients introduce a state-dependent force that acts only on the Rydberg state and not the ground state. This leads to decoherence through two primary mechanisms:

1. **Position Wavefunction Overlap**:

   If the Rydberg state experiences a greater displacement than the ground state, their motional

wavefunctions may become distinguishable. Since the total state of the atom is the tensor product of its spin and motional states, decoherence in the motional degree of freedom causes decoherence in the spin state as well.

Suppose the Rydberg state is displaced by Δr relative to the ground state, and the initial wavepacket width is σ_r. Then the overlap between their motional wavefunctions scales as

$$\exp\left(-\frac{(\Delta r)^2}{2\sigma_r^2}\right)$$

The width σ_r depends on the trap frequency and is typically on the order of 50 nm. We can calculate the relative displacement Δr as a function of the number of charges on the cavity and the atom's distance from it using Eq. 3.11. We further assume a maximum sequence duration of 5 μs, beyond which atomic loss becomes significant.

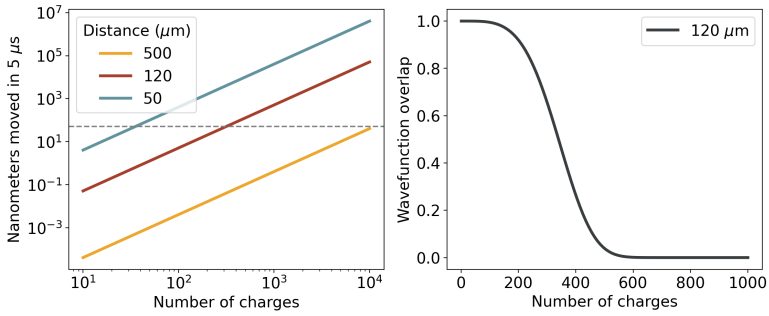


Figure 3.5: (Left) Displacement Δr of the Rydberg state as a function of the number of charges Q on a point charge source, for various initial distances r_0. The vertical dashed line indicates 50 nm, the typical wavepacket width. (Right) Corresponding wavefunction overlap at $r_0 = 120$ μm, showing rapid decoherence for $Q > 200e$.

2. **Differential Accumulated Phase**:

In a Ramsey-type interferometry sequence of duration t, the relative phase $\varphi(t)$ accumulated

between the two $\pi/2$ pulses is given by:

$$\varphi(t) = \int_0^t \Delta(t')\, dt' \tag{3.7}$$

where $\Delta(t)$ is the time-dependent detuning of the Rydberg state from the driving laser frequency. This detuning arises from the Stark shift, which we model as

$$\Delta(t) = \frac{U(r(t))}{\hbar} \tag{3.8}$$

where $U(r)$ is the potential energy of the Rydberg state in the electric field. Assuming small displacements, we Taylor expand $U(r)$ about the initial position r_0:

$$U(r) \approx U(r_0) + \left.\frac{\partial U}{\partial r}\right|_{r_0} \delta r(t) \tag{3.9}$$

Assuming an initial thermal distribution with position x_0 and velocity v_0, and including constant acceleration a, the displacement is:

$$\delta r(t) = x_0 + v_0 t + \frac{1}{2} a t^2 \tag{3.10}$$

where the acceleration is given by:

$$a = \frac{1}{m} \left.\frac{\partial U}{\partial r}\right|_{r_0} \tag{3.11}$$

Substituting into the phase expression, we obtain:

$$\varphi(t) = \frac{1}{\hbar} \int_0^t ma \left(x_0 + v_0 t' + \frac{1}{2} a t'^2 \right) dt' \tag{3.12}$$

with a given explicitly in Eq. 3.11.

We can view a single Rydberg atom in a superposition state as a type of interferometer, where the two paths correspond to the internal states, and can be manipulated by applying π pulses at various times.

We begin by deriving a general expression for the atomic wavefunction in position space as a function of evolution time. As outlined above, the wavefunction evolves into a displaced Gaussian wavepacket accompanied by a phase factor (assuming an initial Gaussian coherent state). Both the displacement and the accumulated phase influence Ramsey-type experiments.

However, the displacement cancels if the two arms of the interferometer are recombined so that they have equal final positions and momenta, that is, if $(x_{\text{final}}, v_{\text{final}})$ are the same for both arms. This condition can be satisfied by applying pulse sequences with two or more π pulses, provided certain relationships between the pulse timing intervals are met. Furthermore, the accumulated phase can exhibit a polynomial time dependence of the form $\sim t^3 + t^2 + t$, which can also be cancelled using a three-pulse sequence.

These results enable two key applications:

- **Extending Rydberg coherence:** Electric field gradients typically limit Rydberg coherence due to motional effects. Our three-pulse sequence cancels both the displacement and the accumulated phase. This approach may be extended to multiple interacting Rydberg atoms, where the interaction scales as $1/r^6$.

- **Electric field gradient sensing:** A two-pulse sequence cancels the displacement of the wavepacket, but leaves a residual phase that is sensitive to the gradient. By tuning the total sequence duration, we can optimize the sensitivity to charge-induced gradients. Alternatively, a single-pulse sequencem would retain sensitivity to both phase and displacement.

Sequence	Cancels Phase?	Cancels Displacement?
$\tau_1 - \pi - \tau_2$	No	No
$\tau - \pi - 2\tau - \pi - \tau$	No	Yes
$\frac{2-\sqrt{2}}{4}\tau - \pi - \frac{\sqrt{2}}{4}\tau - \pi - \frac{\sqrt{2}}{4}\tau - \pi - \frac{2-\sqrt{2}}{4}\tau$	Yes	Yes

3.4.1 Cancelling Phase Space Displacement

To cancel motional differences with a two-pulse sequence (with wait times t_1, t_2, t_3), we require:

Momentum balance:

$$t_1 + t_3 = t_2 \tag{3.13}$$

Position balance:

$$\frac{1}{2}(t_1^2 + t_3^2) + t_1 t_2 + t_1 t_3 = \frac{1}{2}t_2^2 + t_2 t_3 \tag{3.14}$$

Solving these with total time $T = t_1 + t_2 + t_3$ yields:

$$t_1 = t_3 = \frac{T}{4}, \quad t_2 = \frac{T}{2} \tag{3.15}$$

This corresponds to the Carr-Purcell sequence with $N = 2$. More generally, any even number of pulses also satisfies this symmetry.

3.4.2 Remaining Phase Shift

Although the Carr-Purcell sequence cancels displacement, it does not eliminate phase accumulation (as cancellation requires $N \geq 3$ for $\varphi(t) \sim t^3$). The accumulated phase is:

$$\delta\varphi(\tau) = \frac{2}{\hbar}\left(\frac{\partial U}{\partial x}\right)^2 \frac{\tau^3}{m} \tag{3.16}$$

or equivalently:

$$\delta\varphi(T) = \frac{\hbar}{32m}\left(\frac{\partial\Delta}{\partial x}\right)^2 T^3 \tag{3.17}$$

with $T = 4\tau$.

Thus, we expect the ground-state population to vary as:

$$P_g(T) = \frac{1}{2} + \frac{1}{2}\cos(AT^3)$$

where A depends on the electric field gradient, which in turn depends on the distance from a point charge as well as its charge. Figure 3.6 shows the simulated $P_g(T)$ at a distance of 70 μm.

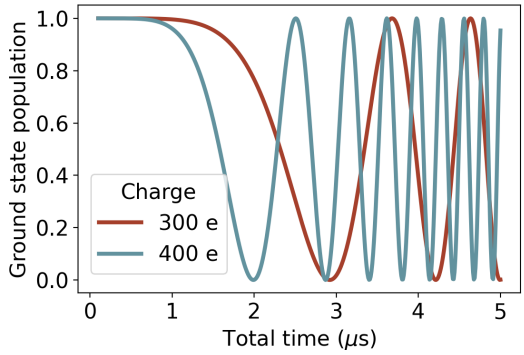


Figure 3.6: Simulated ground state population after a Carr-Purcell sequence ($N = 2$), as a function of total sequence time T, at distance $r_0 = 70$ μm.

If the charge varies shot-to-shot (but remains fixed during each sequence), we can average over a distribution. Figure 3.7 shows the simulation for $q = 200 \pm 10$ e point charge, drawn from a normal distribution.

As a result, this phase will produce a sensative measurement of the electric field gradient that increases in sensativity as a function of time.

$$dP_g = -\frac{1}{2}T^3 \sin(AT^3)dA$$

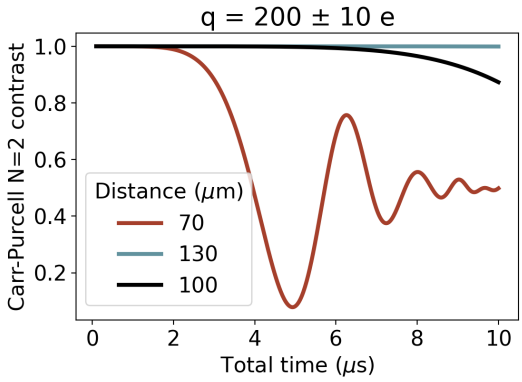


Figure 3.7: Averaged ground state population over a point charge distribution $q = 200 \pm 10\,e$, for varying sequence times and distances.

Let's explore...

Mikhail Lukin

4

Construction of the Fiber Cavity Apparatus

A significant component of my Ph.D. was the construction of the vacuum chamber and the fiber cavity device used in the chapter 7. In this chapter, I will provide an overview of the vacuum chamber and cavity structure design. Both of these designs are inspired by the chamber and mounting structure of the nanophotonic cavity utilized in the chapters 5 and 6.

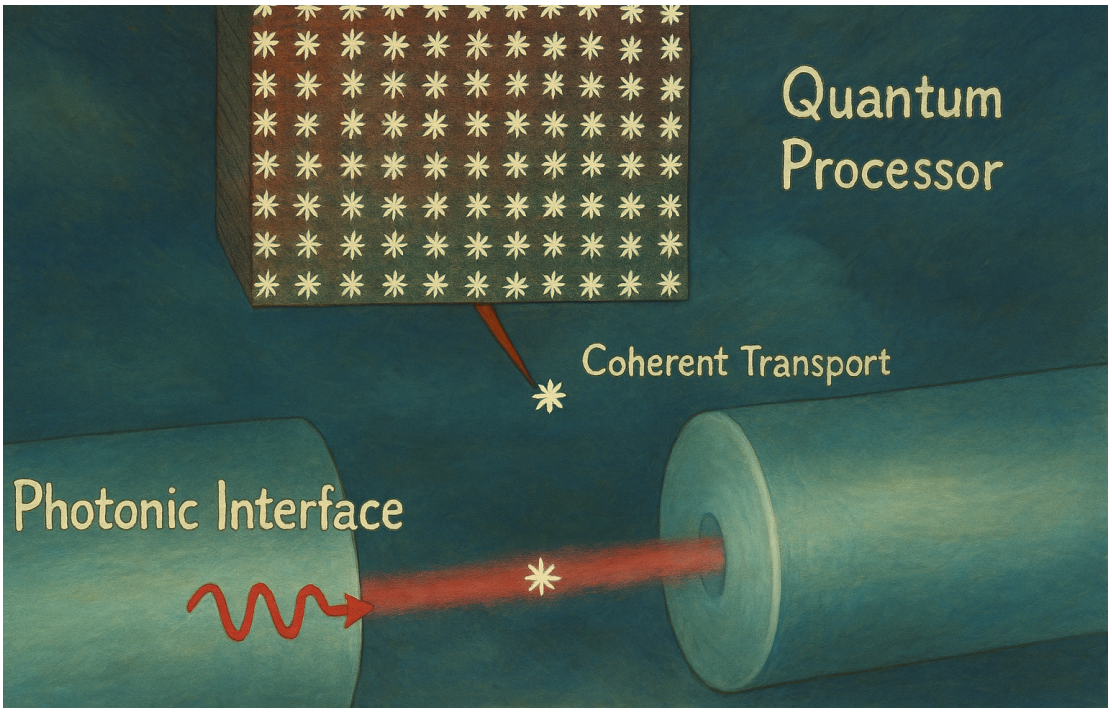


Figure 4.1: A pictorial representation of the fiber cavity experiment, rendered in the style of Studio Ghibli, illustrates an array of atoms trapped above the cavity where entangling operations are performed using Rydberg interactions. Coherent transport is used to shuttle atoms between the quantum processor and the photonic interface. The photonic interface, a fiber-based Fabry–Perot cavity, enables fast readout as well as quantum networking.

4.1 High Finesse Optical Cavities in Ultrahigh Vacuum

Placing high-finesse optical cavities in an ultra-high-vacuum (UHV) environment is challenging, because of the stringent stability and alignment requirements. To give an idea of the stability needed, in order for the cavity detuning to remain constant, the length of the cavity must be stable to within $\frac{\lambda}{2F}$. For our cavity, this corresponds to a length on the order of 10 picometers. Fortunately, these requirements are alleviated by the use of fiber cavities. First, fiber cavities can operate in the near-confocal regime while still maintaining strong coupling. As mentioned in the previous chapter, this regime is less sensitive to misalignment. Additionally, their small size makes it possible to create smaller mounts with reduced susceptibility to mechanical fluctuations. Secondly, the reduced cavity size also allows for kilohertz bandwidth modulation of the length. This high modulation bandwidth enables robust stabilization against noise at acoustic frequencies.

Another important consideration when placing high-finesse cavities in vacuum is that special care must be taken to select appropriate coatings so that the reflectivity does not degrade under UHV conditions. Our fiber cavities are purchased from QLibri, where we specify a radius of curvature of about 150 μm and a 780 nm coating with a finesse of approximately 40,000. The coating is a standard high-reflectivity dielectric stack made of alternating Ta_2O_5 and SiO_2. To prevent reflectivity degradation in UHV, we request an additional protective layer $\lambda/2$ SiO_2 [163].

4.2 Alignment of the Fiber Cavity

Alignment of the fiber cavity is performed using two 3-Axis NanoMax™ NanoPositioning Flexure Stages and mounting the fiber cavities in a fiber chuck mounted in an Adjustable Flexure Fiber Chuck Mount giving an additional 2 degrees of freedom of tip and tilt. Cameras are setup to view the cavity from above and from the side. This setup is shown in fig 4.2. With all degrees of freedom a coarse alignment of the fibers to each other is enough to form an optical cavity between the two

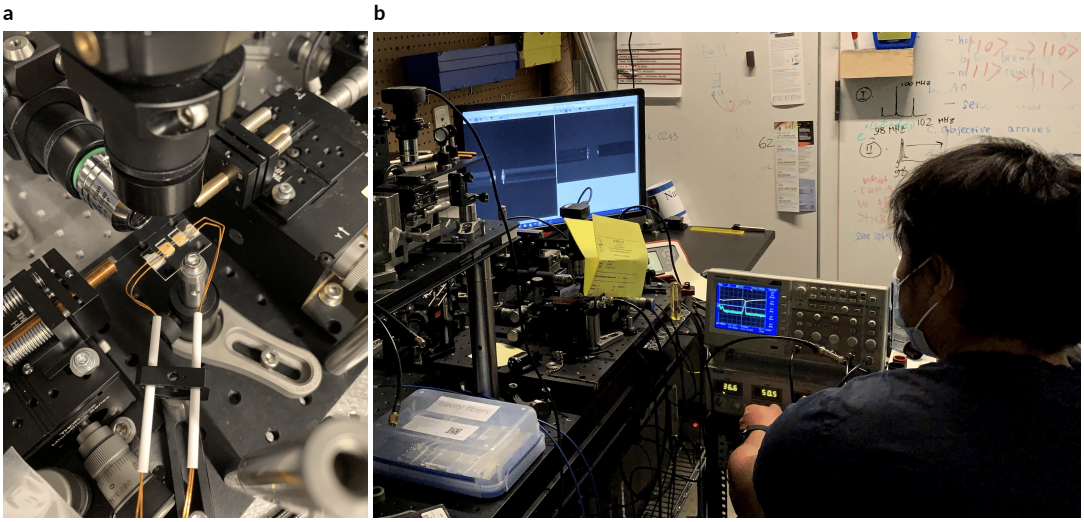


Figure 4.2: (a) An image showing the alignment setup for the fiber cavity when being loaded into the mount. (b) Po aligning the fiber cavity using the x and y plane images.

fibers. This signal can then be further optimized for Finesse and mode matching. fine alignment is performed using a 3-axis piezo controller attached to one of the nanomax stages. The cavity can be monitored from the cameras, while also monitoring the reflection and transmission of the fiber cavity on an oscilloscope. Finesse is measured by modulating the phase of the probing laser with a frequency larger than the linewidth of the cavity. The sidebands produced by this modulation can then be used as a frequency ruler to measure the linewidth of the cavity. In order to find the finesse the length is then approximated using the cameras. A typical setup for the alignment process is shown in fig 4.2b.

Aligning fiber cavities have many differences from their traditional macroscopic cavity counterpart. An important consideration is that, unlike the traditional cavity case, a camera cannot be used to see the profile of the mode being measured. As a result, determining which mode is the TEM_{00} poses a challenge. In order to find the TEM_{00} mode one can take note of the mode spectrum and utilize the way in which the structure of the modes changes as a method to find the mode that be-

haves like the TEM_{00}. Another way of determining the TEM_{00} mode is to form longer cavities and find the mode that is most prominent at these longer lengths. Due to the larger size of higher-order modes, they experience a larger amount of clipping loss and thus appear with lower finesse and have less signal. The reflectivity spectrum of a fiber cavity is carefully described in [56]. The results of this paper show that the reflectivity of a fiber cavity is given by:

$$r(\Delta) = \beta - \langle \psi_f | \psi_c \rangle^2 \frac{\kappa_{in}}{\kappa/2 + i\Delta} \tag{4.1}$$

Here β is a parameter that describes how much of the light is directly reflected off of the mirror and back into the single mode fiber. This is not always 1 due to misalignment of the ablation and the fiber core resulting in an angle at the end of the fiber which reflected light out of the core and into the cladding. $\langle \psi_f | \psi_c \rangle$ is the overlap of the fiber mode $|\psi_f\rangle$ and the cavity mode $|\psi_f\rangle$. The mode matching, which is the amount of light that enters the cavity from the single mode fiber and vice versa, is then given by $|\langle \psi_f | \psi_c \rangle|^2$. In the case of reflection we find a $|\langle \psi_f | \psi_c \rangle|^4$ term, which corresponds to mode matching squared due to the circulating power being proportional to the mode matching and the leakage of that power into the single mode fiber being proportional to mode matching as well, thus resulting in a mode matching squared. Another feature of the fiber cavity reflectivity is that the projection of different modes into the same single mode fiber results in fano-like features. This can be captured by considering the full reflectivity spectrum.

$$r(\Delta) = \beta - \sum_{m,n,q} \langle \psi_f | \psi_{mnq} \rangle^2 \frac{\kappa_{in}}{\kappa_{mnq}/2 + i(\omega_l - \omega_{mnq})} \tag{4.2}$$

Where q denotes the longitudenal mode of the cavity and n and m correspond to the transverse mode of the cavity and ω_{mnq} is the resonance frequency of that mode, κ_{mnq} is the corresponding linewidth, and $|\psi_{mnq}\rangle$ is the spatial electric field profile of the mode. The spatial structure of these

modes and their respective frequencies are discussed in chapter 2. It is important to note that interference between the light from different modes will result in a fano like line shape. One will typically find that minimizing the fano feature on reflection corresponds to proper alignment, this is due to the reduction in the phase shift from higher order modes. If we now write the equation for the transmission:

$$t(\Delta) = -\sum_{m,n,q} \langle \psi_f | \psi_{mnq} \rangle \frac{\sqrt{\kappa_{in}\kappa_{out}}}{\kappa_{mnq}/2 + i(\omega_l - \omega_{mnq})} \tag{4.3}$$

We find that this spectrum will not suffer from these fano effects. Another important thing to note about fiber cavities is their shape. A typical fiber cavity will have a Gaussian shape as a result of ablation with a Gaussian laser. The deviation from the most optimal spherical shape results in diffractive losses, especially at longer lengths of the cavity. This eventually limits the workable length for typically fiber cavities to something on the order of $L < ROC/2$ for a flat to curved fiber cavity configuration. This forces us to work in the near-confocal cavity regime, where we deviate slightly from confocal to maintain a large spacing between the TEM_{00} mode and higher-order modes. Fortunately, due to the small radius of curvature of the fiber cavity, it is not necessary to operate in the concentric regime to maintain a small waist and strong coupling as discussed in Chapter 2. Additionally, a near-confocal cavity is significantly less sensitive to alignment, which will be a useful feature later.

In addition to diffractive losses, the Gaussian shape introduces the interesting effect that misalignment can significantly change the effective radius of curvature of the mirrors because the radius of curvature of a Gaussian varies at different points along it. This results in alignment-dependent birefringence arising from differences in the radius of curvatures from one axis to the other. This can also be seen as splitting of the higher-order modes that will no longer be degenerate.

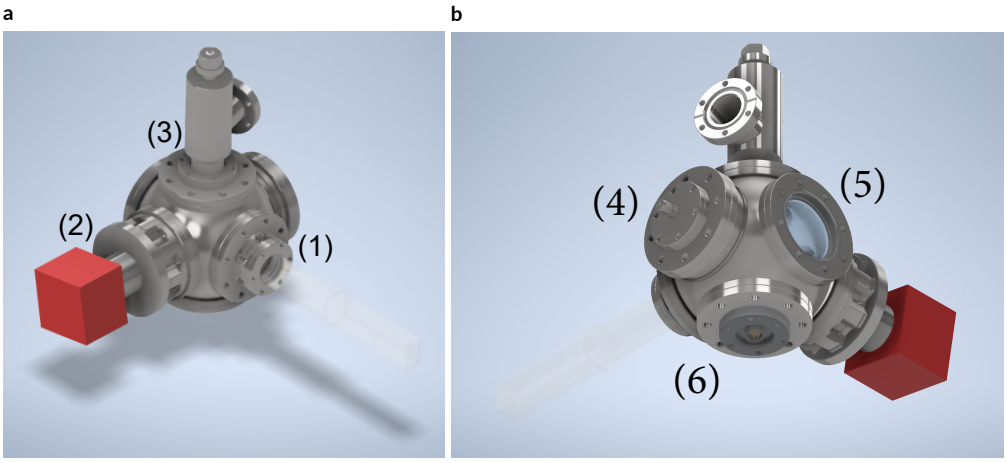


Figure 4.3: (a) shows a top view of our vacuum chamber with ports (1-3) labeled for the glass cell, ion pump, and turbo pump ports. (b) shows a bottom view of our chamber with ports (4-6) labeled for the fiber feedthrough, back viewport, and electrical feedthrough

4.3 Vacuum Chamber Assembly

The vacuum chamber design largely follows that used in Chapters 5 and 6, but with a few modifications. One main difference is the larger central chamber, which consists of a 4.5" spherical cube. Each port in this chamber serves a different purpose, as summarized in Table 4.1 and labeled in Figure 4.3.

In order to prepare the parts for ultra-high vacuum it is necessary to "bake" them. By bringing the parts to a high temperature for a prolonged period of time, it allows the parts to outgas a significant amount of the compounds trapped inside the material. We pre-baked all the steel parts of our chamber in an oven provided by QuEra computing at 450C for 2 days. After assembling the chamber, we then performed an additional vacuum bake at a lower temperature of $\sim$150 due to the limited maximum temperatures of parts such as the glass cell.

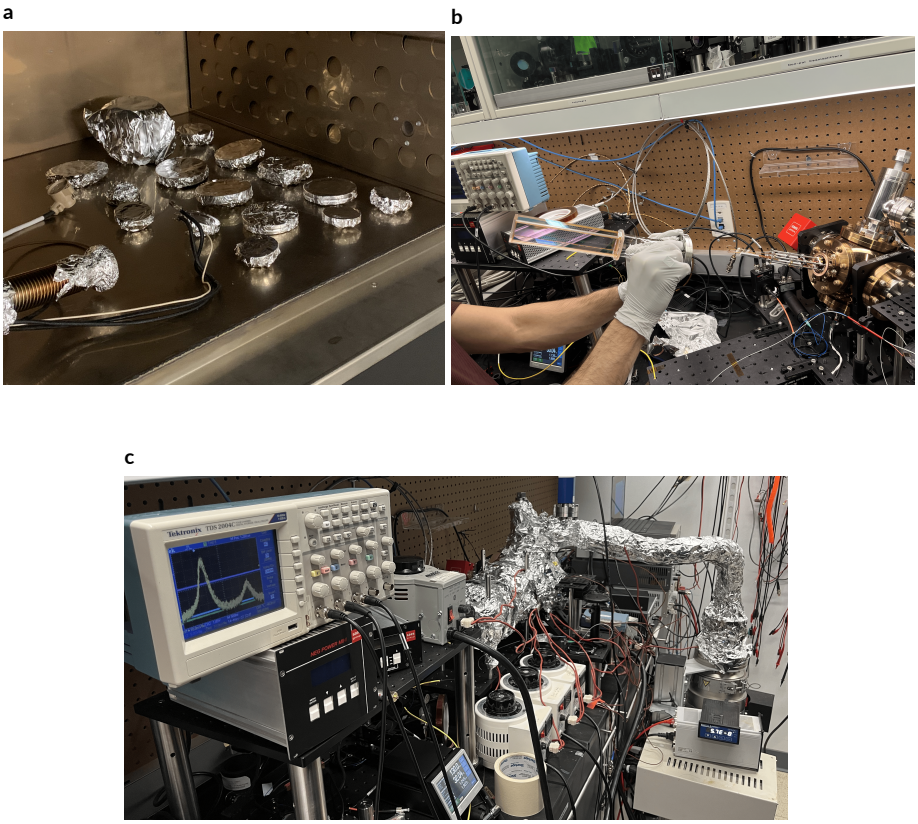


Figure 4.4: (a) Vacuum parts for the chamber are baked in a large oven provided by QuEra Computing, held at 450 °C for two days to reduce outgassing. This process also imparts a brown hue to the parts due to oxidation. (b) The glass cell is carefully placed over the cavity-mount structure. The chamber is tilted upward so that the copper gasket can rest on the "razor blade" of the vacuum chamber. (c) The glass cell is protected by a vacuum-foil wrapping and then wrapped with heater cables. The temperature is monitored at multiple points along the chamber to ensure even heating, which is especially important at the glass–metal interface. For these bakes, we typically go to a temperature of 150 °C for one or two weeks. During the bake, we continuously monitor the fiber cavity to ensure its alignment is not severely shifted. The oscilloscope trace shows the cavity resonance, as well as a sideband used to measure the linewidth.

Port	Parts	Use
1	4.5" to 2.75" zero-length reducer, 2.75" CF Flange Adapter (with groove grabbers), Glass Cell	Flange adapter provides groove grabbers used to mount the cavity rod structure that extends into the glass cell.
2	4.5" to 2.75" zero-length reducer, 2.75" CF to 1/8" Swagelok adapter	Fiber feedthrough for connecting the fiber cavity: a single-mode fiber input and a multimode fiber output.
3	4.5" to 2.75" zero-length reducer, 2.75" CF 10-pin double-ended bayonet feedthrough	Electrical feedthrough for connecting the cavity piezos, heaters, and rubidium dispensers.
4	4.5" fused-silica viewport	Back window for optical access.
5	Double sided faced 4.5" CF, 4.5" CF Close Coupler (with groove grabbers), NEXTorr® D500-5 NEG-ION combination pump	Ion pump for maintaining UHV. The groove grabbers also provide a mounting point for the vacuum chamber.
6	4.5" to 2.75" zero-length reducer, 2.75" right-angle manual bellows valves	Connection to a turbopump during bake-out and for pumping down prior to activating the ion pump.

Table 4.1: Summary of the ports on the vacuum chamber, along with the parts used and their functions.

4.4 Fiber Cavity Mount

The fiber cavity is suspended in the vacuum chamber by a rod structure made from Kimball Physics components, which attach to the groove grabbers on a 2.75" CF flange adapter. At the end of this rod assembly, an aluminum mount extends into the center of the glass cell, and the fiber cavity is affixed to a glass-slide assembly on that mount as shown in figures 4.5 and 4.6.

To construct the fiber-cavity mount, two Noliac shear piezos (model CSAP01) are glued onto a 25.4 mm × 10 mm × 1 mm glass slide. Next, a monolithic V-groove structure is attached on top of the piezos, and the glass connection at the base of the V-groove is severed to allow for freer piezo movement. This V-groove method (adopted from the Childress and Sankey labs at McGill Univer-

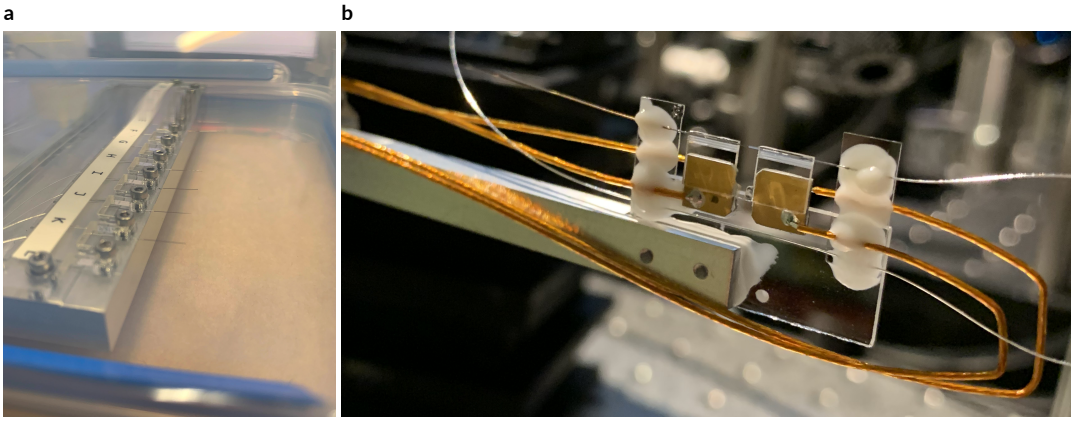


Figure 4.5: (a) We receive our fiber cavities from QLibri in a Tupperware container, in which the fibers are mounted on a machined metal structure. (b) The fiber-cavity mount is shown. The piezos, which modulate the cavity length, are attached to a microscope slide. On top of the piezos is a monolithic V-groove that holds the fiber. Part of this V-groove was deliberately broken to allow the piezos to move freely. The fiber cavity is visible in the V-groove, with a single-mode fiber on the left and a multimode fiber on the right; the latter is bent and redirected down the mount. For strain relief, both the piezo wires and fibers are secured to an additional glass slide.

sity) simplifies the rough alignment of the fiber cavity: simply placing the fibers into the grooves already yields a reasonable initial alignment, requiring only minor tweaks to minimize birefringence and maximize finesse and mode matching.

To test the bake-out's effect on cavity alignment, the Childress and Sankey group provided fiber cavities for a trial setup. A fiber cavity was baked at 150 °C for five days, with continuous monitoring of finesse. No degradation in finesse or mode matching was observed. Bake-outs of the fiber-cavity device described in Chapter 7 also showed minimal shifts in finesse and mode matching. However, the temperature must be raised and lowered very gradually. We found that after a sudden power outage during a bake-out, the rapid temperature change caused a permanent shift in both finesse and mode matching.

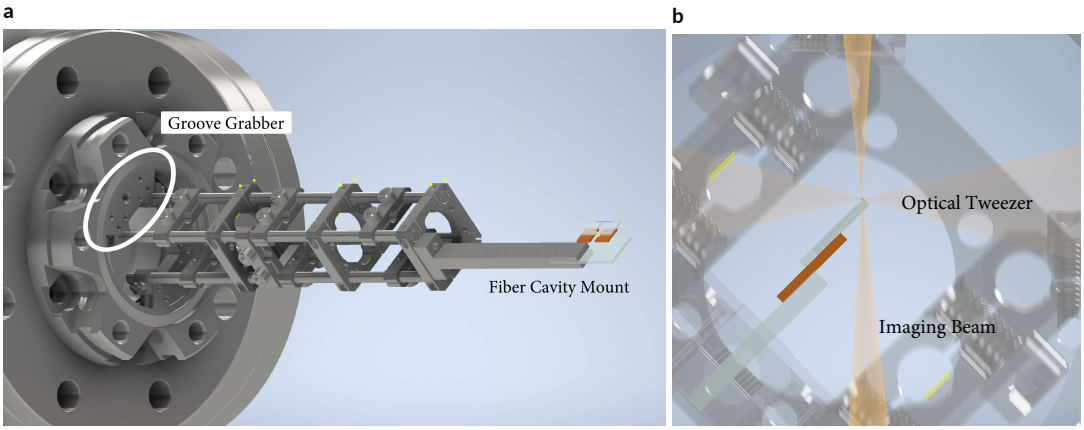


Figure 4.6: (a) The rod structure used to mount the fiber cavity onto the vacuum chamber. (b) A side view of the chamber, looking along the axis of the fiber cavity. The tilt of the cavity mount permits an imaging beam to enter from the bottom of the chamber and pass through the center of the fiber cavity without clipping. Additionally, the high-NA optical tweezers can be introduced from the side without intersecting the cavity or its mount.

Sounds good, let's do it, let's push!

Mikhail Lukin

5

Entanglement Transport

The realization of an efficient quantum optical interface for multi-qubit systems is an outstanding challenge in science and engineering. Using two atoms in individually-controlled optical tweezers coupled to a nanofabricated photonic crystal cavity, we demonstrate entanglement generation, fast non-destructive readout, and full quantum control of atomic qubits. The entangled state is verified in free space after being transported away from the cavity by encoding the qubits into long-lived states and using dynamical decoupling. Our approach bridges quantum operations at an optical

link and in free space with a coherent one-way transport, potentially enabling an integrated optical interface for atomic quantum processors.

Systems of neutral atoms have recently emerged as a powerful platform for quantum simulations and quantum computation [168,49,174,113]. Atom trapping, coherent control, and readout are enabled by optical beam arrays, whereas high-fidelity multi-qubit quantum gate operations are enabled either through tunneling [84] or coherent excitation into atomic Rydberg states [100]. Many potential applications of these systems, from quantum networking to modular quantum computing, require a mechanism for transferring qubit states to optical photons without compromising the ability for multi-qubit control [130,124]. Integration with a quantum optical interface, such as an optical cavity with switchable interactions, would enable the required atom-photon entanglement generation and distribution [196,132,153]. A promising approach to achieve this is by spatially separating the cavity from the array and transporting selected atoms to and from the field as needed, preserving the coherence and scalability of atom array systems (Fig. 1A).

5.1 Experimental Setup

We demonstrate a system with a micrometer-size photonic crystal cavity (PCC) coupled to neutral atoms in movable optical tweezers that can perform high-fidelity single qubit control and measurements as well as generate two-atom entanglement. Following the prior work that demonstrated coupling of atoms to photonic crystal structures [65,28,170], entangling atoms in macroscopic cavities [204,205], and coherently transporting atoms and ions in free space [14,95,145], we demonstrate PCC-mediated entanglement generation that can be preserved and verified after transporting the atoms away from the cavity near-field. This is achieved by engineering a compact high-cooperativity photonic structure, establishing full quantum control in the near-field, encoding the qubits into field-insensitive states, and using dynamical decoupling sequences synchronized with the atomic trans-

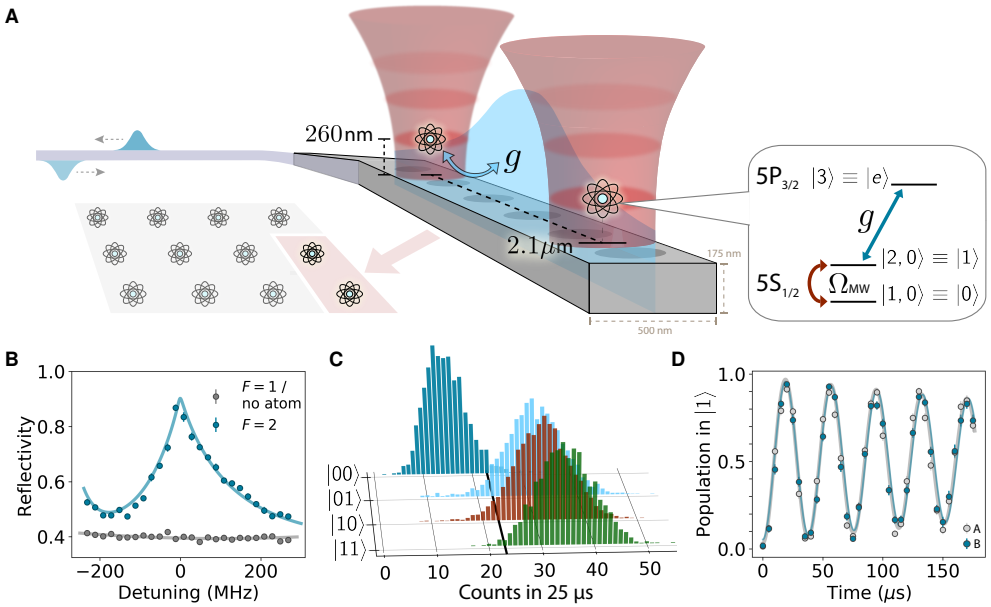


Figure 5.1: Nanophotonic interface for atoms in tweezers. (A) A nanophotonic cavity could act as a photonic link for atom arrays serving as quantum information processors. Our system consists of two atoms in optical tweezers coupled to a fiber-linked cavity capable of a coherent one-way transport. (Inset) Atomic qubit states coupled by a microwave drive Ω_{MW}, with one coupled by the cavity field g to an excited state. **(B)** Cavity reflection spectrum for an atom in a strongly coupled state (blue) and an uncoupled state (gray), described by $(2g, \gamma, \kappa) = 2\pi\times$ (786, 6, 3800) MHz. **(C)** Readout of different two-qubit basis states by using the reflected photon counts. State $|00\rangle$ is distinguished from the others with fidelity $\mathcal{F} = 0.95(3)$. The atoms, cavity, and probe are on resonance. **(D)** Single-qubit Rabi oscillations in the cavity near-field showing preparation and coherent rotation with a π pulse fidelity $\mathcal{F}_\pi = 0.946(3)$.

port.

In our experiments, two ^{87}Rb atoms were trapped in individually controlled optical tweezers and coupled to a PCC attached to a tapered optical fiber, enabling a low-loss photonic link out of the vacuum chamber (Fig. 1A)[195]. The small cross-sectional area of the PCC ($< 0.1\,\mu\text{m}^2$) resulted in a small mode volume $V_m \sim 0.4\lambda^3$ that enabled high atom-photon cooperativity[28] and allowed for switching of the photon interactions by moving the atoms over $\sim 1\mu$m in and out of the cavity near-field. Atoms at the PCC were trapped 260 nm above the surface by a standing wave created with the retro-reflection of the tweezer[193,196,170]A. Loading into the first lattice site of the standing wave was accompanied by a trapping potential deformation that resulted in a $\sim 50\%$ loading probability,

which was increased to 80% by performing polarization gradient cooling during the transport to the PCC A. (An efficiency above 90% without cooling during transport has been achieved with atoms initialized in the motional ground state[193].)

5.2 Atoms Coupled to Photonic Crystal Cavity

The cavity reflectivity strongly depends on the internal atomic state, with qubits encoded in $|0\rangle \equiv |F = 1, m_F = 0\rangle$ and $|1\rangle \equiv |F = 2, m_F = 0\rangle$. The PCC was tuned to be resonant with the $5S_{1/2},\ F = 2 \rightarrow 5P_{3/2},\ F' = 3$ optical transition and addresses all the m_F levels within these manifolds owing to the large cavity width κ. The reflection spectrum of a single atom is characterized by the extracted cooperativity $C = 4g^2/(\kappa\gamma) = 27(1)$ with a fit that accounts for thermal averaging (numbers in parentheses indicate one SD) (Fig. 1B)[170]. When probed on resonance, the difference in reflectivity between an atom in the coupled $F = 2$ and uncoupled $F = 1$ manifold was used to perform a non-destructive single-shot readout. With two atoms, the uncoupled state $|00\rangle$ is distinguished from the other two-qubit states with high fidelity (Fig. 1C). This was used to determine the full two-atom state in all measurements at the PCC. For experiments in free space, readout was performed with state-selective push-out from the trap followed by fluorescence imaging. In both of these regimes, each pair of atoms was simultaneously prepared into $|0\rangle$ by using Raman-assisted state preparation A, and addressed with a global microwave drive to perform single-qubit gates (Fig. 1D).

To coherently move the qubits from the near-field into free space, a millisecond coherence time was necessary. Choosing Zeeman-insensitive hyperfine sublevels as the qubit basis results in coherence times of $T_2' = 2.1(1)$ ms and 9.7(8) ms in the near-field and free space, respectively, measured with a spin-echo pulse sequence (Fig. 2A). In the field-insensitive basis, the coherence is typically limited by the thermal motion that samples varying differential ac Stark shifts in the trap[92,154], and

our measured T_2' in free space is consistent with this model, given the trap parameters. The T_2' at the PCC is likely further reduced by heating intrinsic to the near-field trapping geometry[68] A.

Atomic coherence during transport is additionally affected by the change in differential ac Stark shift when moving between different trapping configurations. To observe this change, a detuned microwave π pulse was applied to single atoms at various times along the $\sim$ 1 μm path from the PCC, where the measured population transfer is proportional to the instantaneous qubit frequency A. From the resulting ramp profile in Fig. 2B, we obtained the minimal time of 650 μs to move from the PCC, limited by the mechanical response bandwidth of the scanning mirrors. Dephasing caused by fluctuations in the atom trajectory can be circumvented by using the Carr-Purcell decoupling pulse sequence (Fig. 2C)[26]. This sequence was tested with the atom beginning in a superposition at the PCC and followed by $N \times \pi$ pulses along its transport, which performed better for an even N because of the symmetry of the ramp profile shown in Fig. 2B. The performance of the decoupling sequence was characterized separately in the two optical tweezers (trap A and trap B): For an optimal $N = 4$, an atom in trap B retains $0.88(5)$ of its initial coherence, limited by the move time and T_2' (Fig. 2C). The lower contrast of $0.64(3)$ for an atom in trap A is ascribed to extra fluctuations in the scanning mirror, given that the traps are otherwise uniform. In addition to decoherence, each atom has a $\sim 15\%$ chance of being lost on the way out of the PCC, which is corrected for in the free space readout A.

5.3 Cavity Carving

To generate an entangled state of atoms using the cavity, we performed a protocol known as "cavity carving" that projectively measures a classical superposition state while maintaining qubit indistinguishability[30,4], which can result in a maximally entangled Bell state[185,204]. To implement the

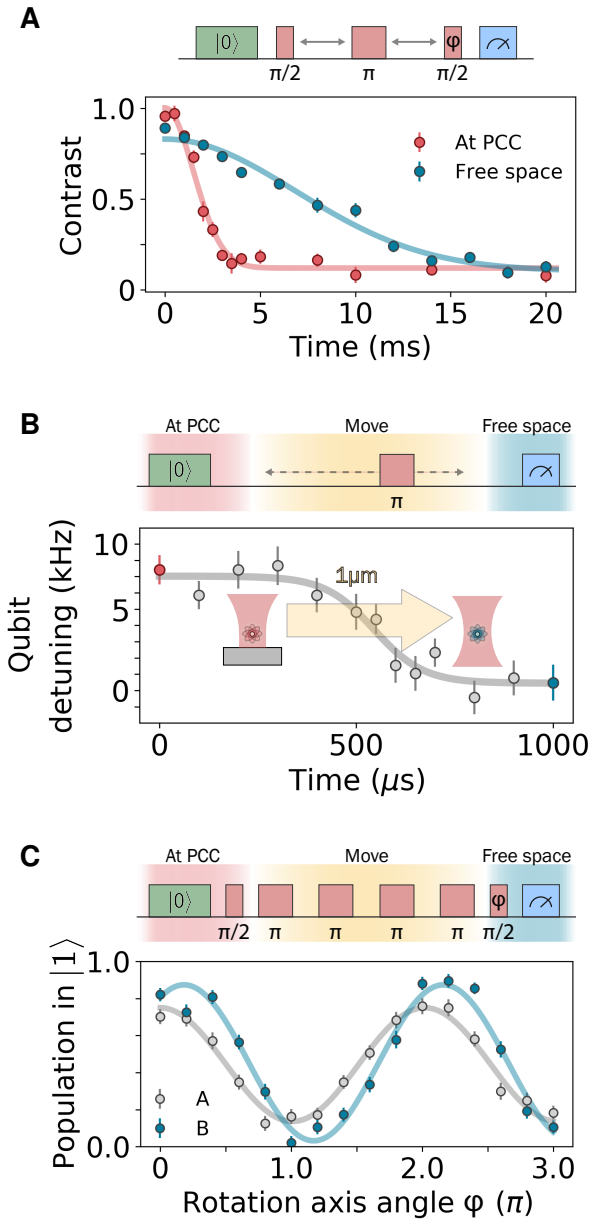


Figure 5.2: Qubit coherence during the transport between the cavity and free space. (A) Measurement of the echo T_2' for stationary traps at the PCC (red) and in free space (blue). **(B)** Changes in the trapping potential configuration during transport cause differences in the light shift and therefore qubit frequency, which can lead to additional dephasing. The gray line indicates fit to the programmed ramp. **(C)** Single-atom coherence for atoms in each trap (labeled "A" and "B") after transport measured in a Ramsey-type sequence. A four-pulse Carr-Purcell sequence symmetric with respect to the qubit frequency profile during transport was used to echo out the light shift variations.

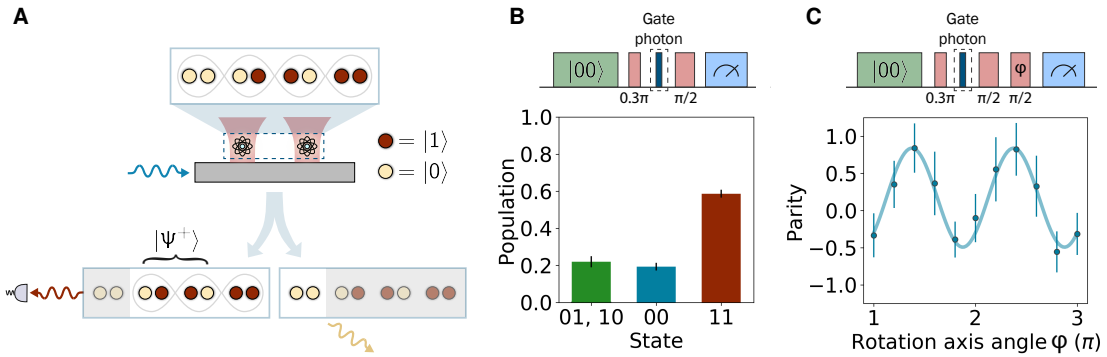


Figure 5.3: Heralded entanglement at the cavity. (A) Protocol description. Post-selection on a photon reflection from a superposition state carves out the $|00\rangle$ component, leaving the atoms predominantly in $|\Psi^+\rangle$. **(B)** Populations of the resulting state in different basis states. A $\pi/2$ pulse was applied before the measurement converting the Bell state $|\Psi^+\rangle$ into $|\Phi^+\rangle$. $\{P_{11}, P_{00}\}$ is extracted {with, without} an additional global π pulse before cavity reflection reflection. P_{01} and P_{10} cannot be distinguished. **(C)** Parity oscillations of the $|\Phi^+\rangle$ state after rotating over a varied axis φ, showing non-classical correlations between the qubits in all bases. The coherence $\rho_{11,00}$ is extracted from the amplitude. The combined coherence and populations gives a Bell state fidelity of $\mathcal{F} = 0.72(3)$.

protocol, we initialized the atoms in $|00\rangle$, and rotated by an angle θ to create the state

$$|\Psi_0\rangle = \cos^2\left(\frac{\theta}{2}\right)|00\rangle - \sin^2\left(\frac{\theta}{2}\right)|11\rangle - i\sin\left(\frac{\theta}{2}\right)\cos\left(\frac{\theta}{2}\right)(|01\rangle + |10\rangle) \tag{5.1}$$

We sent a weak coherent pulse into the cavity mode ($\bar{n} = 0.35$, chosen for negligible scattering error A), and condition on the detection of a reflected photon to project the state $|00\rangle$ out of the two-atom Hilbert space. The angle θ was chosen to maximize the overlap of the resulting state with $|\Psi^+\rangle = (|01\rangle + |10\rangle)/\sqrt{2}$, minimizing the population in $|11\rangle$ while accounting for the finite reflectivity of $|00\rangle$. For our system, the $|00\rangle$ reflectivity is already less than that of the other two-atom states (Fig. 1C). It was further reduced by an interferometer in the detection path and is ultimately limited by the interferometric stability A. After the projection, an additional $\pi/2$ pulse was applied to rotate the Bell state $|\Psi^+\rangle$ into $|\Phi^+\rangle = (|00\rangle + |11\rangle)/\sqrt{2}$ for ease of characterization.

The entangled state was first characterized in situ by using the cavity reflection readout shown

in Fig. 1C. The $|\Phi^+\rangle$ fidelity $\mathcal{F} = \langle\Phi^+|\rho|\Phi^+\rangle = \frac{1}{2}\left(\rho_{00,00} + \rho_{11,11}\right) + \mathrm{Re}(\rho_{00,11})$ was determined by measuring populations and extracting coherence from the parity oscillation contrast upon another $\pi/2$ rotation over different axes[204]A. Populations are plotted in Fig. 3B with $\mathcal{P} = P_{00} + P_{11} = 0.78(3)$; the imbalance between $|00\rangle$ and $|11\rangle$ is discussed and modeled in the supplementary materials A. The parity oscillation in Fig. 3C corresponds to a coherence of $\rho_{11,00} = 0.33(2)$. These measurements give a fidelity of $\mathcal{F} = 0.72(3)$ and a concurrence bound of $\mathcal{C} \geq 0.46(5)$ A. The major part of the error (24%) is accounted for by the chosen initial angle θ for our protocol, with an additional 4% from the initialization imperfections. Although our approach uses a single gate photon, heralding on repeated gates can improve the entanglement fidelity at the expense of the success probability[204].

5.4 Entanglement Transport

Last, the entangled atoms were transported away from the cavity while applying decoupling pulses. The qubit state populations were measured in the ZZ, XX, and YY bases (Fig. 4), giving the population $\mathcal{P} = 0.78(6)$ and the coherence $\rho_{11,00} = 0.26(5)$, corrected for the atomic loss. This resulted in a fidelity of $\mathcal{F} = 0.65(6)$ and a lower bound to the concurrence of $\mathcal{C} \geq 0.35(11)$ ($\mathcal{F}_u = 0.52(5)$ and $\mathcal{C}_u \geq 0.04(10)$ without the readout correction). Both $\mathcal{F} > 0.5$ and $\mathcal{C} > 0$ certify entanglement after transport at a 99% confidence level. The state fidelity is consistent with the decoherence observed for single atoms during transport (Fig. 2C), limited by atomic thermal motion and uncorrelated fluctuations in the programmed trajectories. The trajectory fluctuations can be reduced in the future by using an acousto-optic deflector (AOD) that would speed up the transport and enable atomic displacements of more than 100 μm, which is sufficient for high-fidelity Rydberg state control[90].

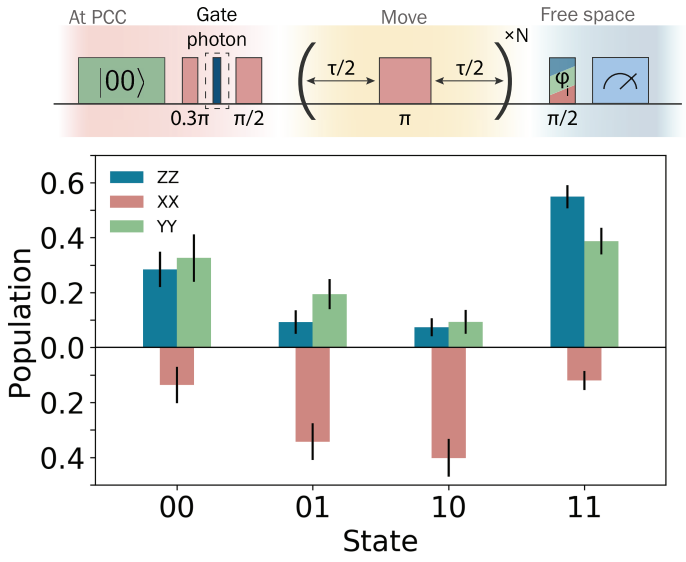


Figure 5.4: Coherent transport of entangled atoms from the cavity to free space. After entangling the atoms at the cavity, the tweezers are moved away while applying dynamical decoupling. Free space readout in different bases after transport shows the remaining entanglement fidelity of $\mathcal{F} = 0.65(6)$, which is larger than the classical limit of 0.5.

5.5 Outlook

These results demonstrate that combining movable atoms in tweezers with nanophotonics constitutes a promising platform for the development of a quantum optical node for large-scale atomic quantum processors. If integrated with a free space atom array, our system could enable quantum teleportation of the atom array states to optical photons [10] or remote entanglement of arrays. This can be accomplished by using the demonstrated one-way transport, in which the atoms that are entangled with a photon at the PCC are then coherently moved to the free space array to interact through Rydberg gates. Extending our demonstration to a general-purpose quantum optical interface with a coherent two-way transport could enable feed-forward protocols such as quantum error correction by means of fast, high-fidelity quantum nondemolition cavity readout. Furthermore, with multiple atoms coupled to nanophotonic waveguides, entangled and arranged into arbitrary

spatial configurations, important classes of many-particle quantum states can be created, such as atomic cluster or graph states [31], large-scale photonic Fock states [139], or Schrödinger cat states [39]. Last, telecom transitions present in both alkaline-earth and alkali atoms [34,121] could extend atom-nanophotonic quantum networking to long-distances, which is crucial for quantum communication and the scale-up of processing power [124].

Every challenge can be an opportunity!

Mikhail Lukin

6

Rydberg Atoms near Nanophotonics

Significant progress is currently being made in developing quantum information processors across a variety of different physical platforms[42]. Further increasing the computational power may require connecting multiple processors via quantum interconnects[123]. In particular, Rydberg atom arrays have recently emerged as a leading platform for quantum simulations and quantum information processing [168,23,48]. While scaling to many thousands of controlled qubits appears feasible[66], significant advances can be achieved by coupling Rydberg arrays to optical, microwave, and elec-

tronic devices. Integration with these devices could enable quantum networking via optical photons [153,132,67,213,150], as well as novel coupling and control techniques via microwave photons [186]. However, in practice, Rydberg qubits experience decoherence near surfaces caused by fluctuating charges.

Over the past decade, coherent excitation to Rydberg states in atomic gases has been achieved near various types of surfaces, including glass [90], quartz [177], inside hollow-core fibers [53], an optical nanofiber [149], atom chips [27,40,41], and superconducting surfaces [64,190,82]. Compensation for the stray electric fields, in part caused by alkali adsorption on these surfaces, has been approached through light-induced desorption [40,41], heating of the surfaces [90,190,177], applying in-vacuum electric fields [27,82], or deposition of a thin metallic alkali layer [64]. However, quantum information applications often require understanding and control of local electric fields at micrometer scales with sub-microsecond temporal resolution that cannot be obtained using sensing with macroscopic atom samples.

In this chapter, we leverage the control over individual atom qubits trapped in moveable optical tweezers to study in detail the spatial and temporal properties of electric fields from a dielectric surface. Specifically, we experimentally demonstrate coherent control of individual Rydberg qubits and entanglement of qubit pairs in close proximity to a nanoscale photonic device made of silicon nitride, used previously to achieve atom-photon and transportable atom-atom entanglement [196,215]. The effects of stray electric fields are minimized by using a small-surface area device and illuminating it with UV light at an optimized power. Remarkably, we find that the electric field from the device resembles a point-charge of $\sim$ 200 single electron charges (e) with quasi-static fluctuations. This enables coherent control via decoupling pulse sequences at distances as close as 100 μm from the device. Moreover, we demonstrate that the electric field noise from the device surface minimally perturbs a two-atom entangled state at these distances. This allows us to map the local electric field gradient by changing the relative orientation of the two entangled atoms, realizing an entanglement-

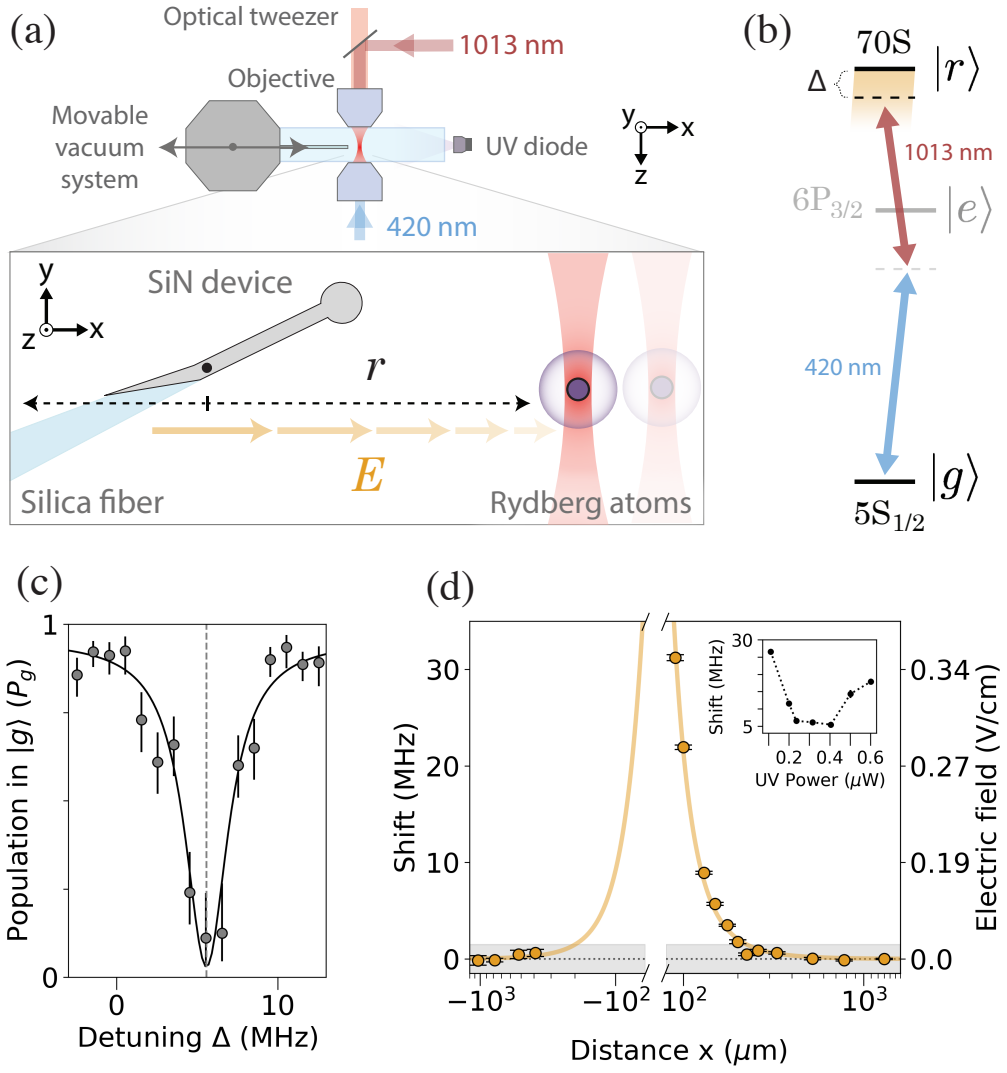


Figure 6.1: Rydberg spectral shift. (a) Experimental setup. (b) Two-photon excitation to the Rydberg state which is shifted by electric fields (yellow shade). (c) Ground state population P_g as a function of the two-photon detuning Δ at $150\ \mu\text{m}$ from the device, where the spectrum center (dashed line) is determined via a Lorentzian fit (black line). (d) Measured spectral shift as a function of distance from the device fitted to a point-charge model (yellow line, Supplement B, Section 2.1). The shift only exceeds the Rabi-broadened linewidth (shaded gray region) for distances less than $250\ \mu\text{m}$. (Inset) Spectral shift dependence on UV power at $160\ \mu\text{m}$.

assisted measurement, based on a decoherence-free subspace. Two-qubit spin echo-based and entanglement assisted measurements are being actively explored in systems involving individual color centers [106,33,148,161], trapped ions [122,160,165,116,129], and atoms [181,143]. Here, these approaches are applied to individual neutral atoms in optical tweezers, enabling novel types of local electrical noise measurements. Together with the recently demonstrated coherent transport of ground state atoms [17,215], our observations pave the way for integrating Rydberg arrays with micro- and nanoscale devices.

6.1 Experimental Setup

In our experiments, individual Rubidium-87 atoms are loaded in optical tweezers from a magneto-optical trap (MOT). The experiment begins when MOT light scattered by the atom is collected via the optical tweezer path to indicate atomic presence, which allows us to select for experiments of either one or two atoms. The device is suspended on a tapered silica fiber connected to a translation stage (Fig. 6.1(a)), allowing it to be positioned $90 - 2600\mu$m from the trapped atoms. Each atom is prepared in $|g\rangle = |5S_{1/2}, F = 2, m_F = 2\rangle$ and excited to the $|r\rangle = |70S_{1/2}, m_J = 1/2\rangle$ Rydberg state via a two-photon transition (Fig. 6.1(b)). Atoms in the Rydberg state in our system are repelled by the tweezer light. While this requires the tweezer light to be pulsed off during experiments, turning the tweezer back on removes the population in the Rydberg state. Therefore, in subsequent fluorescence imaging, Rydberg population is signaled via atom loss.

The Rydberg state in an electric field $\mathbf{E}$ experiences a Stark shift $\Delta\nu = \frac{1}{2}\alpha|\mathbf{E}|^2$ *, with polarizability $\alpha = 534\,\mathrm{MHz}/(\mathrm{V/cm})^2$ [136]. Its spectral shift is measured by exciting the atom and varying the detuning of the 420 nm light in the two-photon transition to take a spectrum (Fig. 6.1c). Each detuning data point of the spectrum is averaged over multiple experimental runs with single atoms. The shift follows the electric field scaling of a point-charge (r^{-4}) located on the 31.5 μm-long de-

*The Rydberg energy level u is typically notated as $u_{\mathbf{E}\neq 0} - u_{\mathbf{E}=0} = \Delta u = -\frac{1}{2}\alpha|\mathbf{E}|^2$ in an electric field $\mathbf{E}$. We instead plot the spectral shift ν where $\nu = -u$ and which is proportional to the electric field magnitude.

vice (Fig. 6.1d). Assuming the charge is at the center of the device, a fit gives an estimated charge q =126(11) e (Supplement B, Section 2). As discussed below, at each distance the shift is minimized by illuminating the experimental setup with a UV diode and optimizing its power (Fig. 6.1(d), inset). Furthermore, the spectral shift is stable only with a relatively constant rate of Rydberg excitation, interpreted as Rydberg-atom ionization creating charges that neutralize the device surface. Similar effects were observed in Rydberg EIT experiments near a quartz surface [177]. The Rydberg spectral shift can be stabilized via both effects as close as 90 μm to the device (Supplement B, Section 3).

6.2 Coherence Properties of Rydberg Atoms near Nanophotonics

The temporal properties of the electric field from the device are probed by measuring the coherence of the ground-Rydberg qubit with various control sequences. By pulsing the 420 nm light, we apply a Ramsey sequence to extract T_2^* as a function of distance from the device (Fig. 6.2(a)). With an echo pulse sequence (Fig. 6.2(b)), the coherence time is extended by nearly an order of magnitude. Extending to a Carr-Purcell (CP) $N = 2$ decoupling sequence (Fig. 6.2(c)), no decay is observed within the 10 μs evolution time at any measured distance. This implies that the electric field noise is quasi-static: stable within a single realization. We construct a model for the decoherence which includes a point-charge electric field from the device that scales with distance and a background electric field that does not, both of which vary between experimental realizations. The standard deviation of each can be extracted by fitting the distance scaling of T_2 and T_2^* (Fig. 6.2(d)). We determine a background field $|E| = 0.367\,\mathrm{V/cm}$ with fluctuation of $0.012\,\mathrm{V/cm}$ and a fluctuation of charges on the device ≤ 8 e. Our model implies that T_2^* is limited by the electric field fluctuations, primarily from the background field, and that T_2 is limited by thermal sampling of the spatially-dependent electric field (Supplement B, Section 4). Therefore, by applying decoupling sequences coherent Ry-

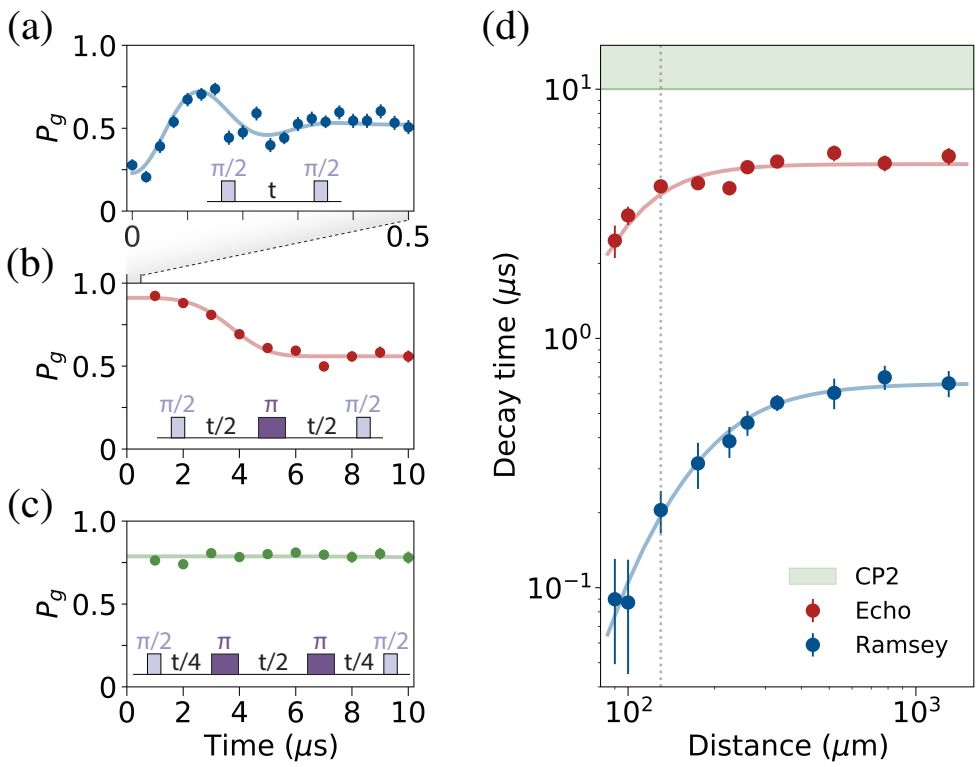


Figure 6.2: Ground-Rydberg qubit coherence. Ground state population P_g as measured after a Ramsey (a), spin-echo (b), and Carr-Purcell (CP) $N = 2$ (c) pulse sequences at $130\,\mu\text{m}$ (dotted line in (d)). A decaying sinusoid fit (blue line) gives $T_2^* = 200(40)$ ns and a Gaussian decay function (red line) gives $T_2 = 4.1(2)\,\mu$s. The CP $N = 2$ data exhibits no decay within the measurement time. (d) Measured T_2 (red circles) and T_2^* (blue circles) as a function of distance from the device. The solid lines are fits to the data given our decoherence model (Supplement B, Section 4). The shaded green region is a lower bound on the CP $N = 2$ coherence time.

dberg manipulations can be performed as close as the range 100-300 μm, which is traversable using commercial microscope objectives [17].

6.3 Rydberg Mediated Entanglement

We next prepare and study entangled atom pairs at various distances from the device. Two atoms 3.15 μm apart experience a Rydberg-Rydberg interaction U in the blockade regime where $U \gg \Omega$, with $U \approx 2\pi \times 685$ MHz and the single-atom Rabi frequency $\Omega \approx 2\pi \times 3$ MHz. The atoms are driven with a π-pulse from $|gg\rangle$ into the symmetric state $|W\rangle = \frac{1}{\sqrt{2}}(|gr\rangle + |rg\rangle)$ (Fig. 6.3(a)). The preparation fidelity $\mathcal{F} = \frac{1}{2}\left(\rho_{rg,rg} + \rho_{gr,gr} + 2|\rho_{gr,rg}|\right)$ is characterized following the method in [99] and corrected for error and loss during preparation. Far from the device at 2.6 mm it is 0.87(6) (uncorrected 0.73(3)) and remains similar close to the device: 0.83(4) (uncorrected 0.70(3)) at 170 μm (Fig. 6.3(b)).

The lifetime of the $|W\rangle$ state T_W is measured through a pulse sequence $\pi - t - \pi$ between the $|gg\rangle$ and $|W\rangle$. Compared to the single-atom ground-Rydberg coherence, T_W remains constant up to 130 μm since the electric field fluctuations are common-mode for the two closely-spaced atoms (Fig. 6.3(c)). T_W is likely limited by thermal position sampling of the electric field gradient, as supported by a theoretical model that only includes atomic temperature as a free parameter (Supplement B, Section 5).

6.4 Entanglement Enhanced Sensing

The $|W\rangle$ state can be used to probe small electric field gradients within the blockade radius. The electric field gradient creates an energy difference between $|gr\rangle$ and $|rg\rangle$ and thus a differential phase, leading to an oscillation between $|W\rangle$ and the anti-symmetric state $|D\rangle = \frac{1}{\sqrt{2}}(|gr\rangle - |rg\rangle)$. The oscillation frequency, observed via the $\pi - t - \pi$ pulse sequence, is proportional to the gradient mag-

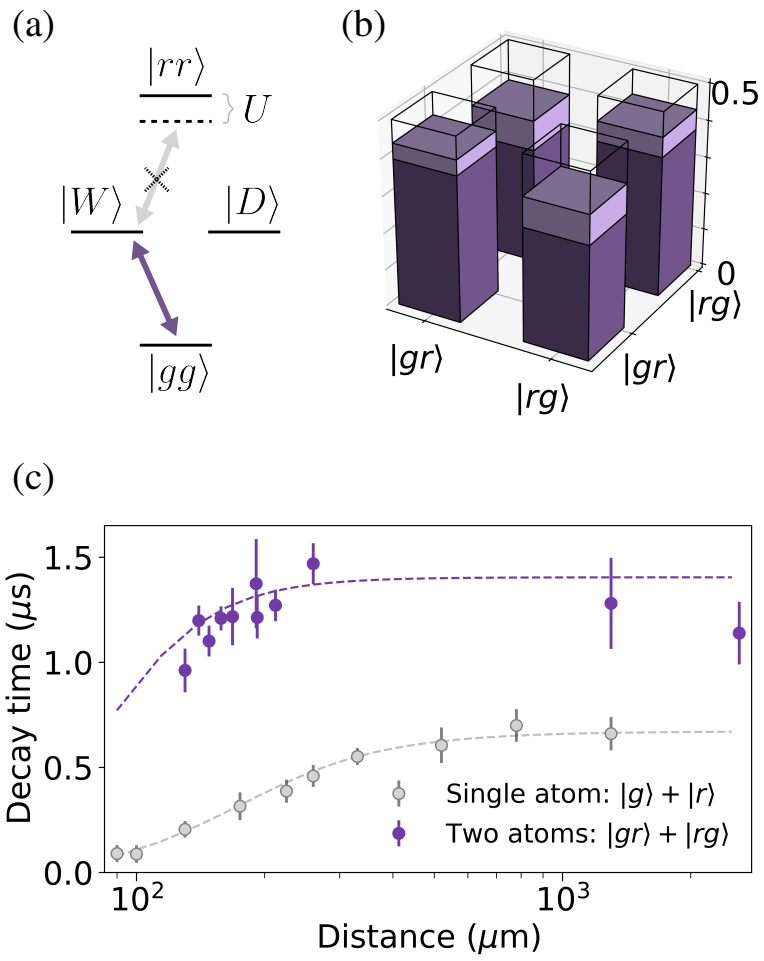


Figure 6.3: Two-atom entangled state. (a) The Rydberg interaction U shifts the $|rr\rangle$ state and allows the preparation of the $|W\rangle = \frac{1}{\sqrt{2}}(|gr\rangle + |rg\rangle)$ state. (b) Tomography of the $|W\rangle$ state (purple) at $170\,\mu\text{m}$. We measure population $\rho_{rg,rg} + \rho_{gr,gr} = 0.87(5)$ and coherence $2|\rho_{gr,rg}| = 0.78(7)$ with correction for preparation error and loss (light purple). (c) Comparison between the two-atom $|W\rangle$ state lifetime T_W (purple circles) and the single-atom ground-Rydberg coherence time T_2^* (gray circles, data and fit from (Fig. 6.2(d))). The dotted purple line is a theoretical prediction (Supplement B, Section 5.4).

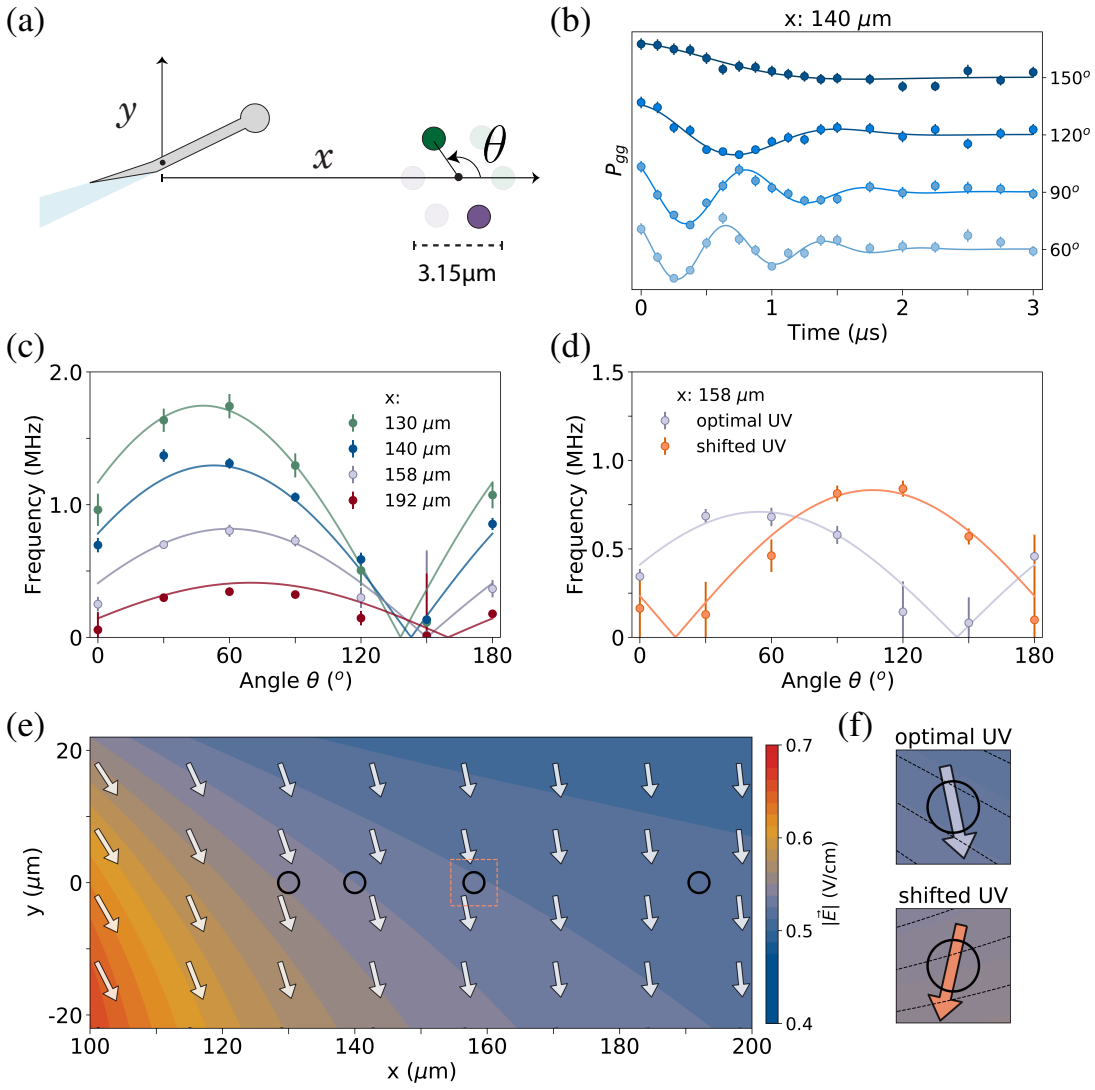


Figure 6.4: Entanglement-assisted sensing of electric field gradients. (a) The orientation of an entangled atom pair is varied with respect to the device. (b) The $|W\rangle$ state lifetime measurement (blue circles) reveals gradient-induced oscillations by fitting to a decaying sinusoid (blue lines) for different θ (offset for clarity). (c) Angular dependence of the fitted oscillation frequency at different x (circles) with solid curves being simultaneous fit (Supplement B, Section 6) to extract background field orientation. (d) A $200\ \mathrm{nW}$ UV-power reduction from its optimized value causes a rotation (53 degrees) of the gradient. (e) Reconstructed electric field magnitude $|\vec{E}|$ (contour scale) and direction (white arrows) given the measurements in (c) at the positions of the black circles. (f) Electric field contour plot reconstructed from (d) showing direction at the optimal UV value (gray arrow) and shifted UV value (orange arrow).

nitude. The minimum detectable frequency is $1/T_W$ and directly limits the minimum detectable electric field gradient, which is $\sim 10\,\mathrm{V/cm^2}$ for the distances studied here (Supplement B, Section 6.4). By contrast, a measurement involving two individual atoms in different experimental realizations for each atom is limited by the electric field fluctuations. For these reasons, the minimum detectable electric field gradient for an entangled pair is higher by the ratio T_W/T_2^*, which is approximately 5 at 150 μm.

By rotating the entangled atom pair by an angle θ with respect to the x-axis, the direction of maximum gradient can be detected via the oscillations induced in the lifetime measurement (Fig. 6.4(a,b)). We perform measurements at four distances between 130 μm and 192 μm, the gradient maximum occurs at $\theta \sim 55°$ for each and its magnitude increases as the atoms approach the device (Fig. 6.4(c)). This differs from the expected 0° gradient orientation for a single point-charge displaced in x, but can instead be described by a minimal model that includes a distance-independent background electric field. A combined fit to the data in (Fig. 6.4(c)) reveals a device charge $q = 190(10)$ e and background field $\mathbf{E} = (E_x, E_y) = (-0.02(1), -0.51(3))\mathrm{V/cm}$. The oscillation frequency follows the point-charge gradient scaling of r^{-5} along $\theta = 0°$ as well as r^{-3} along $\theta = 90°$, justifying the point-charge model. Together with the single-atom Rydberg spectral shifts, this measurement allows us to create a 2D map of the local electric field shown in Fig. 6.4(e) (Supplement B, Section 6). Going further, such maps of the local electric field can be used to study the charge characteristics of different materials that could be integrated with Rydberg atom arrays.

In particular, this measurement can be used to study the effect of UV light on the surfaces present. Many recent Rydberg atom array experiments use $\sim 1\,\mathrm{W}$ of UV light to mitigate electric field noise[207,99], with the current microscopic understanding that light-induced desorption of alkali atoms decreases the number of charges on dielectric surfaces[177,40,110]. Here we observe that much smaller UV powers significantly affect the electric field environment (Fig. 6.1(c), inset). At 158 μm, decreasing the UV power from the optimal value of 400 nW to 200 nW in-

creases the spectral shift by 6.7 MHz and rotates the gradient by $53(4)^\circ$ (Fig. 6.4(d)). Assuming the UV power change modifies the fit parameters q, E_x, E_y from Fig. 6.4(c), we reconstruct the changed electric field (Fig. 6.4(f)). We find a significant change only in the background electric field: $\Delta E_x = -0.21(3)\,\mathrm{V/cm}$ and not in the charge on the device q (Supplement B, Section 6.5). However, we observe that far from the device, the background electric field sensed by the atom does not vary with UV power (Supplement B, Section 3.1).

One way of reconciling our observations is that another surface that moves with the device could be causing the shift in the background electric field, such as the tapered fiber. The minimization of the spectral shift using UV light could then be interpreted as the elimination of charges on the fiber surface. In fact, at the optimum UV power we do not observe any significant charges on the fiber, as indicated by the zero shift at negative x distances where the atom is much closer to the fiber surface than to the device (Fig. 6.1(d)). By contrast, for large UV powers ($\sim$ 30 mW) we find that the Rydberg spectral shift increases dramatically (Supplement B, Section 3.1). This behavior cannot be explained by the common understanding that higher UV power increases the removal rate of adsorbates and further work is needed to develop a full microscopic understanding. Remarkably, by choosing the optimum UV power, we repeatedly stabilize to the same charge configuration as indicated by measurements of the spectral shift (Supplement B, Section 3.3). Finally, while potential improvements to our device include minimizing its surface area and adding in-vacuum electrodes, significant enhancement can be achieved in the current system by lowering the principal quantum number n to balance the Rydberg interaction strength with electric field sensitivity (Supplement B, Section 7).

6.5 Outlook

Our observations indicate that a Rydberg atom array placed $\sim$ 250 μm away would remain minimally perturbed by the nanophotonic device. This could be used to establish a quantum optical channel via teleportation to a photonic state [10], or to a distant quantum processor. A ground-state atom can be entangled with a photon at the device [193,196], and then coherently transported with a single tweezer to the atom array [17,215]. The transported atom can then be entangled with the Rydberg-atom quantum processor. Further, such optical interfaces can also be utilized for fast, nondestructive readout in quantum error correction protocols [32,209]. More broadly, our work motivates the integration of Rydberg atom arrays with other devices of this scale and could provide a helpful understanding for other platforms sensitive to surface charges [42]. For example, with properly designed decoupling sequences and charge stabilization, integration with a mesoscopic superconducting interface is possible, enabling the application of circuit QED techniques and exploration of novel hybrid systems [186,147,107,142].

Some mistakes are ok, as long as they can be corrected...

Mikhail Lukin

7

Error Detected Quantum Operations

Neutral atom quantum processors are a promising platform for large-scale quantum computing. Integrating them with optical cavities enables fast nondestructive qubit readout and access to fast remote entanglement generation for quantum networking. Here, we introduce a platform for coupling single atoms in optical tweezers to a Fabry-Perot Fiber Cavity. Leveraging the strong atom-cavity coupling, we demonstrate fast qubit state readout with $99.960^{+14}_{-24}\%$ fidelity and two methods for cavity-mediated entanglement generation with integrated error detection. First, we use cavity-

carving to generate a Bell state with 91(4)% fidelity and a 32(1)% success rate. Second, we perform a cavity-mediated gate with a deterministic entanglement fidelity of 52.5(18)%, increased to 76(2)% with error detection. Our approach provides a route towards modular quantum computing and networking.

Neutral atom arrays are a promising platform for large scale quantum information systems, enabling quantum algorithms with multiple logical qubits [16] and novel approaches to quantum metrology and clocks [112,212,25,178]. These advancements have been facilitated by the implementation of high-fidelity two-qubit gates and the use of coherent transport for non-local connectivity and reconfigurable architecture [54,111,175,17]. While quantum processors with over 10,000 physical qubits appear within the reach [115], further scaling may benefit from a modular approach, in which quantum computation is distributed across quantum processors connected by fast high-fidelity quantum network channels [124,213,67,133,103,182]. Such an approach requires integration of atom arrays with optical cavities, which provides direct coupling to photons in an optical mode that can be easily collected for fast high-fidelity remote entanglement distribution [153,38]. Integration of individually-controlled atoms in optical tweezers with an optical cavity has only recently been realized experimentally [134,211,108,63].

In this chapter, we demonstrate a platform combining individual control and transport of atoms in optical tweezers with efficient coupling to individual optical photons enabled by a Fabry-Perot fiber cavity (FPFC). These cavities offer large cooperativities ($C \sim 100$) [70,57], while also providing optical access for optical tweezers. This approach can be directly integrated with a reconfigurable architecture where a neutral atom array is placed above the cavity and select atoms are coherently transported in and out of the cavity mode [134,133]. This further enhances the capabilities of neutral atom quantum computer, enabling an efficient distributed processor. We carry out several experiments to demonstrate the capabilities of this platform. Specifically, we demonstrate that the high cooperativity enables fast high-fidelity qubit state readout, which can be important for accelerating

quantum error-correction algorithms. Moreover, we show that error detection can be naturally integrated within this approach to enable robust entanglement generation. Note that unlike previous demonstrations of cavity-mediated entanglement that relied on photon detection, our protocol heralds success based on the atomic state, which increases the success rate of entanglement generation, thereby improving the efficiency of quantum networking scheme that relies on probabilistic Bell measurements[93]. This method can be used for fast and more complex quantum network operations, such as entanglement swapping, purification, and fusion, which can enable the development of an efficient distributed quantum computer[191,183,156].

7.1 Experimental Setup

We couple individually controlled Rubidium-87 atoms trapped in optical tweezers to a Fabry-Perot Fiber Cavity (FPFC). These micro-cavities exhibit low scattering loss and small radii of curvature, which allow for a small mode volume and high cooperativity[70]. Our FPFC design features mirror diameters of 125 μm and a cavity length of 100 μm, providing ample optical access for single atoms in optical tweezers (*S1*C). We load atoms into optical tweezers from a magneto-optical trap (MOT) formed directly above the FPFC. The atoms are then transported approximately 60 μm into the cavity mode and deposited into an optical lattice formed by an 850 nm cavity mode (Fig. 7.1A). The atoms are positioned in the 850 nm mode to maximize their overlap with the 780 nm mode, as described in (*S2.2*C). The FPFC is stabilized using an 810 nm laser referenced to an external ultra-low expansion (ULE) cavity, ensuring that the 780 nm cavity mode remains locked to the $|5S_{1/2}\rangle \leftrightarrow |5P_{3/2}\rangle$ $D2$ transition of Rubidium-87. Additionally, the cavity resonance can be dynamically tuned across the entire hyperfine structure during an experimental sequence, (Fig. 7.1B) (*S2.4*C). The atom-cavity system is characterized by probing the transmission spectrum of the cavity through the single-mode input port using circularly polarized (σ^+) light. By pumping the atoms to

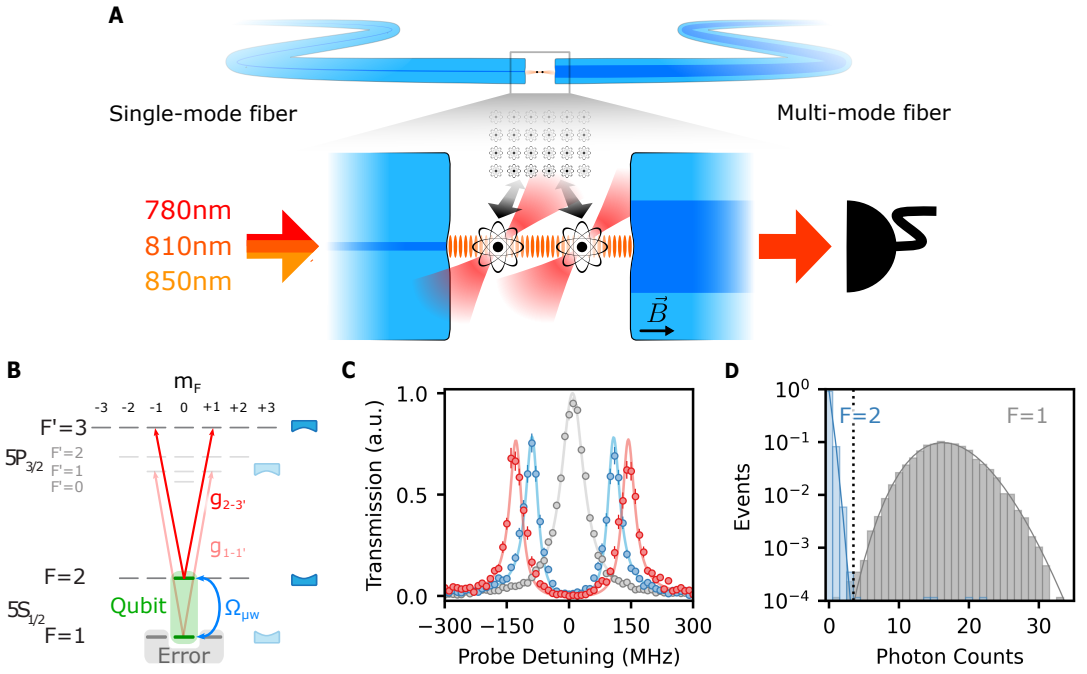


Figure 7.1: Experimental setup and qubit readout. (A) Atoms in optical tweezers are loaded above a Fabry-Perot Fiber Cavity (FPFC) and transported into the cavity mode. The FPFC has a single-mode input port and a multi-mode output port, over which we collect transmitted light. The FPFC length is stabilized using an 810 nm laser and the atoms are trapped in a 850 nm mode of the cavity. The 780 nm mode couples to the D2 line in Rubidium. The magnetic field is aligned along the cavity axis. **(B)** Atomic level diagram of Rubidium-87. Readout is performed with the cavity on resonance with the $2 \leftrightarrow 3'$ transition, while for entanglement generation the cavity is tuned to the $1 \leftrightarrow 1'$ transition. **(C)** Resonant transmission spectra of a bare cavity (gray), one atom (blue), and two atoms (red) coupled to the cavity. The lines are a simultaneous fit yielding parameters g = $2\pi\times100.0(8)$ MHz and κ = $2\pi\times65(1)$ MHz, resulting in a cooperativity of $C = 101(2)$. **(D)** Histograms showing photon counts collected in 10 μs with an atom in the F=1 state (grey) and an atom in the F=2 state (blue), yielding a qubit state readout fidelity of $99.960^{+14}_{-24}\%$.

the stretched state $|F = 2, m_F = 2\rangle$ with the cavity resonant to the $F = 2 \leftrightarrow F' = 3'$ transition, we realize an effective two-level system. The excitation spectrum of a single atom showcases a strong resolvable vacuum-Rabi splitting, showing the hybridization of the atomic and photonic excitations (Fig. 7.1C). Fitting the transmission spectrum to an analytical model (*S4.1*C), we extract an atom-photon coupling strength of $g = 2\pi \times 100.0(8)$ MHz and cavity linewidth (FWHM) of $\kappa = 2\pi \times 65(1)$ MHz. This results in a single-atom cooperativity of $C = \frac{4g^2}{\kappa\Gamma} = 101(2)$, where $\Gamma = 2\pi \times 6$ MHz is the natural linewidth of the excited state. When probed on resonance,

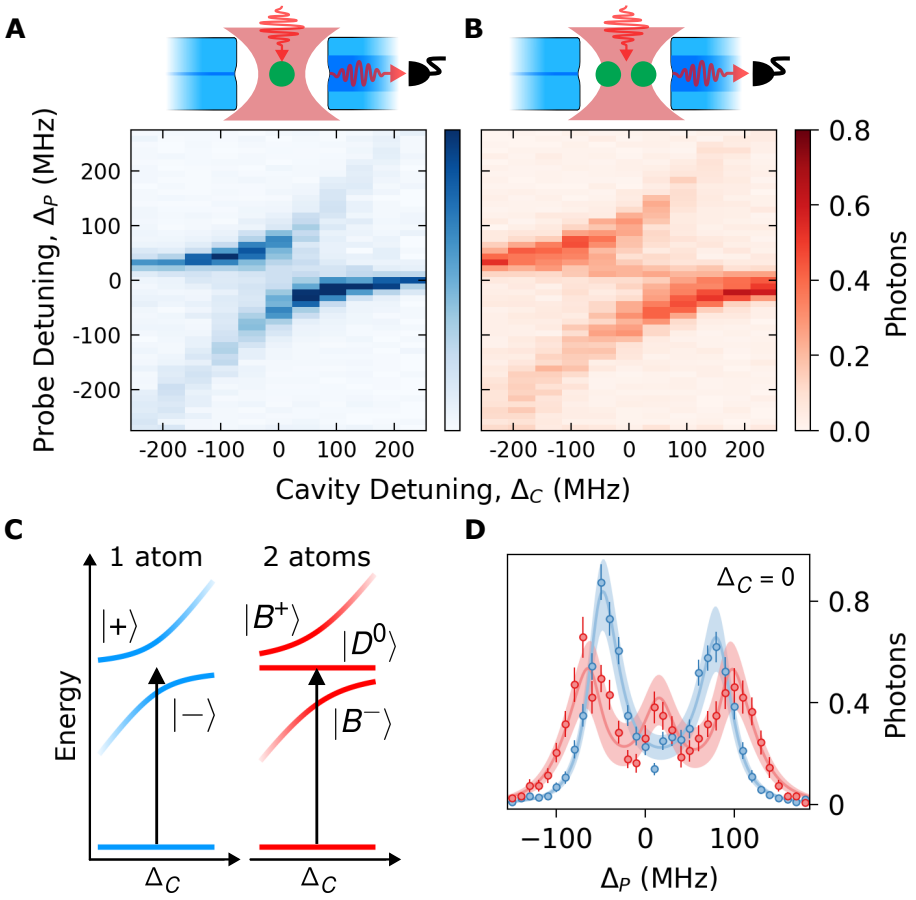


Figure 7.2: Photonic dark state spectroscopy. (A-B) Side drive spectroscopy of one (A) and two (B) atoms coupled to the cavity as a function of cavity and probe laser detuning (Δ_C and Δ_P, respectively). With two atoms coupled to the cavity, the spectrum reveals a feature on resonance with the atomic transition, corresponding to a photonic dark state. **(C)** Energy level diagram of the first excitation manifold for one and two atoms coupled to a single cavity mode, which correspond to the states probed in the spectra plotted against the cavity detuning, Δ_c (*S4.1*C). **(D)** Probe spectroscopy at $\Delta_C = \Delta_A$ for one (blue circles) and two (red circles) atoms coupled to the cavity while probed with a side beam. Lines are simultaneous fits to a numerical model (*S4.2*C).

the difference in transmission between an atom coupled and no atom coupled to the cavity allows for fast non-destructive readout by thresholding transmitted photon counts.[57,18,117,44] Through this measurement, atom presence can be detected with a fidelity of $99.988^{+7}_{-23}\%$ in 10 μs and of $99.950^{+24}_{-49}\%$ in 2.5 μs, limited by the finite atom lifetime (*S3.2.1*C). Additionally, this readout is nearly lossless with a measured loss of $0.034^{+27}_{-6}\%$. In all of our experiments, we post-select on

atomic presence at the end of the experimental sequence (*S2*C). Furthermore, this measurement can differentiate atoms in the qubit manifold, which we encode in the magnetic-field insensitive states: $|0\rangle = |F = 1, m_F = 0\rangle$ and $|1\rangle = |F = 2, m_F = 0\rangle$. During readout, the cavity is tuned to the $2 \leftrightarrow 3'$ transition, so that the $|1\rangle$ state is coupled to the cavity, while the $|0\rangle$ state is not. Using the state dependent coupling we perform fast non-destructive readout of the qubit state with fidelity of $99.960^{+14}_{-24}\%$ in $10\,\mu$s, limited by off-resonant scattering from the 850 nm trap and state preparation. For state readout we collect 0.09(2) photons from the F=2 state and 16.600(1) photons from the F=1 state, as shown in (Fig. 7.1D). Increasing the cooperativity of the cavity would allow for faster readout, and as a result higher readout fidelities (*S3*C). Importantly, readout leaves the $|0\rangle$ state undisturbed while it quickly pumps the $|1\rangle$ state to the stretched $|F = 2, m_F = 2\rangle$ state. In principle, a Raman pulse can be used afterward to reinitialize the atom in $|1\rangle$, making this readout non-destructive to the qubit state (*S3.3*C).

7.2 Photon-Mediated Entanglement Through Dark States

We realize quantum entanglement between two atoms coupled to a cavity using a photonic dark state. This state is an antisymmetric superposition where one atom is excited out of phase with the other, leading to destructive interference in the cavity mode, rendering it dark to the cavity. While such states have been studied previously [127,211], their potential for quantum operations remains largely unexplored.

Specifically, we probe the system by exciting both atoms from the side, rather than through the single-mode input port, and measure the same signal: the light transmitted through the multi-mode optical fiber. We vary both the cavity detuning Δ_C and the probe detuning Δ_P. With a single atom coupled to the cavity, we directly observe an avoided crossing in the energy levels, similar to what is shown in (Fig. 7.1C). Moreover, the dressed states become more atom-like (cavity-like) close to the

atomic (cavity) resonance, resulting in stronger (weaker) coupling to the side beam drive (Fig. 7.2A). With two atoms coupled to the cavity, similar behavior is observed but with an expected $\sqrt{2}$ enhancement of the splitting (Fig. 7.2B). These two features correspond to the "bright states", given by $|B_{\pm}\rangle = \frac{1}{2}(|eg,0\rangle + |ge,0\rangle) \pm \frac{1}{\sqrt{2}}|gg,1\rangle$. In contrast to the spectrum recorded when the cavity mode is excited through the fiber, an additional third feature appears at the atomic resonance that we attribute to a photonic dark state, $|D_0\rangle = \frac{1}{\sqrt{2}}(|eg,0\rangle - |ge,0\rangle)$ (Fig. 7.2C), where $|g\rangle$ and $|e\rangle$ are the atomic ground and excited states of each atom and the number indicates the number of photons in the cavity. Due to the lack of a photonic component, this state can only be driven by exciting the atom and not the cavity. Specifically, for a global drive, a relative phase of π between the drive on the two atoms is required. Due to thermal motion of the atoms, the relative phase between the two atoms and the drive beam changes from shot to shot, and we consistently observe the dark state as a bright feature. Furthermore, a strong drive allows for excitation of the cavity through the dark state. In the rest of our experiments, we individually drive single atoms, which maintains a coupling to both dark and bright states, while being insensitive to the relative phase between the atoms (*S4*C).

To use this dark state to implement cavity-mediated entanglement between the two atoms, we note that when the cavity is resonant with the bare atomic transition, the difference between the single- and two-atom spectra can be interpreted as a conditional resonance. The system can only be excited with a resonant beam if both atoms are coupled to the cavity (Fig. 7.2D). By encoding the $|0\rangle$ and $|1\rangle$ qubit states such that one is coupled to the cavity and the other is uncoupled, the conditional resonance becomes state-dependent, enabling two-qubit quantum operations. However, the fidelity of these operations is limited by errors arising from photon leakage out of the cavity and scattering into free space. We can improve this fidelity by engineering these leakage and scattering events to leave the atom in a specific state, $|err\rangle$, outside the qubit manifold. Through sequences of readout, π-pulses, and local optical pumping, we can measure the qubit states $|0\rangle$ and $|1\rangle$, as well as $|err\rangle$ (*S3.3*C). By postselecting on cases where no error occurred, the fidelity will ultimately be

limited by the presence of undetectable errors.[20,151]

For entanglement experiments, we use the excited state $|e\rangle = |F' = 1, m_F = 0\rangle$ which has branching ratios that result in decay predominantly to the $|err\rangle = |F = 1, m_F = \pm 1\rangle$ states, while selection rules forbid decay to the $|0\rangle$ state (Fig. 7.3A). We perform a local drive on one of the atoms, which we call atom A, resonant with the $2 \leftrightarrow 1'$ transition. This drive couples $|1\rangle_A$ to $|e\rangle_A$. We shift the cavity resonance to the $1 \leftrightarrow 1'$ transition, so that it couples $|err\rangle_A \leftrightarrow |e\rangle_A$ and $|0\rangle_B \leftrightarrow |e'\rangle_B$ where $|e'\rangle = |F' = 1, M_F = \pm 1\rangle$ state. As a result, the two-qubit state $|1\rangle_A |1\rangle_B \equiv |11\rangle$ acts as a single atom coupled to the cavity and experiences a suppressed excitation. By contrast, the $|10\rangle$ state behaves as two atoms coupled to the cavity and experiences a resonant coupling to the photonic dark state, $|D_0\rangle = 1/\sqrt{2}\,(|err\rangle_A |e'\rangle_B - |e\rangle_A |0\rangle_B)$ (*S6*C). This establishes a qubit state-dependent resonance, necessary to perform quantum operations between the two qubits.

7.3 Cavity Carving with Integrated Error Detection

Our first protocol relies on the state-dependent decay of the two-qubit states. This decay mechanism enables us to selectively remove, or "carve out," specific parts of the wavefunction, leaving behind the desired quantum state. Under a weak drive, we observe that the $|11\rangle$ and $|10\rangle$ states both decay into the $|err\rangle_A$ state with different rates. The resonant coupling to the dark state makes the $|10\rangle$ state rapidly decay, while the $|11\rangle$ experiences a suppressed decay (Fig. 7.3B). This allows us to "carve out" the $|10\rangle$ state from the wavefunction.[205,134,151] To prepare an entangled state with this mechanism, we first prepare an equal superposition of all two-qubit states, followed by the application of a drive pulse which carves out the $|10\rangle$ component. A global π-pulse flips the two-qubit state and a second carving pulse once again carves out the $|10\rangle$ component. This sequence

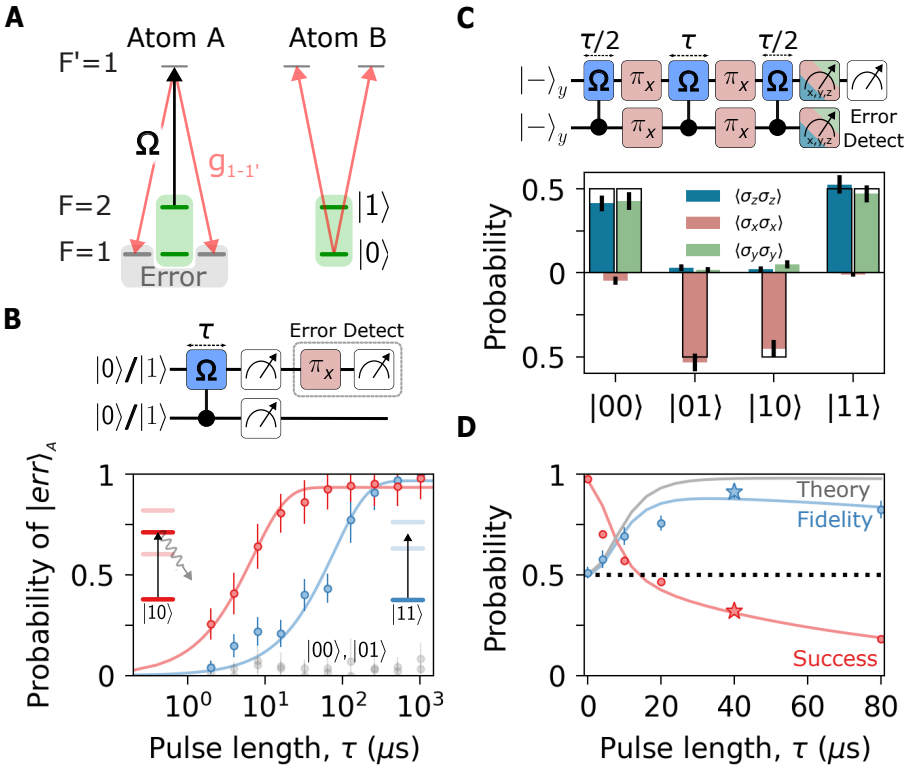


Figure 7.3: Bell state preparation with cavity carving. (A) For entanglement generation, the cavity is tuned to the $1 \leftrightarrow 1'$ transition and a single side drive on the $2 \leftrightarrow 1'$ transition is applied to atom A only. **(B)** (top) Quantum circuit for preparing two-qubit states and measuring the $|err\rangle_A$ population. (bottom) Decay rates into the error states after preparing each of the four two-qubit states. The resonant coupling to the dark state $|D_0\rangle$ results in much faster decay of $|10\rangle$ compared to the off-resonant coupling in $|11\rangle$. $|00\rangle$ and $|01\rangle$ do not couple to the driving beam. **(C)** (top) Quantum circuit of a Carr-Purcell cavity carving scheme which prepares a $|\Phi^-\rangle$ Bell state. (bottom) Measured correlations in the ZZ (blue), XX (red), and YY (green) bases verify that $|\Phi^-\rangle$ is prepared with a Bell state fidelity of $\mathcal{F} = 91(4)\,\%$ and a success probability of $32(1)\,\%$. Direction of histograms denote the expected sign of parity for $|\Phi^-\rangle$ in each bases. **(D)** Bell state fidelity (blue circles) and success probability (red circles) as a function of carving pulse length τ. Stars mark the data presented in (C). Lines are a fit to a semi-classical numerical model, and the gray line is the expected Bell state fidelity without SPAM errors (*S7.1*C). Dotted line denotes the fidelity limit for verifiable entanglement.

prepares a statistical mixture of error states and a Bell state: $\rho = |\Phi^-\rangle\langle\Phi^-| + |err\rangle_A\langle err|$. By post-selecting on the atoms not being in the error state, we are left with the maximally entangled state, $|\Phi^-\rangle = \frac{1}{\sqrt{2}}(|00\rangle - |11\rangle)$. In principle, the minimal application of our scheme would be the spin-echo sequence described above: $\frac{\pi}{2}$-τ-π-τ-$\frac{\pi}{2}$. In practice, we found that the spin-echo scheme was limited due to a coherent linear phase accumulation in the $|11\rangle$ state during the carving pulses that

we attribute to laser phase noise (*S6*C). To cancel this linear phase, we implement a Carr-Purcell decoupling sequence of the form $\frac{\pi}{2}$-$\frac{\tau}{2}$-π-τ-π-$\frac{\tau}{2}$-$\frac{\pi}{2}$. Fig. 7.3C shows the measured correlations in the *ZZ*, *XX*, and *YY* basis, resulting in a Bell state fidelity of $\mathcal{F} = 91(4)\%$ and a success probability of $32(1)\%$.

The theoretical limit on fidelity is set by undetectable errors, i.e. when a scattering event leaves the atoms in the qubit manifold instead of in the error state. The dominant source of undetectable errors arise from scattering from the dark state, which can decay through atom A or through atom B with equal probability. Decay through atom B leaves atom A in the state $|err\rangle_A$, so that this decay is fully detectable. Decay through atom A result in 17% undetectable errors for a single atom given by Clebsch-Gordon coefficients and due to our current readout sequence, which cannot distinguish the F=2 Zeeman sublevels. This leads to total dark state scattering errors being 91.5% detectable. With this, we find a maximum theoretical fidelity of $\sim 96.3\%$ for our carving protocol. As predicted by our model, Fig. 7.3D shows that the entanglement fidelity increases exponentially, but is still limited by unwanted scattering which we attribute to level-mixing of the excited states from our traps, and imperfect polarization. Increasing the cooperativity would enhance the success rate of entanglement generation and enable faster entanglement preparation (*S7.1*C).

7.4 Quantum Phase Gate with Integrated Error Detection

The qubit state dependent resonance can also be used to perform a quantum gate between two atoms. By increasing the strength of the laser, we can drive a coherent optical Rabi oscillation between the $|10\rangle$ state and the photonic dark state $|D_0\rangle$, while the $|11\rangle$ state is blockaded from excitation and both the $|00\rangle$ and $|01\rangle$ states are unaffected by the drive. By performing a full 2π rotation, the $|10\rangle$ will acquire a relative π phase compared to the other three two-qubit states, realizing a controlled phase gate (Fig. 7.4A). This scheme is limited by scattering, however most of these events re-

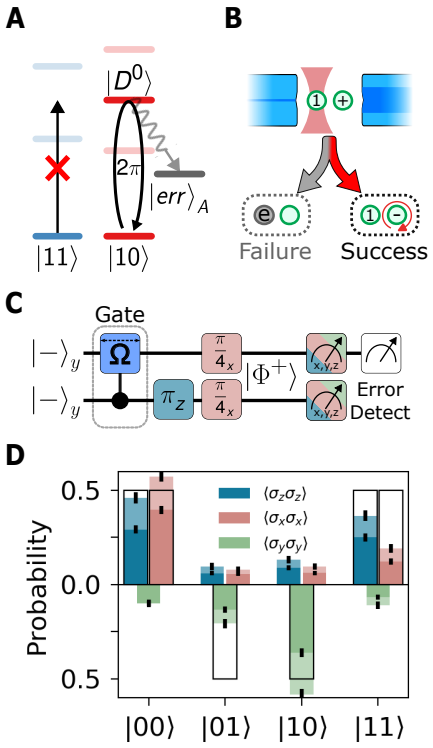


Figure 7.4: Deterministic quantum gate with error detection. (A) Conditional blockade mechanism. A resonant 2π Rabi oscillation can be realized only between the $|10\rangle$ state and the dark state $|D_0\rangle$, causing a phase of π on state $|10\rangle$, while the excitation from the $|11\rangle$ state is blockaded. Unwanted atomic scattering results in mainly detectable $|err\rangle_A$ states. **(B)** Quantum gate flow chart showing the two possible outcomes: "Success" is a conditional phase on atom B and "Failure" is a detectable scattering event **(C)** Quantum circuit of the gate: Following the gate, we apply a local Z_π pulse on atom B and a global microwave $X_{\pi/4}$ pulse to generate the $|\Phi^+\rangle$ Bell state. **(D)** Measured correlations in the ZZ (blue), XX (red), and YY (green) bases verify that $|\Phi^+\rangle$ is prepared. (dark) Without error detection, we measure a deterministic Bell state fidelity of $\mathcal{F} = 52.5(1.8)\%$. (light) Error detection improves the fidelity to $\mathcal{F}' = 76(2)\,\%$ with a success probability of $69(1)\,\%$. Direction of histograms denote the expected sign of parity for $|\Phi^+\rangle$ in each bases.

sult in detectable error states, $|err\rangle_A$, allowing us to increase the fidelity of the measurement through post-selection (Fig. 7.4B).

To characterize the performance of the gate, we prepare an entangled state using the quantum circuit shown in Fig. 7.4C. For a perfect gate, this circuit would prepare the Bell state $|\Phi^+\rangle = \frac{1}{\sqrt{2}}(|00\rangle + |11\rangle)$. Similar to the carving case, we determine the Bell state fidelity by measuring correlations along all three bases (Fig. 7.4D). Notably, without any error detection or post-selection, the measured Bell state fidelity is $\mathcal{F} = 52.5(1.8)\%$ (S_5C). By applying error detection and post-selection, we improve the Bell state fidelity to $\mathcal{F}' = 76(2)\%$, with a success probability of $69(1)\%$. This measurement aligns with the theoretical maximum corrected fidelity of 78% for our cooperativity. The limitation in fidelity is primarily due to the use of atom A as both a qubit and an ancilla to herald the success of the gate. This results in correction creating an imbalance of population between states where atom A is in $|0\rangle_A$ as opposed to $|1\rangle_A$. Additionally, the states used in the current scheme do not have fully detectable errors and suffer from scattering and a light shift from the F=3 states, resulting in a further reduction in fidelity. These limitations can be addressed in future implementations by including an additional ancillary atom and by more careful selection of atomic states[20,151]C. Such an ancilla could be individually addressed and read out, allowing for the detection of gate errors without affecting the data qubits.

7.5 Outlook

Our experiments demonstrate a versatile platform that offers exciting opportunities by combining neutral atom arrays with a high-finesse optical cavity. The demonstrated entanglement schemes offer improvements over many existing quantum networking protocols. For instance, the probabilistic gate performed using photon detection, as in[93], can be replaced with cavity carving that includes error detection of the atomic state, potentially increasing the rate of quantum informa-

tion transmission by at least an order of magnitude. Another extension would be to increase the number of atoms in the cavity, introducing an auxiliary atom to serve as an ancilla for the gate, thereby enhancing gate fidelity[20]. Moreover, incorporating more qubits would allow for the execution of multi-qubit gates[75]. Higher fidelity cavity-mediated gates could unlock new possibilities in quantum networking by utilizing many entangled matter qubits, potentially generating many-photon graph states for error-corrected quantum networking protocols[21,191]. Further improvements can be achieved by fabricating higher-quality mirrors to increase cooperativity[202,80]. Combining our platform with Rydberg gate operations in atom arrays would enable fast, high-fidelity, non-destructive mid-circuit readout for error-correction protocols and facilitate the entanglement of spatially separated quantum processors for distributed quantum computing, thereby increasing the available number of qubits[67,213,182,103]. Finally, our error-biased mechanism can be extended to more general cavity-mediated interactions, such as long-range spin-spin Hamiltonians and spin squeezing[96,36,69,141,131].

What is the experiment that you wish you had done in your PhD?

Mikhail Lukin

8

High Finesse Optical Microcavities

Throughout my Ph.D. I primarily worked with two types of optical cavity, the one-dimensional photonic crystal cavity, and later on the fiber Fabry-Perot cavity. Both cavities have merit as photonic interfaces and have associated technical challenges. Throughout my Ph.D., I focused on developing the fiber cavity as a platform and began to understand some of the pitfalls associated with it. In order to progress this platform, I began exploring other types of microcavity designs and methods for fabrication. In collaboration with the Loncar and Yang labs we were then able to not only

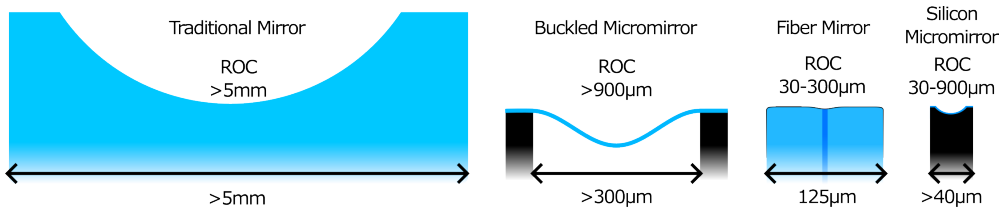


Figure 8.1: Four types of mirrors are shown. The first is the traditional diamond-milled mirror, capable of a radius of curvature (ROC) and diameters greater than 5 mm[44]. The second, a buckled micromirror (discussed further in this chapter), achieves smaller dimensions, with diameters exceeding 300 μm and ROCs above 900 μm[46]. The third type is the CO_2 laser-ablated fiber mirror, with achievable ROCs between 30 and 300 μm[70] (up to 1 mm using special techniques[137]) and a fixed fiber diameter of 125 μm. Lastly, the silicon micromirror offers ROCs ranging from 30 to 900 μm and can have a diameter as small as 40 μm[202].

produce our own micromirrors with existing methods, but also innovate and produce new novel methods for micromirror fabrication shown in figure 8.1. In this chapter, I will describe some of these micromirror efforts.

8.1 CO_2 Laser Ablated Micromirrors

The cavity used in Chapter 7 was fabricated through CO_2 laser ablation, a process in which a high-power 10 μm laser is focused onto a silica substrate (in this case, a fiber tip), ablating the surface of the silica. Because silica strongly absorbs 10 μm light, the laser can rapidly remove material, creating a Gaussian depression that closely follows the intensity profile of the beam[70]. This technique produces surfaces with root-mean-square (RMS) roughness on the order of 2 Å, ensuring sufficiently low scattering loss to realize optical cavities with finesses around 100,000 when coated with high-reflectivity dielectric layers.

Motivated by these advantages, we adopted this method to fabricate our own micromirrors. We purchased a 20 W coherent® Diamond Series CO_2 laser, which, when focused to a spot size of about 15,μm, provides more than enough power to ablate micromirrors on silica substrates. Using the set-up shown in figure 8.2, we were able to produce micromirrors with surface roughness

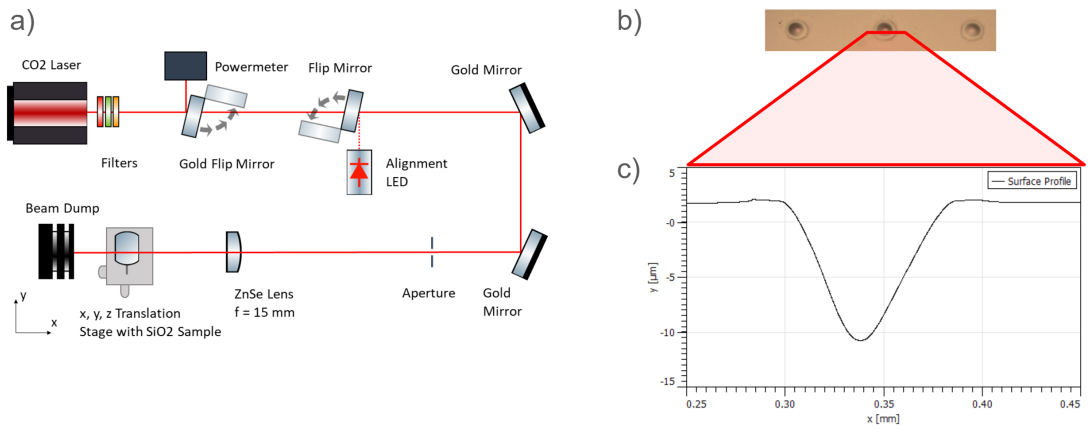


Figure 8.2: (a) Schematic of the CO_2 laser ablation setup. (b) Optical-microscope image of the ablated silica substrate. (c) Scanning stylus profilometer measurement of the ablated surface, showing its overall Gaussian-like shape.

consistent with the state-of-the-art 8.3.

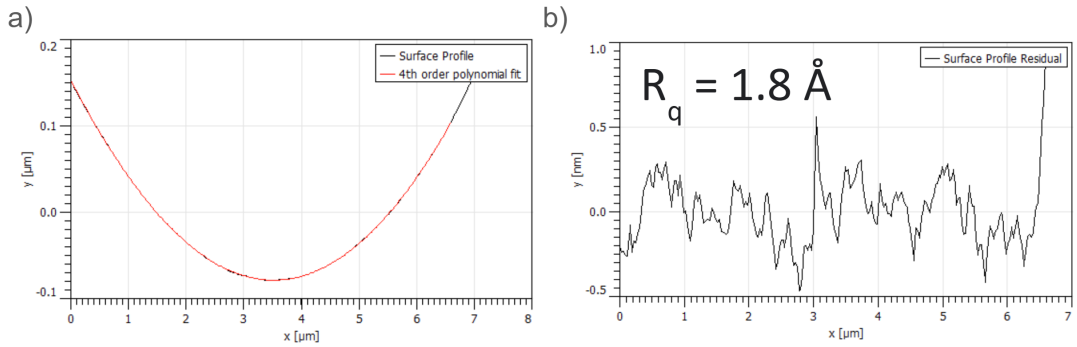


Figure 8.3: (a) Atomic force microscope (AFM) surface profile of the ablation. (b) Residual of a 4th-order polynomial fit to the surface, revealing an RMS roughness (R_q) of 1.8 Å.

One of the motivations for developing these techniques was to attempt to produce arrays of the cavities that could then be utilized in parallel to multiplex atom-photon interfaces. After a significant amount of trial and error, we found that it was difficult to make the ablation process consistent, resulting in a large variance in the depths and radius of the curvatures of the micromirrors produced, as shown in figure 8.4. Additionally, we realized that it is challenging to make closely spaced micromirrors because of the nature of the ablation. For these ablated mirrors, the only usable part

of the cavity is really on the order of $10\mu m$ around the base of the ablation, but the full structure of the ablation is on the order of $100\mu m$. Attempts to space them more closely resulted in interference of the ablation of one micromirror with its nearest neighbor. Combined with the inconsistency, this led us to seek alternative methods for micromirror production.

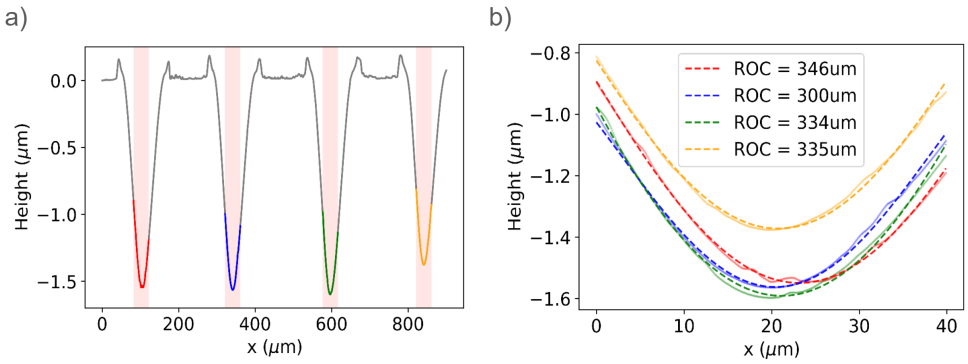


Figure 8.4: (a) Array of CO_2 laser ablation sites measured with a scanning stylus profilometer. (b) Parabolic fits to the bases of the micromirror ablations, indicating the variation in radius of curvature and depth across different ablation sites.

8.2 Silicon Micromirrors

A particularly promising technique based on isotropic etching in silicon was developed at the University of Vienna by the Trupke Group [202], who generously provided us with samples of their silicon micromirrors. These samples demonstrated excellent homogeneity and high yield, with virtually every fabricated mirror showing losses below our measurement limit when tested in our fiber-cavity setup. Furthermore, these mirrors exhibited nearly perfect spherical profiles, allowing them to operate well beyond the confocal regime and offering greater flexibility in the design of experimental cavity geometries. This is highlighted in figure 8.5 where we can see that the total collection efficiency of a fiber cavity will tend to fall off as a function of length due not only to the poor overlap between the cavity mode and the fiber mode, but also due to the increase in diffractive loss for longer cavity

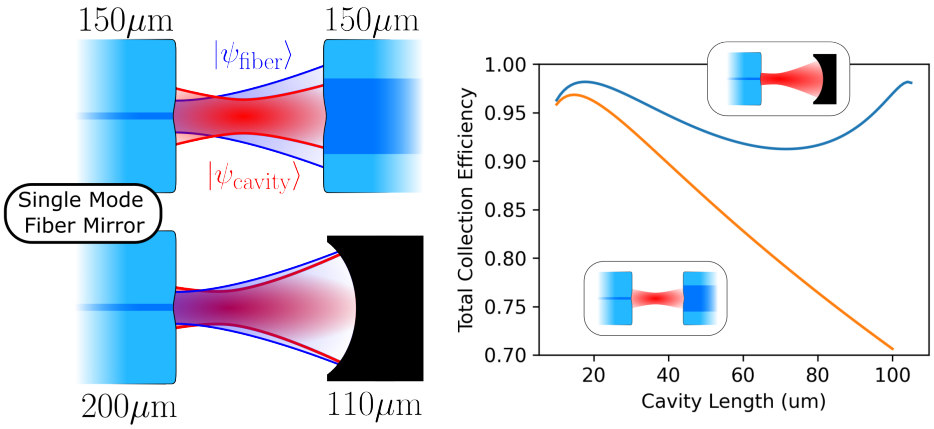


Figure 8.5: Two cavity geometries and their mode matching. The first geometry is a fiber cavity formed by two 150 μm ROC fiber mirrors. The red represents the single-mode fiber output $|\psi_{\text{fiber}}\rangle$ and the blue the cavity mode $|\psi_{\text{cavity}}\rangle$. Their limited overlap results in a low mode matching efficiency (orange curve), $\eta = \left|\langle\psi_{\text{fiber}}|\psi_{\text{cavity}}\rangle\right|^2$. The second geometry is a hybrid cavity employing a 200 μm ROC fiber mirror and a 110 μm ROC silicon micromirror, which enhances mode matching (blue curve). The adjacent plot shows the mode matching as a function of cavity length, highlighting the superior performance of the hybrid configuration.

lengths due to the poor shape.

This spherical profile also enables for tighter mirror spacing, leading to high-density micromirror arrays with outstanding uniformity. Moreover, the surface roughness of these silicon micromirrors, reaching sub-angstrom levels, surpasses that of CO_2-ablated mirrors.

An additional advantage of these mirrors is that they are fabricated on a silicon substrate, which can be patterned using the Bosch etch technique. This capability provides greater flexibility in controlling the shape and size of the mirrors, thereby enabling larger optical access for optical tweezers, even surpassing that of fiber cavities.

To incorporate these techniques into our experiments, we developed the fabrication process in Harvard's clean room following the method described in [202]. First, a resist is spun onto the wafer and then exposed via ultraviolet lithography, after development, this creates small holes in the resist. An initial isotropic etch is performed on the silicon to form a divot, after which the resist is

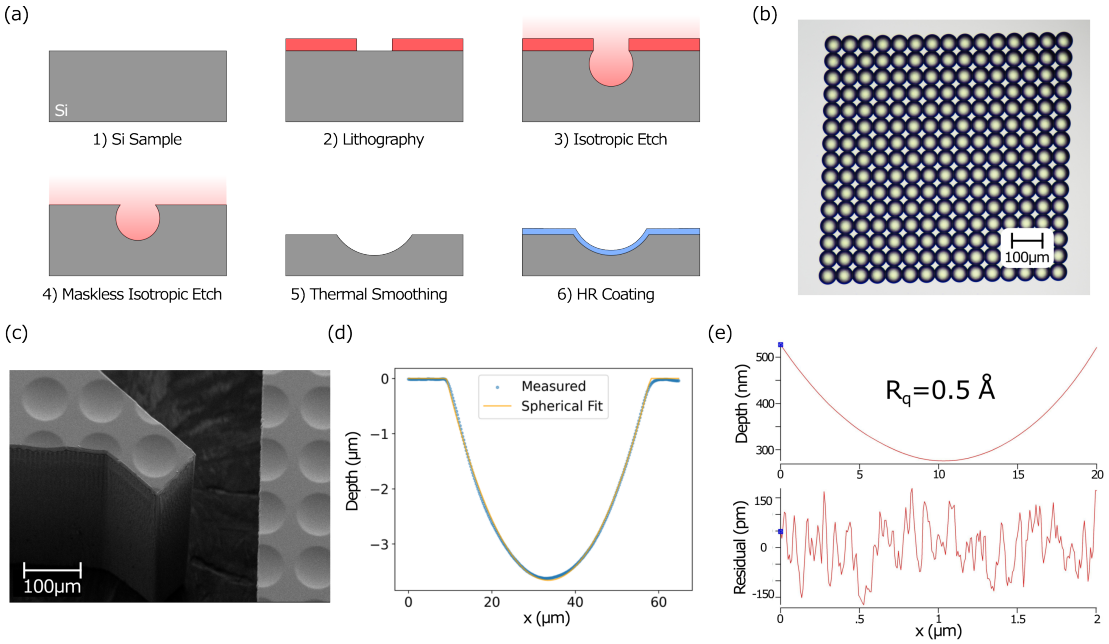


Figure 8.6: Silicon Micromirror Fabrication and Profile Characterization: (a) A diagram illustrating the fabrication flow. (b) A microscope image of a 15×15 array of 60μm-diameter silicon micromirrors, demonstrating the reproducibility and high density achievable with this technique. (c) An SEM image of a Bosch-etched silicon micromirror structure, providing large optical access. (d) The cross-section of a silicon micromirror fit, showing excellent agreement with a spherical model. (e) An AFM image of the silicon micromirror substrate prior to film deposition; the residual from a spherical fit is displayed and used to calculate an RMS surface roughness (R_q) of 0.5 Å.

removed. A second isotropic etch is then executed until the desired radius of curvature is achieved, where radii as large as 900 μm have been demonstrated.

To further reduce the surface roughness, the substrate is thermally oxidized in an oven. The resulting oxide layer is subsequently removed, leading to an overall reduction in roughness. This oxidation-removal cycle is repeated two to three times to reach sub-angstrom surface roughness. Finally, additional Bosch etching steps are applied to shape the micromirrors into configurations that maximize optical access for atom–cavity experiments. The samples are then fastened into a machined 4inch aluminum mount and shipped for coating at FiveNine Optics.

8.3 Buckled Micromirrors

Optical cavities are a critical component widely used in modern science and technology across both quantum and classical applications. Recently, the growing demands for miniaturization and high-performance have fueled the exploration of advanced fabrication methods and novel microcavity geometries beyond traditional polishing techniques and macroscopic mirrors. Visible and near-infrared (NIR) wavelengths are particularly important for quantum applications, where achieving low-loss resonators is more challenging and less explored than in the telecom – presenting unique challenges and opportunities for microcavity systems. Here, we present a novel fabrication method for making ultra-high-finesse NIR microcavities using buckled dielectric membrane mirrors, achieving a record finesse of 0.9 million at 780 nm. We demonstrated flexible device geometries – including singular mirrors, arrays, and cavity packages – with radii of curvature ranging from 1 mm to 10 mm, which are difficult to achieve using traditional methods. The fabrication process offers high uniformity and high yield. We characterize robust cavity performances across varied cavity lengths and fast modulation of 3GHz/us. For the microcavity package, with a compact total volume of 2 mm^3, we measured a linewidth of 5.16 MHz with a free spectral range (FSR) of 3.18 THz. Our results push the frontier of microcavity fabrication and provide new pathways for classical photonic and quantum technologies.

The Fabry–Perot (FP) cavity is one of the most versatile and widely utilized optical devices in modern optics. The high quality factors and frequency stability that state-of-the-art FP resonators offer have enabled significant advances in various fields, including cavity quantum electrodynamics (cQED)[164,141], quantum information science[35,158,61], high precision sensing[37,126,104], and timekeeping[91,159]. Traditionally, the high-performance mirrors that form these cavities are manufactured with macroscopic superpolishing techniques and low-loss dielectric coatings[155]. However, their large diameters and radii of curvature (ROCs) make them less suitable for compact and scal-

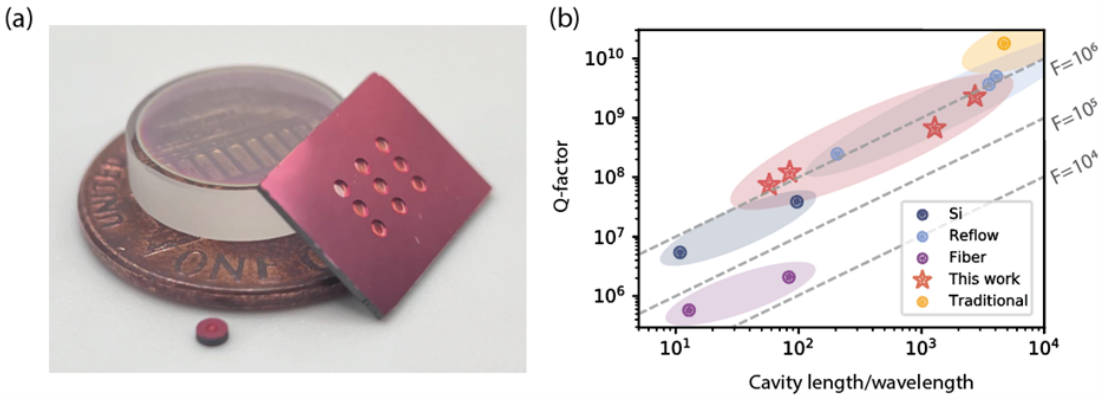


Figure 8.7: Compact micromirror array and device (a) a photo of the fabricated micromirror array and a singular micromirror next to a penny and a half inch diameter Thorlab mirror used in a commercial Fabry Perot cavity. (b) Finesse and quality factors as figures of merit for FP cavities.

able optical systems. Additionally, these ROCs also result in larger mode volumes, which are less useful for quantum applications. In recent years, motivated by the need for microscopic devices that enable photonic integration and efficient quantum light-matter interfaces, several microfabrication techniques, including laser machining and chemical etching, have been developed to address these limitations and produce high-quality micromirrors[70,202,80]. Several merit figures, such as finesse, waist size, form factor, quality factor (Q) and mode matching / coupling efficiency, can be used to present the performance of a FP cavity. Depending on the applications, certain parameters become more important than others. For example, for a highly stable frequency reference [159], the absolute linewidth and its long-term stability are critical. In such a case, the cavity design needs to be optimized to balance stability while maintaining a narrow linewidth, which usually leads to a very large cavity mode volume along with an extremely narrow cavity linewidth; for a light-matter interaction system[61], finesse and waist size are more important, while a moderate cavity linewidth is preferred for larger bandwidth, which tends to favor smaller cavities. The mode matching/coupling efficiency can also play a role in systems with limited photon rates. In general, among these figures of merit, finesse (F) is one of the more fundamental figures of merit, as it is a direct reflection of the loss in the

resonator. The primary limiting parameter is the optical scattering loss (S) dominated by the surface roughness (σ_s) of the mirror, specifically for the FP cavities, due to the fabrication process. Therefore, quantitatively, the finesse limit of a resonator is inversely related to the roughness of the surface by $F \propto \frac{1}{S} \propto \frac{1}{\sigma_s^2}$ [11].

The near-infrared/visible range is particularly interesting for microcavities for two reasons. A lot of quantum applications require light/cavities at shorter wavelengths (λ), putting constraints on material and/or fabrication methods. Microfabricated silicon mirrors [13] have thus far demonstrated exquisitely low loss and strong potential for scalable implementation. However, this approach may no longer be viable due to the intrinsic material loss of silicon at shorter wavelengths. It is important to develop a method that is suitable for the new wavelength regime while maintaining state-of-the-art performances. Also, from a technical point of view, shorter wavelength imposes stricter requirements on surface quality (roughness, e.g.) to achieve ultra-high finesse, since S is inversely proportional to λ^2 ($S = (\frac{4\pi\sigma_s}{\lambda})^2$) [11] Therefore, exploring shorter wavelength microcavity also pushes the limit of fabrications of smooth surfaces.

This work presents a simple, robust, and scalable method for fabricating state-of-the-art visible microcavities with ultra-smooth surfaces using buckled dielectric membrane mirrors (Fig. 1 (a)). These microcavities combine high finesse with compact designs, making them ideal candidates for applications in visible lasers [72], sensing [104,126,37,138], and quantum networking [35,158,86].

8.4 Buckled Micromirror Fabrication

The fabrication of the mirrors relies on accessible cleanroom nano/microfabrication tools and is simple and robust, as shown in Fig. 2 (a). We use commercially available 4" silicon wafers that are double-sided polished. The starting roughness is measured to be around 0.3 nm (Fig. 2 (a) (1)). To smooth the surface, we grow 2.5 um of wet oxide and remove it with 49% HF (Fig. 2 (a) (2)

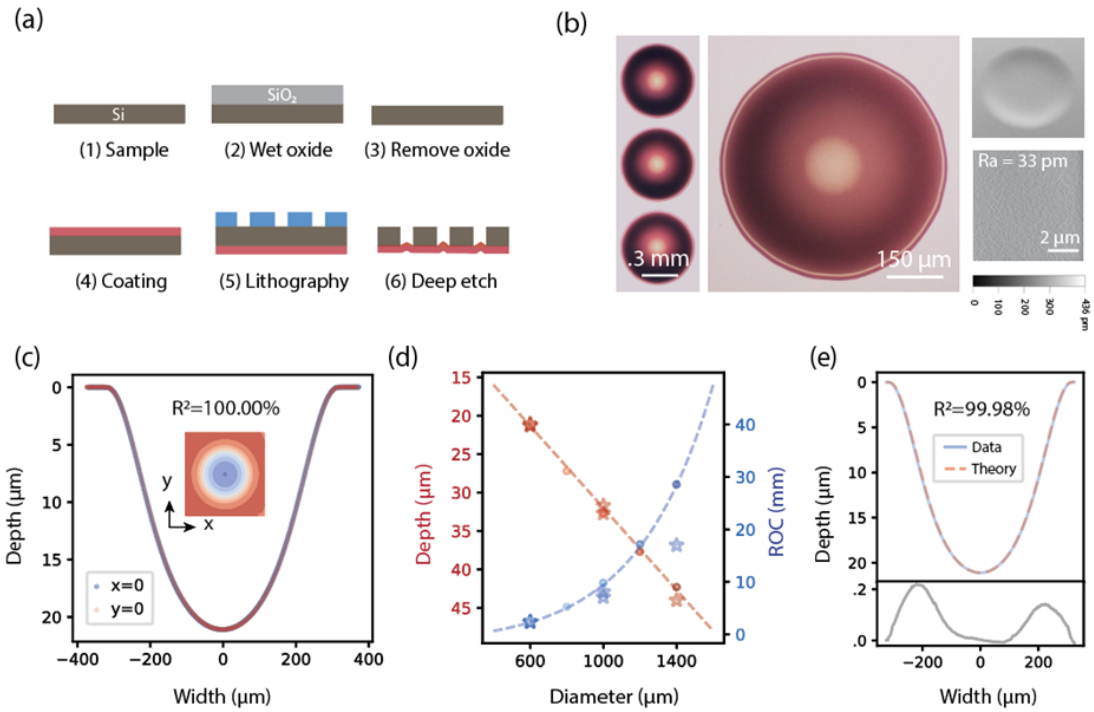


Figure 8.8: Micromirror fabrication and profile characterization (a) The diagram for the fabrication flow. (b) The fabricated micromirrors of d =600 µm. The left two are microscope images. The top right image is an SEM image. The bottom right image is an AFM image of the Si substrate before the film deposition, representing the lower bound of the mirror surface roughness. (c) The simulated mirror shape, assuming a uniform strain of .3% in the film, compared to the measurement, shows almost perfect agreement. (d) The depth and ROC of the fabricated mirrors as a function of the diameter defined by lithography. (e) The fabricated mirror's X and Y cross-section profile shows perfect rotational symmetry. The inset is a contour plot of the mirror profile. The profile data shown in (c) and (e) are taken by PL on a d =600 µm mirror.

and (3)). After two to three rounds of thermal smoothing, we can achieve a surface roughness of <50 pm in a random area of 2 um x 2um on the wafer. The principle of thermal smoothing is to turn outstanding surface features into oxide and remove them. Next, the wafers are deposited with alternating SiO_2 and Ta_2O_5 dielectric coatings (Fig. 2 (a) (4)). The coating is quoted to have 1.4 ppm loss at 780 nm and the coating thickness is about 5 um and visually looks magenta red (see SI). After the coating is protected by PMMA, photolithography and photoresist SPR (7 um) are used to define the mirror shape on the back side (Fig. 2 (a) (5)). The mirrors are suspended by etching through the back of the Si chip/wafer through a Bosch etch process with SF6 and CF_4 (Fig. 2 (a) (6)). The sample was cleaned with PG remove.

The suspended mirrors are naturally buckled because of the compressive strain in the dielectric coating. As shown in Fig. 2 (b), an array of micromirrors, whose diameter (d) is 600 μm, can be created with high yield and uniformity. The surface roughness is around 50 pm, down to 33 pm on the silicon surface before the dielectric coating deposition, measured using atomic force microscopy (AFM). The film does not introduce significant roughness.

The shape of the resulting mirror can be simulated with a high precision of $R^2 = 99.94\%$, as shown in Fig. 2 (c). The simulation is carried out using COMSOL, assuming a compressive deformation of 0.3% in the film and a fixed boundary condition on the circular edge (see SI). The shape cannot be described analytically with a functional form, such as a Gaussian or Bessel function, because of the nonlinearity in the material deformation. To explore the span of resulting geometries, we vary the diameter sizes and can achieve an ROC between 2.5 mm and 18 mm.

Finally, to ensure high finesse of the cavities made from the mirrors, it is important that the shape is rotationally symmetric. Indeed, the orthogonal cross-section profiles from the optical profiler (PL) measurements are identical ($R^2 = 100.00\%$), as shown in Fig. 2 (e).

8.5 Buckled Micromirror Cavity Characterization

Two mirrors are mounted and aligned on translation stages to form a microcavity for the finesse measurement. One of the two mirrors is attached to a piezoelectric transducer to modulate the length with a high frequency over a full free spectral range (FSR) Fig. 3 (b). The micromirrors are characterized using a swept-ring-down method [135,12,146], in which the cavity length, and therefore resonance, are rapidly modulated while a narrowband laser, stabilized at 780.24 nm to a rubidium reference, is sent through the cavity. As the cavity sweeps through the laser wavelength, the photodeterctor collects the transmission data. The detector is connected to an oscilloscope, where the ring-down of the cavity mode can be visualized. To ensure that we measure the TEM00 mode, we monitor the cavity output with a camera as well, so that we can confirm mode purity and optimize alignment. This configuration facilitates measuring high finesse and quality factors (Q) at different cavity lengths (see SI).

The full FSR measurement is shown in Fig. 3 (b). The peaks correspond to different modes, which can be confirmed by the camera image. To extract F and Q from the microcavity, we zoom in on the TEM_{00} peaks to fit the decay. The decay curves that feature the highest F and the highest Q are shown in Fig. 3 (d) and (e), respectively. For the highest point of finesse: $\kappa = 2\pi \times 233 \pm 1\,\mathrm{kHz}$, which translates to $F = 0.89 \times 10^6$. For the highest point Q: $\kappa = 2\pi \times 124 \pm 0.5\,\mathrm{kHz}$, which translates to $Q = 2.3 \times 10^9$.

The fringes in the ring-down signal are a result of light in the cavity leaking out as the length changes and interferes with itself, and are signatures of a high Q. The functional form is a convolution of an exponential decay and a complimentary error function, with a constant offset:

$$I \propto e^{-kt} \left| \mathrm{erfc}\left(\frac{(i+1)}{2} \frac{\kappa/2 \; - \; i\,\alpha\,(t - t_0)}{i\sqrt{\alpha}} \right) \right|^2 . \tag{8.1}$$

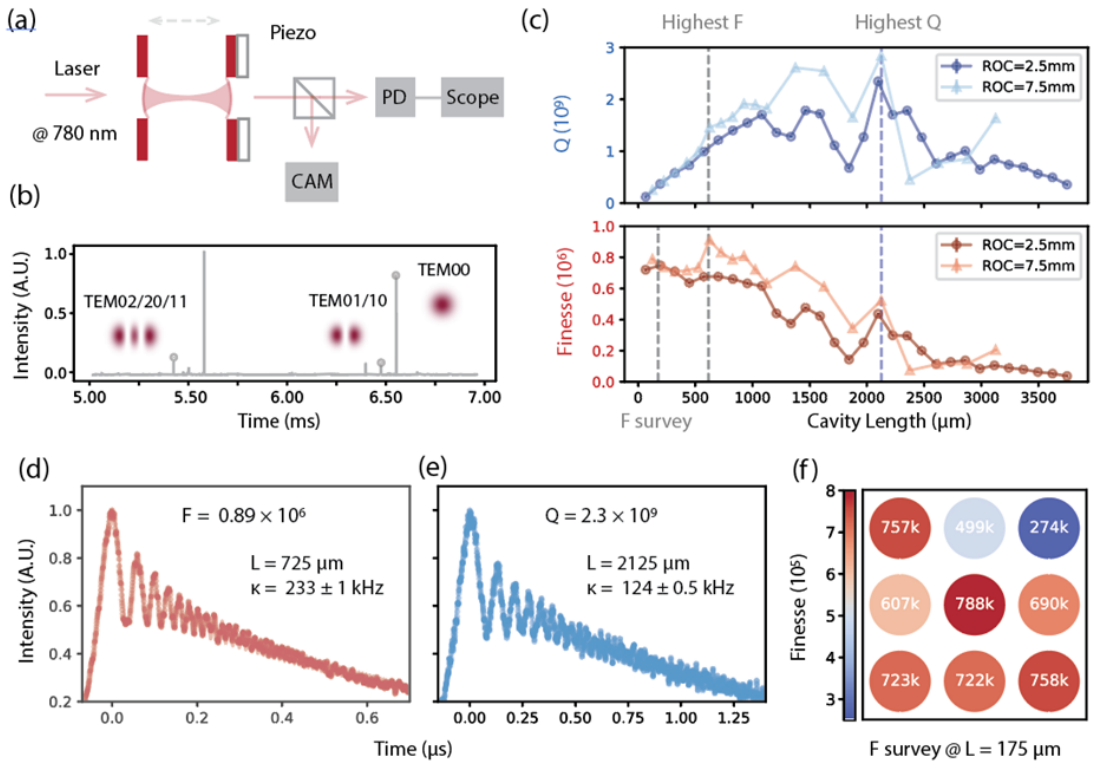


Figure 8.9: Microcavity characterization (a) A diagram for the measurement setup. CAM: camera; PD: photodetector; Scope: oscilloscope. The data is the transmission signal of the cavity while scanning the cavity distance with a piezoelectric transducer. (b) The FSR of the cavity at a cavity length of 58.7 μm is 2.5 THz. There are three modes visible in the range. The modes are confirmed by corresponding the shape of the transmitted light on the camera to the Hermite polynomials. (c) The Q and finesse vs. cavity length data. (d) The data point that corresponds to the highest finesse of 0.9 million. (e) The data point that corresponds to the narrowest linewidth of $\kappa = 2\pi \times 124 \pm 0.5\,\mathrm{kHz}$. (f) The F survey to show the yield on a 3-by-3 chip of d= 600 μm mirrors. They are measured against another d= 600 μm buckled micromirror. Most of them show high finesse at L=175 μm, that are consistent with the data points from (c).

Here, κ is the full width half maximum (FWHM) of the cavity, and α is a parameter that reflects the velocity of the resonance sweep of the cavity, and both parameters are fitted to extract F and Q. In our measurements, α varies with the length of the cavity (L) because the change in frequency is proportional to the FSR. Consequently, α can be used to extract the cavity length together with the FSR in time (Δt_{FSR}) (see SI). F is obtained by:

$$F = \frac{\lambda Q}{L} = \frac{2\,\alpha\,\Delta t_{\mathrm{FSR}}\,\lambda\,Q}{c}. \tag{8.2}$$

An alternative method to extract L uses the mode spacing (between the TEM_{00} and TEM_{01} e.g.) and measured ROC of the mirrors (see SI). We corroborate this measurement with the previous one to precisely determine the cavity length, to account for nonlinearity in the piezo and other errors, especially for short cavity lengths that cannot be physically measured accurately.

We vary the cavity length from 66 to 3750 μm, and measure the F and Q corresponding to L (Fig. 3 (c)). The finesse monotonically drops as the cavity becomes longer due to diffractive loss, related to the shape deviating from a sphere and more imperfection seen by the light. The Q increases at the beginning and plateaus, as both F and L change linearly, then drops as the cavity length significantly exceeds the ROC. This trend is captured in Fig. 3 (c) and can be modeled qualitatively (see SI).

The finesse of a Fabry Perot cavity is dictated by loss in the system: $F = \pi/(T + S + A)$, where T, S, and A represent the transmission, scattering, and absorption loss per mirror. T is dictated by the dielectric stack, which can be designed to be stronger or leakier for different applications; S originated from surface roughness or unideal mirror shapes, which fundamentally sets the limit of a cavity's finesse, usually as a result of a certain fabrication process; A comes from the coating materials, and can be as low as $\sim$ 1 ppm. In our case, it is quoted $T \geq 1.33$ ppm at 781 nm, which is obtained by a transmission measurement (see SI). The measured cavity finesse $F_{780} = 0.89 \times 10^6$ can bound the rest of the loss: $A + S \leq 2.20$ ppm. If we assume that there is no absorption loss,

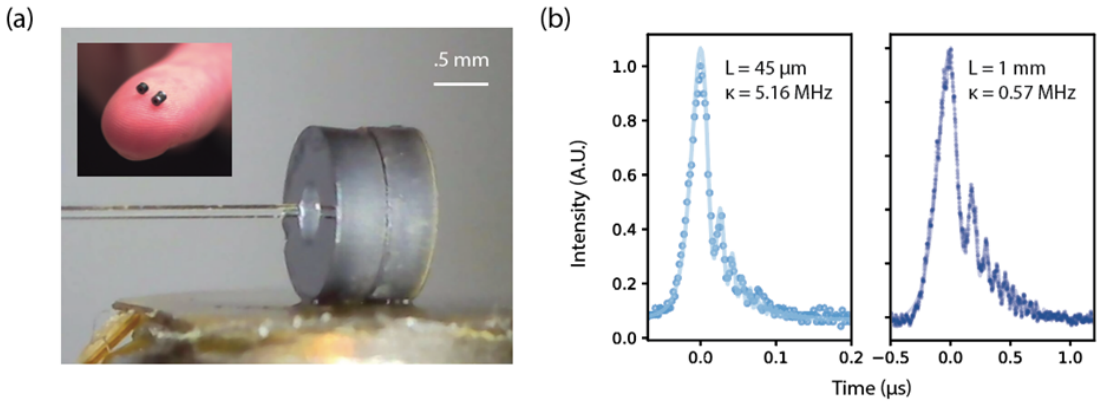


Figure 8.10: Microcavity assembly (a) A photo of the measurement setup and the actual measured cavity device. The fiber is a visible fiber that has been cleaved. The inset shows the cavities with two different lengths (45 µm and 1 mm). The tip is inserted into the cavity mirror slot from the back. (b) The measured ringdown of the cavity for the cavity assembly at different lengths. The laser frequency is swept in this case.

$A = 0$, we can find an upper bound on the surface roughness, $S = \left(\frac{4\pi\sigma_s}{\lambda}\right)^2 \leq 2.20$ ppm, which translates to a surface roughness of $\sigma_s \leq 90$ pm. This value is slightly higher than our measured surface roughness, which is consistent. Notice, $S \propto 1/\lambda^2$, which is one of the fundamental reasons why it is more difficult to achieve high finesse FP cavities at a lower wavelength with the same fabrication process and the resulting surface roughness. More specifically, 780 nm is roughly half of 1550 nm, which means to achieve the same finesse or scattering loss, the surface needs to be 4 times smoother given that state-of-the-art mirrors are roughness limited. In other words, using the measured roughness ($S \sim 2.20$ ppm) and loss values ($T \sim 1.33$ ppm) in our current system, we can extrapolate the performance of these cavities at telecom, where $F_{1550} = 3.5 \times 10^6$. The microcavities shown in this work and the corresponding fabrication process feature state-of-the-art surface roughness, which may be explored for applications beyond FP cavities.

8.6 Buckled Micromirror Cavity Integrability and Scalability

The fabrication method produces micromirrors on the order of 500 μm, allowing for small assembled cavities that can be integrated into a fiber [138] or an integrated photonic chip [91]. We demonstrate this by creating a compact cavity system out of the mirror cutouts of the silicon chip, using only heat-cure glue and manual alignment, that can be easily implemented in a lab setting.

Individual mirror chips can be produced by etching through Si at the same time as suspended mirrors are created, where the outer diameter of the chip is 1.7 mm (Fig. 1(a)). The two chips are directly glued together to produce a cavity with a narrow resonance, with or without a spacer. We made two cavity assemblies with different lengths (see Fig. 1(a) inset). The shorter cavity stack is 1 mm tall and the cavity is formed by the two concave mirror surfaces pressed against each other to form a short cavity of 45 μm. The longer cavity has a 1 mm spacer and is 2 mm tall. The cavity is measured by directly putting a cleaved fiber against the back of the mirror and collecting transmission, as shown in Fig. 4(a), with the short cavity. The measured line width is $\kappa = 2\pi \times 5.16 \pm 0.14$ MHz, with a very large FSR of 3.18 THz, which makes it ideal for compact laser locking applications [101,105,118,94]. The merit figures for this microcavity assembly are measured as: $F_{(45\,\mu\mathrm{m})} = 0.616\times10^5$, $Q_{(45\,\mu\mathrm{m})} = 7.45\times10^7$, $F_{(1\,\mathrm{mm})} = 0.263\times10^6$, and $Q_{(1\,\mathrm{mm})} = 6.74\times10^8$, which are consistent with previous measurements of finesse versus length. The minor drop in finesse is due to the alignment error of a manual gluing process, which also highlights the robustness of this assembly.

8.7 Outlook

We demonstrate a novel method of producing state-of-the-art micromirrors and microcavity systems. The fabrication is simple, robust, flexible, and scalable, and can be achieved in a common cleanroom environment with a high tolerance for error. The resulting devices can be singular mir-

rors, arrays, or cavity assemblies that show robust performance with flexible configurations.

There are a few areas in which this microcavity invention can play an important role in advancing both quantum and classical optical hardware and overcoming technical bottlenecks. The combination of small device size (down to 2 mm^3) and moderate ROC allows for integration with existing architectures for neutral atoms and ion trap architectures as an optical interface for quantum networking. Specifically, this cavity geometry operates in a regime that would mitigate the effects of the dielectric surface on the qubits [189,133], which would otherwise severely limit the operation of Rydberg-mediated quantum gates for neutral atom qubits and similarly limit motional coherence for trapped ion qubits, while still maintaining a small mode volume for strong light-matter interactions [213,182]. Achieving this regime is difficult using mirrors produced by conventional polishing or ablation methods, which yield radii of curvature that are typically too large or too small, respectively. In classical applications, these microcavities can be used as high-efficiency filters, transfer cavities, or external resonators. For example, due to their small size, these optical cavities can be tuned with high-bandwidth piezoelectric modulators, allowing stabilization against acoustic noise, which is challenging for more massive mirrors [166], and provides robust stability to its state-of-the-art linewidth. The stabilized cavity can then be utilized as a compact narrow filter, external cavity for a laser, or transfer cavity for stabilization of lasers of vastly different wavelengths.

It's the second quarter of the 21st century!

Mikhail Lukin

9

Next Generation Experiments and Conclusions

The experiments performed in Chapters 5–8 have laid the foundations for creating a neutral atom quantum processor that can be networked with other processors through state-of-the-art optical interconnects, as illustrated in Figure 9.1. In Chapter 5, we introduced a platform that utilizes atoms coupled to nanophotonic optical cavities, bridging the gap between the free space atom array and

the cavity-coupled operation via coherent transport. This work inspired the research in Chapter 6, where we demonstrated that coherent Rydberg excitation can be performed in the presence of a nanophotonic cavity. In Chapter 7, we presented a platform more compatible with atom arrays while simultaneously exploring new capabilities for quantum computing. These advances were further enhanced by the fabrication techniques detailed in Chapter 8. The next step is to integrate the tools developed in these chapters into a single platform.

In this chapter, I present progress toward achieving this goal. First, the initial experiment will be upgraded to accommodate large arrays of atoms and Rydberg excitations for two-qubit gates. In addition, a second experiment has been constructed to serve as a secondary processor that can connect to the primary system, incorporating the micromirrors developed in Chapter 8. This new experiment also explores promising directions for achieving direct entanglement between atoms and telecom photons.

9.1 Atom Arrays Coupled to Fiber Cavities

All experiments presented in this thesis were conducted using two optical tweezers, each individually controlled by Galvo mirrors. To scale these systems for atom arrays containing hundreds to thousands of atoms, it is necessary to implement trapping using acousto-optic deflectors or spatial light modulators [50,52,6]. In addition to this modification, expanding the field of view is highly beneficial. To achieve this, we have transitioned to using a specialized microscope objective and large-aperture Gooch and Housego acousto-optic deflectors. This enhanced system provides a usable field of view of approximately 400 μm, which simplifies the trapping and cooling of atoms near the cavity compared to the previous limit of about 60 μm. Moreover, the larger field of view improves the prospects for coherent Rydberg excitation in the presence of the cavity.

In contrast to the experiments described in Chapter 6, we have also been developing our own

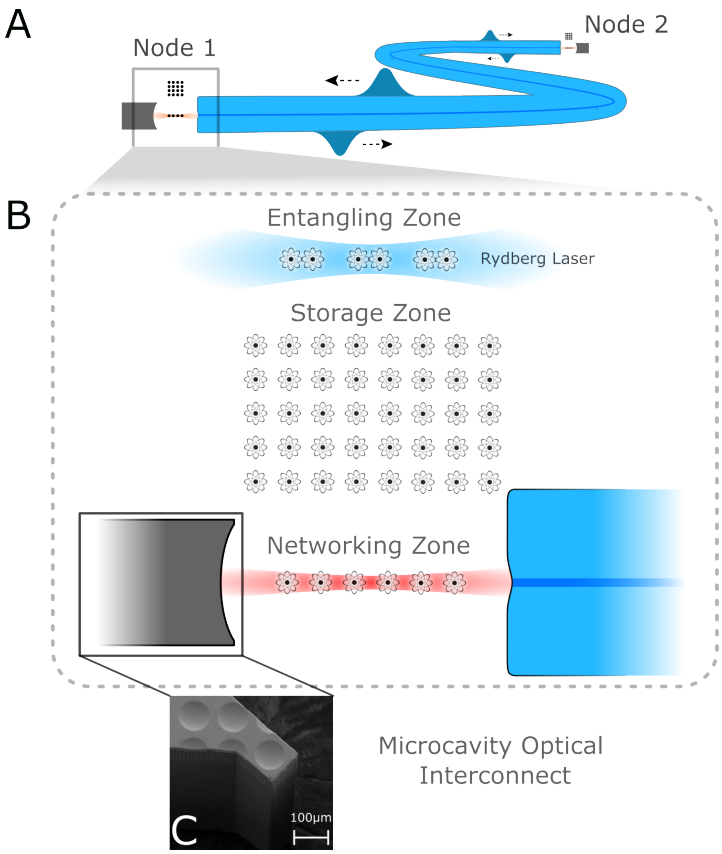


Figure 9.1: (A) Two Neutral atom quantum processor nodes connected by an optical link allowing for distribution of entanglement through photons. (B) The architecture of a single modular quantum processor, which includes an entangling zone for two qubit gates mediated by Rydberg excitation, a storage zone for holding many qubits, and a networking zone where atoms can be entangled with photons, enabling fast high fidelity quantum networking. (C) A scanning electron microscope (SEM) image showing a fabricated microcavity optical interconnect.

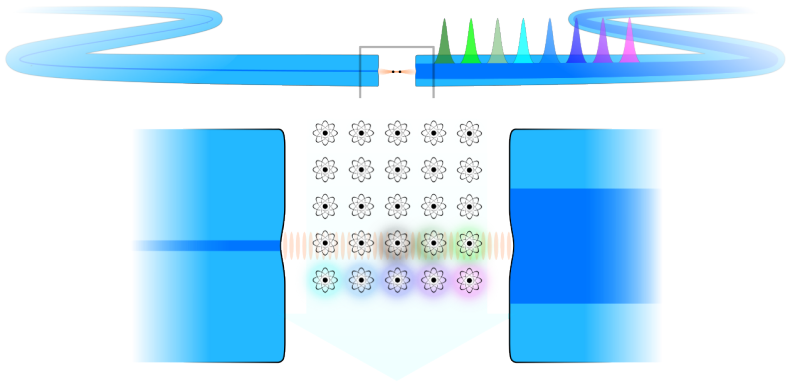


Figure 9.2: Multiplexed atom photon entanglement can be generated by utilizing coherent transport through the cavity while simultaneously emitted photons through the cavity as they travel through the cavity mode, enabling faster entanglement attempt rates.

Rydberg laser system. This new system offers greater flexibility in selecting the Rydberg state and enables exploration of more optimal states that balance Rydberg sensitivity with Van der Waals shifts.

9.2 Multiplexed Atom Photon Entanglement

Furthermore, by utilizing an array of atoms, we can perform multiplexed atom–photon entanglement—a key technique for increasing remote entanglement generation rates. Current experiments are limited by challenges in atom state preparation and cooling. A promising strategy is to employ atom arrays for multiplexed atom–photon emission, allowing idle atoms to be prepared and cooled simultaneously while other atoms emit photons, as shown in figure 9.2. In principle, this technique can yield an N-fold increase in remote entanglement generation rates, where N is the number of atoms that can emit photons while the other atoms are being prepared. These improvements can be further enhanced by integrating optical cavities to boost photon-collection efficiency and increase atom-scattering rates. Recently, the Rempe group demonstrated multiplexed

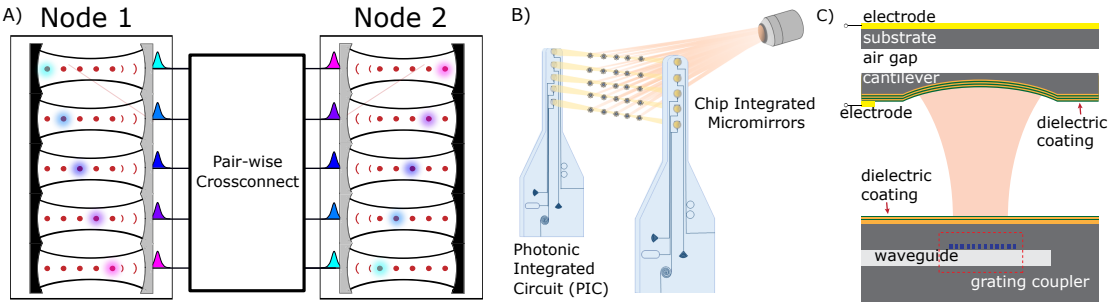


Figure 9.3: (A) Two modules containing arrays of atoms coupled to arrays of optical cavities are used for multiplexed REG. **(B)** Each module will consist of a chip integrated microcavity array coupling to an array of atoms. **(C)** A cross-section showing the material stack of the proposed device. This device will provide fast tuning of the cavity resonance and directed emission into the photonic interface through grating couplers.

atom–photon entanglement by coupling an array of atoms to an optical cavity[63]. The remaining challenges include determining the maximum number of atoms that can be multiplexed and the achievable bandwidth of the optical cavity. Addressing these challenges will require further scaling of the atom number, employing higher-bandwidth optical cavities, or developing multiplexed optical interfaces, which can be realized with the fabrication we have developed.

The exploration of new optical cavity fabrication methods can address several challenges in integrating atom arrays with optical cavities. More advanced fabrication techniques can improve cavity finesse and, consequently, increase atom–cavity coupling strengths[202,80]. These methods can also ensure pristine surface quality, thereby reducing surface charge fluctuations. Furthermore, protective coatings applied during fabrication can mitigate charge fluctuations arising from cavity surfaces, enabling more coherent Rydberg operations near optical interfaces.

Furthermore, fabricated micromirrors offer a scalable and flexible geometry that allows arrays of cavities to be integrated into a single system. By incorporating multiple optical interfaces into one platform, entanglement generation rates can be enhanced for modular quantum computation. Moving toward a fully fabricated approach also introduces opportunities to integrate nanophotonic elements such as on-chip filters, wavelength division multiplexers, beam splitters, and grating

couplers, as shown in figure 9.3.

9.2.1 Cavity Mediated Many-Atom Quantum Operations

The experiments presented in Chapter 7 were limited to using two atoms to perform cavity-mediated atom-atom operations. With more atoms, we can implement multi-qubit entangling operations, while also designating one atom as an ancilla to be used to increase the performance of the gate. Using a dedicated ancilla enables higher fidelities and provides greater flexibility in the choice of qubit states. The two types of operation demonstrated in this chapter can be categorized as follows: (1) state carving, which effectively implements a quantum nondemolition (QND) measurement or dissipative state preparation, and (2) error-biased coherent quantum operations, which can be made fault-tolerant through error detection. Both approaches naturally extend to many-atom systems.

9.3 Many-Qubit State Carving

The operation demonstrated in chapter 7, which we call cavity carving, can be interpreted as a projective measurement of the operator $1 - |01\rangle\langle 01|$, followed by a subsequent π rotation. This effectively realizes a measurement of $1 - |10\rangle\langle 10|$. Upon a successful carve, the system is projected into the even-parity subspace:

$$1 - |01\rangle\langle 01| - |10\rangle\langle 10| = |00\rangle\langle 00| + |11\rangle\langle 11|$$

resulting in entanglement between the two atoms. By detuning the cavity from the atomic transition, its response becomes sensitive to collective multi-qubit states—specifically number states, characterized by the number of atoms in the $|1\rangle$ state. Driving the ancilla at the resonance frequency associated with a particular number state enables selective carving of that component, analogous to

the earlier $|01\rangle$ state carving. A sequence of multi-qubit carving operations, interleaved with local single-qubit rotations, can thus prepare arbitrary many-body states stabilized by specific measured operators. A key application of this is the preparation of logical qubits,.

A simple example is the three-qubit repetition code. The logical states are $|1\rangle_L = |111\rangle$ and $|+\rangle_L = (|000\rangle + |111\rangle)/\sqrt{2}$. To prepare the logical $|+\rangle_L$ state, one must prepare physical qubits in $|+\rangle$ then measure the Z-type stabilizers. In the computational (Z) basis, these correspond to ZZI, IZZ, and ZIZ (i.e., pairwise parity checks), which can be implemented using our carving technique combined with site-specific light shifts to perform effective two-qubit parity measurements and can also realize transversal logic gates directly[214].

The repetition code is capable of correcting errors in only one basis. To protect quantum information against both bit-flip and phase-flip errors, more advanced quantum error-correcting codes are required. These codes typically involve higher-weight stabilizers, necessitating the measurement of multi-qubit operators. Notable examples include the surface code and quantum low-density parity-check (qLDPC) codes. For instance, the 7-qubit Steane code, features the following stabilizers:

IIIXXXX

IXXIIXX

XIXIXIX

IIIZZZZ

IZZIIZZ

ZIZIZIZ

To implement an identity operation on a specific atom, it can be shifted far off resonance so it does not affect the resonance condition of the ancilla. Higher weight parity checks (e.g., $ZZZZ$) can be measured by driving the ancilla at resonance frequencies corresponding to an odd number of atoms coupled to the cavity. This projects out the odd-parity subspace:

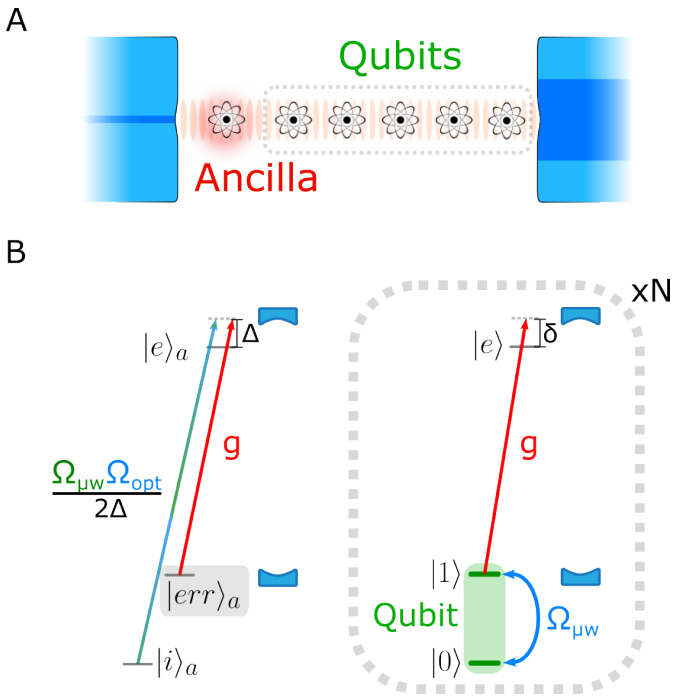


Figure 9.4: (A) An array of atoms coupled to an optical cavity, with one atom designated as an ancilla and the others serving as qubits. The ancilla is locally addressable via a tightly focused beam used for gate operations. (B) Level structure: the ancilla atom has three relevant states—an initial state $|i\rangle_a$, an excited state $|e\rangle_a$, and an error state $|err\rangle_a$. The transition $|i\rangle_a \leftrightarrow |e\rangle_a$ is driven via a two-photon process, with one leg provided by a local optical drive Ω_{opt} and the other by a microwave drive $\Omega_{\mu w}$. This approach enables the use of states in which all gate-induced errors are, in principle, detectable, owing to the suppressed direct coupling between $|e\rangle_a$ and $|i\rangle_a$. The $|e\rangle_a \leftrightarrow |\text{err}\rangle_a$ transition is strongly coupled to the cavity with detuning Δ. Qubit atoms are coupled to the cavity through the $|1\rangle \leftrightarrow |e\rangle$ transition with a detuning of δ, such that the $|1\rangle$ state induces a dispersive shift of the cavity resonance, while the $|0\rangle$ state remains uncoupled.

$$ZZZZ\,|\psi_{\text{odd}}\rangle = -\,|\psi_{\text{odd}}\rangle$$

so that a successful measurement projects the system into the $+1$ eigenspace (even parity). More generally,

$$ZZZZ = \sum_{n\,\text{even}} |n\rangle\langle n| - \sum_{n\,\text{odd}} |n\rangle\langle n|$$

Measurements in other bases can be made by applying local rotations before and after the carving operation.

To enable number-dependent resonances, we introduce an ancilla atom with levels, shown in figure 9.4 $|i\rangle_a$, $|e\rangle_a$, and $|err\rangle_a$. The $|e\rangle_a \leftrightarrow |\text{err}\rangle_a$ transition is strongly coupled to the cavity with a detuning Δ. The relevant eigenstates are:

$$|\psi_{\text{cav}}\rangle = \frac{g}{\Delta}|e\rangle_a|0\rangle_{cav} + |\text{err}\rangle_a|1\rangle_{cav}, \qquad |\psi_{\text{atom}}\rangle = |e\rangle_a|0\rangle_{cav} - \frac{g}{\Delta}|\text{err}\rangle_a|1\rangle_{cav}$$

and we operate using the cavity-like eigenstate. Including N resonant qubits, the eigenstates become:

$$|\psi_{\text{cav},N,\pm}\rangle = \frac{g}{\Delta}|e\rangle_a|0\rangle_{cav}|N\rangle_q + \frac{1}{\sqrt{2}}\left(|\text{err}\rangle_a|1\rangle_{cav}|N\rangle_q \pm |\text{err}\rangle_a|0\rangle_{cav}|W\rangle_q\right)$$

$$|W\rangle_q = \frac{1}{\sqrt{N}}\sum_{j=1}^{N}|1\ldots e_j\ldots 1\rangle_q$$

with eigenenergies:

$$\lambda_{N,\pm} = \omega_{\text{cav}} \pm \sqrt{N}g$$

We drive one of these avoided crossings after preparing the ancilla in $|i\rangle_a$, causing population transfer to $|\text{err}\rangle_a$ if the system has the corresponding number of qubits in the $|1\rangle$ state. Successful detection in the initial state (no transfer) implies projection into the orthogonal subspace.

The transition rate for resonant coupling is:

$$\Gamma_0 \approx \frac{2g^2\Omega^2}{\Delta^2(\kappa+\gamma)}$$

and for N-excitation states, we find a suppressed transition rate:

$$\Gamma_N = \frac{2g^2\Omega^2(\kappa+\gamma)}{\Delta^2(\kappa+\gamma+2\sqrt{N}g)^2}$$

yielding the selectivity ratio:

$$\frac{\Gamma_0}{\Gamma_N} = \left(1+\sqrt{N}\frac{2g}{\kappa+\gamma}\right)^2 \approx N\cdot\frac{4g^2}{(\kappa+\gamma)^2}$$

For large cooperativity C, assuming $\gamma = \kappa$, we find $\Gamma_0/\Gamma_N \approx C$. Failure mechanisms include photon loss into free space via the $|W\rangle$ state, which decoheres the qubits, and photon leakage from the cavity, which is non-destructive to the qubit states. By detuning the qubits, we can bias the failure toward cavity leakage, which preserves coherence. This enables deterministic two-qubit parity measurements by carving out the $N = 1$ state. Due to the QND nature of the measurement not destroying coherence within the $N = 1$ manifold this allows for the measurement of both the +1 and -1 parities. For this scheme the associated errors are: False negative:

$$\varepsilon_n = e^{-\Gamma_1 t}$$

False positive:

$$\varepsilon_p \approx 1 - e^{-\frac{\Gamma_1}{C}t}$$

resulting in a total error:

$$\varepsilon_{\text{tot}} = \varepsilon_p + \varepsilon_n \approx 1 - e^{-\frac{\Gamma_1}{C}t} + e^{-\Gamma_1 t}$$

Minimizing this error yields the optimal measurement time:

$$t_{\text{opt}} = \frac{\ln(1/C)}{\Gamma_1\left(\frac{1}{C} - 1\right)}$$

and the corresponding minimum error:

$$\varepsilon_{\text{min}} \approx \frac{\ln C + 1}{C}, \quad \text{for } C \gg 1$$

As a result, we find that one can perform a deterministic two-qubit parity measurement with a error rate that scales as $\frac{\ln(C)}{C}$.

9.3.1 Cavity-Mediated Many-Atom Quantum Gates

The other quantum operation demonstrated in Chapter 7 is a controlled phase gate, implemented by inducing a π phase shift in one of the qubit states relative to the others. By extending this to multiple qubits, we realize a N-qubit Toffoli-like gate, as explored in [20].

We can generalize this idea further by combining the N-qubit Toffoli mechanism with the Dicke state-dependent cavity shifts described earlier. An intuitive extension is to engineer number-state-dependent phase shifts. A particularly elegant proposal in this direction is found in [79], where the ancilla acts as a control qubit that enables a number state-dependent operation across the entire qubit ensemble. This allows for parity measurement of all qubits in the cavity:

$$|+\rangle_a |0\rangle_{\text{cav}} |\Psi\rangle_q \rightarrow \left(|0\rangle_a |0\rangle_{\text{cav}} + |\text{err}\rangle_a |1\rangle_{\text{cav}}\right) |\Psi\rangle_q .$$

We allow the state $|\text{err}\rangle_a |1\rangle_{\text{cav}} |\Psi\rangle_q$ to evolve for a time τ. Due to the dispersive coupling of the

cavity photon to the qubit ensemble, the system acquires a phase shift dependent on the total number of excitations. The effective Hamiltonian is:

$$H_d/\hbar = \chi S_z, \quad \chi = \frac{g^2}{2\delta},$$

where g is the cavity coupling rate, δ is the detuning, and S_z is the collective spin operator.

After evolution, a reverse pulse maps the cavity photon back into the ancilla atom:

$$|0\rangle_a |0\rangle_{\text{cav}} |\Psi\rangle_q + |\text{err}\rangle_a |1\rangle_{\text{cav}} e^{-iH_d\tau/\hbar} |\Psi\rangle_q \rightarrow |0\rangle_a |\Psi\rangle_q + e^{-iH_d\tau/\hbar} |1\rangle_a |\Psi\rangle_q .$$

If a photon is lost (either through the cavity or by free space scattering during evolution), the ancilla cannot return to the initial state $|1\rangle_a$. Thus, detecting the ancilla in the state $|\text{err}\rangle_a$ at the end of the sequence indicates a gate failure. The success probability (no photon loss) is:

$$P_{\text{succ}} = \exp\left[-\left(\kappa + N\frac{g^2\gamma}{\delta^2}\right)\tau\right],$$

where κ is the cavity decay rate and γ is the atomic decay rate.

To apply a π phase shift to all odd-parity states, we evolve for a time:

$$\tau = \frac{\pi}{2\chi} = \frac{\pi\delta}{2g^2},$$

The resulting state after this time evolution will then take the form:

$$|0\rangle_a |\Psi\rangle_q + \prod_n \sigma_n^z |1\rangle_a |\Psi\rangle_q .$$

and have a corresponding success probability of:

$$P_{\text{succ}} = \exp\left[-\left(\kappa + N\frac{g^2\gamma}{\delta^2}\right)\cdot\frac{\pi\delta}{2g^2}\right].$$

The optimal detuning that maximizes this probability is:

$$\delta = g\sqrt{\frac{N\gamma}{\kappa}},$$

which yields a maximum success probability of:

$$P_{\text{succ}} = \exp\left[-\pi\cdot\frac{\sqrt{N\gamma\kappa}}{g}\right] \approx 1 - 2\pi\sqrt{\frac{N}{C}},$$

for large cooperativity $C = \frac{4g^2}{\kappa\gamma}$. As shown in Chapter C, the fidelity of this gate can be brought close to unity by applying an additional rotation between $|0\rangle_a$ and $|\text{err}\rangle_a$.

For this particular gate time, we effectively implement the operator $\prod_n \sigma_n^z$. Measurement of the ancilla on the X basis projects the qubit register onto an eigenstate of this operator, similar to state carving. However, unlike the dissipative carving process, this interaction is coherent and allows one to distinguish the $+1$ and -1 stabilizer eigenspaces.

In general, the failure probability of these cavity-mediated gates scales as

$$P_{\text{fail}} \approx \frac{1}{\sqrt{C}},$$

which determines the fidelity of the gate in a deterministic setting. However, with error detection, this can be improved to

$$P_{\text{fail}} \approx \frac{1}{C},$$

or even lower by engineering favorable error channels. This opens the possibility of leveraging

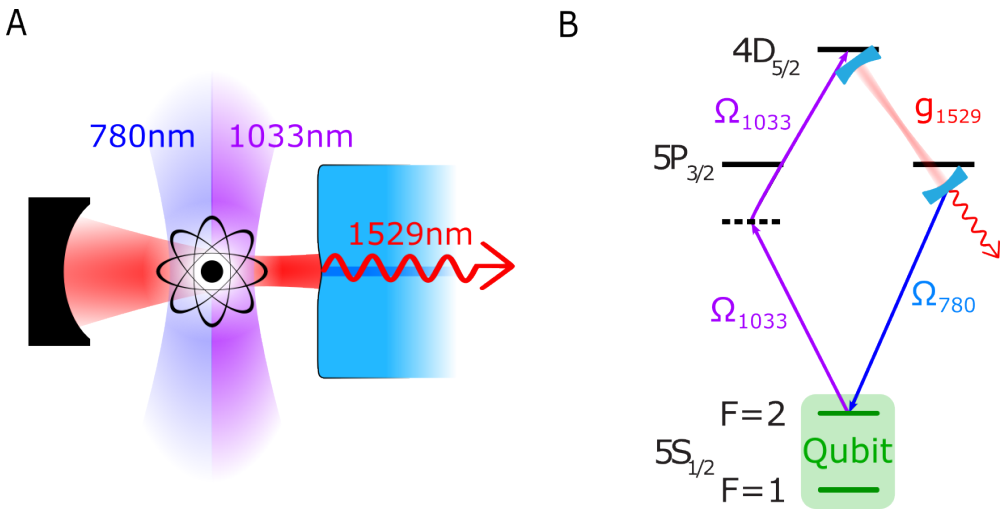


Figure 9.5: (A) An atom in a fiber mirror–silicon micromirror cavity driven from the side by 1033 nm and 780 nm laser fields. These drives produce 1529 nm telecom photons can be entangled with the atomic qubit states.(B) Energy level diagram illustrating the two-photon process used for atom–photon entanglement: a 1033 nm excitation, Ω_{1033}, couples the $|5P_{3/2}\rangle$ and $|5S_{1/2}, F = 1\rangle$ states, resulting in the emission of a 1529 nm photon via strong coupling to the cavity with strength g_{1529}. An additional 780 nm, drive, Ω_{780}, on the $|5S_{1/2}\rangle \leftrightarrow |5P_{3/2}\rangle$ transition coherently maps the system back to the qubit manifold, thereby generating an entangled pair between the telecom photon and the atomic qubit.

erasure detection in quantum error correction, which can significantly increase the threshold [169,3]. For achievable cooperativities on the order of $C \sim 10^4$, gate success probabilities can reach the percent level, while fidelities can, in principle, approach unity. This would comfortably exceed the thresholds for many erasure-biased codes. Combined with the natural advantages of the platform, such as fast qubit readout and integrated quantum networking, this presents a promising direction for future research.

9.4 Atom-telecom Photon Entanglement

In addition to the upgrades, it is now known as the "Main experiment". We have constructed a second atom-cavity experiment that we hope to one day link to the existing system, establishing a two-node quantum network test bed. In addition to this long term goal, the second experiment

will begin utilizing the fabrication that was developed in Chapter 8. These micromirrors provide many advantages over the fiber-cavity platform. Additionally, because fabrication is an in-house process, we are allotted more flexibility in our coatings. In particular, we can have our mirrors coated for multiple wavelengths in Rubidium. A transition that is particularly interesting in Rubidium is the $|5P_{3/2}\rangle \leftrightarrow |4D_{5/2}\rangle$ transition at a wavelength of 1529nm, as shown in figure 9.5B. Importantly, this transition falls within the telecommunications C-band, these photons can be transmitted through optical fiber with ultra-low loss, experiencing attenuation below 0.2 dB/km (compared to 4 dB/km for 780 nm). This allows entanglement links to span tens of kilometers[200,88]. Thus, one of the main goals of this experiment is to achieve strong coupling on the telecom transition and utilize schemes for directly generating atom-photon entanglement between the spin and a telecom photon. This approach may have an advantage over some of the previous methods involving quantum frequency conversion in terms of complexity, fidelity, and rate[88].

There is already existing work on schemes for generation atom-photon entanglement on higher lying transitions like those we plan to use. These are typically diamond schemes that rely on three lasers with fast pulsing[121,199]. This becomes a technical challenge involving the stabilization of three narrow lasers. In order to reduce this complexity, we plan to replace the two-resonant drive excitation with a single drive two-photon off-resonant excitation. In the case of $|5P_{3/2}\rangle \leftrightarrow |4D_{5/2}\rangle$, this corresponds to a 1033nm transition. This laser can be stabilized using one-color, two-photon spectroscopy[162]. These methods for laser stabilization are common for vapor cell optical clocks due to their narrow lines and Doppler-free nature.

9.4.1 Dual Resonance Cavity

The optical cavity design that will be utilized is a hybrid cavity with an input mirror being the fiber cavity and a back mirror being a silicon micromirror. Due to the spherical shape of the micromirror, it is possible to work with a configuration where the radius of curvature of the fiber cavity is larger

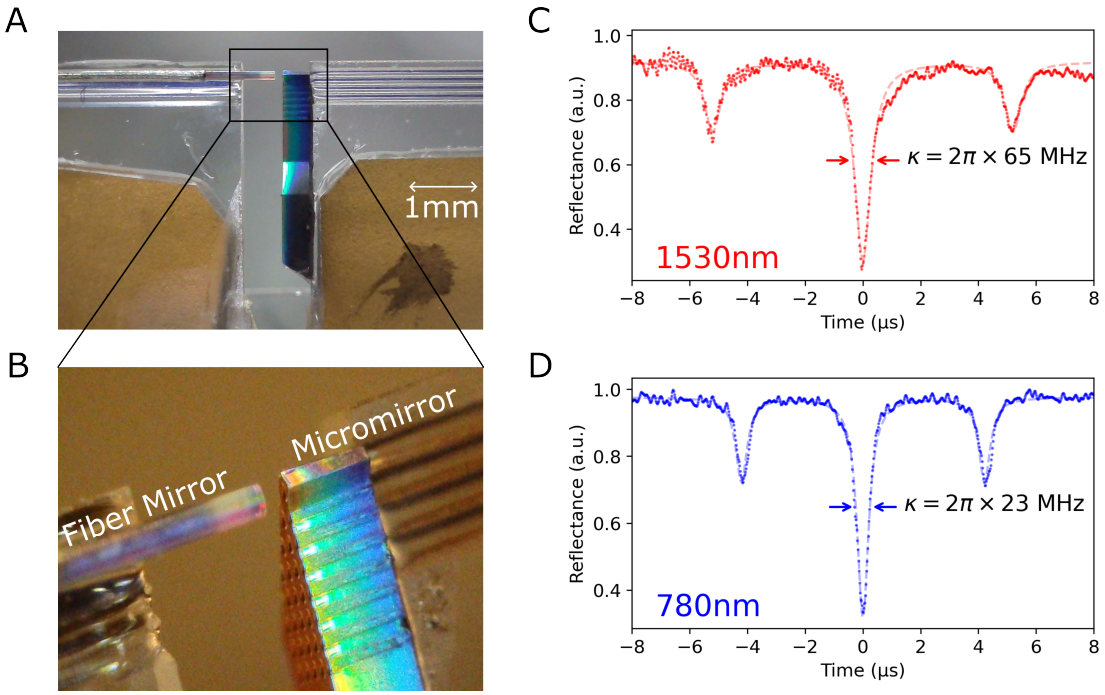


Figure 9.6: (A) An image of the fiber mirror-silicon micromirror device shows the fiber cavity mounted in the v-groove structure, with the micromirror cavity glued to the side of the v-groove. The v-groove is then mounted on two shear plate piezos, as seen in the lower left and right. (B) A zoomed-in image of the fiber mirror-silicon micromirror device demonstrates that the micromirror design offers ample optical access. (C-D) The linewidths of the 1530 nm and 780 nm resonances of the cavity were measured using sideband spectroscopy with sidebands of 200Mhz and 500MHz, respectively. The 1530 nm line exhibits a linewidth of $2\pi \times 65$ MHz, corresponding to a finesse of 30,000, while the 780 nm line has a linewidth of $2\pi \times 23$ MHz, corresponding to a finesse of 81,000.

than that of the micromirror and operate where the length of the cavity is nearly the radius of curvature of the micromirror. This will result in a mode shape that places the cavity waist on the fiber cavity, as described in chapter 8. By ensuring that this mode overlaps with the core of the fiber, one will achieve a high collection efficiency of photons from the cavity mode directly into the optical fiber. In addition to this feature, the silicon micromirror can be coated to have significantly higher reflectivity than the fiber cavity, resulting in an overcoupled cavity where most of the photon emission will exit into the fiber. Combined, these two considerations will result in a high total collection efficiency going directly into the fiber.

Building this optical cavity presents several challenges, one of which is that we are interested in aligning this cavity so that the total collection efficiency is maximized. Unfortunately, if we revisit the cavity reflectivity equation, we find that the size of the signal (reflection dip) shrinks as the collection efficiency increases:

$$r = 1 - \eta \frac{2\kappa_{in}}{\kappa + 2i\Delta} \tag{9.1}$$

Where η is the modematching between the cavity mode and the single mode of the input fiber. This makes looking at the reflection a difficult signal to optimize. However, for the fiber cavity used in chapter 7, the mirrors were coated symmetrically, resulting in a critically coupled cavity ($\kappa_{in} = \kappa_{out} = \kappa_{tot}/2$), thus a signal (reflection dip) that always improves with better alignment, making alignment in reflection relatively easy.

This becomes more challenging when considering that this would also mean that the reflection dip of higher-order modes will appear larger than those of the TEM_{00} mode. In order to do proper alignment, we must find a signal that can give a definitive measurement of the mode matching. One signal that comes to mind, that we already work with frequently, is the PDH signal. The PDH error signal is given by:

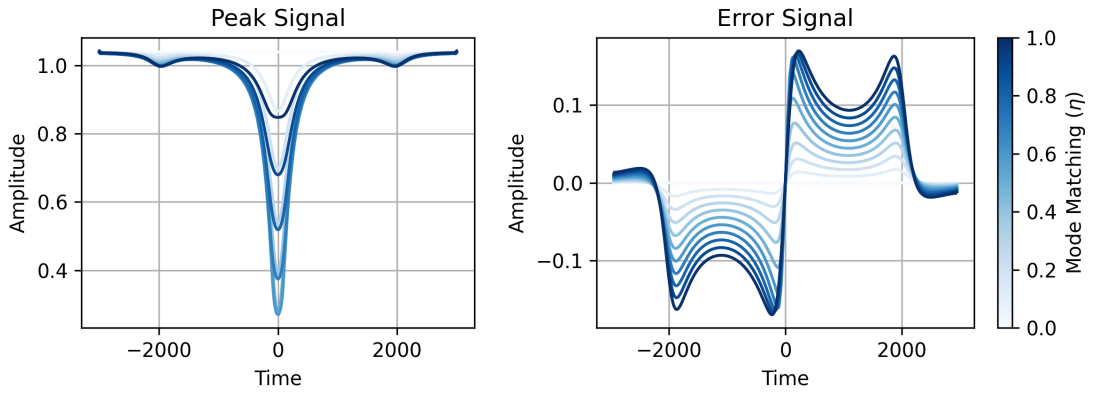


Figure 9.7: (Left) The low passed reflection signal showing sidebands on the laser. This reflection signal is plotted for a variety of mode matching values showing that the depth of the signal increases and then begins to decrease again, making it challenging to determine the mode matching. (Right) the PDH error signal generated when demodulating the laser light from the cavity . This is plotted as a function of mode matching to show that as the mode matching increases this signal increases.

$$E(\Delta) = Re[r(\Delta)r^*(\Delta + \omega_{sb}) - r^*(\Delta)r(\Delta - \omega_{sb})] \tag{9.2}$$

By plotting this as a function of the mode matching for standard cavity parameters, as shown in figure 9.7, we find that the amplitude of the error signal strictly increases as the mode matching gets larger, making this a better signal to optimize.

Another important consideration is trying to find cavity lengths where it is possible to have a dually resonant feature that would allow for simultanious strong coupling on the 780nm transition as well as the 1529nm. In order to ensure this condition we must align and measure our cavities with lasers that are stabilized to the 780nm and 1529nm transitions. We perform this stabilization using DROP (Dual-Resonance Optical Pumping) spectroscopy [125]. When measuring the cavities with all degrees of freedom, allowing for tip, tilt, and position we are able to find lengths where the 1529nm resonance and the 780nm resonances will be near eachother. Further tuning of the tip and tilt can then allow for fine-tuning of the modes to overlap with each other. We attribute this tuning

to misalignment of the mode with respect to the mirrors, which changes the effective penetration depth of the coatings.

The alignment of a fiber cavity device is performed by holding the ends of the fiber and then gluing the end of the fiber into a v-groove mount. We can extend upon this design by replacing one of the mirrors with a microcavity mirror. Alignment and positioning of the micromirrors can be performed using a combination of glue and micromanipulation, but for fine alignment, the method that we have developed is to attach the micromirror to a manipulator with kapton tape or a polydimethylsiloxane (PDMS) stamp. This provides enough clamping to allow us to manipulate the micromirror with even more control than the fiber cavity. The device is then made by gluing the fiber cavity into the groove allowing us to modulate the length of the cavity with the shear plate piezo on the fiber cavity side of the v-groove. Then we used the 5-axis stage to position the micromirror onto the other side of the monolithic v-groove structure. We then performed the same slow UV cure of the micromirror that we performed for the fiber cavity device to glue the micromirror into place. After the glue has fully cured, we can remove the micromirror from the kapton tape or PDMS stamp and find only a small change in the alignment of the cavity.

With this alignment, we are able to measure finesse consistent with losses limited only by the coating and losses of the fiber cavity with negligible loss from alignment or micromirror loss. The device made for this experiment is formed using a QLibri fiber cavity with a dual resonance coating with an AL1300 fiber ablated to a radius of curvature of $193\mu m$ with a transmission loss of 780 nm 60 ppm and a coating of 1550 nm with transmission loss of 160 ppm. The measured finesse. The finesse of this fiber cavity, when measured against a highly reflective ultra-smooth substrate, corresponds to the fiber cavity having a loss corresponding to 285ppm loss at the 1529nm and 84ppm loss at 780nm. After the device is made, we measure a linewidth of 65MHz on the 1529nm resonance and a linewidth of 23MHz on the 780nm resonance. With a cavity length of $80\mu m$ This corresponds to a finesse of 30,000 and 81,000 meaning that there is negligible loss due to the silicon

micromirror in both clipping, scattering, and transmission. Also, corresponding to record cooperativities of $\sim$ 290 at 1529nm and $\sim$ 240 at 780nm on the stretched-state transitions. It is also interesting to note that the cooperativity of the 1530nm transition is even larger than that of the 780nm transition despite finesse being over a factor of 2 lower. If we return to our definitions of cooperativity in chapter 2 it becomes clear that there is a favorable scaling of cooperativity with wavelength due to the density of states. Furthermore, longer wavelengths will have less scattering and transmission loss as described in chapter 8. These considerations make the use of telecom transitions favorable not only for long-distance communication but also for overall strong coupling. An additional direction of interest is access to silicon photonics that cannot be utilized for near-IR or visible light, but are extremely well developed for telecom photonics. The ability to introduce nanophotonic elements in conjunction with an efficient quantum interface offers a number of exciting directions to be explored.

The reflection dip can be used to determine the total collection efficiency of light from the cavity $\eta\frac{\kappa_{in}}{\kappa} \approx .7$. We attribute the loss in collection efficiency to the scattering loss from the fiber cavity. The coating is quoted to have a loss of 160 ppm, however, the measured finesse yields a total loss of 210ppm. These measurements would suggest $\frac{\kappa_{in}}{\kappa} = .76$, producing a mode matching $\eta = .92$ that is consistent with what is expected from this cavity geometry.

The device made in this section utilizes the fabrication techniques developed in chapter 8 to exceed all former photonic interfaces in both cooperativity and total collection efficiency. This device also promises exciting directions towards strong coupling on two different transitions in rubidium allowing for exploration of direct atom telecom photon entanglement.

9.5 Conclusion

In this thesis, we investigated photonic interfaces for neutral-atom quantum computers with the goal of establishing fast, high-fidelity interconnections between quantum processing units. Our work has focused on integrating optical cavities with state-of-the-art neutral-atom quantum processors, yielding several key insights and advancements toward scalable quantum computation and networking. Many of these components have been demonstrated separately, including:

1. **Coherent transport:** Demonstrated coherent transport between a free-space atom array and a photonic interface.

2. **Coherent Rydberg excitation:** Achieved coherent Rydberg excitation in the presence of a photonic interface, which can be utilized to perform high-fidelity two-qubit gates.

3. **Integrated microcavity interface:** Developed a microcavity photonic interface that is more compatible with existing atom array architectures, facilitating fast readout and additional quantum operations.

4. **Advanced optical cavity fabrication:** Established novel techniques for fabricating state-of-the-art optical cavities designed for integration with neutral atom quantum computers.

As described in this chapter, our ongoing efforts are now directed toward developing a system that integrates all these components on a single platform, thereby enabling modular quantum computing.

These contributions represent a significant step toward realizing large-scale, distributed quantum computing. Future work will further refine these photonic interfaces and integrate them with next-generation neutral-atom platforms, ultimately enabling quantum processors that operate over long distances with high fidelity. The methods and insights developed herein are expected to lay the foundation for subsequent advances in scalable quantum technologies.

A

Supplement of Chapter 5

A.1 Cooperativity estimate

The reflectivity amplitude of an atom-cavity system driven at a frequency ω can be calculated as [170]:

$$r = \kappa_{wg}\left(\frac{\kappa}{2} - i\Delta_c + \frac{g^2}{\frac{\gamma}{2} - i\Delta_a}\right)^{-1} - 1 \tag{A.1}$$

where γ is the atomic spontaneous decay rate, g is the single-photon Rabi frequency, $\Delta_a = \omega - \omega_a$ is the atomic detuning, and $\Delta_c = \omega - \omega_c$ is the cavity detuning. The cavity decay rate κ is the sum of decay into the waveguide κ_{wg}, and the decay elsewhere at κ_{sc}. The single-atom cooperativity is defined as $C = 4g^2/(\kappa\gamma)$. The measured reflection spectra correspond to $|r(\omega)|^2$. The entanglement protocol implemented in this work is done with the atom, cavity, and probe photons on resonance, in which case the reflectivity simplifies to

$$R = |r|^2 = \left|1 - \frac{2\kappa_{wg}}{\kappa}\frac{1}{C}\right|^2 \tag{A.2}$$

showing a highly nonlinear dependence on cooperativity. For our measured cooperativity, the atom-cavity system acts as a near-perfect mirror already with a single coupled atom.

The reflection spectrum in Fig. 1B appears asymmetric due to the coupling to $F' = 1$ and $F' = 2$ excited states in addition to the main $F' = 3$ and is fitted using the theoretical model described in [170]. According to this model, the thermal motion of a trapped atom next to the cavity results in a distribution of cooperativities sampled by the atom. Using the independently measured radial trap frequency of $2\pi \times 115$ kHz, axial trap frequency of $2\pi \times 550$ kHz, and final temperature of $T = 70\,\mu$K, we fit for the cooperativity an atom would experience if it were stationary and obtain $C_0 = 47(1)$. The distribution of the cooperativities an individual atom samples has a mean value of 27(1), and a standard deviation of 25(2). We adjust the two trap positions relative to the cavity mode to match their individual mean cooperativities while not overlapping their traps, resulting in a 2.1 μm distance between the atoms centered around the mode maximum. At the mode maximum of the cavity the mean single-atom cooperativity is measured to be 71(4) [170].

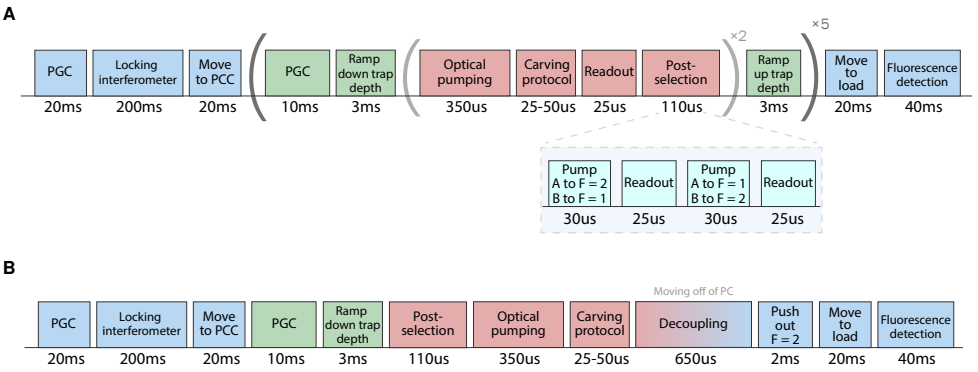


Figure A.1: Experimental sequence. **(A)** Time breakdown of a typical two-atom entanglement sequence between atom-A and atom-B. **(B)** An experimental sequence for the coherent transport of the atomic states that incorporates phases both at the cavity (red and green) and in free space (blue).

A.2 Experimental sequence

The total run time can be separated into periods of experimental run ($\sim$ 85% of the total time), equipment programming, and setup calibration. Confocal tracking of the cavity position accounts for most of the setup calibration and is needed to consistently move atoms to the same position in the cavity mode. This is achieved by imaging the cavity in different focal planes for 2 minutes every 25 minutes and recalibrating the coordinates for each dipole trap. The cavity resonance is tuned by heating the cavity with an off-resonant infrared beam, thus without introducing additional elements or electric fields near the atoms. The lock provides active feedback throughout the experiment but can be frozen or jumped to a different cavity detuning value if needed.

A typical experimental sequence is outlined in Fig. A.1. We load atoms from a magneto-optical trap with the tweezers positioned 50 μm from the cavity [170]. Each experimental trial begins upon detection of atomic fluorescence indicating presence of both atoms. At this position, we perform polarization gradient cooling (PGC) and bring the temperature of the atoms down to 15 μK. The dipole traps are subsequently moved to the cavity with galvanometer mirrors. During transport, the trap transforms from a Gaussian beam into a 1D optical lattice with tight axial confinement due

to its reflection from the PCC. The increase in the trap frequencies results in a higher atomic temperature. To counteract this heating, we apply PGC again while attempting to load the atoms into the first lattice site closest to the PCC. We achieve 80% single atom loading probability with a final temperature of 70 μK, up from a 50% loading probability without cooling during loading. In the case with cooling, we have determined that the remaining 20% consists of approximately 15% loss and 5% higher lattice site loading. These values were characterized by combining a measurement evaluating the two-way survival of an atom, a reflection measurement determining the presence of an atom in the first lattice site immediately after loading, and the survival of an atom moved to free space after confirming its presence in the first lattice site. While at the cavity, the atoms experience a higher heating rate than in free space, reducing their trap lifetime to 180 ms. Photon scattering due to state readout through the cavity causes additional heating, limiting the number of experimental repetitions at the cavity. Furthermore, to reduce light shift-induced inhomogeneities, we reduce the trap depth from $2\pi \times 50$ MHz to $2\pi \times 32$ MHz before preparing the qubit state (see Section 2.1 below), which increases the loss probability. For the experiments where the atoms are kept next to the PCC the entire time (such as in Figs. 1 and 3 in the main text), we re-cool the atoms every two repetitions, and repeat the experiment up to 10 times, as shown in Fig. A.1A. For a typical experiment, two atoms are on average present in 4 of those iterations. For experiments which incorporate phases both at the cavity and in free space (such as in Figs. 2 and 4 in the main text), we do not re-use the same atom pair (Fig. A.1B).

Since the atoms can be heated out of the traps during the experimental attempts, we postselect the experiments based on atomic presence detected via the cavity. As shown in Fig. 1C, the cavity reflection cannot distinguish the number of coupled atoms. By adding individual addressing beams co-propagating with the dipole traps and resonant with the $5S_{1/2} \rightarrow 5P_{1/2}$ transition, we can selectively pump either atom to the coupled state ($F = 2$) while leaving the other in the uncoupled state ($F = 1$). This allows us to perform entanglement experiments where both atoms are loaded with

>99% and to overcome the common problem of probabilistic loading from which all nanophotonic platforms suffer[58,85,120].

Combining the probabilistic loading at the cavity, the two-atom initial trigger rate, and the single photon detection rate for the entanglement experiments gives a Bell pair generation rate of 0.5 events/min. The largest contribution to the low data rate is the number of collected photons from the coupled level during the gate pulse. The total number of collected photons is equal to $N_{collected} = T_{int}\eta N_{sent} = 10^{-2}$, where $\eta = 0.28$ is the total detection efficiency, $N_{sent} = 0.35$ is the number of photons sent to the cavity, and $T_{int} = 0.1$ is the throughput from the interferometer in the undercoupled cavity regime. We discuss the interferometer throughput T_{int} in detail in the section about the entanglement scheme implementation. The total detection efficiency η consists of the single-photon counter (PerkinElmer SPCM-AQR-16-FC) quantum efficiency (0.6), fiber taper coupling efficiency (0.6), and optical path throughput (0.8), and can be readily improved with superconducting nanowire detectors and a higher PCC-fiber coupling efficiency.

A.3 State preparation

To prepare an atom in the qubit state $|F, m_F\rangle = |1, 0\rangle \equiv |0\rangle$ we perform a frequency-selective Raman-assisted optical pumping protocol. The protocol consists of sequentially pumping the atomic population into the $F = 1$ ground state manifold followed by driving $|1, \pm 1\rangle \rightarrow |2, \pm 1\rangle$, leaving the target qubit state dark. The latter is accomplished through driving Raman transitions between the two ground state hyperfine manifolds with a circularly polarized beam. This beam is 100 GHz detuned from the $5S_{1/2} \rightarrow 5P_{1/2}$ transition and contains two frequency components detuned by the hyperfine splitting of 6.8 GHz generated by an amplitude modulator (Jenoptik AM785). It co-propagates with one of the dipole traps through the objective and is large enough to equally address both atoms which are separated by 2.1 μm. We begin the optical pumping cycle

with the atomic population coarsely pumped to $F = 1$, prepared with the MOT beams tuned to the $F = 2 \rightarrow F' = 2$ transition. The Raman beat note is generated from the microwave source (SRS SG 384) operated in the frequency-shift keying (FSK) mode which allows rapid frequency switching to sequentially drive the $|1, \pm 1\rangle \rightarrow |2, \pm 1\rangle$ ground state transitions, thus leaving the final population in $|1, 0\rangle$ (Fig. A.2). Afterwards, we apply the global MOT beams again to pump the population from $F = 2$ back to $F = 1$. We repeat this cycle 40 times, with each Raman pulse taking 2 μs and the MOT pumping pulse taking 2.2 μs. The optical pumping sequence takes 340 μs in total and results in a $0.98(2)$ preparation fidelity in $|1, 0\rangle$. The optical pumping fidelity estimation is extracted via the Rabi oscillation contrast (Fig. 1D), where the $|1, 0\rangle \rightarrow |2, 0\rangle$ transition is driven and the resulting $F = 2$ population is read out with the cavity. This optical pumping fidelity is corrected for the cavity readout infidelity. Our optical pumping scheme overcomes the challenge of maintaining polarization purity near the PCC, where the atom samples near-field polarization variation of an optical field reflected from the nanostructure. This makes other polarization-based optical pumping schemes inapplicable for high-fidelity state preparation. Our scheme, however, relies only on frequency selectivity between the different magnetic sublevels, enabled by a Zeeman shift of 12 MHz ($B = 17$ Gauss).

The state preparation is performed on both atoms simultaneously, while they are strongly coupled to the PCC. The resonant cavity picks up stray light very efficiently, so we pay special attention to shuttering off all the unused light sources. Other than that, we observe no adverse effects of the strong coupling on the preparation fidelity. Since the state preparation scheme uses only optical sources, it can be adapted so that it prepares each atom individually, without disturbing the atoms in the surrounding tweezers, which may be useful for the proposed integration with a free-space atom array.

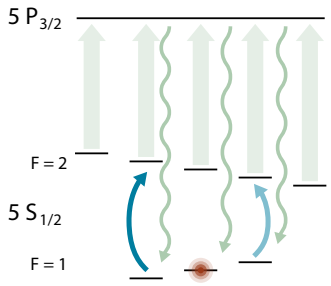


Figure A.2: An illustration of the Raman-assisted state preparation. Cycling between repumping the atom into $F = 1$ (green) and depleting the population in $m_F = \{-1, 1\}$ (blue) leaves the atom in $|1, 0\rangle$.

A.4 Two-atom readout in free space

The experiments described in the main text performed with tweezers positioned away from the PCC rely on the standard push-out state detection. We apply a pulse resonant with the $F = 2 \rightarrow F' = 3$ transition that removes atoms in $F = 2$ and record fluorescence to detect the atoms remaining in $F = 1$. The push-out pulses and fluorescence detection are performed $\sim 1\,\mu$m and $50\,\mu$m away from the PCC respectively. We characterize the readout contrast by preparing the atoms in the $F = \{1, 2\}$ manifolds at the PCC, moving the tweezers away at a trap depth of $2\pi \times 32$ MHz, and performing the push-out readout, obtaining the retention probability of $\sim \{0.80, 0.05\}$. We recalibrate the retention levels every half an hour in parallel with running the entanglement experiments. The finite retention of $F = 2$ is limited by imperfections in the push-out procedure. The retention of $F = 1$ is primarily limited by transport loss ($\sim 15\%$) and loss from collisions with the MOT atoms during the imaging ($\sim 5\%$). The transport loss depends on the trap depth and initial temperature, and for our parameters can be suppressed at a trap depth of $2\pi \times 50$ MHz.

As the finite contrast of the push-out detection limits the single-shot detection fidelity, we infer the population components from the readout probability after collecting meaningful statistics based on the readout calibration described above. In the case of two-atom experiments, the probabilities

of retention $\mathcal{R}$ are given by

$$\mathcal{R} = \begin{pmatrix} R_{00} \\ R_{01} \\ R_{10} \\ R_{11} \end{pmatrix} = \mathcal{K} \begin{pmatrix} P_{00} \\ P_{01} \\ P_{10} \\ P_{11} \end{pmatrix}, \tag{A.3}$$

where R_{ij} denotes the results corresponding to the four possibilities of retention of the two atoms, P_{ij} are the populations in the corresponding two-atom states, and $\mathcal{K}$ is a correction matrix given by

$$\mathcal{K} = \mathcal{K}_{\mathcal{A}} \otimes \mathcal{K}_{\mathcal{B}} = \begin{pmatrix} h_A h_B & h_A(1-h_B) & (1-h_A)h_B & (1-h_A)(1-h_B) \\ h_A l_B & h_A(1-l_B) & (1-h_A)l_B & (1-h_A)(1-l_B) \\ l_A h_B & l_A(1-h_B) & (1-l_A)h_B & (1-l_A)(1-h_B) \\ l_A l_B & l_A(1-l_B) & (1-l_A)l_B & (1-l_A)(1-l_B) \end{pmatrix}^{\mathsf{T}} \tag{A.4}$$

where $\{h_i, l_i\}$ denote the retention probabilities of atom i prepared in $F = \{1, 2\}$. For a generic two-atom measurement, we multiply the inverse of the correction matrix with the measurement result to obtain the populations [13].

A.5 Readout through the cavity

The measurements in Fig. 1 and 3 in the main text were done by reading the atomic states using the cavity reflection. As shown in the Fig. 1C, readout through the PCC distinguishes the state $|00\rangle$ from the rest of the states in the two qubit manifold. By integrating for 25 μs and choosing a photon count threshold, we perform a single shot readout which distinguishes $|00\rangle$ from the other states with the fidelities reported in Table A.1. The confidence intervals for the fidelities were ob-

State	Mean	Confidence interval
$\|00\rangle$	0.956	[0.936, 0.975]
$\|01\rangle$	0.949	[0.922, 0.964]
$\|10\rangle$	0.948	[0.921, 0.961]
$\|11\rangle$	0.991	[0.987, 0.996]

Table A.1: Readout fidelities of different two-atom states

tained by changing the threshold by ± 1 photon.

A.6 Fidelity extraction from parity

To characterize the state after the carving protocol and its overlap with $|\Phi^+\rangle$, we perform two sets of measurements. In the first we measure the populations P_{00} and P_{11} and in the second we measure the parity oscillations of the state $|\Phi^+\rangle$. The populations in $|00\rangle$ and $|11\rangle$ are extracted by reading out the states without and with a global π pulse applied before the cavity reflection detection respectively. Using the normalization condition $\sum P_{ij} = 1$, we also extract the population in the odd states, $P_{odd} = P_{01} + P_{10} = 1 - (P_{00} + P_{11})$. We can therefore measure the parity of the state, defined as

$$\Pi \equiv P_{00} - P_{01} - P_{10} + P_{11} = 2(P_{00} + P_{11}) - 1 \tag{A.5}$$

We calculate the fidelity of preparing the Bell state $|\Phi^+\rangle$ as $\mathcal{F} = \langle\Phi^+|\rho|\Phi^+\rangle = \frac{1}{2}\left(\rho_{00,00} + \rho_{11,11} + \rho_{00,11} + \rho_{11,00}\right)$ by measuring the populations $\{\rho_{00,00}, \rho_{11,11}\}$ and the coherences $\{\rho_{11,00} = \rho^*_{00,11}\}$. The total population is directly measured from the cavity readout. The coherence is recorded after a $\pi/2$ rotation over a variable axis φ [167,204] and is extracted from the amplitude of the parity oscillation as

$$\Pi(\varphi) = 2\,\mathrm{Re}(\rho_{10,01}) + 2\,\mathrm{Im}(\rho_{11,00})\sin(2\varphi) + 2\,\mathrm{Re}(\rho_{11,00})\cos(2\varphi) \tag{A.6}$$

Combining these two measurements gives the reported fidelity of $\mathcal{F} = 0.72(3)$. Note that the data in Fig. 3 and the reported entanglement fidelity at the PCC are not corrected for the finite readout fidelity.

The fidelity measurement after the transport is done in an analogous way. All four populations P_{ij} are extracted from the free space fluorescence detection. The phase of the coherence term $2\varphi_0 = \arg(\rho_{11,00})$ is calibrated using each individual atom's Ramsey fringes, after which the resulting two-atom state coherence is extracted from the difference in the parity measurements $\Pi(\pi/2) - \Pi(0)$ between the bases {parallel, orthogonal} to φ_0, labeled $\{XX, YY\}$ (Fig. 4B). Combining this measurement with the populations (ZZ basis) gives the measured fidelity of $\mathcal{F} = 0.65(5)$.

A.7 Concurrence bound

Concurrence is a basis-independent measure of how entangled a state is and is therefore a more general entanglement measure than the fidelity of preparing a certain state. In practice, however, measuring the concurrence requires knowledge of the full density matrix of the prepared state. For this reason, a lower bound is often used to check if a state is entangled[208]. A concurrence of $C > 0$ proves entanglement.

Given the amplitude of the parity oscillations we obtain a lower bound on the concurrence, following[128]. In the ZZ basis, we primarily prepare $|\Phi^+\rangle = (|00\rangle + |11\rangle)/\sqrt{2}$. The lower bound for the concurrence is then

$$\mathcal{C} \geq 2(|\rho_{00,11}| - \sqrt{\rho_{01,01}\rho_{10,10}}) \tag{A.7}$$

Using the Eqn. A.7, we directly extract concurrence after moving of $\mathcal{C} \geq 0.35(11)$. At the cavity we only measure the sum of the two populations $P_{01} + P_{10} = 0.22 \pm 0.03$. To get a lower bound, we want the maximum of their product, which occurs when they are equal $P_{01} = P_{10}$. Using this, we extract $\mathcal{C} \geq 0.46(5)$.

A.8 Entanglement scheme using the interferometer

The entanglement fidelity of the coherent photon reflection protocol is determined by the reflection amplitudes of different two-atom basis states. In turn, the reflection amplitudes determine the optimal initial rotation angle θ. The four qubit states have reflectivities given by Eqn. A.2, which for our parameters are $R_{00} = 0.40$, $R_{01} = R_{10} = 0.94$, $R_{11} = 0.97$. Since the entanglement protocol relies on distinguishing $|01\rangle$, $|10\rangle$ and $|11\rangle$ from $|00\rangle$ as well as possible, we add an interferometer in the detection path to eliminate the uncoupled reflectivity R_{00}. The cancellation is achieved using a Mach-Zehnder interferometer with the relative phase tuned for destructive interference of the uncoupled reflectivity (Fig. A.3). In this way, any cavity with a finite reflectivity on resonance can be used to implement entanglement via photon carving. The interferometer can be switched on and off during an experiment by changing the AOM driving amplitudes to allow for both the single photon gating (interferometer on) and atomic state detection (interferometer off).

In the case of a perfect interferometer, $R_{00} \to 0$ and would yield a fidelity of $\mathcal{F} = 1/(1 + \tan(\theta/2))^2$, which in principle can be $\mathcal{F} \to 1$ with an infinitesimaly small angle θ. The contrast of our interferometer is limited by the noise on the cavity lock to $(R_{max} - R_{min})/(R_{max} + R_{min}) = 0.96$. This gives finite reflectivities to all the states, such that after a postselection on the reflected photon we are left with the components of both states $|00\rangle$ and $|11\rangle$ as error terms. For a given interferometer contrast, there is an optimal initial rotation angle that balances and minimizes the infidelities. The dependence of the maximal Bell state fidelity on the interferometer contrast and the initial

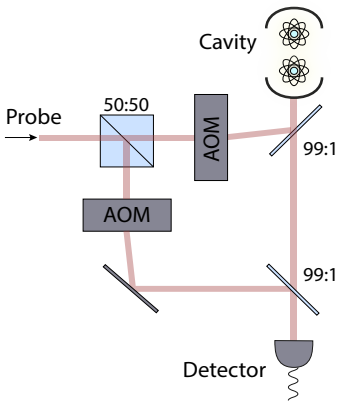


Figure A.3: Sketch of the interferometer in the detection path used to improve the reflection contrast between a cavity with and without coupled atoms.

angle is shown in Fig. A.4 (left panel). Bell state fidelity is defined as the overlap between $|\Psi^+\rangle$ and the state created right after the photon reflection. For our interferometer contrast, we choose the initial angle of 0.3π and expect the maximal fidelity of 0.76. Given an initial angle and interferometer contrast, one can calculate the probability of having a photon reflected from the atom-cavity system, which for our parameters is $T_{int} = 0.1$.

The protocol can be improved using a cavity with a smaller R_{00}, given that the maximal fidelity is intrinsically bounded by this value. Note that for our cavity linewidth the uncoupled reflectivity R_{00} is equivalent to the empty cavity reflectivity. Fig. A.4 (right panel) shows the dependence of the maximal fidelity and success probability on R_{00}. Assuming that the interferometer contrast stays the same, the fidelity can be improved to 0.9 by reducing R_{00} from 0.4 (our parameter, black dot in the figure) to 0.1. The tradeoff between the fidelity and the success probability is demonstrated by the opposite slopes of the solid and dotted curves in Fig. A.4.

Finally, there are other avenues for improving the carving protocol beyond improving the interferometer contrast. For example, reflecting two gate photons separated by the coherent rotations could achieve a higher entanglement fidelity at the expense of a lower success rate, as demonstrated in [204]. The success probability of the protocol can be increased by using a single photon source in-

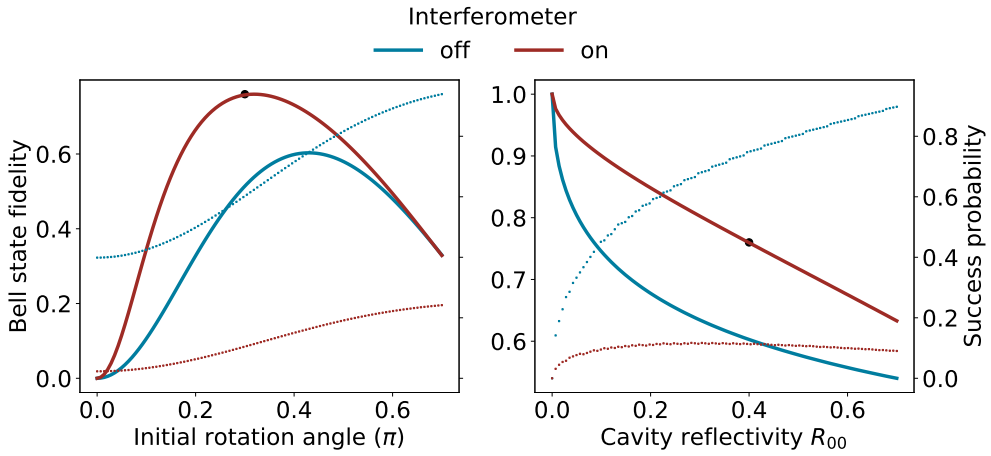


Figure A.4: Parameters that determine the entanglement fidelity. (Left) Dependence of the maximal Bell state fidelity (solid lines, left y axis) and protocol success probability (dotted lines, right y axis) on the initial angle and interferometer contrast. Not using the interferometer would limit the maximal fidelity to ~ 0.6. With our measured interferometer contrast of 0.96, the fidelity is limited to 0.76 (black dot). (Right) Keeping the interferometer contrast the same, the protocol maximal fidelity can be improved by using a cavity with a smaller reflectivity R_{00}.

stead of an attenuated coherent pulse. In the case of an attenuated coherent pulse, the atomic coherence decays by a factor of $e^{-\lambda N_{sent}}$, where $\lambda = 4(\kappa_{wg}/\kappa)C/(C+1)^2$ is the spontaneous emission probability of a strongly coupled atom [185]. We optimized N_{sent} by measuring the retained coherence of single atoms after projecting them with coherent gate pulses and chose $N_{sent} = 0.35$ so that the spontaneous emission effect is negligible.

A.9 Theoretical models for the entanglement protocol

A.9.1 Coherent model

Ideally, the carving protocol for entanglement generation is fully coherent and results in a pure state. Here we model the effect of a coherent photon reflection and post-selection on detection. The model assumes that the photons reflected from different two-atom states differ by the reflection probability but are otherwise completely indistinguishable. Under this assumption, throughout the

experiment the two atoms are in pure states, which are different superpositions of the Bell triplet states $|\Phi^{\pm}\rangle$ and $|\Psi^{+}\rangle$. The target entangled state from the main text is $|\Phi^{+}\rangle$, and we define the entanglement fidelity as the overlap $\mathcal{F} = \langle\Phi^{+}|\rho\,|\Phi^{+}\rangle$.

We define the phase of our rotations such that a native rotation is over the axis x, so that after a rotation by angle θ we obtain $R_{0,\theta}\,|00\rangle = |\Psi_{\theta}\rangle$:

$$\begin{aligned}|\Psi_{\theta}\rangle = &\cos^2\left(\frac{\theta}{2}\right)|00\rangle - \sin^2\left(\frac{\theta}{2}\right)|11\rangle \\ &- i\sin\left(\frac{\theta}{2}\right)\cos\left(\frac{\theta}{2}\right)(|01\rangle + |10\rangle)\end{aligned} \tag{A.8}$$

After preparing the state $|\Psi_{\theta}\rangle$, we reflect a photon and post-select on its detection. Given the reflection amplitudes for each state (r_{00}, r_{01}, r_{10}, r_{11}), we are left with

$$\begin{aligned}|\Psi^{cond}\rangle = &\frac{1}{N}(r_{00}\cos^2\left(\frac{\theta}{2}\right)|00\rangle - r_{11}\sin^2\left(\frac{\theta}{2}\right)|11\rangle \\ &- i\,r_{01}\sin\left(\frac{\theta}{2}\right)\cos\left(\frac{\theta}{2}\right)(|01\rangle + |10\rangle))\end{aligned} \tag{A.9}$$

where N is a normalization factor. If we relabel different state amplitudes as $\varepsilon_0 = r_{00}\cos^2\left(\frac{\theta}{2}\right)/N$, $\varepsilon_1 = r_{11}\sin^2\left(\frac{\theta}{2}\right)/N$, and $f = r_{01}\sqrt{2}\sin\left(\frac{\theta}{2}\right)\cos\left(\frac{\theta}{2}\right)/N$, we can rewrite the state $|\Psi^{cond}\rangle$ as

$$\begin{aligned}|\Psi^{cond}\rangle &= \varepsilon_0\,|00\rangle - \varepsilon_1\,|11\rangle - if|\Psi^{+}\rangle \\ &= \left(\frac{\varepsilon_0 - \varepsilon_1}{\sqrt{2}}\right)|\Phi^{+}\rangle + \left(\frac{\varepsilon_0 + \varepsilon_1}{\sqrt{2}}\right)|\Phi^{-}\rangle - if|\Psi^{+}\rangle\end{aligned} \tag{A.10}$$

Before analyzing the state, we apply $R_{0,\pi/2}$ and get the final state in the ZZ basis

$$\begin{aligned}|\Psi_{zz}\rangle &= R_{0,\pi/2}\otimes R_{0,\pi/2}\,|\Psi^{cond}\rangle \\ &= -i\left(\frac{\varepsilon_0 - \varepsilon_1}{\sqrt{2}}\right)|\Psi^{+}\rangle + \left(\frac{\varepsilon_0 + \varepsilon_1}{\sqrt{2}}\right)|\Phi^{-}\rangle - f|\Phi^{+}\rangle\end{aligned} \tag{A.11}$$

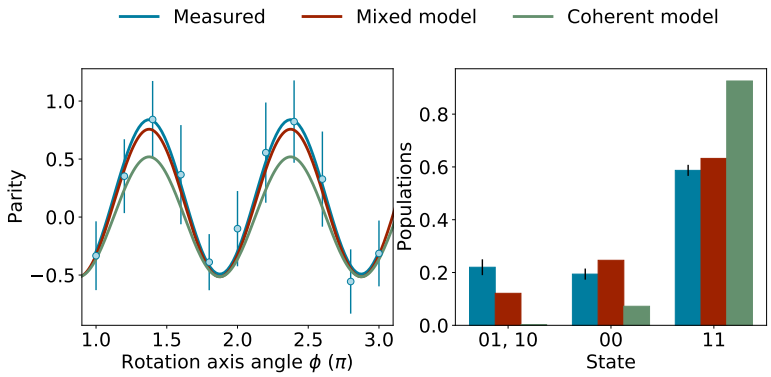


Figure A.5: Comparison of the experimental measurements (blue), mixed model predictions (red), and coherent model predictions (green) for the parity measurement (left panel) and the ZZ basis populations (right panel).

Based on Eqn. A.11, the entanglement fidelity is given by $\mathcal{F} = |f|^2$. The idea of the "cavity carving" protocol is to maximize the amplitude f. This can be done by 1) having ($r_{00} \ll r_{01} \approx r_{11}$), which would result in a small ε_0, and 2) using a small initial rotation angle θ, which would result in a small ε_1.

From Eqn. A.11 we can determine the population in the four basis states:

$$P_{00} = \frac{1}{2}\left|\frac{\varepsilon_0 + \varepsilon_1}{\sqrt{2}} - f\right|^2 \tag{A.12}$$

$$P_{11} = \frac{1}{2}\left|\frac{\varepsilon_0 + \varepsilon_1}{\sqrt{2}} + f\right|^2 \tag{A.13}$$

$$P_{01} = P_{10} = \frac{1}{4}\left|\varepsilon_0 - \varepsilon_1\right|^2 \tag{A.14}$$

Note that finite values of ε_0 and ε_1 cause the populations in $|00\rangle$ and $|11\rangle$ to be unbalanced (as seen in Fig. 3B).

A.9.2 Mixed model

The coherent model above assumes that the post-selection on the reflected photon leaves the system in a pure state. However, spontaneous scattering and temporal mismatch can both reveal the which-path information of photons reflected from $|00\rangle$. When the photons reflected from the uncoupled and coupled states are distinguishable, the system is left in a mixed state. Spontaneous scattering from the gate photons in the coherent pulses containing more than one photon leave the atom in a different hyperfine level within the $F = 2$ manifold. In addition, while the response from the state $|0\rangle$ is instantaneous, the bandwidth of the response from the state $|1\rangle$ is $C\gamma$ and may lead to a temporal mismatch. The atom samples a distribution of cooperativities due to thermal motion, which for $C \sim 1$ results in a 26 ns delay in the atomic response. This is longer than the pulse duration of 20 ns (FWHM) and would make the photons distinguishable.

We can model distinguishability by assuming that a photon reflection corresponds to the following projections:

$$M_u = |00\rangle \langle 00| \tag{A.15}$$

$$M_c = -M_u \tag{A.16}$$

If the probability that a detected photon was reflected from $|00\rangle$ is p_u and from the coupled manifold is $p_c = 1 - p_u$, post-selection on a photon detection projects the system into

$$\rho' = p_u M_u \rho M_u^\dagger + p_c M_c \rho M_c^\dagger \tag{A.17}$$

where ρ is the density matrix of the state before reflection, $\rho = |\Psi_\theta\rangle \langle \Psi_\theta|$ (Eqn. A.8). The prob-

ability p_u can be calculated as the ratio of effective reflectivities of the uncoupled and coupled states (assuming that $R_{10} \approx R_{11}$):

$$p_u = \frac{R_{00}}{R_{00} + R_{01}} \tag{A.18}$$

When using an interferometer, R_{00} and R_{01} would correspond to reflectivities with the interferometer engaged. For our measured interferometer contrast of 0.96, $p_u = 0.087$.

The mixed model differs from the coherent model in that the reflection post-selection destroys the initial coherences between $|00\rangle$ and the coupled states: $\rho_{00,01}$,$\rho_{00,10}$,$\rho_{00,11}$. When the state is further rotated and analyzed, such as in the populations and parity oscillation measurement, this will result in different theoretical predictions. However, we note that the entanglement fidelity prediction of the two models is identical, since the entanglement relies on the reflection preserving the initial coherence between $|01\rangle$ and $|10\rangle$ ($\rho_{01,10}$) after the gate pulse, which happens in both models. We confirm this statement numerically, by calculating the overlap with $|\Phi^+\rangle$ with different models, and arriving at the same values.

Given that both the coherent and the mixed model give predictions for the state populations and measured parity, we here compare them with the measured data. Figure A.5 shows the experimental measurement (blue), predictions from the coherent model (green), and mixed model (red) for the parity oscillation (left panel) and ZZ basis populations (right panel). The mixed model agrees better with the measurements in both datasets.

A.10 Coherence properties of atoms next to the photonic crystal cavity

The qubit relaxation time T_1 in our system is limited by contributions of various scattering processes. The tweezer depth next to the PCC (32 MHz) would limit T_1 to 60 ms. However, with

the cavity tuned into resonance with the atom, we observe additional scattering that significantly reduces T_1 to 1.2 ms. With the cavity tuned 14κ away from the atomic resonance, we recover the expected T_1. For the experiments that require long coherence, such as for atomic state transport, we detune the cavity right after the gate by jumping the cavity lock in sequence. The source of the resonant scattering remains under investigation.

Magnetic-field-insensitive qubit encoding minimizes the influence from vector light shifts, a near-field effect intrinsic to tightly-focused light and further exacerbated by the standing wave potential next to the PCC [194]. The spin dephasing is characterized by the transverse decay time T_2 and is primarily limited by thermal motion leading to varying differential AC Stark shifts. This dephasing can be decomposed into the reversible (T_2^*) and the irreversible (T_2') component as $1/T_2 = 1/T_2' + 1/T_2^*$. Shown in Fig. A.6A is a Ramsey decay measurement $(\pi/2 - \tau - \pi/2)$ of an atom next to the PCC, giving a $T_2 = 0.35(4)$ ms. As discussed in [92,154], the main source of reversible dephasing in optical dipole traps is atomic motion coupled with a finite differential light shift. If we assume that the energy distribution of atoms in the trap obeys the Boltzmann distribution with temperature T, the reversible dephasing time T_2^* can be expressed as $T_2^* = 2\hbar/(\zeta k_B T)$ [92]. The factor ζ depends on the dipole trap wavelength and the atomic energy spectrum. We experimentally confirm the linear dependence of $1/T_2$ on the temperature and measure $\zeta = 5.4 \times 10^{-4}$ (Fig. A.6B). The dephasing induced by a constant temperature can be reversed with a spin echo sequence.

Using the spin echo pulse sequence $(\pi/2 - \tau - \pi - \tau - \pi/2)$, we measure $T_2' = 9.7(8)$ ms in free-space and 2.1(1) ms at the cavity. The difference cannot be explained with the sources common to the free space and the PCC such as fluctuating magnetic fields, microwave power and pulse duration, and we therefore attribute it to extra heating at the cavity. Any heating process would translate to irreversible dephasing, in the same way constant temperature causes reversible dephasing. At the cavity, we measure a lifetime of 180(7) ms at a trap depth of 2.7 mK (Fig. A.7), giving a heating rate of 14.6 mK/s, an order of magnitude higher than in free space. The irreversible dephasing time

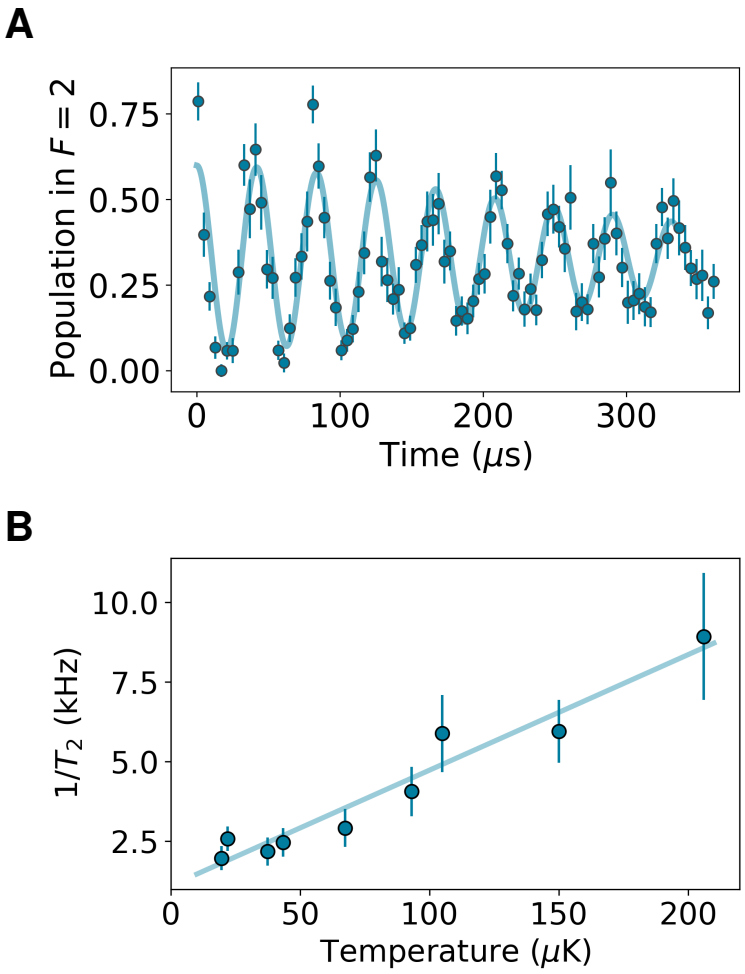


Figure A.6: Temperature-limited Ramsey decay. **(A)** Ramsey decay of an atom next to the PCC fitted using the model described in [92], giving $T_2 = 0.35(4)$ ms. **(B)** Linear dependence of the Ramsey dephasing rate on the temperature.

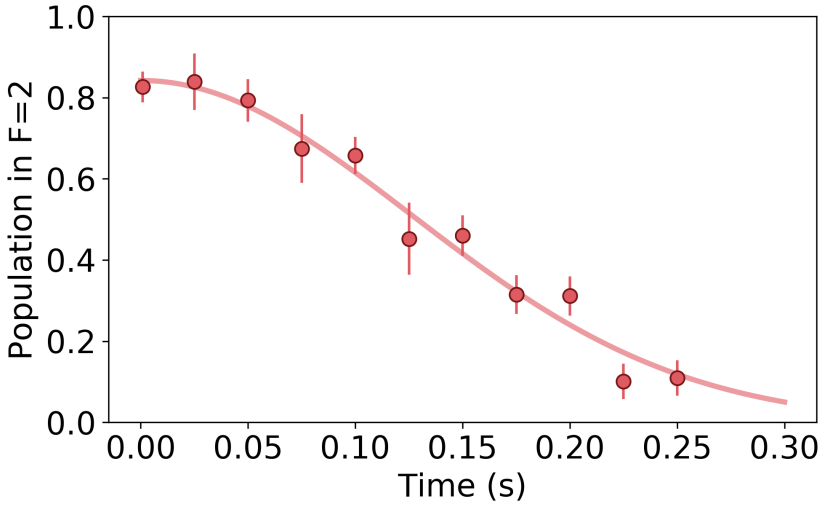


Figure A.7: Measured lifetime of $180(7)$ ms at a trap depth of 2.7 mK next to the PCC.

depends on the heating rate as $T_2' \propto (dT/dt)^{-1/2}$ [92].

Two main sources of heating we consider are trap potential fluctuations and atomic recoil due to scattering. To estimate the heating rate due to atomic recoil, we use the scattering rate given by $1/T_1$ and obtain $dT/dt = 4.1 \cdot 10^{-3}$ mK/s (cavity out of lock) and 0.15 mK/s (cavity in lock). Both estimates differ by orders of magnitude from the lifetime-deduced heating rate. Therefore, we speculate that the contributions to additional heating near the nanophotonic cavity include trap fluctuations due to mechanical vibrations of the nanostructure [68] and higher sensitivity of the axial trap frequency to the fast intensity noise [172].

A.11 Phase accumulation while moving

A.11.1 Dipole potential for different trap configurations

The potential energy of a two-level system in a detuned optical field in the rotating-wave approximation is given by:

$$U(r) = \frac{3\pi c^2 \gamma}{2\omega_0^3 \Delta} I(r)$$

where Δ is the field detuning, γ the spontaneous emission rate, and $I(r)$ the intensity of the field[60]. When the field is red-detuned ($\Delta < 0$), the atoms are attracted to the maximum of the field intensity $I(r)$. Based on the different configurations of the laser beams, $I(r)$ can have different spatial dependence, resulting in different effective trap frequencies. In our experiment, we change the trapping configuration from a focused Gaussian beam to a standing wave. Here we will explore how the potential changes for those two configurations.

A focused Gaussian beam creates a potential

$$U(r,z) = U_0 \exp \frac{-2r^2}{w(z)^2} \tag{A.19}$$

where $w(z) = w_0\sqrt{1+\frac{z^2}{z_r^2}}$, w_0 is the beam waist, and $z_r = \pi w_0^2/\lambda$ is the Rayleigh range. Expanding this expression around $r, z = 0$ gives

$$U(r,z) \approx -U_0 \left(1 - 2\left(\frac{r}{w_0}\right)^2 - \left(\frac{z}{z_r}\right)^2\right) \tag{A.20}$$

which can be rewritten as a harmonic potential in the radial and axial direction

$$U(r,z) \approx -U_0 + \frac{1}{2}m\omega_r^2 r^2 + \frac{1}{2}m\omega_z^2 \tag{A.21}$$

with the oscillator frequencies $\omega_r = \sqrt{\frac{4U_0}{mw_0^2}}$ and $\omega_z = \sqrt{\frac{2U_0}{mz_r^2}}$. When the atoms are near the nanophotonic cavity, part of the tweezer beam is reflected back and interferes with the forward-propagating beam. The tweezer then forms a standing wave potential of the form

$$U(r,z)' = -\alpha U_0 \cos(kz)^2 \left(1 - 2\left(\frac{r}{w_0}\right)^2 - \left(\frac{z}{z_r}\right)^2\right) \tag{A.22}$$

where α is the interference contrast (measured to be $\alpha = 1.2$ in our experiment), and $k = 2\pi/\lambda_0$. Expanding this expression and rewriting it as a harmonic potential gives the oscillator frequencies $\omega_r' = \sqrt{\frac{4\alpha U_0}{mw_0^2}}$ and $\omega_z' = \sqrt{\frac{2\alpha U_0}{mz_\lambda^2}}$, where $z_\lambda = \lambda_0/(2\pi)$. Therefore, moving from the focused beam to a standing wave changes the oscillator frequencies from $\omega_r \to \omega_r'$ and $\omega_z \to \omega_z'$.

A.11.2 Differential light shift during the transport

The main contribution to the shift of the qubit resonance for the magnetic-field-insensitive states is the differential light shift. For a given maximal light shift U_0, the differential light shift δ_0 is given by

$$\hbar\delta_0 = \zeta(-U_0 + \overline{E_p}) \tag{A.23}$$

where $\zeta \propto \omega_{HFS}/\Delta$ ($\zeta = 5.4 \times 10^{-4}$ for our system), and $\overline{E_p}$ is the average potential energy of the atom in the trap. From the virial theorem, $\overline{E_p} = \overline{E}/2$. For the three-dimensional harmonic oscillator, the average total energy is given by

$$\begin{aligned}\overline{E} &= \sum_{i=x,y,z} \hbar\omega_i \left(\frac{1}{2} + \frac{1}{\exp\frac{\hbar\omega_i}{k_b T} - 1}\right) \\ &= \sum_{i=x,y,z} \hbar\omega_i \left(\frac{1}{2} + n_i\right)\end{aligned} \tag{A.24}$$

where T is the temperature of the atom, and n_i is the average occupation number in the direction i. Combining the Eqn. A.23 and A.24, we arrive at the expression for the differential light shift of a moving atom:

$$\delta_0(t) = -\zeta\frac{U_0(t)}{\hbar} + \frac{\zeta}{2}\left(2\omega_r(t)\left(\frac{1}{2} + n_r(t)\right) + \omega_z(t)\left(\frac{1}{2} + n_z(t)\right)\right) \tag{A.25}$$

As seen in the previous section, $U_0(t)$, $\omega_r(t)$ and $\omega_z(t)$ necessarily vary in time as the trap potential changes. The average occupation number $n_i(t)$ depends on whether the atom makes motional state transitions during the transport. If the trap deformation is adiabatic, the atom does not change the motional energy level and $n_i = const$. This is equivalent to $\omega(t)/T(t) = const$, which would imply an increase in temperature as the trap frequency increases (adiabatic heating) and vice-versa (adiabatic cooling)[198]. The entire time dependence of $\delta_0(t)$ would then be in $U_0(t)$, $\omega_r(t)$ and $\omega_z(t)$. If the atom does make motional state transitions because of the noise in the trapping potential, $\delta_0(t)$ will stochastically vary and cause qubit dephasing.

A.11.3 Phase accumulation and cancellation

Given that δ_0 varies in time as shown in the Eqn. A.25, a moving atom will acquire a phase shift $\varphi(T) = \int_0^T \delta_0(t)dt$. If the detuning ramp during transport is the same for every atom, i.e. if the acquired phase is constant, it can be corrected for with a local σ_z gate.

We apply a voltage ramp $V(t) \propto \tanh(t)$ to the scanning mirrors to move the atoms. If the atoms were to follow the mirror position instantaneously, the detuning ramp would have the shape as plotted in Fig. A.8. The ramp is symmetric with respect to $T/2$. An even number of π pulses in a Carr-Purcell (CP: $\pi/2 - (\tau - \pi - \tau)^N - \pi/2$) sequence would cancel out the acquired phase.

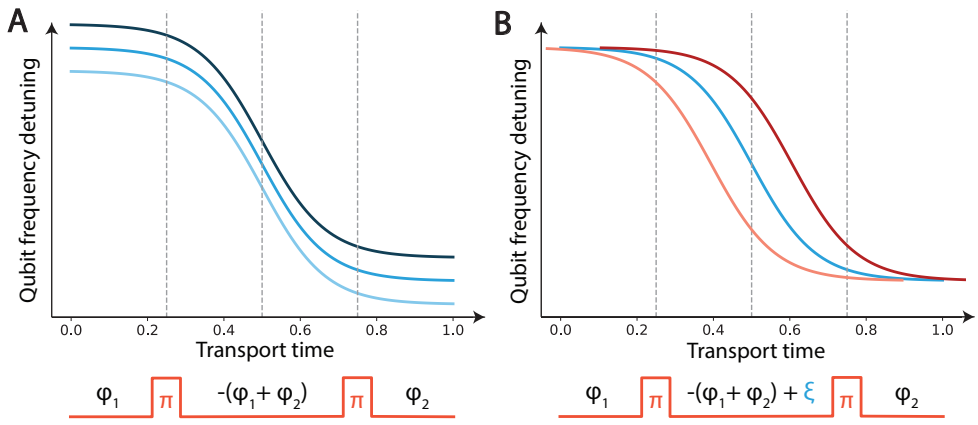


Figure A.8: Sketches of how variations in detuning can cause dephasing. **(A)** Variations in the overall qubit frequency offset (vertical variations), caused by atom's finite temperature, can be echoed out with an even number of CP pulses. **(B)** Variations in the moving trajectory (horizontal variations), caused by trap pointing instabilities, cannot be echoed out exactly and contribute to extra dephasing.

The statistical variations in the total energy in one experimental run that come from a finite temperature would result in a variation in the offset of the detuning ramp (Fig A.8A), which is the same as the variation that limits the free precession time in a Ramsey sequence. Analogously to echoing out the phase with one spin echo in a static case, an even number of spin echo pulses would echo it out in the symmetrically changing case. Importantly, this configuration would echo out the phase variation due to the finite temperature, thus reverting qubit dephasing. If the trap pointing varies in time such that the detuning symmetry axis varies (Fig A.8B), the symmetric echo would not correct for the temperature-induced variations, and the moving atoms would have an extra dephasing channel. The pointing variations are minimized by tracking the cavity position periodically. To move the traps, we use different scanning mirrors (trap A: Cambridge Technology 8310K, trap B: Physik Instrumente S-330.4SL). We have observed differences in coherence properties between the two traps after transport, which we attribute to larger fluctuations in trap A.

In order to distribute the pulses symmetrically, we map out the detuning profile during the transport. We probe each of the atoms by starting in the state $|0\rangle$ and applying a detuned π pulse at a

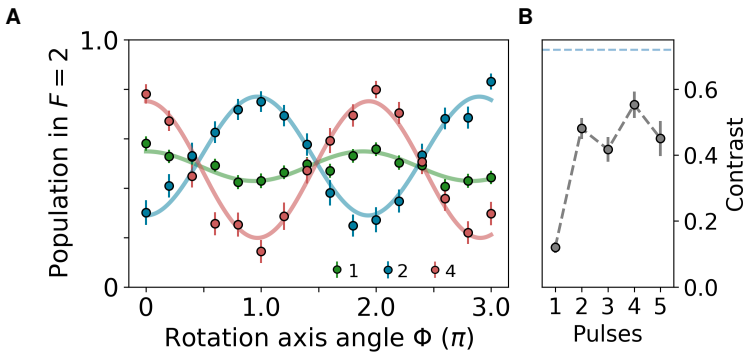


Figure A.9: Optimizing the number of pulses in the CP sequence for a moving atom. **(A)** CP sequences of $N = (1, 2, 4)$ pulses that begin with an atom at the cavity and end with an atom in free space. Decoupling pulses are applied in parallel with the transport. **(B)** Fitted contrast of the CP sequences versus the number of CP pulses.

variable point during the transport. The population transfer to $|1\rangle$ will depend on the qubit frequency at the time of the π pulse according to the Rabi lineshape. We measure and account for the delay in response for each galvanometer mirror and calibrate their input voltage to symmetrize the ramp with respect to the moving time, as shown in Fig. 2B. Furthermore, the bandwidth of the trap B mirror limits the step response time to $\sim$ 650 μs, and we program the ramp of trap A to match. This is the time over which the CP sequence is applied as described in the main text.

We optimize the number of pulses in the CP sequence by preparing an atom in a superposition state at the PCC, moving it away while applying CP, and studying the remaining coherence contrast after a variable number of pulses, as shown in Fig. A.9. The even number of pulses performs better than the odd one, as expected, and we find the optimal number to be four for our system parameters. Higher frequency noise components could be addressed by having faster π pulses (in our system $T_\pi = 20\,\mu$s). In the main text, we report on the retained coherence of the trap B after moving to be 0.88(5) (Fig. 2C). For a stationary atom, $N = 4$ CP sequence gives $T_2' = 4.9(4)$ ms (17(2) ms) for atoms at (away from) the PCC. If we assume that half of the move time (325 μs) is spent at the cavity and half in free space, we expect to retain 0.92 of the coherence for a T_2'-limited

transport, which is within the uncertainty of our measured result. From here we deduce that the used decoupling sequence is effective at canceling out the moving-induced dephasing.

A.12 Modeling losses upon loading into the cavity near-field

Integration of our platform with a free space atom array would require low losses upon loading into the cavity near-field. Here, we theoretically model what those losses depend on and derive requirements for lossless loading. We study the effects of transferring the atom from the tweezer potential to the optical lattice potential in the near-field of the cavity, resulting from the reflection of the tweezer off of the cavity.

We numerically study classical trajectories of a single particle in an evolving gaussian potential and observe that an adiabatic increase in the trap frequency introduces heating that ultimately leads to losses, the reverse process of adiabatic cooling (see Section 8.1) [198,2]. The thermal loss fraction can be determined by averaging trajectories over the phase space weighted by the Boltzmann factor. As there are two relevant axes that transform upon tweezer arrival $(\omega_r, \omega_z) \rightarrow (\omega_r', \omega_z')$ [193], we generate the loss fraction as a function of the temperature for the principal axes separately and deduce the survival from the joint probability. Our model assumes separability between the two principal axes, continuity of the trap deformation, and no extra heating caused by the trap rotation. The losses as functions of temperature are generated with parameters extracted from independent trap frequency measurements.

Figure A.10 shows the theoretical predictions for the loading survival probability as a function of the initial atomic temperature and trap depth. Our survival measurements without cooling at different initial temperatures and a trap depth $U_0 = k_B \times 1.6$ mK are marked with yellow circles. The initial temperature is varied by changing the free space PGC parameters, and the temperature values are extracted from drop-recapture measurements. Our observations follow the same trend as

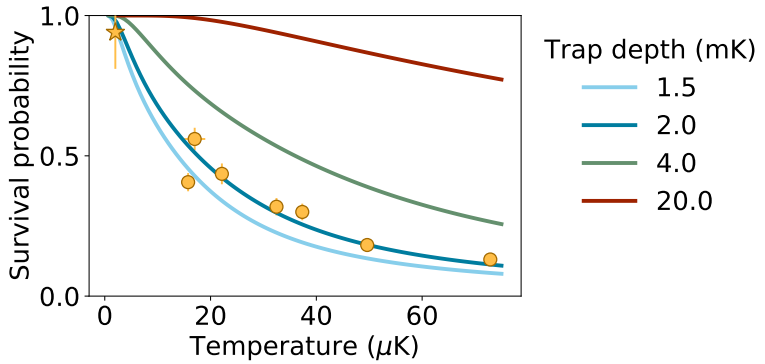


Figure A.10: The effects of temperature and trap depth on the survival probability of an atom loading into the cavity near-field. The theoretical curves are generated by averaging over classical trajectories weighted by the Boltzmann factor with no free parameters. Our experimental observations (yellow circles) are taken at a trap depth of 1.6 mK. Previous work on our platform with Raman sideband cooling before transport observed $0.94(6)$ survival probability (yellow star)[193].

the theoretical model.

Our numerical results suggest several ways in which the arrival losses can be remedied. Since loading into the near-field causes heating, applying cooling in parallel with the transport would counter some of it. We employ this method in this work by performing polarization gradient cooling (PGC) in parallel with the transport and achieve a survival probability of 0.8. This method is not suitable if the atomic internal states need to be preserved. In that case, other loading improvements are possible. The most immediate one is to cool to the motional ground state prior to loading, which would also improve coherence properties of atoms by reducing the sensitivity to light shifts. Previous work on our platform utilizing Raman sideband cooling prior to transport (Fig. A.10, yellow star) has achieved a survival probability of 0.94(6) at $T = 2\,\mu$K and a trap depth $U_0 = k_B \times 2.1\,$mK[193]. Without additional cooling, ramping the trap depth up could increase the survival probability, but at the expense of reduced coherence due to higher light shifts. Finally, in our model the losses come from the change in trap frequencies, and applying additional light shift during transport could compensate for that change. This could be achieved with additional trapping beams perpendicular to

the current traps that would increase the initial motional frequencies, and that would be ramped down as the traps approached the cavity.

Based on the model presented here, there should be no loss upon departure from the cavity since the trap frequencies decrease. Yet, at a trap depth of $U_0 = k_B \times 1$ mK we observe a 15% loss. Further investigation is needed to model the loss at low trap depths, but we observe a lossless transport at a trap depth of $U_0 = k_B \times 1.6$ mK, making our current system already suitable for protocols that rely on one-way transport.

B

Supplement of Chapter 6

B.1 Setup details

The setup consists of a vacuum chamber with a glass cell on a translation stage [LinTech LTE 170SERIES-4] which can be moved in and out along the $x-$axis relative to the optical beams and magnetic field coils. This allows the distance between the atoms trapped in the tweezers and the SiN device, attached to the vacuum chamber, to be varied with precision of about $1-2\mu$m for dis-

tances within the field of view of the imaging system (< 225 μm). For distances outside of the field of view of the imaging system, the movement is calibrated given the pitch of the translation stage main screw with precision of ~ 15 μm. This calibration is corroborated within our field of view. Two objectives [Mitutoyo G Plan Apo 50X] on either side of the glass cell focus the tweezer, optical pumping, and Rydberg beams. The tweezers use 815 nm light. The atoms in the tweezers are loaded from a MOT, followed by polarization-gradient cooling, after which the atoms are pumped into the $|F, m_F\rangle = |2, 2\rangle$ Zeeman level of the ground $|5S_{1/2}\rangle$ state via optical pumping. The optical pumping uses a focused circularly-polarized 780 nm beam addressing the $F = 2$ manifold, while the $F = 1$ manifold is addressed by the MOT repumper beam. The tweezers are turned off during Rydberg excitation.

Ground-state atoms are excited to the $|70S, J = 1/2, m_J = 1/2\rangle$ state by a two-photon transition using 420 nm and 1013 nm light detuned by 2 GHz from the intermediate $|F, m_F\rangle = |3, 3\rangle$ level in the $6P_{3/2}$ manifold. The 420 nm light comes from an injection-locked TopGan 418 nm diode seeded by frequency-doubled Ti:Sapphire laser [M Squared, 15 W pump]. The frequency of the Ti:Sapphire laser is stabilized by locking the fundamental mode to an ultra-low expansion (ULE) reference cavity (notched cylinder design from Stable Laser Systems), with finesse $\mathcal{F} = 30000$ at 840 nm. The 1013 nm light comes from an external-cavity diode laser [Toptica DL Pro], which is locked to the same reference cavity ($\mathcal{F} = 50000$ at 1013 nm). It is used as a seed for an injection-locked Toptica AR 1060 nm diode, which then seeds a MogLabs 1013 nm TA.

For the single-atom data, these beams are focused from the front and the back objectives, such that they counter-propagate to minimize Doppler shifts. The single-photon Rabi frequencies in this case are $\Omega_{420} = 2\pi \times 170(5)$ MHz and $\Omega_{1013} = 2\pi \times 73(3)$ MHz with spot sizes of $w_{420} \approx 3$ μm and $w_{1013} \approx 1.5$ μm $1/e^2$ radius. For the two-atom data, the Rydberg excitation beams were expanded with spot sizes of $w_{420} \approx 11.5$ μm and $w_{1013} \approx 16$ μm $1/e^2$ radius, while the single-photon Rabi frequencies are kept roughly unchanged. To enlarge the Rydberg excitation beams it became

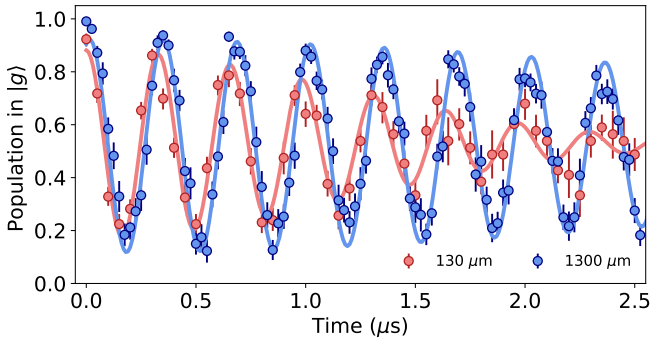


Figure B.1: Single-atom Rabi oscillations near (130 μm) and far (1300 μm) from the device. The decay time τ decreases close to the device with $\tau_{130} = 1.6(1)$ μs and $\tau_{1300} = 4.9(2)$ μs.

necessary to make them co-propagating, focused via a doublet lens which replaced one objective, such that now both counter-propagating to the optical tweezers.

The single-atom Rabi oscillations are plotted in Fig. B.1 for two distances (130 and 1300 μm). The solid lines are fits of the form:

$$f(t) = a\cos(2\pi f t)e^{-(t/\tau)^2} + c \tag{B.1}$$

where we find only the decay time τ is significantly different and both curves agreeing with $\Omega = 2\pi \times 3$ MHz within errorbars. Assuming that at far distances detuning noise from electric field fluctuations is small, the decay of the Rabi oscillations corresponds to 1.5 % Rabi frequency fluctuations. This could be due to sampling of different Rydberg laser intensities due to beam pointing given the small beam sizes. At closer distances, the Rabi decay time is limited by detuning noise. In particular, for the 130 μm distance, quasi-static detuning noise with 2 MHz standard deviation could explain the observed decay time.

B.2 Electric field from the device

B.2.1 Point-charge model

We consider a minimal model in which the SiN device acts as a point charge q and there is a homogeneous background electric field $\mathbf{E}_0$. The point-charge approximation is appropriate given that the device is 31.5 μm long and we explore distances from 90 μm to 3 mm. Our model assumes that the charge is located in the middle of the device Fig. B.2(a). The spectral shift of the Rydberg state is:*

$$\nu(r) = \frac{1}{2}\alpha \left| \frac{kq}{r^2}\hat{\mathbf{r}} + \mathbf{E}_0 \right|^2 \tag{B.2}$$

where α is the polarizability of the Rydberg state, which for $|70S\rangle$ is $\alpha \approx 534\,\mathrm{MHz}/(\mathrm{V/cm})^2$, and $\mathbf{r}$ is the distance between the Rydberg atom and the device. The spectrum we measure in Fig. 1 in the main text is referenced to our farthest distance. As a result we measure a differential shift given by:

$$\Delta\nu \equiv \nu(r) - \nu(\infty) = \frac{1}{2}\alpha \left(\frac{(kq)^2}{r^4} + \frac{2kq}{r^2}\mathbf{E}_0 \cdot \hat{\mathbf{r}} \right) \tag{B.3}$$

This model fits well to the measured spectral shift, which exhibits a clear $\propto r^{-4}$ scaling with distance. Assuming a 1D geometry, we extract values of $q = 126(11)$ charges and a small $E_x = 0.05(1)\,\mathrm{V/cm}$ field. This value of q is extracted by assuming the charge is located at the center of the device, however we fit for values $80 - 180$ charges if assumed at either end of the device. This point-charge model is used throughout the main text for single atoms and is expanded to a 2D geometry when using two-atoms.

*As noted in the main text, we use the spectral shift of the Rydberg state ν as opposed to its energy level u, where $u = -\nu$. This convention arose from the fact that we used the negative first order of the acousto-optic modulator (double-passed) that scanned the frequency of the Rydberg-excitation beam to obtain the spectra, and allowed us to keep the frequency shift and the electric field magnitude the same sign.

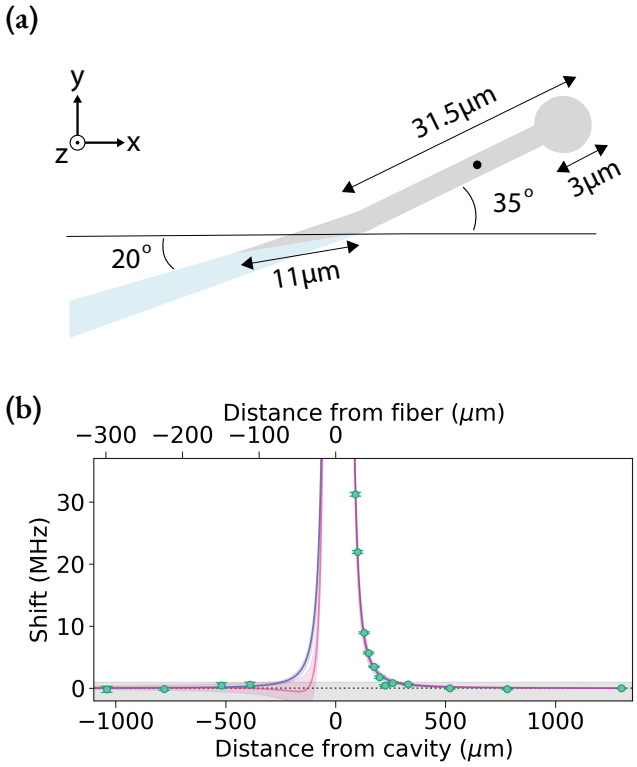


Figure B.2: SiN device attached to a silica fiber. **(a)** Diagram showing the dimensions and angles of the device with respect to the x—axis. **(b)** Measured spectral shift (green circles) as a function of distance from both the device and the fiber surface. We fit the measured shifts to a point-charge (blue) and a line-charge (pink) model, finding good agreement with charges on the SiN device and not on the fiber.

B.2.2 Line charge model

We can evaluate the point-charge approximation by going one step further and constructing a model which takes into account the silica tapered fiber that the SiN device is attached to, as shown in Fig. B.2(a). We assume a semi-infinite linear charge density λ_{fib} for the fiber with its end-point at the origin and at -20° with respect to the $x-$axis and a second finite linear charge density λ_{dev} for the device starting at the origin, with length $L = 31.5$ μm and at 35° with respect to the $x-$axis. This model allows us to differentiate between the possible surface charge characteristics of each material. Here we assume a 2D geometry with a fixed perpendicular field along $\hat{y}$ to $E_y = -0.51\,\text{V/cm}$ (in accordance with our gradient measurements in Section B.6). The fit is shown in Fig. B.2(b) and returns the parameters: $\lambda_{\text{dev}} = 4.8(2)\,\text{e}/\mu\text{m}$, $\lambda_{\text{fib}} = -0.01(1)\,\text{e}/\mu\text{m}$, and $E_{0,x}$=0.06(1) V/cm. These parameters agree with a total number of $Q = 152(5)$ e charges equally distributed over the length of the device and no charges on the fiber.

For the linear charge distribution model Fig. B.2(a), the fit takes into account all points from Fig. 1 in the main text. The points with negative values correspond to points where the distance between the atom and the device is larger than the distance between the atom and the fiber surface given the geometry of the setup. Our observation of no spectral shift up to 100 μm from the fiber surface reinforces the conclusion that the vast majority of the charges are confined to the SiN device. This allows us to simplify the charge distribution as a point-charge in the main text. Further investigation is required to explain how working at the optimal UV power zeros the tapered fiber of charge, as it could help the design of future photonic link architectures for Rydberg atom arrays.

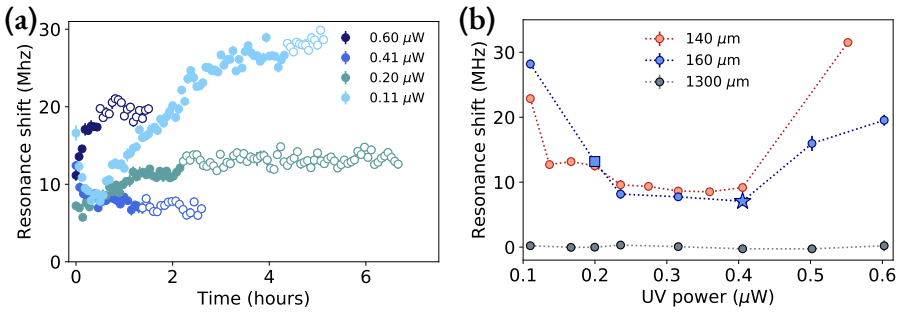


Figure B.3: UV power tuning. **(a)** Rydberg spectral shift settling after changing the UV power at 160 μm. **(b)** Settled shift at different distances as a function of the UV power. The 160 μm curve is generated from the averages of white-faced points in (a). For Fig. 4(D) in the main text the UV power is changed from the optimal value (star) to the shifted value (square).

B.3 Stabilizing the Rydberg spectral shift

B.3.1 UV power tuning

We observe that in order to stabilize the Rydberg spectral shift close to the device, a small amount of UV power is required. We shine a 395 nm diode [Thorlabs M395L5] on the entire system from the side as depicted in Fig. 1 of the main text. After changing the power of the UV diode, the spectral shift takes about an hour to settle. This is shown in Fig. B.3(a) for different UV powers at 160 μm. The settled Rydberg spectral shifts are denoted with white-face symbols and the averages of those points are plotted as a function of the power in Fig. B.3(b). Surprisingly, we find that there is a minimum in the Rydberg spectral shift as a function of UV power observed at distances closer than $\sim$ 800 μm from the device. Our observations in Section B.6.5 further imply that tuning the UV power primarily affects the local background electric field at close distances. For larger distances, we see no effect of the Rydberg spectral shift when the UV power is changed in this range. As noted in the main text, we interpret this to signify the presence of another surface close to the device (e.g. the tapered fiber) which is affected differently by the UV power. The minimum is then due to the sum of the two electric fields for surfaces with a different UV power dependence.

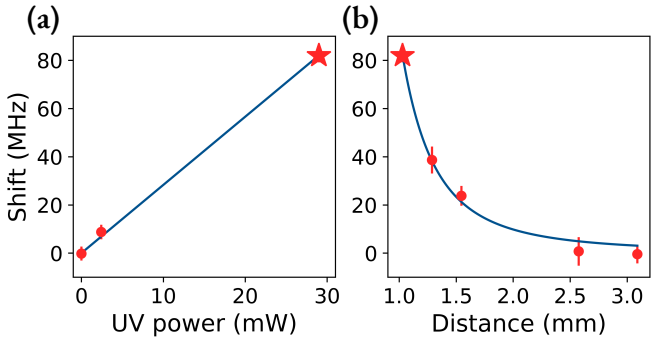


Figure B.4: Effect of large UV power. **(a)** Measured spectral shift as a function of UV power at a distance of 1 mm from the device. A single parameter linear fit is included as a guide to the eye. **(b)** Spectral shift as a function of distance from the device at a UV power of 29 mW. The line is a fit to a point-charge model with $Q = 3.4(3) \times 10^4$e charges and $E_x = 0.08(4)$ V/cm. The points marked by in a star are the same data point.

Larger UV powers further increase the Rydberg spectral shift. This is illustrated for a distance of 1mm in Fig. B.4(a). Keeping the power at 29 mW and varying the distance from the device, we plot the Rydberg spectral shift in (Fig. B.4(b)). Using a point-charge model, we fit $\approx 34,500$ elementary charges at the device and a background field of $E_x = 0.08(4)$ V/cm. This charge is more than two orders of magnitude larger than the 126(11) charges we obtain when using low UV powers that minimize the spectral shift, as seen in the main text. Further, at a distance of 3.9 mm, UV powers in the range 0-30 mW do not significantly change the spectral shift. This bounds the maximum change with UV power of the background electric field from the glass cell that the atom can sense to be $|\Delta \mathbf{E}_0|_{\max} \sim 0.05$ V/cm.

B.3.2 Effect of Rydberg production

In addition to UV illumination, we observe that a constant rate of exciting Rydberg atoms close to the device is required to stabilize the spectral shift. When Rydberg atoms are not being excited, the Rydberg spectral shift increases to higher energies signifying that the electric field has increased. When Rydberg atoms are excited again, the shift settles back to its original value, typically in less than an hour. This effect is illustrated in Fig. B.5. In Fig. B.5(a), we demonstrate the spectral shift

sensitivity to single atoms. After the spectral shift initially settled for this distance of 130μm, the experimental sequence was run without an atom in the tweezer for a period of time. Afterwards, we returned to exciting single atoms to the Rydberg state and observe that the spectral shift returns to its original settled value.

We can interpret this behavior as the result of ionization by the 815 nm tweezer light creating free charges that partially neutralize the charge on the device or the attraction of Rydberg-excited atoms toward the device and becoming ionized upon or before reaching the surface. Again, note that in the presence of an electric field $\mathbf{E}$, the energy level of the Rydberg state u is altered by $u_{\mathbf{E}\neq 0} - u_{\mathbf{E}=0} = \Delta u = -\frac{1}{2}\alpha|\mathbf{E}|^2$, which in our notation is opposite sign to the spectral shift $\Delta\nu$. Therefore, this experimental demonstration suggests that the settling behavior cannot be an effect of any background atoms. Instead, the charge on the device seems sensitive to the addition of single atoms. Note that similar effects were observed in Rydberg EIT experiments near a quartz surface[177].

From this measurement we can approximate the rate at which the free charges reach the device to lower the overall charge. Using a simple linear fit to the slope of the second half of Fig. B.5(a) we estimate a rate of 1.7(1) charges per minute ($\sim$ 0.03 Hz) which we can compare to our experimental duty cycle of $\sim$ 1.3 Hz. In Fig. B.5(b), we study the effect of Rydberg production on the spectral shift over many hours between periods of not sending the Rydberg excitation beams and observe the same characteristic behavior. While Fig. B.5(a-b) were both taken for a distance of 130μm from the device, we observe similar behavior for distances less than $\sim$ 500μm.

B.3.3 Rydberg spectral shift stability and reproducibility

After the Rydberg spectral shift has been minimized and settled, it remains stable. This is shown in Fig. B.6(a), where the Rydberg spectral shift is monitored over several hours at different distances. Although the magnitude of fluctuations of the spectral shift increases as we approach the device, it

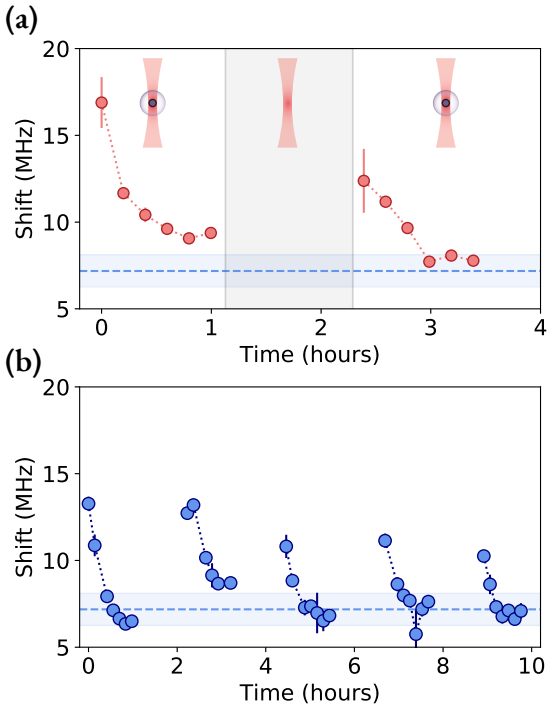


Figure B.5: Rydberg production studied at 130μm. **(a)** After the initial settling of the Rydberg spectral shift over the first hour, the experiment is run without an atom in the tweezer. When the single atom is again loaded, the spectral shift settles. The dashed blue line and shaded region is the average settled value and standard deviation from (b). **(b)** The Rydberg spectral shift monitored between periods of running the experiment with no Rydberg excitation by not sending the 420nm or 1013nm light. The dashed blue line and shaded region is the average settled value and standard deviation respectively.

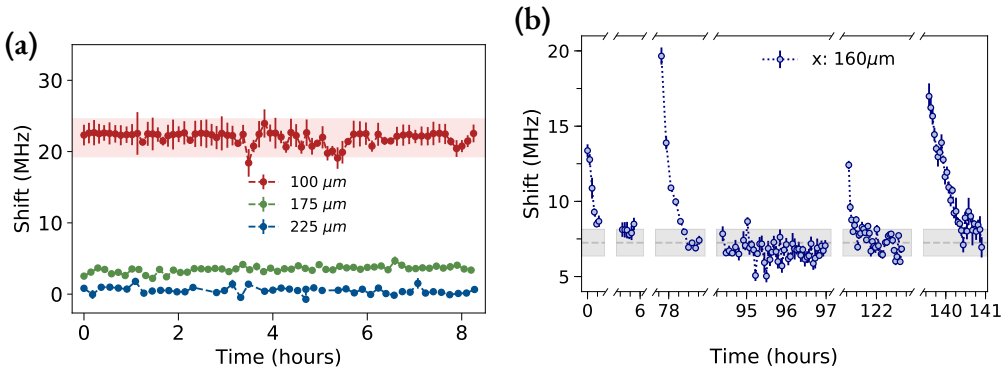


Figure B.6: Rydberg spectral shift stability in time. **(a)** Stability shown over 8 hours at several distances after the initial settling of the spectral shift. The shaded area here is the Rabi-broadened linewidth of 3MHz. **(b)** Reproducibility over 6 days at 160μm where many settling periods can be seen, each after a period of either not running the experiment or not exciting Rydberg atoms. The shaded area is one standard deviation ($\pm$ 0.9 MHz) around the average settled value (7.2 MHz) of all curves.

remains below the Rabi-broadened linewidth of 3 MHz as close as 90 μm.

We observe that the spectral shift and thus the electric field environment is reproducible. For example, we have monitored the Rydberg spectral shift over the course of a week during normal operation as shown in Fig. B.6(b). Several settling behaviors are observed throughout the week after periods of no Rydberg production. We observe that the Rydberg spectral shift repeatedly returns to within a linewidth of the average settled value.

Remarkably, we observe similar behavior even over longer periods of time. For example, the data in Fig. 1 and Fig. 4 in the main text were taken about 6 months apart. We plot the Rydberg spectral shifts at the distances used in Fig. B.15. We see that the Rydberg shifts lie within the Rabi broadened linewidth of 3 MHz from each other at each given distance. Furthermore, each Fig. 4 data point lies on the point-charge fit from Fig. 1, except for the 130 μm data point. This data point in fact was taken at a UV value that slightly deviated from its optimum value, as explained below. The ability to bring the Rydberg spectral shift back to this curve even after 6 months indicates that by tuning the UV power and producing Rydbergs at a constant rate, we can stabilize to the same charge environment repeatedly.

B.4 Single-atom coherence

The presence of an electric field which has both a spatial dependence and time fluctuations will cause decoherence between the Rydberg state and the ground state, since only the Rydberg state is sensitive to the electric field. The time fluctuations will cause detuning noise on the ground-Rydberg transition. A thermal atom will sample different electric fields, also causing detuning noise.

B.4.1 Ramsey and Echo decay measurements

To study the coherence of a Rydberg atom in this environment, we use a Ramsey sequence $\pi/2 - t - \pi/2$ and measure the population in the ground state as a function of time $P_g(t)$. We pulse on the 420 nm beam during the $\pi/2$ pulses while the 1013 nm beam is kept on throughout the experiment, similar to[99]. Since it is far-detuned, the 1013 nm beam does not cause scattering. For a general two-level system, the Ramsey measurement results in a measurement of the differential phase accumulation $\Delta\varphi$ between $|g\rangle$ and $|r\rangle$. The evolution of the ground state population as a function of the hold time between the two $\pi/2$ pulses is then:

$$P_g(t) = \frac{1}{2}\left(1 + \cos(\Delta\varphi(t))\right) \tag{B.4}$$

In our model (see Section B.4.3), the main decoherence effect is detuning noise from electric field fluctuation, such that $\Delta\varphi = \delta t$ for detuning δ. We can assume δ is normally-distributed around δ_0, which in our case is the light shift of the 420 nm beam, with a standard deviation σ_δ and that the noise is quasi-static: at each realization of the experiment we probe one value from this distribution. As we average over the distribution, we obtain a decay:

$$\begin{aligned} P_g(t) =& \int \frac{1}{2}\left(1 + \cos(\delta t)\right) e^{-(\delta-\delta_0)^2/2\sigma_\delta^2} d\delta \\ =& \frac{1}{2}\left(1 + \cos(\delta_0 t) e^{-t^2\sigma_\delta^2/2}\right) \end{aligned} \tag{B.5}$$

We see that the characteristic decay time is:

$$\tau = \frac{\sqrt{2}}{\sigma_\delta} \tag{B.6}$$

Therefore, to obtain the decay time τ we use a fitting function of the form:

$$f(t) = a\cos(2\pi ft + \varphi_0)e^{-(t/\tau)^2} \tag{B.7}$$

The echo pulse sequence is $\pi/2 - t - \pi - t - \pi/2$. Again, the population in the ground state is measured and the decay time τ is obtained by a fit of the form:

$$f(t) = a\cos(2\pi ft + \varphi_0)e^{-(t/\tau)^4} \tag{B.8}$$

Since the quadratic decay is cancelled out by the echo sequence, the echo signal has the next order in the time dependence.

B.4.2 Theoretical model

Given a point charge distribution and a background electric field, as in Eq. (B.2), we can develop a model for the dependence of T_2^* and T_2 on the distance from the device. For simplicity we will work with angular frequencies, ω, such that the energy shift from the electric field is:

$$\delta\omega(r) = 2\pi\delta\nu(r) \approx \pi\alpha|\frac{kq}{r^2}\hat{\mathbf{r}} + \mathbf{E}_0|^2 \tag{B.9}$$

At each distance r, the spatial dependence of the energy shift is approximately linear with distance around the position of the atom. We use the local energy gradient $\nabla\delta\omega(r)$ to simplify our model of dephasing. Additionally we assume that the motional state of the atom is described by a thermal Maxwell-Boltzmann distribution of the initial position $\mathbf{r}_0$ and initial velocity $\mathbf{v}_0$. We find that this results in the Rydberg state experiencing a time-dependent detuning given by:

$$\delta\omega(t) = \delta\omega_0 + \nabla\delta\omega \cdot (\mathbf{r}_0 + \mathbf{v}_0 t + \frac{\mathbf{a}}{2}t^2) \tag{B.10}$$

where $\delta\omega_0$ is the initial detuning and the acceleration $\mathbf{a}$ is the result of the force from the electric field gradient and is given by:

$$\mathbf{a} = \frac{\hbar}{m}\nabla\delta\omega \tag{B.11}$$

It is only when the atom is in the Rydberg state that it accelerates and in each pulse sequence the atom will exist in a superposition of the Rydberg and ground state for some time. In order to account for the state-dependent force, we can define a function $f_{+,-}(t)$ such that:

$$f_+(t) = 1 - f_-(t) \tag{B.12}$$

which can be written into the time-dependent detuning of the Rydberg state:

$$\delta\omega_{+,-}(t) = \delta\omega_0 + \nabla\delta\omega \cdot (\mathbf{r}_0 + \mathbf{v}_0 t + \int_0^t \int_0^t \mathbf{a} f_{+,-}(t')dt'dt'') \tag{B.13}$$

We can then calculate the relative phase acquired by the Rydberg state and ground states:

$$\varphi(t) = 2\pi \int_0^\tau f_+(t)\delta\omega_+(t) - f_-(t)\delta\omega_-(t)dt \tag{B.14}$$

The function $f_{+,-}(t)$ is determined by the positioning of π pulses in each decoupling sequence, given as:

$$f_{\text{Ramsey}}(t) = \begin{cases} 1 & \text{if } 0 < t < \tau \end{cases}$$

$$f_{\text{Spin Echo}}(t) = \begin{cases} 1 & \text{if } 0 < t < \tau/2 \\ 0 & \text{if } \tau/2 < t < \tau \end{cases}$$

$$f_{\text{CPN=2}}(t) = \begin{cases} 1 & \text{if } 0 < t < \tau/4 \\ 0 & \text{if } \tau/4 < t < 3\tau/4 \\ 1 & \text{if } 3\tau/4 < t < \tau \end{cases}$$

B.4.3 Single-Atom Ramsey

Solving Eq. (B.14) for the Ramsey sequence, we find that the phase acquired will have a dependence on the variance in position and velocity of the atom. However, for our experiments their contribution to the total dephasing is small and we find that the single-atom Ramsey decay time is limited by shot-to-shot fluctuations of the $\delta\omega_0$ term, caused by electric field fluctuations. Therefore, T_2^* is given by the variance of the detuning $\sigma^2_{\delta\omega_0}$:

$$T_2^* \approx \sqrt{\frac{2}{\sigma^2_{\delta\omega_0}}} \tag{B.15}$$

From the stability measurement of the spectral shifts in Fig. B.6 we find that the fluctuations have a Gaussian distribution. We assume that both the charge on the device q and the background electric field $\mathbf{E}$ fluctuate with variances σ_q and $\sigma_{\mathbf{E}}$ respectively. To first order, the total variance can be written as:

$$\sigma^2_{\delta\omega_0} = \left(\frac{d\delta\omega}{d\mathbf{E}}\right)^2 \sigma^2_{\mathbf{E}} + \left(\frac{d\delta\omega}{dq}\right)^2 \sigma^2_q \tag{B.16}$$

Using Eq.(B.9), this expression becomes:

$$\begin{aligned} \sigma^2_{\delta\omega_0} = 4\pi^2\alpha^2\Big(\Big(&\frac{k^4}{|\mathbf{r}|^8}q_0^2 + \frac{2k^3}{|\mathbf{r}|^6}E_x q_0 + \frac{k^2}{|\mathbf{r}|^4}E_x^2\Big)\sigma_q^2 + \\ &\frac{k^2}{|\mathbf{r}|^4}q_0^2\sigma^2_{E_x} + |\mathbf{E}|^2\sigma^2_{|\mathbf{E}|}\Big) \end{aligned} \tag{B.17}$$

where the $x-$direction is along the axis of movement in the distance-dependent measurements.

Using this expression for $\sigma^2_{\delta\omega_0}$, we can extract whether the dominant source of noise is charge

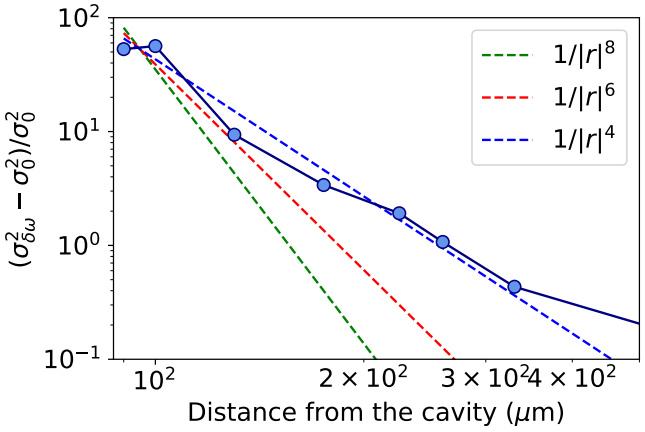


Figure B.7: Variance of the Rydberg shift detuning as a function of distance. Plotted are different distance scalings, suggesting that the measured variance scales as $1/|r|^4$.

fluctuations or background electric field fluctuations, due to the difference in the distance scaling of the different terms. We use the measured $T_2^*(r)$ and convert it to variance using Eq. (B.15). We then subtract a constant offset from the variance to account for any contribution to the dephasing which does not scale with distance, such as Doppler dephasing. We use the form $\sigma_0^2 = 2/(T_2^*(r_{\max}))^2$ for this constant offset. This is plotted in Fig. B.7, showing that the variance $\sigma^2_{\delta\omega_0} - \sigma_0^2$ scales as $|r|^{-4}$. Fitting for the two variances shows that for the distances considered here, the noise is dominated by fluctuations of the electric field background. This model is used to generate the theoretical fit of the Ramsey decay time in Fig. 2(D).

In Fig. B.8 we compare a fit with only charge fluctuations and a fit which includes both charge and background field fluctuations to further emphasize the presence of background field fluctuation.

B.4.4 Single-Atom Spin Echo

Solving Eq. (B.14) for the spin echo pulse sequence we find that the dephasing is insensitive to low frequency noise, such as shot-to-shot fluctuations of $\delta\omega_0$. However, we find that in an electric field

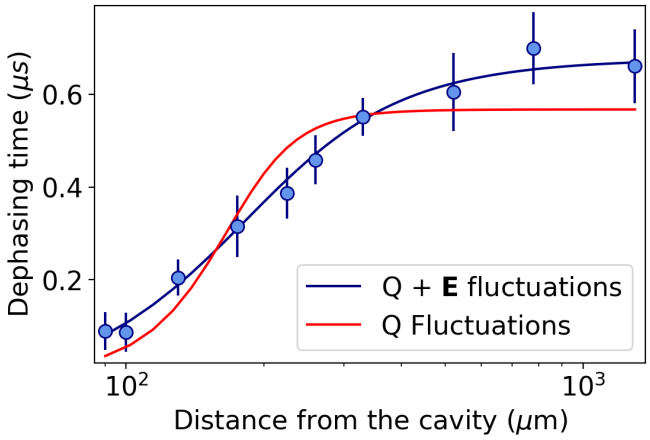


Figure B.8: Model comparison of Ramsey decay time. We compare a model taking into account only charge fluctuations and constant baseline T_2^* (red) to the model that incorporates both charge and $\mathbf{E}$ fluctuations (blue).

gradient, even in the absence of charge fluctuation, the spin echo dephasing rate is limited by thermal effects. The total phase acquired during the spin echo sequence will be given by:

$$\varphi = \nabla\delta\omega \cdot \frac{\mathbf{v}}{4}\tau^2 \tag{B.18}$$

In our experiment we find that the velocity fluctuations dominate the dephasing, resulting in a phase variance of:

$$\sigma_\varphi^2 = |\nabla\delta\omega|^2 \frac{\tau^4}{16}\frac{k_b T}{m} \tag{B.19}$$

From this we find that the variance increases as τ^4. This results in an expected decay going as $e^{-(t/T_2)^4}$ as opposed to the typical Gaussian decay. We can then solve for the thermally limited coherence time, $T_{thermal}$:

$$T_{\text{thermal}} = 2\sqrt{\frac{\sqrt{2}}{|\nabla\delta\omega|\sqrt{\frac{k_b T}{m}}}} \tag{B.20}$$

From this equation we find a distance dependence from the $|\nabla\delta\omega|$ term. By simplifying this equation, we find an approximate scaling of:

$$T_{\text{thermal}} \propto \frac{r^{2.5}}{q\sqrt{\alpha\sqrt{T}}} \tag{B.21}$$

We then assume some baseline dephasing of σ_0 to yield an overall T_2 of:

$$T_2 = \sqrt{\frac{2}{\sigma_0^2 + \frac{1}{2}|\nabla\delta\omega|\sqrt{\frac{k_b T}{2m}}}} \tag{B.22}$$

This model is used to generate the theoretical fit of the spin echo decay time in Fig. 2(D). Due to the dependence on the electric field gradient, this model can also provide a measurement of the background electric field in not only the $x-$direction, but also orthogonal directions. From this model we extract that there is a background field orthogonal to the $x-$field with a magnitude of $0.4(1)$ V/cm.

B.4.5 Carr-Purcell N=2

Using Eq. (B.14) to solve for the two-pulse Carr-Purcell sequence, we find that the atom becomes insensitive to thermal sampling. However, there is a term that is sensitive the the electric field gradient given by:

$$\varphi = \nabla\delta\omega \cdot \frac{\mathbf{a}}{384}\tau^3 \tag{B.23}$$

We can rewrite the phase acquired during the CP N=2 pulse sequence when taking into account Eq.(B.11) as:

$$\varphi = \frac{\hbar\tau^3}{384m}|\nabla\delta\omega|^2 \tag{B.24}$$

Charge instability will cause variance in $|\nabla\delta\omega|$, leading to variance in the phase. However, while charge instability sets a limit on the coherence time for the CP N=2, there exists a class of pulse sequences that can decouple dephasing of this form.

B.4.6 Cancelling polynomial phase

The noise that we have analyzed in this section is unique as it is noise that has a polynomial time dependence. For example, this noise is constant for positional dephasing, linear with velocity dephasing, and quadratic in dephasing due to acceleration. If we assume that the phase accumulated with time has a functional form of:

$$\varphi(t) = \sum_{j=1:k} a_j t^j \tag{B.25}$$

where a_j are constants that may be varying due to some external noise, and k is the maximal polynomial order. We want to design a pulse sequence which will cancel out the accumulated phase $\varphi(t)$ regardless of the values of a_j.

We apply $N\,\pi$ pulses at times $t_2, t_3, ..., t_{N+1}$. As a convention, $t_1 = 0$ is the beginning of the phase accumulation and the sequence length is T, such that $t_{N+2} = T$. We can now rewrite the accumulated phase as:

$$\varphi(t) = \sum_{i=1:N+1} -(-1)^i \sum_{j=1:k} a_j (t_{i+1}^j - t_i^j) \tag{B.26}$$

In the simplest case, $\varphi(t) = at$ is the constant rate of phase accumulation. Then:

$$\varphi(t) = \sum_{i=1:N+1} -(-1)^i a (t_{i+1} - t_i) \tag{B.27}$$

To find the times when we should apply the pulses, we set $\varphi(t) = 0$ and solve for $t_2, ..t_{N+1}$. In this

case, we know that one pulse will echo out the phase, so $N = 1$:

$$\varphi(t) = a(t_2 - t_1) - a(t_3 - t_2) = 0 \tag{B.28}$$

Furthermore, $t_1 = 0$ and $t_{N+2} = t_3 = T$, so

$$at_2 - aT + at_2 = 0$$

$$t_2 = T/2 \tag{B.29}$$

This results in the pulse sequence that we know as the Spin echo, which decouples from DC noise.

For $k > 1$, we posit that $N = k$. We will then get a system of k equations with k unknown times. We can split them into contributions for different a_j, and set all contributions to zero:

$$\sum_{i=1:N+1} -(-1)^i(t_{i+1}^j - t_i^j) = 0, \forall j \in (1, N) \tag{B.30}$$

When solving these equations for k=N=2 we recover the Carr-Purcell N=2 sequence. Now, we can solve these equations for $k = N = 3$:

$$t_2 - t_3 + t_4 - T/2 = 0$$

$$t_2^2 - t_3^2 + t_4^2 - T^2/2 = 0$$

$$t_2^3 - t_3^3 + t_4^3 - T^3/2 = 0$$

and as always, $t_1 = 0, t_5 = T$. We would apply the pulses at t_2, t_3, t_4. The equations above in general have multiple solutions, but we restrict the solutions to real numbers, and $T > t_4 > t_3 > t_2 > t_1$.



Figure B.9: Pulse sequence that cancels polynomial phase noise up to t^2 contribution.

This imposes a unique solution to the set of the equations above, resulting $\pi-$pulses at times:

$$t_2 = (\frac{2-\sqrt{2}}{4})T$$

$$t_3 = T/2$$

$$t_4 = (\frac{2+\sqrt{2}}{4})T$$

From this solution we find that the pulse sequence would take the form illustrated in Fig. B.9 with evolution periods $A = \left(\frac{2-\sqrt{2}}{4}\right)$ and $B = \frac{\sqrt{2}}{4}$.

The resulting function is given as:

$$f_{\text{k=N=3}}(t) = \begin{cases} 1 & \text{if } 0 < t < (\frac{2-\sqrt{2}}{4})\tau \\ 0 & \text{if } (\frac{2-\sqrt{2}}{4})\tau < t < \tau/2 \\ 1 & \text{if } \tau/2 < t < (\frac{2+\sqrt{2}}{4})\tau \\ 0 & \text{if } (\frac{2+\sqrt{2}}{4})\tau < t < \tau \end{cases}$$

B.5 Two-atom coherence

B.5.1 W-state Fidelity measurement

In order to characterize the fidelity of preparing the state $|W\rangle = \frac{1}{\sqrt{2}}(|gr\rangle + |rg\rangle)$, we follow the procedure in [99]. We can express the fidelity of the entangled state with elements of the density matrix

ρ:

$$\begin{aligned}\mathcal{F} &= \langle W|\rho|W\rangle \\ &= \frac{1}{2}\left(\rho_{gr,gr} + \rho_{rg,rg} + \rho_{gr,rg} + \rho_{rg,gr}\right)\end{aligned} \tag{B.31}$$

We extract the diagonal elements $\rho_{rg,rg}$ and $\rho_{gr,gr}$ by measuring the populations, P_{rg} and P_{gr}, after preparing the $|W\rangle$ state with a $\pi-$pulse from $|gg\rangle$.

The off-diagonal elements can be extracted by applying a local phase shift $\Delta\varphi = \delta t$ to one of the atoms, embedded in a Ramsey-type sequence: $\pi - \delta t - \pi$. The accumulation of differential phase rotates between $|W\rangle$ and $|D\rangle = \frac{1}{\sqrt{2}}(|gr\rangle - |rg\rangle)$:

$$|\Psi\rangle = \frac{1}{\sqrt{2}}\left(|gr\rangle + e^{i\delta t}|rg\rangle\right) \tag{B.32}$$

$$= \cos(\delta t/2)|W\rangle + \sin(\delta t/2)|D\rangle \tag{B.33}$$

The final $\pi-$pulse maps the population in $|W\rangle$ to population in $|gg\rangle$. Since the dark state $|D\rangle$ does not couple to $|gg\rangle$, this sequence measures the time evolution of the population in $|W\rangle$. For a general density matrix, the amplitude of these oscillations will be equal to the off-diagonal density matrix elements, $\rho_{rg,gr} = \rho_{gr,rg}$[99]:

$$P_{gg}(t) = |\rho_{gr,rg}|\cos(\delta t + \varphi) + C \tag{B.34}$$

In order to mitigate sensitivity to dephasing we embedd this phase shift in a spin echo sequence[99] where each period of phase acquisition is fixed to 1 µs. The trap is applied for a varying amount of time within that 1 µs. Fig. B.10 compares two measurements with and without an added echo pulse. For the data in this paper, we use the echo sequence to extract the coherences.

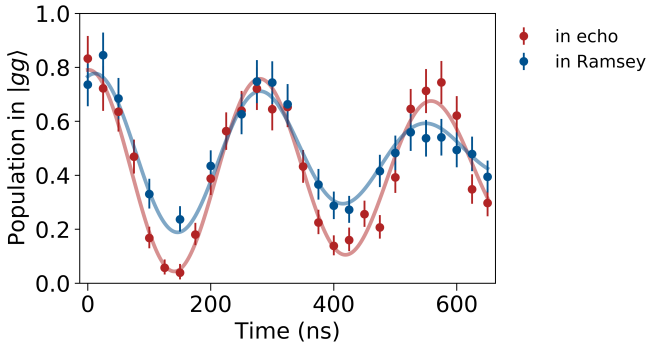


Figure B.10: $|W\rangle$-state coherence measurement embedded in a Ramsey-type sequence (blue) $\pi - \delta \cdot t - \pi$ and embedded in an echo-type sequence (red) $\pi - \delta \cdot t - 2\pi - t - \pi$. The fitted decays are $\tau_{\text{in Ramsey}} = 570 \pm 10$ ns, $\tau_{\text{in echo}} = 930 \pm 10$ ns.

The contrast of the coherence oscillation can either be obtained by taking the difference between the maximum and the minimum points or by using a decaying sinusoidal fit. We use the former because it is independent of the functional form of the decay.

B.5.2 W-state fidelity at two distances

We measure the $|W\rangle$-state preparation fidelity at two distances from the device: both far (2.6 mm) and close (170 μm). We observe little dependence of the fidelity on distance as shown in Fig. B.11, suggesting that the preparation fidelity in our case is limited by factors other than electric field noise, for example, laser intensity and phase noise.

B.5.3 W-state fidelity at different orientations

At 170 μm we explore the $|W\rangle$-state fidelity at three different orientations of the two atoms which are compared in Fig. B.12. In each case, the fidelity is calculated both by using the coherence contrast obtained by taking the difference between the maximum and the minimum, as in the rest of the paper, and by using a decaying sinusoidal fit of the form $f(t) = a\cos(\delta t + \varphi)e^{-(t/\tau)^2}$. While the two methods give similar results, the contrast fit has smaller errorbars since the data did not av-

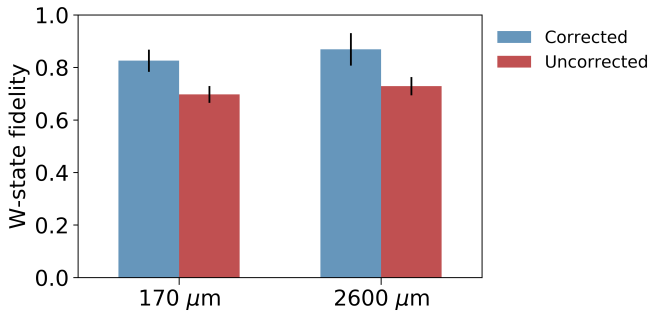


Figure B.11: Preparation fidelity of the $|W\rangle$-state at two distances from the device. Both the SPAM corrected (blue) and the uncorrected (red) fidelities are shown. We observe little dependence of the fidelity on distance from the device.

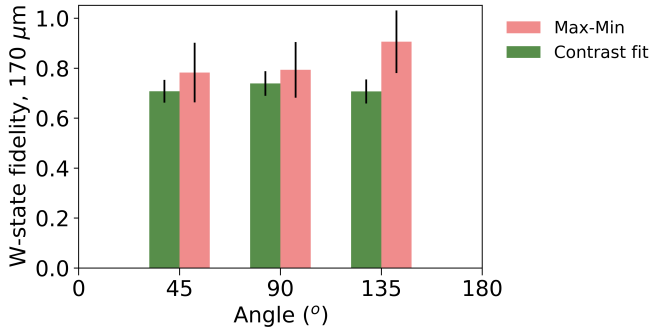


Figure B.12: $|W\rangle$ state fidelity for three different orientations with inter-atomic distance 3.15 μm. The energy differences between the atoms for $\theta = 45^o, 90^o, 135^o$ are 0.11 MHz, 0.63 MHz, 0.84 MHz respectively.

erage for as long as data used in the main text. The coherence extracted from the fit gives a stronger indication that the fidelity value is independent of the angle. Fig. B.12 shows that the $|W\rangle$-state preparation fidelity is insensitive to the electric field gradient between the positions of the two atoms for the values of the gradient at this distance.

B.5.4 W-state lifetime

Similarly to the discussion of the single-atom coherence, here we consider several possible dephasing mechanisms for two atoms in an electric field gradient. However, for two entangled atoms, we need to consider only effects which cause a differential phase accumulation between $|gr\rangle$ and $|rg\rangle$, i.e.

processes which rotates $|W\rangle$ into $|D\rangle$:

$$|\Psi\rangle = \frac{1}{\sqrt{2}}\left(|gr\rangle + e^{i\Delta\varphi_{rg,gr}}|rg\rangle\right) \tag{B.35}$$

where $\Delta\varphi_{rg,gr}$ is the differential phase. As we outline below, the main sources of decoherence in our setup are Doppler dephasing and thermal sampling of an electric field gradient.

We use the Ramsey-type sequence described above $\pi - t - \pi$ and measure the decay time of the population $P_{gg}(t)$:

$$P_{gg} = \frac{1}{2}\left(1 + \cos(\Delta\varphi_{rg,gr}t)\right) \tag{B.36}$$

When an atom with velocity $\mathbf{v}$ is excited to the Rydberg state, it experiences a Doppler shift $\mathbf{k}_{\text{eff}}\mathbf{v}$, where in our case $\mathbf{k}_{\text{eff}} = \mathbf{k}_{420} + \mathbf{k}_{1013}$ for co-propagating beams, which includes the effective wavevectors of the 420 nm and 1013 nm lasers. If the atomic velocity follows a thermal Maxwell-Boltzmann distribution with width σ_v, this will cause dephasing of the $|W\rangle$ state because each atom in $|r\rangle$ will experience a different velocity sampled from this distribution.

Similarly, in the presence of an electric field gradient, each thermal atom will locally sample a different electric field and will experience a different Rydberg spectral shift as a function of its initial position and velocity. The atom samples a different velocity and position for each realization of the experiment, resulting in a quasi-static phase noise.

The differential phase between $|rg\rangle$ and $|gr\rangle$ can be written in terms of the differences between each atom's velocity $\mathbf{v}_{a,b}$ and position $\mathbf{r}_{a,b}$:

$$\Delta\varphi(t) = \nabla\delta\omega \cdot (\mathbf{\Delta r} + \mathbf{\Delta v}t) \tag{B.37}$$

where $\mathbf{\Delta v} = \mathbf{v}_a - \mathbf{v}_b$ and $\mathbf{\Delta r} = \mathbf{r}_a - \mathbf{r}_b$. After evolving for time τ the state will become:

$$|\Psi\rangle = |rg\rangle + e^{i(\mathbf{k_{eff}}\cdot\mathbf{\Delta v})+i\int_0^\tau \Delta\varphi dt}\,|gr\rangle \tag{B.38}$$

The rotation between $|W\rangle$ and $|D\rangle$ caused by the gradient follows an oscillation of the form:

$$\frac{1}{2} + \frac{1}{2}\cos\Big((\Delta\mathbf{r}\cdot\nabla\delta\omega)\tau\Big) \tag{B.39}$$

and experiences an overall exponential decay of the form:

$$e^{-\frac{1}{2}(\mathbf{k}\cdot\sigma_{\Delta\mathbf{v}})^2\tau^2-\frac{1}{2}(\nabla\delta\omega\cdot\sigma_{\Delta\mathbf{r}})^2\tau^2-\frac{1}{8}(\nabla\delta\omega\cdot\sigma_{\Delta\mathbf{v}})^2\tau^4} \tag{B.40}$$

where we can neglect the small contribution from the term $\propto \tau^4$. Assuming Gaussian distributions with widths $\sigma_{\Delta\mathbf{v}}$ and $\sigma_{\Delta\mathbf{r}}$, we solve for the following expression for the decay time of the $|W\rangle$ state:

$$T_W = \sqrt{\frac{2}{\sigma_\varphi^2}} \tag{B.41}$$

where

$$\sigma_\varphi^2 = (\mathbf{k}\cdot\sigma_{\Delta\mathbf{v}})^2 + (\nabla\delta\omega\cdot\sigma_{\Delta\mathbf{r}})^2 \tag{B.42}$$

While for larger distances, the Doppler term dominates. For distances around 130 μm, the contributions of the two terms start to become comparable. A curve generated from this model using only the atom temperature, trap parameters, point-charge field and electric field background is plotted in Fig. 3(D) of the main text.

B.5.5 W-State Spin Echo

For the W-state, we are also able to apply a spin echo sequence to make the coherence insensitive to DC noise in the differential phase acquired. As a result, we find that the coherence time should no

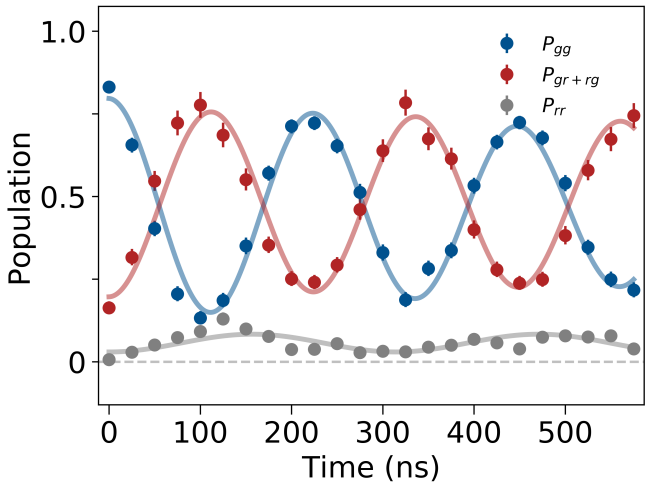


Figure B.13: Uncorrected Rydberg-blockaded Rabi Oscillation. This data corresponds to the corrected data for the diagonal elements shown in Fig. 3(B) of the main text. We observe a blockaded Rabi frequency of $\Omega_{Blockade} = 2\pi \times 4.46(3)$ MHz between the $P_{|gg\rangle}$ (red) and $P_{|gr\rangle} + P_{|rg\rangle}$ (blue) populations. Additionally, the $P_{|rr\rangle}$ population oscillates at $\Omega = 2\pi \times 3.2(1)$ MHz agreeing with the expected non-blockaded Rabi frequency and therefore expected behavior given uncorrected single-atom loss.

longer be limited by the Doppler dephasing and only by the thermal sampling of the electric field gradient.

$$\Delta\varphi(t) = \nabla\delta\omega \cdot \frac{\Delta \mathbf{v} t^2}{4} \tag{B.43}$$

Similar to the single-atom spin echo, we find that the coherence time of the W-state is limited by the thermal variance of velocities. The variance of the phase acquired during the pulse sequence will be set by the difference between the two atom's velocities, making the decoherence time a factor of $\sqrt{2}$ smaller than the single-atom decay:

$$T_2 = 2\sqrt{\frac{1}{|\nabla\delta\omega|\sqrt{\frac{k_b T}{m}}}} \tag{B.44}$$

B.5.6 SPAM correction

We correct our data using the method described in the supplement of[113]. The main source of preparation error is the loss of an atom after the experimental run is triggered but before the Rydberg excitation occurs. The survival rate of an atom in each tweezer is approximately 90 %. Due to the loss, the uncorrected data has extra contributions from initial states which have only one atom instead of two. Given that we detect Rydberg population through loss, uncorrected data shows increased Rydberg population $P_{|rr\rangle}$. This is apparent in the uncorrected two-atom blockaded Rabi oscillation in Fig. B.13, where the Rydberg population $P_{|rr\rangle}$ is clearly oscillating. In fact, the frequency of this oscillation occurs at the single-atom Rabi frequency and therefore can be explained by single-atom evolution when the dynamics began with only one populated tweezer. To appropriately account for single-atom evolution in a two-atom experiment with finite preparation loss, the SPAM correction requires two extra datasets to be taken concurrently using the same parameters as the data intended for correction. The two extra datasets use the same experimental sequence but each has only one atom present. Additionally, we correct for the 97(1) % finite probability of initializing the atoms in the correct initial hyperfine ground state, although this results in a much smaller correction.

B.6 Electric field gradient

More information can be gained about the electric field configuration and its dependence on UV power by using two atoms. As illustrated in Fig. 4 in the main text, by preparing the W-state and measuring its time evolution, we can detect an electric field gradient at the position of the atoms.

B.6.1 Fitting the oscillation frequency

By changing the relative orientation of the two atoms, we can study the spatial dependence of the electric field. We pick seven different orientations of the two atoms spanning a semi-circle. Our full

setup is described in [170] and here we give a brief overview. We control the positions of the atoms using two galvo mirrors in the path of the optical tweezers. The coordinates of the two galvo mirrors can each be referenced to the nanoscale device. This is done by sending light through the device via the fiber and collecting the fluorescence of a few points on the device on two APDs placed along the tweezer paths when varying the galvo mirror positions, allowing us to map one coordinate system to the other. This gives us nanoscale precision of the orientation of the two atoms relative to each other of ~ 50 nm [170].

By measuring $P_{gg}(t)$ for the pulse sequence $\pi - t - \pi$, we can extract the differential phase accumulation during the free evolution time t, which corresponds to the energy difference at the positions of the two atoms. We measure this time evolution at each orientations and do a simultaneous fit to all seven with the fitting function for each distance:

$$P_{gg,j}(t) = a_j \cos(2\pi f_j t + \varphi_j) e^{-(t/\tau)^2} + c \tag{B.45}$$

where each orientation j has independent amplitude a_j, frequency f_j, and phase φ_j parameters and the decay time τ and offset c parameters are common to all. Given the dependence of oscillation frequency on angle at each distance, we are now ready to develop a model for the electric field distribution.

B.6.2 2D Electric field gradient model

Given our measurements, we can try to reconstruct the background electric field $E(x, y)$ in 2D. Note that we do not have access to information about E_z which is along the tweezer propagation direction. The oscillation frequency between $|W\rangle$ and $|D\rangle$ is a measure of the energy difference

between the two atoms, here denoted as A and B:

$$\nu_{AB} = |\nu_A - \nu_B| \tag{B.46}$$

At each distance, we also obtain the average spectral shift over all orientations and the two atoms:

$$\Delta\nu = \nu(r) - \nu(\infty) \tag{B.47}$$

Note that one could also consider directly measuring ν_{AB} from the individual spectral shifts $\Delta\nu_A$ and $\Delta\nu_B$ of the two atoms. However, these shifts are sensitive to noise and decoherence, making this measurement extremely challenging. It is the entanglement between the two atoms which allows us to perform a differential measurement for which the majority of these noise sources are common mode, that allows us to obtain ν_{AB} more precisely.

To reconstruct the electric field $E(x, y)$, we adopt the same model used for the single-atom data. The nanoscale device acts as a point charge q located in the middle of the device and there is a constant homogeneous electric field background $\mathbf{E}_0$, see Eq. (B.2). In 2D:

$$\begin{aligned}\nu(x, y) =& \frac{1}{2}\alpha\left(\frac{kQ}{(x^2+y^2)^{3/2}}x + E_x\right)^2 + \\ & \frac{1}{2}\alpha\left(\frac{kQ}{(x^2+y^2)^{3/2}}y + E_y\right)^2\end{aligned} \tag{B.48}$$

The energy difference between the two atoms can be expressed in terms of the $x-$ and $y-$derivatives of this function at the position between the two atoms and the distance between the two atoms r_{AB}:

$$\nu_{AB}(r, \theta) = r_{AB}\left(\frac{\partial\nu}{\partial x}\cos(\theta) + \frac{\partial\nu}{\partial y}\sin(\theta)\right) \tag{B.49}$$

with θ as defined in Fig. 4. Assuming the charge is at position (x_0, y_0) with respect to the origin

(fiber-device junction depicted in Fig. B.2(a)), and given that we can move the device along the $x-$direction, so $y = 0$, the partial derivatives become:

$$\begin{aligned}\frac{\partial v}{\partial x} &= -\alpha kQ\left(\frac{2kQ\tilde{x}}{r^6} + \frac{E_x(2\tilde{x}^2 - y_0^2) - 3E_y\tilde{x}y_0}{r^5}\right), \\ \frac{\partial v}{\partial y} &= \alpha kQ\left(\frac{2kQy_0}{r^6} + \frac{E_y(\tilde{x}^2 - 2y_0^2) + 3E_x\tilde{x}y_0}{r^5}\right)\end{aligned} \tag{B.50}$$

where $\tilde{x} = x - x_0$ and $r = \sqrt{(x - x_0)^2 + y_0^2}$.

To get a sense of the distance-scaling, we consider a charge at the origin ($x_0 = y_0 = 0$). The gradient components further simplify to:

$$\begin{aligned}\frac{\partial v}{\partial x} &= -2\alpha kQ\left(\frac{kQ}{r^5} + \frac{E_x}{r^3}\right) \\ \frac{\partial v}{\partial y} &= \alpha kQ\frac{E_y}{r^3}\end{aligned} \tag{B.51}$$

We can see that the angle of maximum gradient of the energy is given by:

$$\theta_{max} = \arctan(-\frac{1}{2}\frac{E_y}{\frac{kQ}{r^2} + E_x}) \tag{B.52}$$

Using the fitted oscillation frequencies $f_j(r, \theta)$, we can extract this power law scaling. At each orientation angle θ we take the four fitted oscillation frequencies and fit a power law of the form:

$$f_j(x) = a\frac{1}{x^n} \tag{B.53}$$

The fitted powers are plotted as a function of angle in Fig. B.14. In our convention, $x-$axis lies along $\theta = 0^o$ and the $y-$axis lies along $\theta = 90^o$. We fit the following powers: For $\theta = 0^o$: $n = 4.6 \pm 0.6$ where we expect $n = 5$ given Eq. (B.51) since $E_x \approx 0$; For $\theta = 90^o$: $n = 3.4 \pm 0.2$

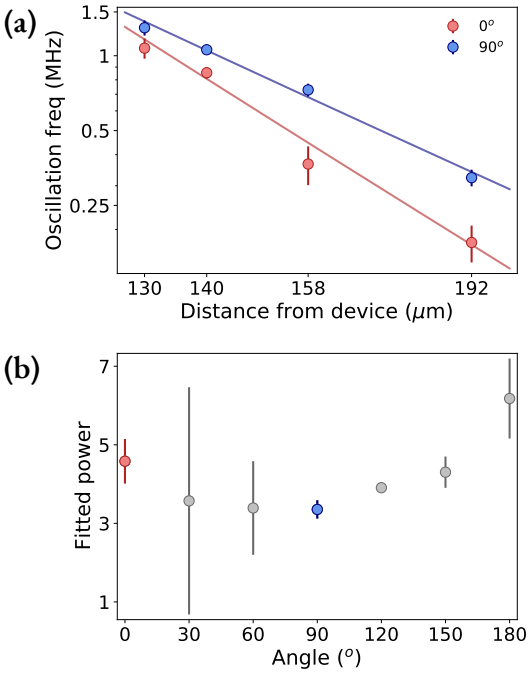


Figure B.14: Gradient scaling with distance from the device. **(a)** The oscillation frequency at two angular orientations of the atom pair. **(b)** Extracting the power law scaling a/r^n of the gradient magnitude for each angular orientation measured. For $\theta = 0^o$: $n = 4.6 \pm 0.6$ where we expect $n = 5$. For $\theta = 90^o$: $n = 3.4 \pm 0.2$ where we expect $n = 3$.

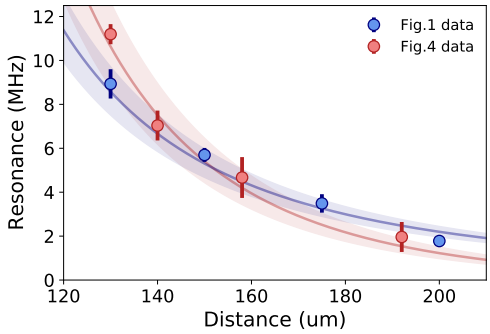


Figure B.15: Rydberg spectral shift as a function of distance from the device. Comparing data used in Fig. 1 in the main text (blue) where the UV value was optimized for each point, and data from Fig. 4 (pink) where the UV value was kept at the value that minimized the shift at 160μm for each point. The two datasets were taken 6 months apart but a similar electric field environment could be stabilized.

where we expect $n = 3$ for a finite value of E_y. Given that we have only four points to fit a power law, these numbers agree with our expectation.

B.6.3 Fitting the model to the data

We can now use this model to reconstruct the electric field $E(x, y)$. We use the expression for the energy difference between the two atoms $\nu_{AB}(x, \theta)$ in Eq. (B.49) to fit the measured oscillation frequencies $f_j(x, \theta)$ as a function of angle θ and distance to the device x. We also use the expression for the Rydberg spectral shift $\nu(r) - \nu(\infty)$ from Eq. (B.48) to fit the measured Rydberg spectral shifts at each distance. We combine the two and obtain $q = 190(10)$ e, and $(E_x, E_y) = (-0.02(1), -0.51(3))$V/cm. Note that if we perform a fit to only the gradient data $\nu_{AB}(x, \theta)$ with Eq. (B.49), we obtain values which are the same within errorbars: $q = 196(17)$ e, and $(E_x, E_y) = (-0.03(2), -0.47(4))$V/cm.

These values compare well with the data from Fig. 1 in the main text, which finds $q = 126(11)$ and $Ex = 0.049(12)$. In the two-atom data, the UV was kept constant, while in the single-atom data it was varied to minimize the Rydberg spectral shift. The two are plotted together in Fig. B.15

along with the corresponding model fit values. While different UV powers are necessary to minimize the Rydberg spectral shift over larger distances, over the small distance range of 130-192 μm used here, the same UV power produces the minimum Rydberg spectral shift, except at the 130 μm point which begins to deviate.

B.6.4 Minimum detectable electric field gradient

Given our single-atom coherence measurements, we can assume that the electric field from the device is constant over the time of the measurement with shot-to-shot fluctuations. We can determine the minimum resolvable electric field gradient $(dE/dr)_{\min}$ for the entanglement-assisted measurement. First, since we measure frequency differences $d\nu$, we need to convert:

$$\begin{aligned} \nu(r) &= \frac{1}{2}\alpha(E(r)+E_0)^2 \\ \frac{d\nu}{dr} &= \alpha(E(r)+E_0)\frac{dE}{dr} \\ \frac{dE}{dr} &= \frac{1}{\alpha(E(r)+E_0)}\frac{d\nu}{dr} \end{aligned} \tag{B.54}$$

where we assume a fixed distance $dr = r_{ab} = 3\,\mu m$ between the two atoms. The $(dE/dr)_{\min}$ is the one for which the signal-to-noise ratio SNR = 1. For our measurements:

$$\begin{aligned} SNR = \frac{d\nu}{(1/\tau)} &= 1 \\ \rightarrow d\nu_{\min} &= \frac{1}{\tau} \end{aligned} \tag{B.55}$$

where τ is the coherence time, which fundamentally limits the minimum resolvable frequency $d\nu_{\min}$. We replace that in Eq.(B.54):

$$\left(\frac{dE}{dr}\right)_{\min} = \frac{1}{\alpha(E(r)+E_0)}\frac{d\nu_{min}}{r_{ab}} = \frac{1}{\alpha(E(r)+E_0)}\frac{1}{r_{ab}}\frac{1}{\tau} \tag{B.56}$$

From Eq.(B.56), we can see that since the two single-atom measurement is limited by T_2^*, while the entangled state measurement is limited by T_W, we gain a factor of $T_W/T_2^* \sim 5$ in the minimum detectable electric field gradient. For the distances presented $(dE/dr)_{\min} \sim 10\text{V/cm}^2$ for the entangled-state measurement.

B.6.5 Effect of UV on electric field gradient

We use a similar approach to reconstruct the total electric field (E_x, E_y) at a different UV power. We combine the measurement of the energy difference between the two atoms $\nu_{AB}(x,\theta)$ with the shift of the Rydberg spectrum referenced to the infinite-distance energy of the previous measurement using the fitted values q, E_x, E_y from above. We have verified that the UV power shift used does not change the Rydberg spectral shift at 1300μm (see Fig. B.3), which we take to be the infinite-distance value. For the UV-shifted data we obtain $q = 201(6)$ e, and $(E_x, E_y) = (-0.25(1), -0.528(4))\text{V/cm}$. This results in $\Delta q = 11(12)$, and $(\Delta E_x, \Delta E_y) = (-0.23(3), -0.02(3))\text{V/cm}$ relative to the UV-shifted data. This suggests that at 160 μm a change of UV power of $\sim$ 200 nW mostly affects the background field in x rather than the charge on the SiN device.

Finally, we point out that the reconstruction of the electric field environment relies on the point charge and constant homogeneous background electric field model. Nevertheless, there are other dielectric surfaces present in the vacuum system in the vicinity of the device which could also be af-

fected by changing the power of the UV. A detailed study of these surfaces is beyond the scope of this paper, but their presence can be sensed by the behavior of the Rydberg spectral shift with UV at close and at far distances Fig. B.3. At far distances, we have seen that changing the UV power affects the background electric field by at most $\Delta|\mathbf{E}| \leq 0.05$ V/cm (Section B.3.1). This behavior is not captured by our minimal model. The reconstruction of the electric field given the UV-shifted data in Fig. 4 suggests that tuning the UV power over this range does not change the charge on the device but rather changes the background field by 0.23(3) V/cm. Having an additional surface which responds differently to the change of UV power could reconcile this by adding another distance-dependent electric field. Nevertheless, it is clear that tuning the UV power even by 200 nW can affect the charges on dielectric surfaces and can have a sizeable effect on the electric field environment in hybrid systems.

B.6.6 Anisotropic Rydberg blockade softening

The presence of an electric field from the device admixes nearby energy levels to the $|70S\rangle$ state, which are not circularly symmetric. This makes the Rydberg-Rydberg interaction strength anisotropic as a function of orientation of the two atoms. To probe this, we measure Rydberg blockade softening at 140 μm from the device and at an inter-atomic distance of 6.3 μm, manifested in population in the $|rr\rangle$ state after a π-pulse:

$$P_{rr} \approx \left(\frac{\Omega}{U}\right)^2 \tag{B.57}$$

Using this equation, we extract the Rydberg-Rydberg interaction U as a function of the relative angle θ between the inter-atomic axis and the $x-$axis, as depicted in Fig. 4 in the main text. In Fig. B.16 we compare the measured values of the Rydberg-Rydberg interaction with numerical calculations using the Pair Interaction Python package[203]. In the calculation, we use the fitted back-

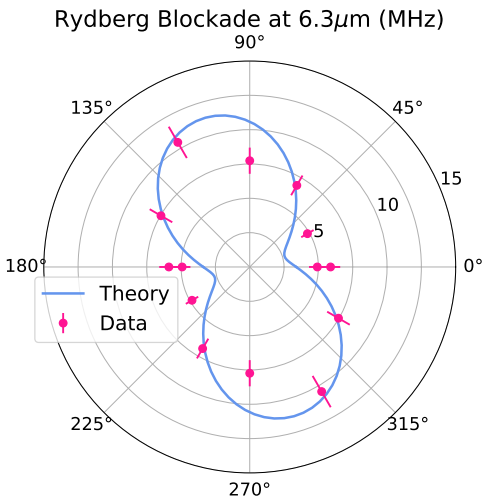


Figure B.16: Rydberg blockade softening at an inter-atomic distance of $6.3\,\mu$m. Polar plot of measured (pink) and calculated (blue) Rydberg-Rydberg interaction strength. We find reasonable agreement between data and theory when using the electric fields found by fitting the measured gradient as shown in Fig. 4(C) of the main text.

ground electric fields from the gradient measurements shown in Fig. 4(C) of the main text. We find good agreement between our measured data and theory, as one expects to have more blockade violations in the axis perpendicular to the electric field vector. This independent measurement provides further evidence that the electric field environment sensed through the gradient measurements is correct.

B.7 Optimizing the Rydberg quantum number n

In this experiment, we used the $|70S\rangle$ Rydberg state of ^{87}Rb. Due to the exploratory nature of this work, our Rydberg laser system is generated by seeding laser diodes using borrowed light from the neighboring Rydberg atom array lab [49], thereby using the same Rydberg state. However, the principal quantum number n could be optimized by taking into account the electric field noise measured in this paper. Since different properties scale differently with n, a better choice of n could be made for Rydberg atoms near our device. In particular, the polarizability α scales very rapidly as $\alpha \propto n^7$

and decreasing n would decrease the sensitivity to electric field noise. One could optimize n for two-atom gate fidelity, which when implemented with Rydberg atoms, typically relies on Rydberg blockade with $U \gg \Omega$. Since $U \propto C_6 \propto n^{11}$ and in our experiment $U/\Omega \sim 230$, n could be decreased to $n \sim 55$ without inducing significant Rydberg blockade errors, but reducing the sensitivity to electric field noise by a factor of ~ 5. While it is important to note that the lifetime of the Rydberg state decreases with n: $\tau_{sp} \propto n^3$ for spontaneous emission and $\tau_{BB} \propto n^2$ for black-body radiation, in the range of n between 50 and 70, this should not limit the gate fidelity.

C

Supplement of Chapter 7

C.1 Fiber Cavity Mounting and Parameters

Our fiber cavities are purchased from the company, Qlibri, with a coating with a reflectivity $> 99.993\%$ centered around 780 nm. A protective layer of SiO_2 is added as a final layer to the coating to prevent degradation in vacuum (*46*). We work with a single-mode (SM) fiber (IVG Cu800) with a radius of curvature (ROC) of 165 μm for the input mirror. For the output mirror, we use

a multi-mode (MM) fiber (Art Photonics MM50) with an ROC of 145 µm. Each fiber has a diameter of 125 µm. Our tweezers are formed with a 0.5 NA objective (Mitutoyo G Plan Apo 50X Objective). To allow for enough optical access for the optical tweezers, we choose a cavity length of 100 µm. The fiber cavities are mounted on a monolithic glass V-groove structure glued onto two shear piezo (CSAP02), which are glued on top of a glass slide. The fiber cavities are mounted into the V-grooves, then low expansion glue (Optocast 3410 Gen2-40K) is applied to the fibers. This is then mounted into an aluminum structure that secures the glass slide, as shown in the photos of Fig. C.1A.

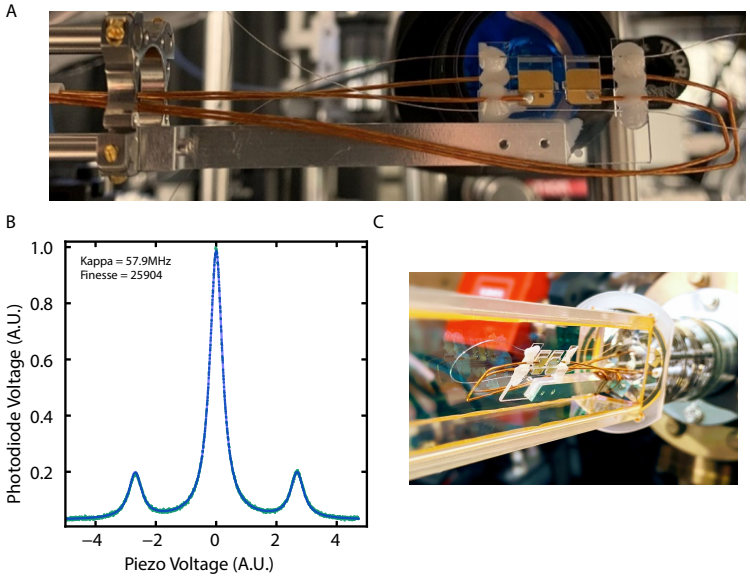


Figure C.1: FPFC Mounting and Characterization. (A) Photo of the mounting structure for the Fabry-Perot Fiber Cavity. (B) Cavity transmission *vs.* piezo voltage (blue circles) when probed with resonant light using 300 MHz sidebands. A fit to 3 Lorentzians (blue line) reveals the cavity linewidth $\kappa = 2\pi\times 57.9\,\mathrm{MHz}$ and finesse $\mathcal{F}_{cav} = 25904$ assuming a 100 µm length. (C) The mounting structure for the Fabry-Perot Fiber Cavity in vacuum

Both fibers are guided out of the vacuum chamber through a fiber feed-through. The fiber feed-through is composed of a two-hole Teflon piece tightened into a Swagelok (*47*). Upon placement in the vacuum chamber, the finesse of the cavity exceeded 40 000. During the bake-out, a sudden

change in temperature caused the cavity to become misaligned. This misalignment reduced the finesse to $\sim$ 25 000 and reduced the coupling between the mode out of the fiber and the mode of the cavity.

Finesse is measured by producing 300 MHz sidebands on an input laser with a fiber electro-optical modulator (EOM). These sidebands can then be used to measure the cavity linewidth by providing a way to transform piezo voltage into megahertz, assuming linear response. With this measurement and a separate measurement of the length of the cavity we can calculate a finesse of $F = 25,904$ as shown in Fig. C.1B. We find that the finesse is sensitive to temperature fluctuations. In particular the MOT beams and tweezers hitting the cavity result in small shifts of the resonance as well as the finesse. Upon running full experimental sequences we measured a κ of $2\pi\times65(1)$ MHz.

C.2 Experimental Methods

C.2.1 MOT and Tweezer Loading

Atoms are loaded in optical tweezers from a Magneto Optical Trap (MOT) which is formed above the FPFC. Fluorescence from atoms loaded in the tweezers is collected on single-photon avalanche detectors (SPADs) co-aligned with the tweezers. However, scattering of the MOT beams from the cavity and its mount prevents the MOT from forming within the cavity and also overwhelms the SPADs. To overcome these problems, we clip the horizontal MOT beams using razor blades placed in MOT beam paths. We fine-tune their position to optimize the atom loading into the tweezers. In addition, to reduce background counts from the light scattering by the MOT beams off the FPFC, we include an additional imaging beam that propagates along the MOT beam perpendicular to the FPFC. This beam is focused through the cavity such that, there is very little scattering. This beam is then pulsed out of phase with the MOT and the tweezers at 2 MHz. The experimental sequence for

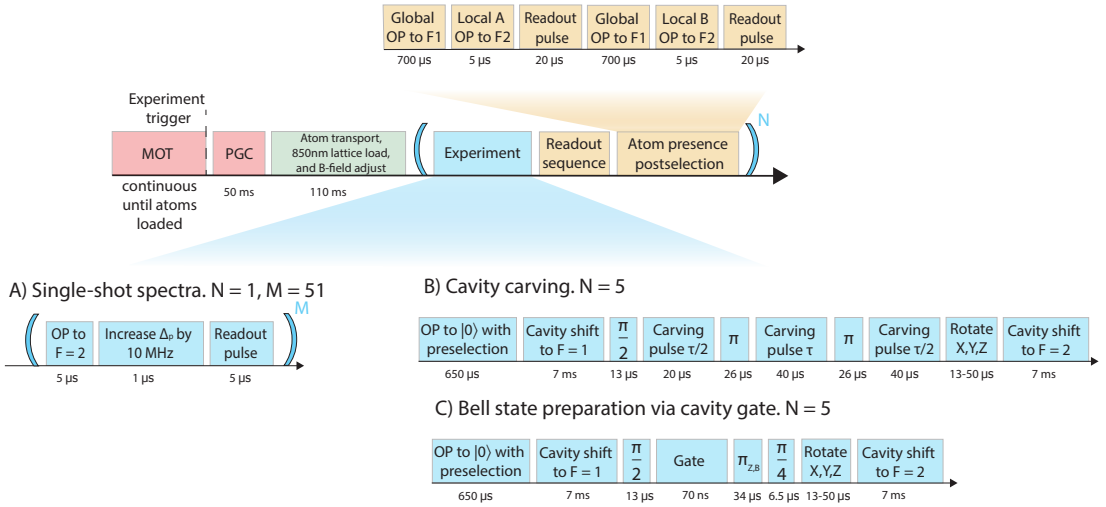


Figure C.2: Experimental Sequence for: A) the experiments presented in Figs. 1-2 in the main text; B) cavity carving and the data in Fig. 3 in the main text; and C) Bell state preparation using an error-detected gate and the data in Fig. 4 in the main text.

each of the experiments presented in the main text is shown in Fig. C.2. The sequence begins with polarization gradient cooling (PGC) for 50 ms, which reduces our temperatures to approximately 70 µK. The atoms are then transported to the cavity mode in 110 ms.

C.2.2 Atom Positioning in The Fiber Cavity

In order to ensure that the atoms are always coupled to the cavity mode, we use an additional optical lattice formed by an 850nm laser which is resonant with a cavity mode. The atoms are transported by the tweezers using galvo mirrors and loaded into the 850nm lattice. The 850nm and the 780nm modes are incommensurate and form a beat note with a period of 4.7 µm with regions where their maxima overlap. We position each of the tweezers in one such region. Fig. C.3, shows transmission spectra when a single atom is placed at different positions along the lattice. We place our atoms at the regions of maximum splitting between the hybridized atom-photon modes correspond to maxi-

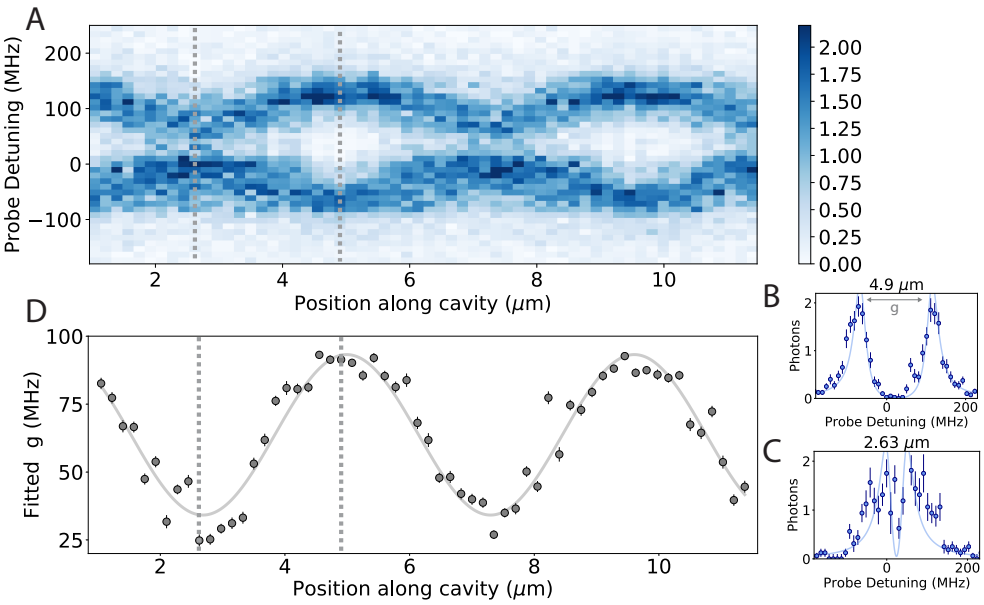


Figure C.3: Atom positioning in the cavity mode. **A** Single-shot spectra (averaged) of single atoms placed at different positions along the cavity. **B** and **C** Two such spectra at positions of minimum (2.64 um) and maximum (4.95 um) coupling. The solid lines are fits of the form $T(\delta)$ in (C.5). **D** Fitted atom-cavity coupling strength g as a function of position along the cavity. The solid line is a fit of the form $g(x) = a\cos(2\pi(x-x_0)/P) + c$. Note that we use the fitted period P to calibrate the distance along the cavity.

mum coupling g.

Before transitioning to the 850 nm lattice used in the experiments presented in the manuscript, we utilized an 810 nm lattice to characterize the cooperativity as a function of position over a 60 μm range, shown in Fig.C.4. These measurements validate that the cooperativity closely follows theoretical predictions for the cavity mode profile.

The usable area of the cavity is theoretically limited by clipping of the optical tweezers on the fiber cavity mirrors. Given the diameter of the fiber cavity 125 μm and the numerical aperture (NA = 0.5) of our optical tweezers, the unclipped region is expected to extend 32.5 μm in the center of the cavity. However, in practice, we achieve a usable range exceeding 60 μm with only a minor reduction in loading probability near the edges. This range is currently limited by the travel range of our optical tweezers, which could be extended in future experiments to further enhance the usable area.

Within the 60 μm usable region and given the 4.7 μm beat note of the 850 nm lattice, we can place up to 12 atoms at the antinodes of the cavity field. If we position atoms using our optical tweezers at a spacing of $3 \times 780nm$, we ensure alignment with antinodes while avoiding tweezer interactions. This configuration allows for the placement of up to 25 atoms within the unclipped cavity region. Across this range, the cooperativity varies between 70% and 100% of its maximum value, ensuring sufficient uniformity for high-fidelity operations on all atoms.

C.2.3 State Preparation

Atoms are prepared in the $|0\rangle = |F = 1, m_F = 0\rangle$ by applying a linearly polarized drive on the $|5S_{1/2}, F = 1\rangle \leftrightarrow |5P_{1/2}, F' = 1\rangle$ D1 transition while simultaneously applying a drive on the $|5S_{1/2}, F = 2\rangle \leftrightarrow |5P_{3/2}, F' = 1\rangle$ D2 transition with mixed polarization. With these drives, the $|F = 1, m_F = 0\rangle$ is a dark state, and the population is pumped there in 15 μs. Imperfect polarization limits this state preparation. To improve this scheme, we extend the duration of the D1 beam by

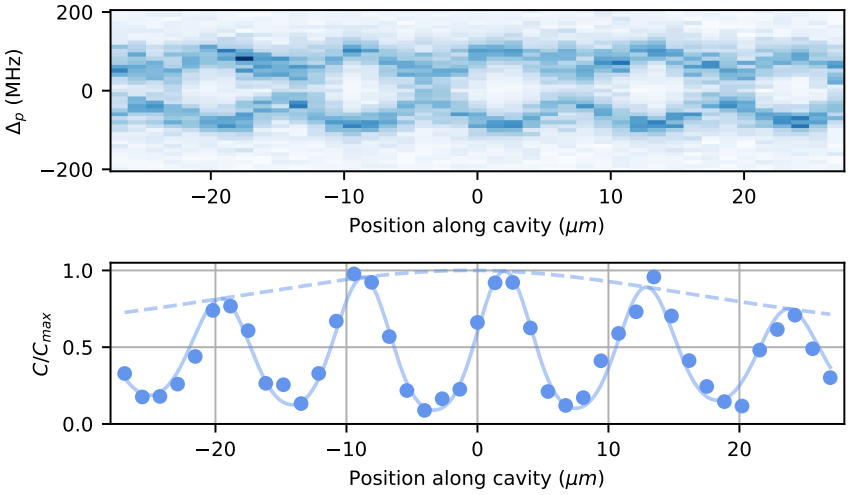


Figure C.4: Atom Positioning in the 810 nm Cavity Mode: We present single-shot spectra (averaged) of single atoms placed at various positions along the cavity using the 810 nm lattice. The cooperativity as a function of position is fit to a model based on the intensity profile of a standing-wave Gaussian beam. From this fit, we extract a Rayleigh range of $62(10)$ µm, consistent with a cavity waist of $3.9(3)$ µm. Additionally, the beat note between the 810 nm trap and the 780 nm mode yields a spatial period of approximately 11 µm.

3 µs, pumping the residual population from the $|F = 1, m_F = \pm 1\rangle$ states in to the $F = 2$ manifold. We then apply a readout pulse, resonant with the $2 \rightarrow 3'$ transition and postselect and discard the data when an atom in $F = 2$ is detected. This allows us to preselect the cases when optical pumping (OP) was successful before we begin the experiment. Note that this readout pulse does not affect the $|0\rangle$ state. The final state preparation fidelity is $> 99\,\%$.

C.2.4 Cavity and Laser Locking and Jumping

Fig. C.5shows a diagram of the cavity locking system. We stabilize the cavity length using a shear piezo and a Pound Drever Hall (PDH) lock, which uses the cavity reflection signal from an 810 nm DBR laser (Photodigm 808DBRH-TOSA). The frequency of the DBR laser is locked and controlled using an offset phase lock (Vescent D2-135) to reference it with a 810 nm ECDL laser (Toptica DL100 Pro ECDL). The ECDL laser, is locked to an ultra-low expansion (ULE) cavity using

a PDH lock to act as a stable reference. This system allows us to dynamically tune the cavity length and resonance. Using an analog channel and tunable voltage controlled oscillators (VCOs), we can dynamically tune the relative frequency between the tunable DBR laser and the stable ECDL laser. Taking advantage of the large current controlled mode-hop free range of the DBR laser, we achieve a tunability of up to $\sim$ 10 GHz, which correspond to $\sim$ 2 nm changes in the length of the cavity. By choosing correctly the reference line of the ULE cavity, we can match this tunable range to the D2 line of ^{87}Rb when locking the FPFC to the DBR laser. This system allows us to dynamically tune the cavity resonance through the whole hyperfine splitting of ^{87}Rb, which is 6.837 GHz.

Thanks to the small size of the FPFC, we can do this relatively quickly in $\sim$ 7 ms, limited only by resonant frequencies related to the lever-arm mechanical modes of the dangling fibers. After learning how to load atoms directly from a MOT close to these types of micro-cavities, we plan to increase the bandwidth of a next iteration by reducing the lever-arm length in the design. The resonance frequency of the lever arm scales as $\propto \frac{1}{L^2}$. By reducing the protruding fiber length by a factor of two, we can increase the system's bandwidth by a factor of four, without compromising our optical access.

An additional 850 nm DBR laser is used as a trap for the atoms, and it is continuously locked to the cavity with a PDH lock on the laser diode current. The circulating power of the 850 nm is $\sim$ 20 mW resulting in $\sim$ 24 MHz lightshift on the $2 \leftrightarrow 3'$ transition and similar magnitude trap depth. The circulating power of the 810 nm lock laser is $<$ 0.5 mW in comparison and has negligible trapping or lightshift effects.

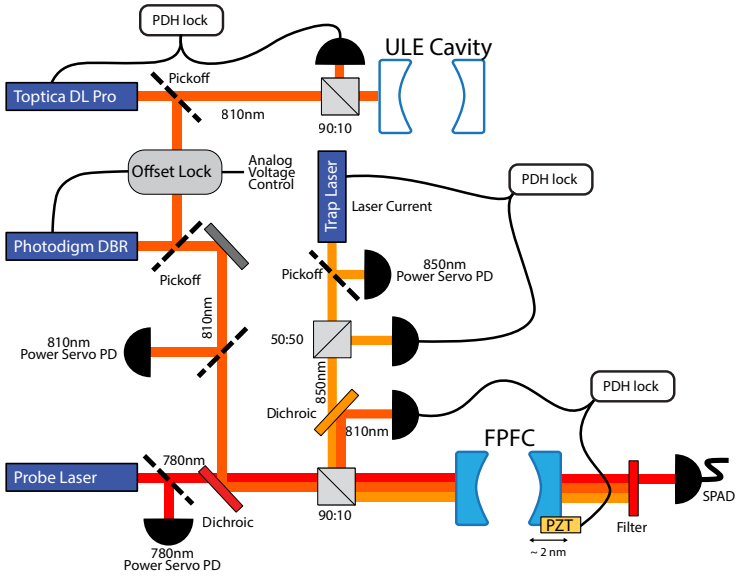


Figure C.5: FPFC laser system. Diagram of the lasers coupled to the FPFC and the different locking systems for the cavity and each laser. Waveplates and fiber couplings have been ommitted.

C.3 Readout

C.3.1 Detector System and Characterization

Readout is performed by measuring the difference in transmission with and without an atom coupled to the cavity. We collect the transmitted photons through the Multi-mode (MM) port of the FPFC. After filtering of the trap light, 780 nm light is then split on a 50:50 MM fiber beamsplitter and sent to two SPCM-AQRH-16-FC single photon avalanche detectors (SPADs) which are counted using a Swabian Time Tagger Ultra. We use two SPADs to effectively reduce the detector dead-time, increasing the bandwidth, and allowing for faster readout. We measure the effective detector dead-time by fitting the measured count-rate C_M versus the expected probe count-rate C_P

using the model:

$$C_M = (C_P + C_D)\, e^{-t_D(C_P+C_D)\tau_0} \tag{C.1}$$

Where we find that the detector dead time to be $t_D = 17(1)$ ns, C_D is the dark count-rate, and $\tau_0 = 50$ μs is the integrated time in the measurement (Fig. C.6A). The dead time limits the linearity of the detector to count rates below $\sim$ 10 Mcps. We find that the atom starts to be saturated well below this limit, even accounting for collection efficiency. Therefore, the readout is limited by the power with which we can drive the system before the atom is saturated, and we leave the weak-probe regime.

We directly measured the dark count-rate to be 115 cps, finding it to be much smaller than even the coupled atom count rates. As such, the dark count-rate can be ignored from the model.

C.3.2 Readout Fidelity

We perform a readout measurement by probing the cavity with a 780 nm laser pulse that is σ^+ circularly polarized and resonant with the $2 \leftrightarrow 3'$ cycling transition and the cavity. The polarization helps increase the readout fidelity, as it quickly pumps the atoms into the stretched $|2, 2\rangle$. For example, when reading out the clock state $|2, 0\rangle$, due to the degeneracy of the cavity, we quickly pump into the $|2, 2\rangle$ stretched state at a rate set by κ scattering a single photon. This result arises from coupling to a state described by $g_{\sigma^-} |2, 0\rangle |1\rangle_{\sigma^+} - g_{\sigma^+} |2, 2\rangle |1\rangle_{\sigma^-}$, as depicted in the lambda system in Fig. C.6B. Given the transition strengths of these particular transitions, the state is given by $\sqrt{\frac{1}{7}} |2, 0\rangle |1\rangle_{\sigma^+} - \sqrt{\frac{6}{7}} |2, 2\rangle |1\rangle_{\sigma^-}$.This state that decays into the stretched state $|2, 2\rangle$ with a probability of 86%. Consequently, on average, only 1.16 photons are needed for an atom initially in $|2, 0\rangle$ to be pumped into the stretched state. This state decays at a rate set by the cavity, making this pumping more rapid than one would expect from the atomic scattering rate γ. Additionally,

this pumping quickly places us into a state with a cycling transition without any atomic excitation, allowing us to take advantage of the cycling transition in the system for the highest readout fidelity.

When counting photons on transmission, there are two possible rates we can measure. When the cavity is empty, or the atoms inside are in an uncoupled state ($F = 1$ ground-state manifold), we observe a high (H) count rate C_M, shown in Fig. C.6A. We define 'high counts' as the photon detection rate observed when the cavity is empty or the atoms are in an uncoupled state ($F = 1$ ground-state manifold), leading to higher photon transmission through the cavity. Conversely, 'low counts' refer to the photon detection rate observed when atoms inside the cavity are in a coupled state (F = 2 ground-state manifold). In this case, the coupled atom effectively detunes the excited atom-cavity manifold, blockading the probe light and resulting in significantly reduced photon transmission, as shown in Fig. C.6C. C_{Atom} is about 2 orders of magnitude lower than C_M as the coupled atom effectively detunes the excited atom-cavity manifold and blockades the probe light. Both rates depend on the input probe power, which is directly proportional to the implied probe count-rate C_P. In the case of the coupled atom, we commonly work at a probe rate of $C_P \approx 1.75$ Mcps which sits right at the onset of where high counts start being affected by the detector dead-time and the low counts leave the linear weak-probe regime.

Readout Characterization

In practice, there are two different types of readout pulses we perform, which we call atom- and state-readout. The only difference between the two is whether we are concurrently optically pumping the atoms into the coupled state manifold. In this way, atom-readout measures presence by always having the atoms in the coupled state, and we use mostly for post-selection on atom survival. We characterize our readout fidelity by measuring a train of subsequent atom- and state-readout pulses initializing an atom in either coupled or uncoupled states using optical pumping, finalizing on an atom-readout pulse to post-select on atom presence. To ensure consistency and minimize

any potential sources of drift, the data for different probe powers were taken in parallel during the experiment over the course of 7 hours. Fig. C.6D shows a 2D histogram of the photon counts of subsequent atom- and state- readout pulses for atoms in the coupled and uncoupled states, as well as an empty cavity for comparison. To get good statistics at the high fidelities we are measuring, we have to accrue thousands of data points. We characterize loss by considering the number of events where atom presence is detected in the first measurement and not in the second measurement. Here we find that this occurs in 3 of 8687 events, setting a loss probability of $0.034^{+27}_{-6}\%$. The data presented is the same as for Fig. 1D of the main text, it corresponds to $C_P \approx 1.75$ Mcps and an integration time of 10 μs, which gives us the the highest measured state-readout fidelity of $99.960^{+14}_{-24}\%$ presented in the main text and corresponds to the usual probe power used throughout our experiments.

To measure readout fidelity, we need to understand the nature of photon counts, which can be described by the Poissonian distribution $P(\mu, k) = \frac{\mu^k e^{-\mu}}{k!}$. The curves on the count histograms of Fig. 1D of the main text are fits to this distribution. The fits give us two possible distributions: Low counts for atoms in a coupled stated with $\mu_L = 0.09(2)$ photons and High counts for atoms in an uncoupled state with $\mu_H = 16.600(1)$ photons. From these, we can calculate an optimal threshold by equating both distributions and finding an analytical form of $k_T = \left\lfloor \frac{\mu_H - \mu_L}{\log \mu_H - \log \mu_L} \right\rfloor = 3$ photons, where an atom will be labelled (L) as coupled if the measured counts are $\leq k_T$, or (H) and uncoupled otherwise. As such, we can theoretically estimate the expected False positive probability to be $P_{FP} = 1 - \sum_{k=0}^{k_T} P(\mu_L, k) = 2.7 \times 10^{-6}$ and the expected False negative probability to be $P_{FN} = \sum_{k=0}^{k_T} P(\mu_H, k) = 57 \times 10^{-6}$. while the analytical formula provides the theoretical expectation for setting an optimal threshold, in practice, we experimentally select the threshold that minimizes the error during calibration. Experimentally, we calculate the False positive and negative rates to be $P_{FP} = 4.6^{+3.6}_{-2.2} \times 10^{-4}$ and $P_{FN} = 3.5^{+3.3}_{-1.9} \times 10^{-4}$. This fidelity is calculated with no assumption about the distribution, relying solely on an optimized choice of threshold based on

the measurements. The fidelity is determined by dividing the number of events above or below the threshold by the total number of repeated measurements, with error bars derived from the thresholding process using the Clopper-Pearson interval. For simplicity, we quote a single Infidelity probability $P_{Inf} = (P_{FP} + P_{FN})/2$ to be the average of the two, given an atom can only be in one of two states every readout pulse. The quoted readout fidelities are then $(1 - P_{Inf}) \times 100\,\%$. The estimated error for these measurements is the Clopper-Pearson interval.

Optimal integration time and Limitations

Using time-tagged photon counts, we are able to extract an infidelity curve against integration time τ (Fig. C.6E). As expected from theory, the larger time we integrate the more separated both cases get as $\mu_L = C_{Atom}\tau$ and $\mu_H = C_M\tau$, and the lower the infidelity gets. However, we observe that for longer integration times, the infidelity stops decreasing. One observation is that atom-readout is always better than state-readout, which can be explained by unwanted off-resonant scattering from the 850 nm optical trap which state-readout does not correct for as there is no optical pumping. Even for scattering timescales on the order of 100 ms, at an integration time of 10 μs the infidelity is already limited to the order of $\sim 10^{-4}$. The rest of the measured infidelity, we attribute to imperfect state preparation during the characterization experiment, which can be further optimized.

We can also look at the best measured infidelity as a measure of probe power, as shown in Fig. C.6F. At low powers, the count-rates are lower, so we need to integrate further. Therefore, the unwanted scattering becomes a more prominent limitation. At high powers, the weak-probe regime is broken and the effective ratio C_M/C_{Atom} decreases, which sets the possible difference between High and Low counts and is proportional to the attainable readout fidelity. Therefore, we find an optimum at $C_P \sim 1.75$ Mcps. We can, however, work at the stronger powers before the infidelity grows too large and have high-fidelity non-destructive state readout in the μs scale, limited by the effective dead-time of our detectors and our cavity linewidth κ.

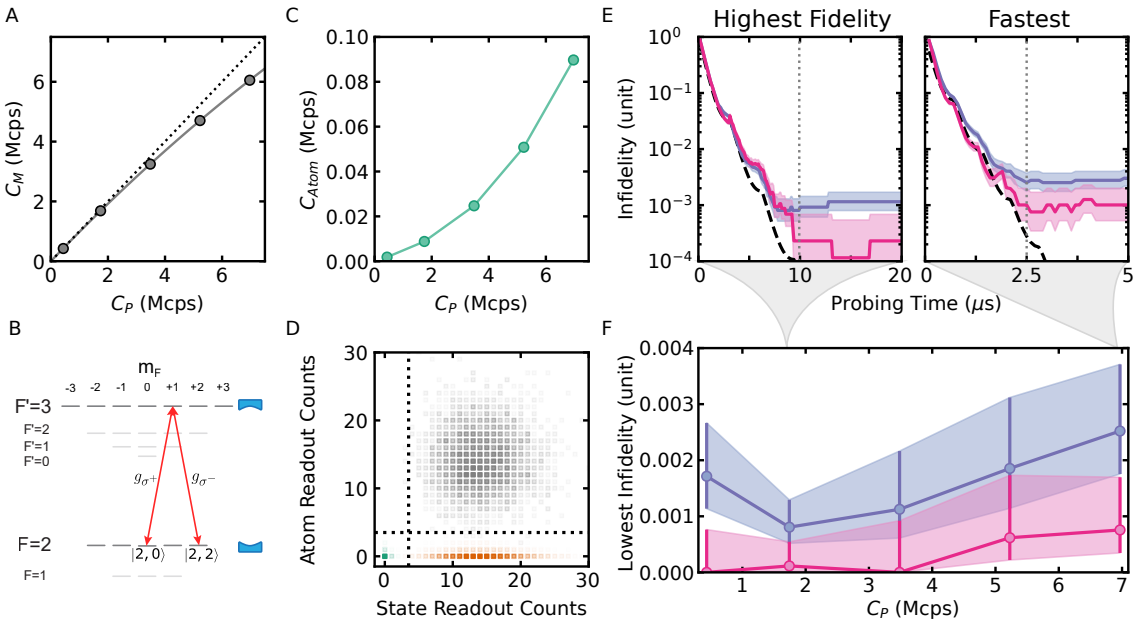


Figure C.6: Readout Characterization. (A) Measured count-rate C_M *vs.* probe count-rate C_P (gray circles) of our detection system with a fit (gray line) to model in Eqn. C.1 used to extract detector dead time. (B) Degenerate cavity allows for fast pumping into stretched state for enhanced coupling during readout. (C) Photon count-rate when with coupled atom C_{Atom} *vs.* probe count-rate C_P showing the breakdown of the linear weak-probe regime. (D) 2D histogram of readout pulse characterization, showing the counts of subsequent state- and atom-readout pulses for atoms in the coupled (green) and uncoupled (orange) ground state manifolds, as well as for an empty cavity (gray). Transparency is proportional to occurrence, normalized to the highest of each case. Dotted lines are optimal threshold to minimize infidelity. (E) Measured infidelity for atom (pink) and state (purple) readout *vs.* probing time for two different probe powers. Black dotted curves are the theoretical expected infidelity from the known count-rates. Gray dotted lines are the measured best probing time in each case to find minimum fastest infidelity. (F) Lowest measured infidelity for atom (pink) and state (purple) readout *vs* probe count-rate, which is proportional to the probe power.

C.3.3 Error detection through Readout pulse sequences

Single atom Readout

To read out the qubit states along with error states, we perform sequential readouts interspersed with coherent microwave rotations between our qubit states. We rely on our readout being non-destructive to the $|0\rangle$ state. Another important mechanism is that reading out an atom in the $|1\rangle$ state will quickly pump the atom into the $|2, 2\rangle$ stretched state. This pumping brings the atom out of the qubit manifold, resulting in no rotation when subsequent microwaves pulses are applied. Our single-atom readout sequence entails two successive readouts with a microwave π pulse applied in-between. Then, taking the above mechanisms into account, we find that the information from the two readout pulses will discriminate between the $|0\rangle$, $|1\rangle$ and error $|err\rangle$ states (Fig. C.7A). We denote a readout result as high (H) or low (L) depending on if the measured counts are above or below a selected threshold. This measurement determines whether an atom is in the coupled or uncoupled ground-state manifold.

Two atom Readout

To extend this to two atoms, we perform three sequential readouts with the addition of a local pumping beam that pumps atom B into the uncoupled $F = 1$ ground-state manifold, effectively "hiding" it from the readout. We note that when two atoms are coupled to the cavity, if either of the atoms is in the $|1\rangle$ state, the transmission of the cavity will be blocked. To distinguish which of the two atoms was in the coupled state, we must pump one of the two atoms out of the coupled state. To measure information about the two-atom state we first perform readout on both atoms, then hide atom B using a local depumping beam and then perform the single-atom readout sequence only on atom A. This allows us to extract full information about the state of atom A, while also extracting some information about the two-atom state.

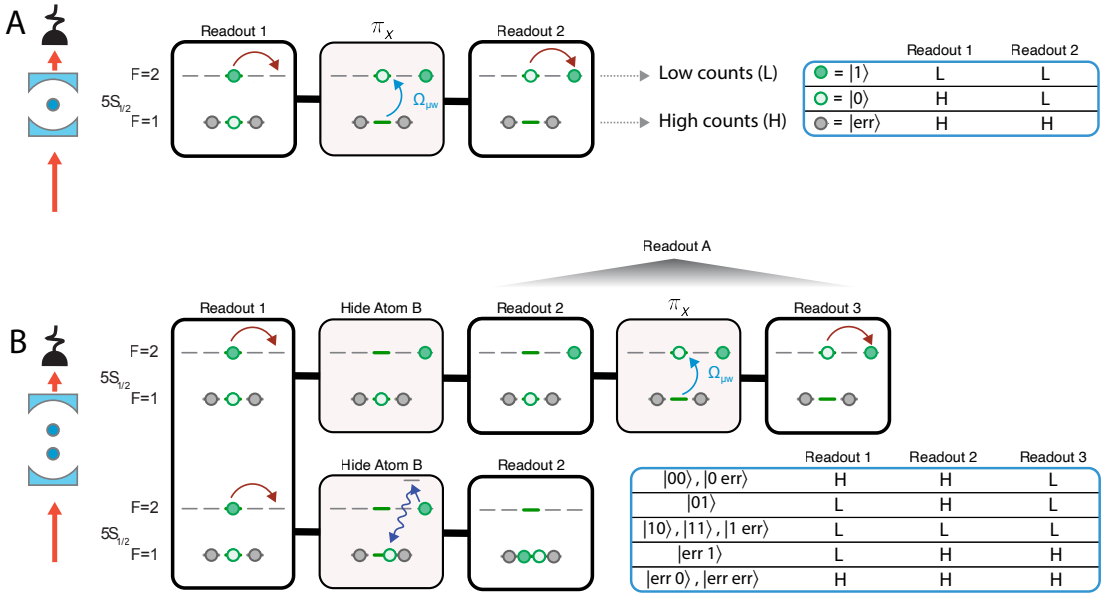


Figure C.7: Readout sequences for one (A) and two (B) atoms. The tables show the corresponding readout labels for each group of distinguishable states.

We find that this readout sequence can uniquely identify the populations in the $|00\rangle$ and $|01\rangle$ two-qubit states, while also being able to distinguish states where atom A has an error $|err\rangle_A$ (Fig. C.7B). We note that states where atom B is in the error state $|err\rangle_B$ are not distinguishable from $|0\rangle_B$. However, as explained in the entanglement generation section, these kinds of errors are suppressed.

C.4 Cavity Spectra

In the main text, we measure the spectra of the atom-cavity system under various driving conditions and number of atoms coupled to the cavity. The way that we do these measurements is in a "single-shot" as shown in Fig. C.7A. To understand the underlying physics of these spectra, we can consider the simplified Jaynes- and Tavis-Cummings Hamiltonians for one and two two-level atoms coupled to a single cavity mode. Using the rotating-wave approximation with respect to a drive, we can

express the Hamiltonian in the rotating frame as:

$$\hat{H}/\hbar = \Delta_c \hat{a}^\dagger \hat{a} + \sum_{\alpha=A,B} \left(\Delta_a \left|e\right\rangle \left\langle e\right|_\alpha + g_\alpha \left(\left|e\right\rangle \left\langle g\right|_\alpha \hat{a} + \left|g\right\rangle \left\langle e\right|_\alpha \hat{a}^\dagger \right) \right) \tag{C.2}$$

Where g_i is the single photon Rabi frequency of the atom i coupled to the cavity. Furthermore, Δ_c and Δ_a are the cavity and atom detuning from the drive, respectively. The driving terms can be expressed as:

$$\hat{H}_{probe}/\hbar = \Omega_{probe} \left(\hat{a}^\dagger + \hat{a} \right) \tag{C.3}$$

$$\hat{H}_{side}/\hbar = \sum_{\alpha=A,B} \frac{\Omega_{side,\alpha}}{2} \left|e\right\rangle \left\langle g\right|_\alpha + \frac{\Omega^*_{side,\alpha}}{2} \left|g\right\rangle \left\langle e\right|_\alpha \tag{C.4}$$

Where $\hat{H}_{probe}$ is a drive of the cavity by probing it as we do for readout, and η is the strength of said drive. Additionally, $\hat{H}_{side}$ considers a drive from the side of the cavity directly on the atoms, as we do for entanglement generation, where Ω_i is the strength of the side drive.

C.4.1 Weak-Probe Regime

For the purposes of the spectra shown in Figs. 1-2 of the main text, assuming this simplified two-level system we can find an analytical form for the spectra assuming a steady-state solution, which we use to extract our cavity parameters. In the following, we expand on the derivation show in the supplement of Ref. (*48*) accounting for multiple atoms and a side drive. From this treatment we

arrive at equations for intracavity photon number for side and cavity probe given by:

$$\left\langle a^\dagger a \right\rangle_{probe} \propto \left| \frac{\Omega_{probe}\sqrt{\kappa}}{\left(1+\tilde{C}_A+\tilde{C}_B\right)\tilde{\kappa}} \right|^2 \tag{C.5}$$

$$\& \qquad \left\langle a^\dagger a \right\rangle_{side} \propto \left| \sqrt{\frac{\gamma}{\tilde{\kappa}\tilde{\gamma}}} \frac{\left(\Omega_{side,A}\sqrt{\tilde{C}_A}+\Omega_{side,B}\sqrt{\tilde{C}_B}\right)}{\left(1+\tilde{C}_A+\tilde{C}_B\right)} \right|^2 \tag{C.6}$$

Where $\tilde{\kappa} = \frac{\kappa}{2} + i\Delta_c$ and $\tilde{\gamma} = \frac{\gamma}{2} + i\Delta_a$. The detunings Δ_a and Δ_c are defined as the detunings between the atom and the probe laser frequency, and the cavity and the probe laser frequency, respectively. We define a cooperativity given by $\tilde{C}_i = \frac{g_i^2}{\tilde{\kappa}\tilde{\gamma}}$. In this steady-state solution the number of leaked photons over some integration time will be directly proportional to the intracavity photon number. As a result, we use these analytical solutions to fit our cavity parameters to different spectra.

It is important to note that the effective cooperativity for the side probe differs from that for the cavity probe. This difference is due to the coupling to distinct atomic transitions. For the cavity probe, we send circularly polarized light along the cavity axis, which rapidly pumps the atom into the stretched state $|2,2\rangle$. In this state, the pump light couples only to the $|3,3\rangle$ excited state realizing a cycling two-level system, which for the Rb 87 level structure has the largest transition dipole moment, leading to a high cooperativity. However, with the magnetic field aligned along the cavity axis, it is not possible to drive the atom from the side using circularly polarized light. Instead, the atom occupies a mixture of other m_F states, which reduces the effective coupling strength and cooperativity. This reduction contributes to the observed difference in the vacuum Rabi splitting between Fig. 1C (cavity probe) and Fig. 2D (side probe).

Side Spectra

In practice, we always see the peaks corresponding to bright and dark states at the same time, as shown in Fig. 2 of the main text. We attribute this observation to thermal sampling of the atomic wave functions, leading to an effective incoherent drive of the system. For the purposes of fitting spectra, we build a fitting function that solves the master equation for Eqn. C.2 and averages both the case of in-phase and out-of-phase side drive. The fit is shown in Fig. 2D of the main text. Another interesting observation from these fits is that they account for an effective "broadening" of the dark-state line due to strong Ω_{side} driving.

We observe that the separation between the bright states is lesser than observed in the situation of the probe spectra. We understand this as an effect of weaker Clebsch-Gordan coefficients of the atomic steady-state solution. Our side drive Ω_{side} is linearly π^0 polarized. Due to this polarization, the steady state solution of the atomic states will fall around the middle m_F Zeeman sublevels. This is unlike the cavity probe, where circular polarization quickly pumps the atoms into the stretched state and effective two-level system. Since our magnetic field is aligned with the cavity axis, it is impossible to drive from the side with pure circular polarization. However, this polarization is what allows us to take advantage of the decay branching rations for error detection and entanglement generation.

As an addition, Fig. C.8 shows a side-spectra of the complete hyperfine manifold for a single atom under a side drive. This is just a more complete spectrum for the one shown in Fig. 2A of the main text. It also showcases how the Clebsch-Gordan coefficients affect the relative drive strength of Ω_{side} for different transitions.

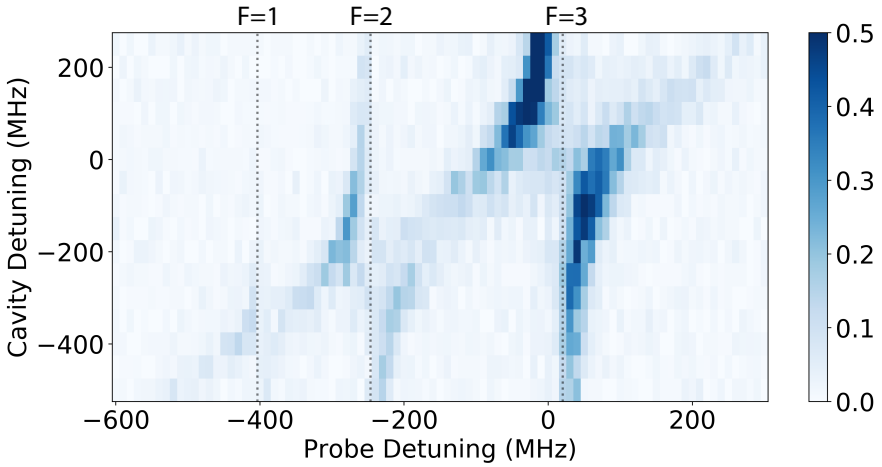


Figure C.8: Side spectrum of the ^{87}Rb D_2 line showing the avoided crossings and the hyperfine structure.

C.4.2 Two-level Numerical Simulation

An important result in our manuscript is the observation and use of photonic dark-states $|D_0\rangle$. These states can only be driven through a side drive, Ω_{side}, directly pumping excitation on the atoms. This is because the $|D_0\rangle$ states do not have any photonic component. To theoretically explain the measured spectra of our experiment, we cannot simply rely on the weak-probe regime analytical form of Eqn. C.6, as described in (*48*). This analytical form is sufficient to show the bright states $|B_\pm\rangle$ and $\sqrt{2}$ enhancement, but since the main approximation is that no atom ever gets excited, it cannot show any feature due to the photonic dark state.

To correctly account for full two atom spectra, we instead solve for the steady-state using the master equation of the two-level atom Hamiltonian, shown in Eqn. C.2 using the python package QuTiP (*49*). A surprising initial observation, shown in Fig C.9B, is the detection of photons in the cavity at the dark-state resonance. This is the result of excitations from the dark state to a state where both atoms are excited, $|gg,0\rangle \leftrightarrow \sqrt{1/2}(|eg,0\rangle - |ge,0\rangle) \leftrightarrow \sqrt{2/3}|ee,0\rangle - \sqrt{1/3}|gg,2\rangle$. The $\sqrt{2/3}|ee,0\rangle - \sqrt{1/3}|gg,2\rangle$ state contains a photonic component, thus producing intracavity

photons at the dark-state resonance. This process is observed in and described in Ref. *(20)*.

Furthermore, it is important to note that the side drive Ω_{side} acts on both atoms. Whether we excite the dark state (antisymmetric superposition) or the bright state (symmetric superposition) depends on both the relative coupling of the atoms to the cavity mode, determined by their spatial position along the cavity, and the relative phase between the atoms and the incident beam, determined by their spatial position along the driving beam. In practice, we always see the peaks corresponding to bright and dark states at the same time, as shown in Fig. 2 of the main text. We attribute this observation to thermal sampling of the atom positions in the direction of propagation of the drive beam causing a difference in the phase of the drive for the two atoms. For the purposes of fitting spectra, we build a fitting function that solves the master equation for Eqn. C.2 and averages both the case of in-phase and out-of-phase side drive equally. The fit is shown in Fig. 2D of the main text. Another interesting observation from these fits, is that they account for an effective "power broadening" of the dark-state line due to strong Ω_{side} driving.

To make coupling to the bright or dark states robust to this thermal sampling, we choose to work with a local driving beam, instead of the global drive that we have described above. With this configuration, we are able to couple to the dark state and bright state regardless of the position of the two atoms relative to each other or the phase of the driving beam. We model these dynamics with $\Omega_{side,B} = 0$.

C.4.3 "Loss" Spectra

One interesting observation of our entanglement generation protocol is the ability to conditionally couple atom A to a photonic dark state based on the state of atom B (Fig. 3A of main text). Particularly, in the carving scheme we quickly pump state $|10\rangle$ into the detectable error states $|err\rangle_A$ while other states like $|11\rangle$ are pumped much slower. This asymmetry in their decay, which is shown in Fig. 3B of the main text, is what allows us to carve out parts of the state and generate high fidelity

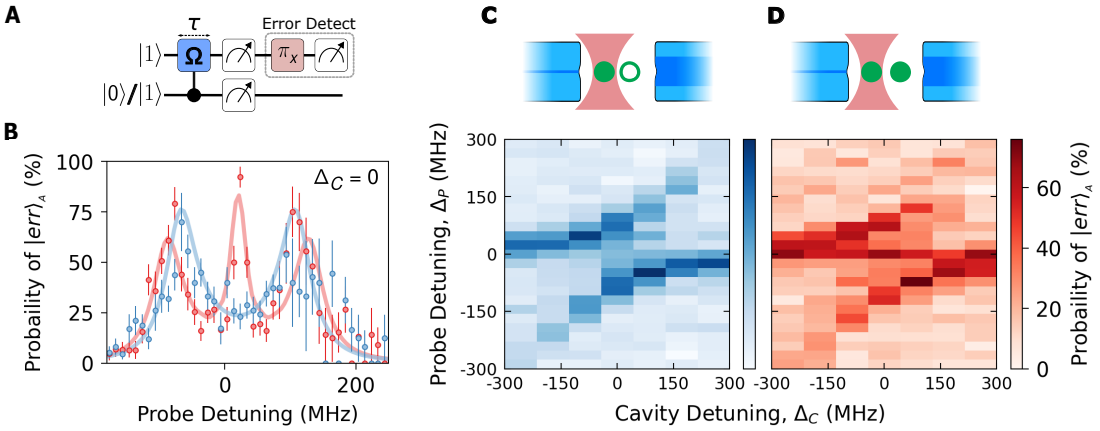


Figure C.9: (A) Quantum circuit for preparing two-qubit states and measuring the $|err\rangle_A$ population. (B) With the cavity tuned to the $2 \leftrightarrow 1'$ transition, we measure the probability of transferring population to the $|err\rangle_A$ state as a function of probe detuning for the $|11\rangle$ state (blue) and the $|10\rangle$ state (red). The solid line shows theoretical simulations of the system with characteristic parameters. This curve shows relative agreement of the numerical model with experimental data, and is not used to extract any specific parameters. (C-D) Measurements of the probability of transferring population to the $|err\rangle_A$ as a function of both probe detuning and cavity detuning for the $|11\rangle$ state (C) and the $|10\rangle$ state (D)

Bell states. However, it does depend on the side drive on atom A being exactly in resonance with the photonic dark state in the $2 \leftrightarrow 1'$ transition. We calibrate this detuning by measuring what we call "loss" spectra.

We can understand the "loss" spectra as simply a measurement of the probability of being in the error state $|err\rangle_A$ after a pulse of some short length. For example, we can choose a pulse length from Fig. 3B where state $|10\rangle$ has not been completely pumped into the error state and vary the probe detuning.

C.5 Experimental Characterization of the Entanglement Fidelity

C.5.1 Measuring Entanglement Fidelity

In our experiments, we use two different entanglement generation schemes to prepare two-qubit B Bell states of the form $|\Phi^{\pm}\rangle = \frac{1}{\sqrt{2}}(|00\rangle \pm |11\rangle)$. If we assume that after an experiment, our

two-atom state is described by a density matrix ρ, then the entanglement fidelity is simply:

$$\mathcal{F}_{|\Phi^{\pm}\rangle} = \langle\Phi^{\pm}|\rho\,|\Phi^{\pm}\rangle = \frac{1}{2}\left(\rho_{00,00} \pm \rho_{00,11} \pm \rho_{11,00} + \rho_{11,11}\right) \tag{C.7}$$

The fidelity of the $|\Phi^{+}\rangle$ state is used to define the fidelity for the carving results, while the fidelity of the $|\Phi^{-}\rangle$ state is used to evaluate the results of the phase gate.As explained in the main text, we measure the diagonal elements of the quantum state in all three possible bases XX, YY, and ZZ by controlling the relative phase of global microwave pulses and rotating state ρ. We measure the population in $|11\rangle$ and $|10\rangle$ by performing a π-pulse for a total of 6 measurements: 2 measurements per each basis. This gives us a total of 12 data points corresponding to the 4 diagonal populations in each basis (i.e., $P_z(|00\rangle) = P^{z}_{00} = \rho_{00,00}$). The ZZ basis is the one in which we define our state. The XX and YY basis are accessed using $\pi/2$ rotations into the equator of the generalized Bloch sphere. With our measurements, we have direct access to both the parity of the state and its trace as measured in different basis:

$$\Pi_i = P^{i}_{00} - P^{i}_{01} - P^{i}_{10} + P^{i}_{11} \tag{C.8}$$

$$\mathrm{Tr}_i = P^{i}_{00} + P^{i}_{01} + P^{i}_{10} + P^{i}_{11} \tag{C.9}$$

Where $i = x, y, z$ is the measurement basis, Π_i is the state parity in basis i, and Tr_i is the measure trace over the qubit manifold in basis i. Importantly, since the qubit rotations do not take us out of the qubit manifold, it is easy to show that:

$$\mathrm{Tr}_x = \mathrm{Tr}_y = \mathrm{Tr}_z = \rho_{00,00} + \rho_{01,01} + \rho_{10,10} + \rho_{11,11} \tag{C.10}$$

In the case where there are no errors, $\mathrm{Tr}_i = 1$, as expected for a valid density matrix ρ. However, this is not the case of states which have component in error states outside the qubit manifold as in

the case of our deterministic entanglement measurement. Furthermore, the parities in the different bases can be expressed as:

$$\Pi_x = -\rho_{00,11} + \rho_{01,10} + \rho_{10,01} - \rho_{11,00} \tag{C.11}$$

$$\Pi_y = +\rho_{00,11} + \rho_{01,10} + \rho_{10,01} + \rho_{11,00} \tag{C.12}$$

$$\Pi_z = +\rho_{00,00} - \rho_{01,01} - \rho_{10,10} + \rho_{11,11} \tag{C.13}$$

This relations let us rewrite the entanglement fidelity in terms of the trace and state parity as:

$$\mathcal{F}_{|\Phi^{\pm}\rangle} = \frac{1}{4}\left(\langle \mathrm{Tr}\rangle \pm \Pi_x \mp \Pi_y + \Pi_z\right) \tag{C.14}$$

Here, $\langle \mathrm{Tr}\rangle = \frac{1}{3}\left(\mathrm{Tr}_x + \mathrm{Tr}_y + \mathrm{Tr}_z\right)$ represents the average qubit population measured across the three measurement bases. By averaging the traces across all measurement bases, we reduce the error due to a larger sample size (drawing from all three measurements) and mitigate the effects of imperfect microwave rotations, which can otherwise lead to inaccurate assessments of the qubit state population. The sign for the X and Y parities reflects what is expected for each Bell state and is explicitly shown in the choice of direction for the measured correlations in Fig. 3C and Fig. 4D of the main text. To extract the entanglement fidelity, we substitute the values in Eqn. C.14, using the expressions for the parity (Eqn. C.8) and trace (Eqn. C.9) in terms of the 12 measured values and propagate uncertainty assuming uncorrelated errors. This equation has the benefit that it is agnostic to whether or not we are using error detection in our measurement, and is how we are able to measure verifiable deterministic entanglement.

C.6 Theoretical Models

C.6.1 First excitation manifold

Our entanglement scheme relies on the fact that the strong cooperativity in our system, allows us to spectroscopically resolve a photonic two-atom dark-state from all other possible states. This capability enables conditional operations using a ground-state qubit encoding between cavity coupled $|1\rangle$ and uncoupled $|0\rangle$ states.

Our scheme can be simply understood considering the simplified two-level atom system described by the Tavis-Cummings Hamiltonian shown in Eqn. C.2. When both the cavity, atom, and drive are resonant such that $\Delta = \Delta_a = \Delta_c = 0$, it is easy to diagonalize the Hamiltonian and find the eigenvalues of the single-excitation manifold. In the case of only atom A coupled to the cavity where $g_B = 0$ (i.e., Atom B is in the uncoupled state $|0\rangle$, the eigenstates take the form:

$$|\pm\rangle = \frac{1}{\sqrt{2}} \left(|e, 0\rangle \pm |g, 1\rangle \right) \tag{C.15}$$

With their eigenvalues being $E_\pm = \pm g_A$. This strong vacuum-Rabi splitting effectively suppresses the drive excitation rate proportionally to the single-atom cooperativity C.

However, when both atoms are equally strongly coupled to the cavity $g_A = g_B = g_0$, there are now three eigenstates:

$$|B_\pm\rangle = \frac{1}{2} \left(|eg, 0\rangle + |ge, 0\rangle \right) \pm \frac{1}{\sqrt{2}} |gg, 1\rangle \tag{C.16}$$

$$|D_0\rangle = \frac{1}{2} \left(|eg, 0\rangle - |ge, 0\rangle \right) \tag{C.17}$$

The two "bright" states $|B_\pm\rangle$ are analogous to the single atom eigenstates with a stronger repulsion due to it being two atoms $E_\pm = \sqrt{2} g_0$. We denote these states as "bright" states due to their cavity-

like components that allow them to decay through the cavity. In contrast, we also find a third zero energy eigenstate $|D_0\rangle$. We label this a photonic "dark" state due to the lack of a cavity excitation. One can understand this state as a sub-radiant state in which the emission from the two atoms destructively interferes with each other's emission into the cavity, resulting in a state that cannot decay through the cavity.

C.6.2 Carving protocol

Now we can consider a more complicated level structure, as shown in Fig. C.10, in which one of the atoms, atom A, has a level structure composed of two qubit states, $|0\rangle_A$ and $|1\rangle_A$, an excited state, $|e\rangle_A$, and a state we will denote as the error state, $|err\rangle_A$. The $|err\rangle_A \rightarrow |e\rangle_A$ transition is coupled to the cavity, while the qubit states are not. Atom B will have similar structure with qubit states, $|0\rangle_B$ and $|1\rangle_B$, and the excited state, $|e\rangle_B$, in this atom the $|0\rangle_B \rightarrow |e\rangle_B$ state will be coupled to the cavity. Utilizing this level structure we can engineer a qubit state dependent decay that can be used to produce entanglement by effectively "carving out" parts of the wavefunction. This "carving" can be performed with a global beam; however, this requires a well-defined phase of the drive between the two qubits. To circumvent this issue, we perform the carving by driving only atom A on the $|1\rangle_A \rightarrow |e\rangle_A$ transition.

Now, with qubit states we can consider the evolution of each state, as shown in Fig. C.10. For the states where atom A is in $|0\rangle_A$ there is no evolution, the interesting cases are when atom A is in state $|1\rangle_A$. For the initial state, $|11\rangle$, the transition to the excited state will be allowed through this two-atom dark state due to the second atom being in a state coupled to the cavity, $|0\rangle_B$. For the initial state $|10\rangle$, the evolution will be the same as if only atom A were coupled to the cavity, resulting in a blockade of the excitation. If we treat this case more carefully, we will find a single atom dark state

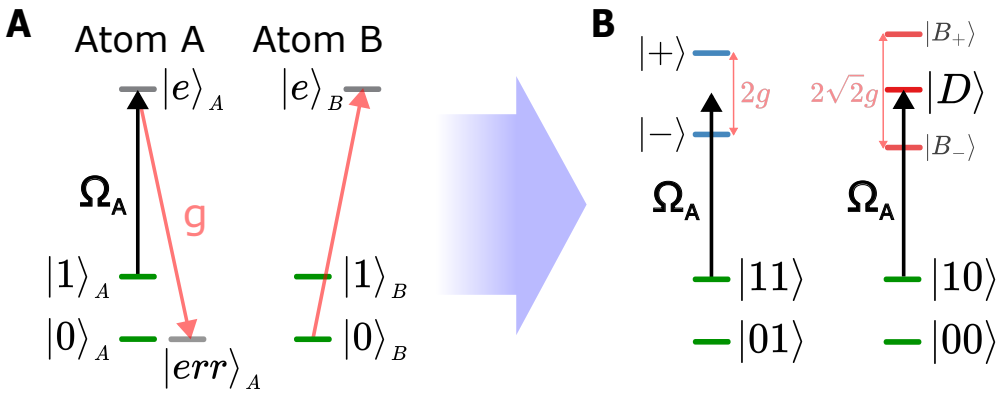


Figure C.10: (A) The level structure for both the carving and CZ gate protocols. The cavity is coupled to the $|err\rangle_A \leftrightarrow |e\rangle_A$ transition and the $|0\rangle_B \leftrightarrow |e\rangle_B$ transition. Atom A is driven from the side by a drive Ω_A that couples $|1\rangle_A$ and $|e\rangle_A$. (B) Upon diagonalization of the states coupled to the cavity, we show the effective level structure for a weak drive Ω_A. Here, the $|11\rangle$ state experiences a suppressed excitation due to the avoided crossing formed by the splitting of the states $|\pm\rangle = |e\rangle_A|0\rangle_{ph} \pm |err\rangle_A|1\rangle_{ph}$. The $|10\rangle$ state couples resonantly to the dark state $|D\rangle = \frac{1}{\sqrt{2}}\left(|e\rangle_A|0\rangle_B - |err\rangle_A|e\rangle_B\right)|0\rangle_{ph}$ while being detuned from the bright states $|B_\pm\rangle = \frac{1}{\sqrt{2}}|err\rangle_A|0\rangle_B|1\rangle_{ph} \pm \frac{1}{2}\left(|e\rangle_A|0\rangle_B + |err\rangle_A|e\rangle_B\right)|0\rangle_{ph}$.

that is formed between the states given by:

$$\frac{g}{\sqrt{\Omega_A^2+g^2}}|1\rangle_A|0\rangle_{ph} - \frac{\Omega_A}{\sqrt{\Omega_A^2+g^2}}|err\rangle_A|1\rangle_{ph} \tag{C.18}$$

This will result in decay through the cavity into the $|err\rangle_A|0\rangle_{ph}$ state with a rate given by:

$$\gamma_{|11\rangle} = \frac{\Omega_A^2}{\Omega_A^2+g^2}\kappa \approx \frac{\Omega_A^2}{C\gamma} \tag{C.19}$$

Now we investigate the $|10\rangle$ case. We can approximate the dynamics of this state by assuming $g > \Omega$ thus the drive is a small perturbation coupling the $|10\rangle$ state to the dark state, $|D\rangle = \frac{1}{\sqrt{2}}\left(|e\rangle_A|0\rangle_B - |err\rangle_A|e\rangle_B\right)|0\rangle_{ph}$. The drive term takes the form of $H_{dr} = \Omega_A|e\rangle\langle 1|_A + \Omega_A^*|1\rangle\langle e|_A$. Under these approximations we can assume that the rotation between an effective two-level system with the ground state, $|10\rangle$ and excited state, $|D\rangle$ with a transition dipole matrix element given by:

$$\hat{H}_{eff} = \frac{\Omega_A}{\sqrt{2}} |D\rangle \langle 10| + \frac{\Omega_A^*}{\sqrt{2}} |10\rangle \langle D| \tag{C.20}$$

We find that the dark state will decay at the same rate as an atom in free space, γ. As a result, the drive will depopulate the $|10\rangle$ state at a rate given by:

$$\gamma_{|11\rangle} = \frac{\Omega_{eff}^2}{\gamma} = \frac{\Omega_A^2}{2\gamma} \tag{C.21}$$

The excitation of the dark state can decay through atom A or atom B with a 50% probability due to the equal superposition of excitation. If the decay were to be through atom B, this would trap atom A in the error state, resulting in a fully detectable error. If atom A were to decay, the population will not always go to the error states, this decay will be determined by the branching ratios of the excited state. Through careful selection of atomic states, this ratio can be large and allow for almost fully detectable errors. This branching ratio sets a limit on the fidelity that one can achieve with this approach.

Due to the large ratio of decay between the $|11\rangle$ and $|10\rangle$ states, we can pump one state into the error state much faster than the other. Upon post selection of not being in the error state, this will then "carve out" one of the two states. We model this as applying a matrix:

$$\hat{U}_g = \begin{pmatrix} 1 & 0 & 0 & 0 \\ 0 & 1 & 0 & 0 \\ 0 & 0 & e^{-\gamma_{|11\rangle} t/2} & 0 \\ 0 & 0 & 0 & e^{-\gamma_{|10\rangle} t/2} \end{pmatrix} \tag{C.22}$$

Applying a π pulse in between two of these pulses will result in a matrix:

$$\hat{U}_{carve} = \hat{U}_g \hat{R}_x(\pi) \hat{U}_g = \begin{pmatrix} e^{-\gamma_{|10\rangle} t/2} & 0 & 0 & 0 \\ 0 & e^{-\gamma_{|11\rangle} t/2} & 0 & 0 \\ 0 & 0 & e^{-\gamma_{|11\rangle} t/2} & 0 \\ 0 & 0 & 0 & e^{-\gamma_{|10\rangle} t/2} \end{pmatrix} \tag{C.23}$$

By applying this matrix and renormalizing the population, we find that fidelity will exponentially approach unity while the success rate linearly decreases for large cooperativities.

$$P_{succ} = \langle \Psi_0 | \hat{U}^\dagger_{carve} \hat{U}_{carve} | \Psi_0 \rangle = \frac{e^{-\frac{\Omega_A^2}{C\gamma} t} + e^{-\frac{\Omega_A^2}{2\gamma} t}}{2} \tag{C.24}$$

$$\mathcal{F} = \left| \frac{\langle \Phi^+ | \hat{U}_{carve} | \Psi_0 \rangle}{\sqrt{\langle \Psi_0 | \hat{U}^\dagger_{carve} \hat{U}_{carve} | \Psi_0 \rangle}} \right|^2 = \frac{e^{-\frac{\Omega_A^2}{C\gamma} t}}{e^{-\frac{\Omega_A^2}{C\gamma} t} + e^{-\frac{\Omega_A^2}{2\gamma} t}} = \frac{e^{-\frac{\Omega_A^2}{C\gamma} t}}{2 P_{succ}} \tag{C.25}$$

C.6.3 Simplified Two-Level Model for CZ Gate

Using the same setup as the carving procedure, depicted in C.10, we can also perform a controlled phase gate. The difference between the carving case and this case is that we drive with a stronger field, such that one performs a full 2π rotation between the ground state and the dark state. This understanding of the gate assumes that we are in a regime where the dark state is defined well with respect to the strength of the drive and that the drive is fast enough to perform a coherent 2π rotation. Overall, this results in the condition $g > \Omega > \gamma$. The scattering off the dark state will determine the success rate of the gate.

$$\varepsilon_{|S_1\rangle} = 1 - e^{-\frac{\pi\gamma}{2\Omega}} \approx \frac{\pi\gamma}{2\Omega} \tag{C.26}$$

The fidelity will then be limited to how much of this scattering results in a detectable error. Decay out of the second atom will be completely detectable because the excitation of the second atom is correlated with the first atom being in the error state. For the other part of the wave function, we consider decay to states with undetectable errors, for example, decaying back into the qubit manifold. We can denote this decay as γ_{bad}. This results in a total uncorrectable error, given by:

$$\varepsilon_{uncorr} \approx \frac{\gamma_{bad}}{\gamma} \frac{\pi\gamma}{2\Omega} \tag{C.27}$$

For now, we will consider $\gamma_{bad} = 0$ and see how the fidelity will scale. We can consider the case with the initial state $|S_e\rangle$. For this state we can treat the system as if it is a single atom coupled to the cavity as shown in the carving protocol. Given the gate time, $\frac{\pi}{\Omega}$, this will result in a decay of the $|S_e\rangle$ state into the $|err\rangle_A$ state of:

$$\varepsilon_{|S_e\rangle} = 1 - e^{-\frac{\pi\gamma_{eff}}{\Omega}} \approx \frac{\pi\Omega\kappa}{\Omega^2 + g_{1-1'}^2} \approx \frac{\pi\Omega}{C\gamma} \tag{C.28}$$

In principle, all these errors should be detectable. Now, we must consider what correction does to our final state. The unitary that the gate will apply is given below. Here we do not include the error state manifold making this matrix not conserve population:

$$\hat{U}_g = \begin{pmatrix} 1 & 0 & 0 & 0 \\ 0 & 1 & 0 & 0 \\ 0 & 0 & -e^{-\frac{\pi\gamma}{2\Omega}} & 0 \\ 0 & 0 & 0 & e^{-\frac{\pi\Omega\kappa}{\Omega^2+g_{1-1'}^2}} \end{pmatrix} \tag{C.29}$$

If we consider the ideal CZ gate to be:

$$\hat{U}_{CZ} = \begin{pmatrix} 1 & 0 & 0 & 0 \\ 0 & 1 & 0 & 0 \\ 0 & 0 & -1 & 0 \\ 0 & 0 & 0 & 1 \end{pmatrix} \tag{C.30}$$

Then we can define a gate fidelity as:

$$\mathcal{F} = \left| \langle \Psi_0 | \, \hat{U}_{CZ}^{\dagger} \hat{U}_g \, | \Psi_0 \rangle \right|^2 = \frac{1}{16} \left(2 + e^{-\frac{\pi\gamma}{2\Omega}} + e^{-\frac{\pi\Omega\kappa}{\Omega^2 + g_{1-1'}^2}} \right)^2 \tag{C.31}$$

Where $|\psi_0\rangle$ is an equal superposition of all two qubit states. Given that we are in the strong coupling regime we can use the approximations from Eqn. C.26 and Eqn. C.28 to simplify this equation. We can then maximize fidelity by finding an optimal Rabi frequency. We find an optimal Rabi frequency and maximum fidelity, given by:

$$\Omega_{opt} = \sqrt{\frac{g_{1-1'}^2}{\frac{2\kappa}{\gamma} - 1}} \approx \sqrt{\frac{C}{2}}\gamma \tag{C.32}$$

$$\mathcal{F}_{uncorr} \approx \left(1 - \frac{\pi}{2\sqrt{2C}} \right)^2 \tag{C.33}$$

We find that the optimal fidelity is found when the loss of the $|10\rangle$ and $|11\rangle$ are symmetric. After post-selection, the state will be projected out of the error state using the projection matrix $\hat{M} = 1 - |err\rangle \langle err|$. Since the gate operator $\hat{U}_g$ is not population conserving, we can estimate the fully

corrected gate fidelity as:

$$\mathcal{P}_{success} = \langle \Psi_0 | \hat{U}_g^\dagger \hat{U}_g | \Psi_0 \rangle = 1 - \frac{\pi}{\sqrt{2C}} \tag{C.34}$$

$$\mathcal{F}_{corr} = \frac{\mathcal{F}_{uncorr}}{\mathcal{P}_{success}} = \frac{\left(1 - \frac{\pi}{2\sqrt{2C}}\right)^2}{1 - \frac{\pi}{\sqrt{2C}}} \tag{C.35}$$

We find that the fidelity is limited by the correction creating an imbalance of population between states where atom A is in $|0\rangle_A$ and states where atom A is in $|1\rangle_A$. By introducing a rotation, α, between the $|0\rangle_A$ and $|err\rangle_A$ we can improve the fidelity of the gate. This would modify Eqn. C.29 to:

$$\hat{U}_{g,\alpha} = \begin{pmatrix} \alpha & 0 & 0 & 0 \\ 0 & \alpha & 0 & 0 \\ 0 & 0 & -e^{-\frac{\pi\gamma}{2\Omega}} & 0 \\ 0 & 0 & 0 & e^{-\frac{\pi\Omega\kappa}{\Omega^2 + g_{1-1'}^2}} \end{pmatrix} \tag{C.36}$$

By including this operation in the gate and using the results for the optimal drive strength above, we find that there exists a value for α such that the corrected gate fidelity is unity at the cost of success probability. This condition can be met by finding a value of α such that $\hat{U}_{g,\alpha} \propto \hat{U}_{CZ}$. Upon renormaliation of the qubit states this will result in $\hat{U}_{g,\alpha} = \hat{U}_{CZ}$ This α can be intuitively understood as matching the loss of all qubit states:

$$\alpha = e^{-\frac{\pi}{\sqrt{2C}}} \tag{C.37}$$

$$\mathcal{F}_{uncorr} = \mathcal{P}_{success} = e^{-\frac{2\pi}{\sqrt{2C}}} \approx 1 - \frac{2\pi}{\sqrt{2C}} \tag{C.38}$$

$$\mathcal{F}_{corr} = \frac{\mathcal{F}_{uncorr}}{\mathcal{P}_{success}} = 1 \tag{C.39}$$

C.7 Theoretical Modelling for Rb-87

The full hyperfine structure of the ^{87}Rb D_2 line is shown in Fig. C.11. We assume negligible Zeeman splitting, such that all states in the same $F(F')$ manifold are degenerate in energy and that we are operating on two-photon resonance such that $\omega_c - \omega_L + \omega_0 - \omega_1 = 0$, where ω_c is the cavity resonance frequency, ω_L is the laser frequency, and ω_0 (ω_1) is the frequency of qubit state $|0\rangle$ ($|1\rangle$). Under these assumptions, only a small subset of states will be coupled by the laser driving and cavity field when both atoms start out in the qubit manifold and only atom A is driven. This allows us to write down the Hamiltonian of the two-atom system as

$$\begin{aligned}
\hat{H} \;=\;& \Delta\big(\,|e,0\rangle\,|0,0\rangle_c\,\langle e,0|_c\,\langle 0,0| + |e,1\rangle\,|0,0\rangle_c\,\langle e,1|_c\,\langle 0,0| + |S_e\rangle\,\langle S_e|\,\big) + \Delta_2\,|\tilde{S}_e\rangle\,\langle\tilde{S}_e| \\
&+\Delta_3\big(\,|e_3,0\rangle\,|0,0\rangle_c\,\langle e_3,0|_c\,\langle 0,0| + |e_3,1\rangle\,|0,0\rangle_c\,\langle e_3,1|_c\,\langle 0,0|\,\big) \\
&+\Big(\Omega\big(\,|e,0\rangle\,|0,0\rangle_c\,\langle 1,0|_c\,\langle 0,0| - \sqrt{9}\,|e_3,0\rangle\,|0,0\rangle_c\,\langle 1,0|_c\,\langle 0,0| + |e,1\rangle\,|0,0\rangle_c\,\langle 1,1|_c\,\langle 0,0| \\
&-\sqrt{9}\,|e_3,1\rangle\,|0,0\rangle_c\,\langle 1,1|_c\,\langle 0,0|\,\big) + h.c.\Big) \\
&+\left(g(|S_e\rangle\,\langle S_0| + \sqrt{2}\,|e,0\rangle\,|0,0\rangle_c\,\langle S_0| + \sqrt{2}\,|e,1\rangle\,|0,0\rangle_c\,\langle S_1| + \sqrt{\frac{1}{8}}\,|\tilde{S}_e\rangle\,\langle S_0|) + h.c\right)
\end{aligned} \tag{C.40}$$

as well as Lindblad operators describing spontaneous emission (γ) and cavity decay (κ):

$$\hat{L}_{c1} = \sqrt{\frac{\kappa}{2}}(|-,0\rangle |0,0\rangle_c \langle S_0| + |-,1\rangle |0,0\rangle_c \langle S_1|), \tag{C.41}$$

$$\hat{L}_{d} = \sqrt{\gamma_d}(|O_d,0\rangle |0,0\rangle_c \langle e,0|_c \langle 0,0| + |O_d,1\rangle |0,0\rangle_c \langle e,1|_c \langle 0,0|), \tag{C.42}$$

$$\hat{L}_{3d} = \sqrt{\gamma_{3d}}(|O_{3d},0\rangle |0,0\rangle_c \langle e_3,0|_c \langle 0,0| + |O_{3d},1\rangle |0,0\rangle_c \langle e_3,1|_c \langle 0,0|), \tag{C.43}$$

$$\hat{L}_{e1} = \sqrt{\frac{\gamma}{2}} |-,O_1\rangle |0,0\rangle_c \langle S_e| , \tag{C.44}$$

$$\hat{L}_{\tilde{e}1} = \sqrt{\frac{\gamma}{2}} |-,\tilde{O}_1\rangle |0,0\rangle_c \langle \tilde{S}_e| , \tag{C.45}$$

$$\hat{L}_{c2} = -\sqrt{\frac{\kappa}{2}}(|+,0\rangle |0,0\rangle_c \langle S_0| + |+,1\rangle |0,0\rangle_c \langle S_1|), \tag{C.46}$$

$$\hat{L}_{nd} = \sqrt{\gamma_{nd}}(|O_{nd},0\rangle |0,0\rangle_c \langle e,0|_c \langle 0,0| + |O_{nd},1\rangle |0,0\rangle_c \langle e,1|_c \langle 0,0|), \tag{C.47}$$

$$\hat{L}_{3nd} = \sqrt{\gamma_{3nd}}(|O_{3nd},0\rangle |0,0\rangle_c \langle e_3,0|_c \langle 0,0| + |O_{3nd},1\rangle |0,0\rangle_c \langle e_3,1|_c \langle 0,0|), \tag{C.48}$$

$$\hat{L}_{e2} = \sqrt{\frac{\gamma}{2}} |+,O_2\rangle |0,0\rangle_c \langle S_e| , \tag{C.49}$$

$$\hat{L}_{\tilde{e}2} = \sqrt{\frac{\gamma}{2}} |+,\tilde{O}_2\rangle |0,0\rangle_c \langle \tilde{S}_e| . \tag{C.50}$$

Here the notation $|x,y\rangle |1,0\rangle_c$ denotes atom A (2) in state $|x\rangle$ ($|y\rangle$) with one (zero) σ_+ (σ_-) polarized cavity photon. Additionally, we have defined the states

$$|S_x\rangle = \tfrac{1}{\sqrt{2}} \left(|-,x\rangle |1,0\rangle_c - |+,x\rangle |0,1\rangle_c\right) \tag{C.51}$$

$$|S_e\rangle = \tfrac{1}{\sqrt{2}} \left(|-,e_+\rangle |0,0\rangle_c + |+,e_-\rangle |0,0\rangle_c\right) \tag{C.52}$$

$$|\tilde{S}_e\rangle = \tfrac{1}{\sqrt{2}} \left(|-,\tilde{e}_+\rangle |0,0\rangle_c - |+,\tilde{e}_-\rangle |0,0\rangle_c\right) , \tag{C.53}$$

and the decay states $|O_d\rangle$ ($|O_{nd}\rangle$) to capture spontaneous emission to detectable (non-detectable) states from state $|e\rangle$ and similarly $|O_{3d}\rangle$ ($|O_{3nd}\rangle$) for state $|e_3\rangle$. Note that $\gamma_{nd} + \gamma_d = \gamma_{3nd} + \gamma_{3d} = \gamma$, where γ is the natural linewidth of the D2 transition. The ratio between the different decay rates

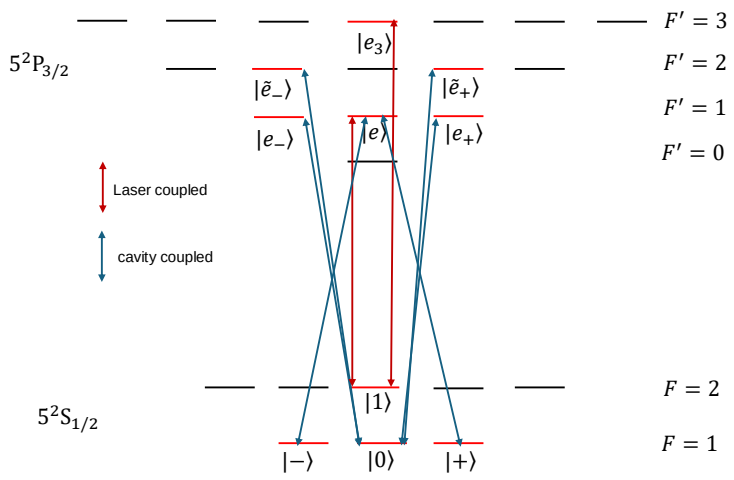


Figure C.11: Hyperfine structure of the D_2 line in ^{87}Rb. The laser driving and cavity field couples only a small subset of the hyperfine states marked in red under the assumptions mentioned in the main text.

into detectable and non-detectable states can be derived from the Clebsch-Gordan coefficients of the corresponding transitions. The decay states $|O_1\rangle$, $|O_2\rangle$, $|\tilde{O}_1\rangle$, $|\tilde{O}_2\rangle$ are introduced to capture decay from the excited states $|S_e\rangle$ and $|\tilde{S}_e\rangle$ in atom B, which is always detectable since it leaves atom A in state $|\pm\rangle$. This simplified model neglects additional higher-order dynamics following spontaneous emission from the atoms, which should be a valid approximation in the regime of weak driving and strong cooperativity considered here.

C.7.1 Carving protocol

For the carving protocol, the laser drive is weak ($\Omega \ll \gamma, g$), which allows us to adiabatically eliminate the entire excited subspace of the two-atom cavity system. Using the effective operator formalism from Ref. (*50*), we can analytically derive an effective Hamiltonian and effective Lindblad

operators describing the evolution of the qubit ground states. We find that these are of the form:

$$\hat{H}_{\text{eff}} = -\tilde{\Delta}_3 \left|1,0\right\rangle \left|0,0\right\rangle_c \left\langle 1,0\right|_c \left\langle 0,0\right| - \tilde{\Delta}_4 \left|1,1\right\rangle \left|0,0\right\rangle_c \left\langle 1,1\right|_c \left\langle 0,0\right|, \tag{C.54}$$

$$\hat{L}_{3d} = \sqrt{\Gamma_{3d}} \left|d\right\rangle \left\langle 1,0\right|_c \left\langle 0,0\right|, \tag{C.55}$$

$$\hat{L}_{3nd} = \sqrt{\Gamma_{3nd}} \left|nd\right\rangle \left\langle 1,0\right|_c \left\langle 0,0\right|, \tag{C.56}$$

$$\hat{L}_{4d} = \sqrt{\Gamma_{4d}} \left|d\right\rangle \left\langle 1,1\right|_c \left\langle 0,0\right|, \tag{C.57}$$

$$\hat{L}_{4nd} = \sqrt{\Gamma_{4nd}} \left|nd\right\rangle \left\langle 1,1\right|_c \left\langle 0,0\right|, \tag{C.58}$$

where we have introduced the notation $|d\rangle$ ($|nd\rangle$) to denote a non-specified subspace of detectable (non-detectable) error states. Driving on resonance ($\Delta = 0$), we can simplify the full analytical expressions in the large cooperativity limit ($C \gg 1$) to obtain

$$\tilde{\Delta}_3 \approx \left(\frac{9}{\Delta_3} + \frac{1}{36\Delta_2}\right)\Omega^2 \tag{C.59}$$

$$\tilde{\Delta}_4 \approx \frac{9\Omega^2}{\Delta_3} \tag{C.60}$$

$$\Gamma_{3d} \approx \frac{8\gamma + 4\gamma_d}{9}\frac{\Omega^2}{\gamma^2} \tag{C.61}$$

$$\Gamma_{3nd} \approx \frac{4\gamma_{nd}}{9}\frac{\Omega^2}{\gamma^2} \tag{C.62}$$

$$\Gamma_{4d} \approx \frac{\Omega^2}{2\gamma^2 C}\gamma + \frac{9\Omega^2}{\Delta_3^2}\gamma_{3d} \tag{C.63}$$

$$\Gamma_{4nd} \approx \frac{\Omega^2}{16\gamma^2 C^2}\gamma_{nd} + \frac{9\Omega^2}{\Delta_3^2}\gamma_{3nd}, \tag{C.64}$$

where we have also taken the limit of $\Delta_3, \Delta_2 \gg \gamma$.

For the carving protocol, the atoms are first prepared in the state $(|0,0\rangle + |0,1\rangle + |1,0\rangle + |1,1\rangle)/2$ and a laser drive is applied to atom A for a time t. After this, the qubit states are flipped and the same pulse is applied. Assuming that the single qubit operations are perfect and that all detectable error

states are perfectly detected, the atoms will be prepared in a state

$$\rho = \frac{1}{P}\left(|\psi\rangle\langle\psi| + \frac{1}{2}\left(\frac{\Gamma_{4nd}}{\Gamma_4}(1-e^{-\Gamma_4 t}) + \frac{\Gamma_{3nd}}{\Gamma_3}(1-e^{-\Gamma_3 t})\right)|nd\rangle\langle nd|\right), \tag{C.65}$$

where

$$|\psi\rangle = \frac{1}{2}\left(e^{(i\tilde{\Delta}_4-\Gamma_4/2)t}|0,0\rangle + e^{(i\tilde{\Delta}_3-\Gamma_3/2)t}|0,1\rangle + e^{(i\tilde{\Delta}_3-\Gamma_3/2)t}|1,0\rangle + e^{(i\tilde{\Delta}_4-\Gamma_4/2)t}|1,1\rangle\right), \tag{C.66}$$

and $\Gamma_3 = \Gamma_{3d} + \Gamma_{3nd}$, $\Gamma_4 = \Gamma_{4d} + \Gamma_{4nd}$. The success probability (i.e. probability not to detect the atoms in an error state) is

$$P = \frac{\Gamma_4\Gamma_3 - \frac{1}{2}(\Gamma_{4d}\Gamma_3 + \Gamma_4\Gamma_{3d})}{\Gamma_3\Gamma_4} + \frac{1}{2}\left(\frac{\Gamma_{4d}}{\Gamma_4}e^{-\Gamma_4 t} + \frac{\Gamma_{3d}}{\Gamma_3}e^{-\Gamma_3 t}\right). \tag{C.67}$$

The fidelity with the target Bell state $|\varphi\rangle = (|0,0\rangle + |1,1\rangle)/\sqrt{2}$ is $F = \langle\varphi|\rho|\varphi\rangle = \frac{1}{2P}e^{-\Gamma_4 t}$.

C.7.2 CZ-gate

For the CZ-gate, the laser drive is stronger, and we are in the regime $g \gg \Omega \gg \gamma$. We can therefore not directly adiabatically eliminate the entire excited manifold, as in the case of the carving protocol. Nonetheless, the dynamics can be treated separately depending on whether the initial atomic state is $|1,0\rangle$ ($|1,0\rangle|0,0\rangle_c$) or $|1,1\rangle$ ($|1,1\rangle|0,0\rangle_c$). Specifically, we can write the Hamiltonian in Eqn. (C.40)

as $\hat{H} = \hat{H}_3 + \hat{H}_4$, where

$$\begin{aligned}
\hat{H}_3 &= \Delta(|e,0\rangle|0,0\rangle_c\langle e,0|_c\langle 0,0| + |S_e\rangle\langle S_e|) + \Delta_3|e_3,0\rangle|0,0\rangle_c\langle e_3,0|_c\langle 0,0| + \Delta_2|\tilde{S}_e\rangle\langle\tilde{S}_e| \\
&\quad + \left(\Omega(|e,0\rangle|0,0\rangle_c\langle 1,0|_c\langle 0,0| - \sqrt{9}|e_3,0\rangle|0,0\rangle_c\langle 1,0|_c\langle 0,0|) + h.c.\right) \\
&\quad + \left(g(\sqrt{2}|e,0\rangle|0,0\rangle_c + |S_e\rangle + \sqrt{1/8}|\tilde{S}_e\rangle)\langle S_0| + h.c.\right) \qquad \text{(C.68)} \\
\hat{H}_4 &= \Delta|e,1\rangle|0,0\rangle_c\langle e,1|_c\langle 0,0| + \Delta_3|e_3,1\rangle|0,0\rangle_c\langle e_3,1|_c\langle 0,0| \\
&\quad + \left(\Omega(|e,1\rangle|0,0\rangle_c\langle 1,1|_c\langle 0,0| - \sqrt{9}|e_3,1\rangle|0,0\rangle_c\langle 1,1|_c\langle 0,0|) + h.c.\right) \\
&\quad + \sqrt{2}\left(g|e,1\rangle|0,0\rangle_c\langle S_1| + h.c.\right), \qquad \text{(C.69)}
\end{aligned}$$

and consider the evolution under each Hamiltonian separately. The corresponding Lindblad operators for the two subsystems are

$$\begin{aligned}
\hat{L}^{(3)}_{c1} &= \sqrt{\frac{\kappa}{2}}|-,0\rangle|0,0\rangle_c\langle S_0|, & \hat{L}^{(3)}_{c2} &= -\sqrt{\frac{\kappa}{2}}(|+,0\rangle|0,0\rangle_c\langle S_0|), \\
\hat{L}^{(3)}_{d} &= \sqrt{\gamma_d}|O_d,0\rangle|0,0\rangle_c\langle e,0|_c\langle 0,0|, & \hat{L}^{(3)}_{nd} &= \sqrt{\gamma_{nd}}(|O_{nd},0\rangle|0,0\rangle_c\langle e,0|_c\langle 0,0|), \\
\hat{L}^{(3)}_{3d} &= \sqrt{\gamma_{3d}}|O_{3d},0\rangle|0,0\rangle_c\langle e_3,0|_c\langle 0,0|, & \hat{L}^{(3)}_{3nd} &= \sqrt{\gamma_{3nd}}(|O_{3nd},0\rangle|0,0\rangle_c\langle e_3,0|_c\langle 0,0|), \\
\hat{L}^{(3)}_{e1} &= \sqrt{\frac{\gamma}{2}}|-,O_1\rangle|0,0\rangle_c\langle S_e|, & \hat{L}^{(3)}_{e2} &= \sqrt{\frac{\gamma}{2}}|+,O_2\rangle|0,0\rangle_c\langle S_e|, \\
\hat{L}^{(3)}_{\tilde{e}1} &= \sqrt{\frac{\gamma}{2}}|-,\tilde{O}_1\rangle|0,0\rangle_c\langle\tilde{S}_e|, & \hat{L}^{(3)}_{\tilde{e}2} &= \sqrt{\frac{\gamma}{2}}|+,\tilde{O}_2\rangle|0,0\rangle_c\langle\tilde{S}_e|,
\end{aligned} \qquad \text{(C.70)}$$

and

$$\begin{aligned}
\hat{L}^{(4)}_{c1} &= \sqrt{\frac{\kappa}{2}}|-,1\rangle|0,0\rangle_c\langle S_1|, & \hat{L}^{(4)}_{c2} &= -\sqrt{\frac{\kappa}{2}}|+,1\rangle|0,0\rangle_c\langle S_1|, \\
\hat{L}^{(4)}_{d} &= \sqrt{\gamma_d}|O_d,1\rangle|0,0\rangle_c\langle e,1|_c\langle 0,0|, & \hat{L}^{(4)}_{nd} &= \sqrt{\gamma_{nd}}|O_{nd},1\rangle|0,0\rangle_c\langle e,1|_c\langle 0,0|, \\
\hat{L}^{(4)}_{3d} &= \sqrt{\gamma_{3d}}(|O_{3d},1\rangle|0,0\rangle_c\langle e_3,1|_c\langle 0,0|), & \hat{L}^{(4)}_{3nd} &= \sqrt{\gamma_{3nd}}|O_{3nd},1\rangle|0,0\rangle_c\langle e_3,1|_c\langle 0,0|.
\end{aligned} \qquad \text{(C.71)}$$

Focusing on the dynamics of $\hat{H}_4$ first, we see that if we introduce the states $|E_\pm\rangle = \frac{1}{\sqrt{2}}\left(|e,1\rangle|0,0\rangle_c \pm |S_1\rangle\right)$ and assume that we are driving on resonance ($\Delta = 0$), the Hamiltonian simplifies to

$$\begin{aligned}\hat{H}_4 &= \Delta_3 |e_3,1\rangle|0,0\rangle_c \langle e_3,1|_c \langle 0,0| + \sqrt{2}g\left(|E_+\rangle\langle E_+| - |E_-\rangle\langle E_-|\right) \\ &\quad + \left(\Omega\left(\frac{1}{\sqrt{2}}\left(|E_+\rangle + |E_-\rangle\right) - \sqrt{9}|e_3,1\rangle|0,0\rangle_c\right)\langle 1,1|_c\langle 0,0| + h.c.\right). \quad \text{(C.72)}\end{aligned}$$

Since we are in the regime where $g \gg \Omega$, we can continue by eliminating the excited state manifold using the effective operator formalism as in the carving scheme. This gives the effective operators

$$\hat{H}_{4eff} \approx -\tilde{\Delta}_4 |1,1\rangle|0,0\rangle_c \langle 1,1|_c \langle 0,0| \quad \text{(C.73)}$$

$$\hat{L}_{4d} \approx \sqrt{\Gamma_{4d}}|d\rangle\langle 1,1|_c\langle 0,0| \quad \text{(C.74)}$$

$$\hat{L}_{4nd} \approx \sqrt{\Gamma_{4nd}}|nd\rangle\langle 1,1|_c\langle 0,0|, \quad \text{(C.75)}$$

where

$$\tilde{\Delta}_4 \approx \frac{9\Omega^2}{\Delta_3} \quad \text{(C.76)}$$

$$\Gamma_{4d} \approx \frac{9\Omega^2}{\Delta_3^2}\gamma_{3d} + \frac{\Omega^2}{2c}\gamma \quad \text{(C.77)}$$

$$\Gamma_{4nd} \approx \frac{9\Omega^2}{\Delta_3^2}\gamma_{3nd} + \frac{\Omega^2}{16c^2}\gamma_{nd}, \quad \text{(C.78)}$$

in the limit $\Delta_3 \gg \gamma$ and $c \gg 1$ as in the carving protocol.

We now turn to the dynamics under the Hamiltonian $\hat{H}_3$ (still operating at resonance, i.e., $\Delta = 0$). Assuming that $\Delta_3 \gg \sqrt{9}\Omega$ and that $\Delta_2 \gg \sqrt{1/8}g$, we can adiabatically eliminate the coupling

to the excited states $|e_3,0\rangle\,|0,0\rangle_c$ and $|\tilde{S}_e\rangle$. This results in the effective Hamiltonian

$$\begin{aligned}\hat{H}_3 \;\approx\; & -\frac{36\Delta_3\Omega^2}{4\Delta_3^2+\gamma^2}\,|1,0\rangle\,|0,0\rangle_c\,\langle 1,0|_c\,\langle 0,0| - \frac{1}{2}\frac{g^2\Delta_2}{4\Delta_2^2+\gamma^2}\,|S_0\rangle\,\langle S_0| \\ & + \Big(\Omega\,|e,0\rangle\,|0,0\rangle_c\,\langle 1,0|_c\,\langle 0,0| + g(\sqrt{2}\,|e,0\rangle\,|0,0\rangle_c + |S_e\rangle)\,\langle S_0| + h.c.\Big) \end{aligned} \tag{C.79}$$

and approximate Lindblad operators

$$\begin{aligned} &\hat{L}^{(3)}_{3d} \approx \frac{2\sqrt{9\gamma_{3d}}}{2\Delta_3 - i\gamma}\,|O_{3d},0\rangle\,|0,0\rangle_c\,\langle 1,0|_c\,\langle 0,0|\,, \qquad \hat{L}^{(3)}_{3nd} \approx \frac{2\sqrt{9\gamma_{3nd}}}{2\Delta_3 - i\gamma}\,|O_{3nd},0\rangle\,|0,0\rangle_c\,\langle 1,0|_c\,\langle 0,0|\,, \\ &\hat{L}^{(3)}_{\tilde{e}1} \approx \frac{\sqrt{\gamma}}{2}\frac{g}{2\Delta_2 - i\gamma}\,|-,\tilde{O}_1\rangle\,|0,0\rangle_c\,\langle S_0|\,, \qquad \hat{L}^{(3)}_{\tilde{e}2} \approx \frac{\sqrt{\gamma}}{2}\frac{g}{2\Delta_2 - i\gamma}\,|+,\tilde{O}_2\rangle\,|0,0\rangle_c\,\langle S_0|\,. \end{aligned} \tag{C.80}$$

We now find the bright (has a cavity photon component) and dark states (no cavity photon component) of the Hamiltonian by diagonalizing the part that involves the cavity coupling between states $|e,0\rangle\,|0,0\rangle_c$, $|S_0\rangle$, and $|S_e\rangle$. In the limit where $\Delta_2 \gtrsim g$, we find that the bright states are

$$|B_\pm\rangle \approx \frac{1}{\sqrt{2}}\,|S_0\rangle \pm \left(\frac{1}{\sqrt{3}}\,|e,0\rangle\,|0,0\rangle_c + \frac{1}{\sqrt{6}}\,|S_e\rangle\right), \tag{C.81}$$

while the dark state is $|D\rangle \approx \sqrt{\frac{2}{3}}\,|S_e\rangle - \frac{1}{\sqrt{3}}\,|e,0\rangle\,|0,0\rangle_c$. The Hamiltonian expressed in this basis is

$$\begin{aligned}\hat{H}_3 \;\approx\; & -\frac{36\Delta_3\Omega^2}{4\Delta_3^2+\gamma^2}\,|1,0\rangle\,|0,0\rangle_c\,\langle 1,0|_c\,\langle 0,0| + \Delta_+\,|B_+\rangle\,\langle B_+| + \Delta_-\,|B_-\rangle\,\langle B_-| \\ & + \Big(\Big(\Omega_+\,|B_+\rangle + \Omega_-\,|B_-\rangle - \Omega/\sqrt{3}\Big)\,\langle 1,0|_c\,\langle 0,0| + h.c.\Big)\,, \end{aligned} \tag{C.82}$$

where $\Delta_\pm \approx \mp\sqrt{3}g$ and $\Omega_\pm \approx \Omega/\sqrt{3}$. It is seen that we are driving the transition to the dark state on resonance, while the transitions to the bright states are off resonant. Consequently, we adiabatically eliminate the bright state dynamics, which results in an effective Hamiltonian and

Lindblad operators

$$\hat{H}_{3eff} \approx -\tilde{\Delta}_3 \left|1,0\right\rangle \left|0,0\right\rangle_c \left\langle 1,0\right|_c \left\langle 0,0\right|, \tag{C.83}$$

$$\hat{L}_{3d} \approx \sqrt{\Gamma_{4d}} \left|d\right\rangle \left\langle 1,0\right|_c \left\langle 0,0\right|, \tag{C.84}$$

$$\hat{L}_{3nd} \approx \sqrt{\Gamma_{4nd}} \left|nd\right\rangle \left\langle 1,0\right|_c \left\langle 0,0\right|, \tag{C.85}$$

$$\hat{L}_{Dd} \approx \sqrt{\Gamma_{Dd}} \left|d\right\rangle \left\langle D\right|, \tag{C.86}$$

$$\hat{L}_{Dnd} \approx \sqrt{\Gamma_{Dnd}} \left|nd\right\rangle \left\langle D\right|, \tag{C.87}$$

where

$$\tilde{\Delta}_3 \approx \frac{9\Omega^2}{\Delta_3} + \frac{1}{36}\frac{\Omega^2}{\Delta_2^2}, \tag{C.88}$$

$$\Gamma_{3d} \approx \frac{9\Omega^2}{\Delta_3^2}\gamma_{3d} + \frac{2\Omega^2}{9c}\gamma, \tag{C.89}$$

$$\Gamma_{3nd} \approx \frac{9\Omega^2}{\Delta_3^2}\gamma_{3nd}, \tag{C.90}$$

$$\Gamma_{Dd} \approx \frac{1}{3}\gamma_d + \frac{2}{3}\gamma, \tag{C.91}$$

$$\Gamma_{Dnd} \approx \frac{1/3}{\gamma_{nd}}. \tag{C.92}$$

Here the Lindblad operator $\hat{L}_{Dd}$ ($\hat{L}_{Dnd}$) describes decay from the dark state to detectable (non-detectable) states. It is seen that if the initial state is the ground state $\left|1,0\right\rangle \left|0,0\right\rangle_c$, a driving time of $t_g \approx \sqrt{3}\pi/\Omega$, will drive the population fully to the dark state and back again resulting in π-phase shift of the ground state up to a phase of $\tilde{\Delta}_3 t_g$.

Using the effective Hamiltonians and Lindblad operators from Eqns. (C.73)-(C.78) and Eqns. (C.83)-(C.92), we find that starting from an initial, unentangled state of $\frac{1}{2}\left(\left|0,0\right\rangle + \left|0,1\right\rangle + \left|1,0\right\rangle + \left|1,1\right\rangle\right)$, the final state following a successful CZ gate (i.e., no detectable

errors) will be

$$\rho \approx \frac{1}{P_g}\left(|\psi_g\rangle\langle\psi_g| + \frac{1}{4}\left(\frac{\Gamma_{4nd}}{\Gamma_4}(1-e^{-\Gamma_4 t}) + \frac{\tilde{\Gamma}_{3nd}}{\tilde{\Gamma}_3}(1-e^{-\tilde{\Gamma}_3 t})\right)|nd\rangle\langle nd|\right), \tag{C.93}$$

where

$$|\psi_g\rangle = \frac{1}{2}\left(|0,0\rangle + |0,1\rangle + e^{(i\tilde{\Delta}_3-\tilde{\Gamma}_3)/2)t_g}|1,0\rangle + e^{(i\tilde{\Delta}_4-\Gamma_4/2)t_g}|1,1\rangle\right), \tag{C.94}$$

with $\Gamma_4 = \Gamma_{4d} + \Gamma_{4nd}$, $\tilde{\Gamma}_{3d} = (\Gamma_{3d} + \Gamma_{Dd})/2$, $\tilde{\Gamma}_{3nd} = (\Gamma_{3nd} + \Gamma_{Dnd})/2$, and $\tilde{\Gamma}_3 = \tilde{\Gamma}_{3d} + \tilde{\Gamma}_{3nd}$. The success probability (i.e., probability not to detect the atoms in an error state) is

$$P_g \approx 1 - \frac{1}{4}\left(\frac{\Gamma_{4d}}{\Gamma_4}\left(1-e^{-\Gamma_4 t}\right) + \frac{\tilde{\Gamma}_{3d}}{\tilde{\Gamma}_3}\left(1-e^{-\tilde{\Gamma}_3 t}\right)\right). \tag{C.95}$$

The fidelity with the target Bell state of $(|0,0\rangle + |0,1\rangle - |1,0\rangle + |1,1\rangle)/2$ is

$$F \approx \frac{1}{16P_g}\left|2 + e^{(i\tilde{\Delta}_3-\tilde{\Gamma}_3)/2)t_g} + e^{(i\tilde{\Delta}_4-\Gamma_4/2)t_g}\right|^2. \tag{C.96}$$

Notably, this target Bell state is however not the optimal one due to the phase accumulation. This phase accumulation can be corrected using a local shift on one of the atoms.

D

Supplement of Chapter 8

D.1 Properties of the dielectric coating

The coating is performed by FiveNine Optics. They are quarter-wave stacks of 21 layers, with alternating materials of different refractive indices (n): SiO_2 ($n \sim 1.47$) and Ta_2O_5 ($n \sim 2.10$). The total thickness of the coating is, therefore 4.74 μm. Based on measurements provided by the vendor, the center wavelength where the mirrors are the most reflective is $\lambda = 781$ nm, and the transmission

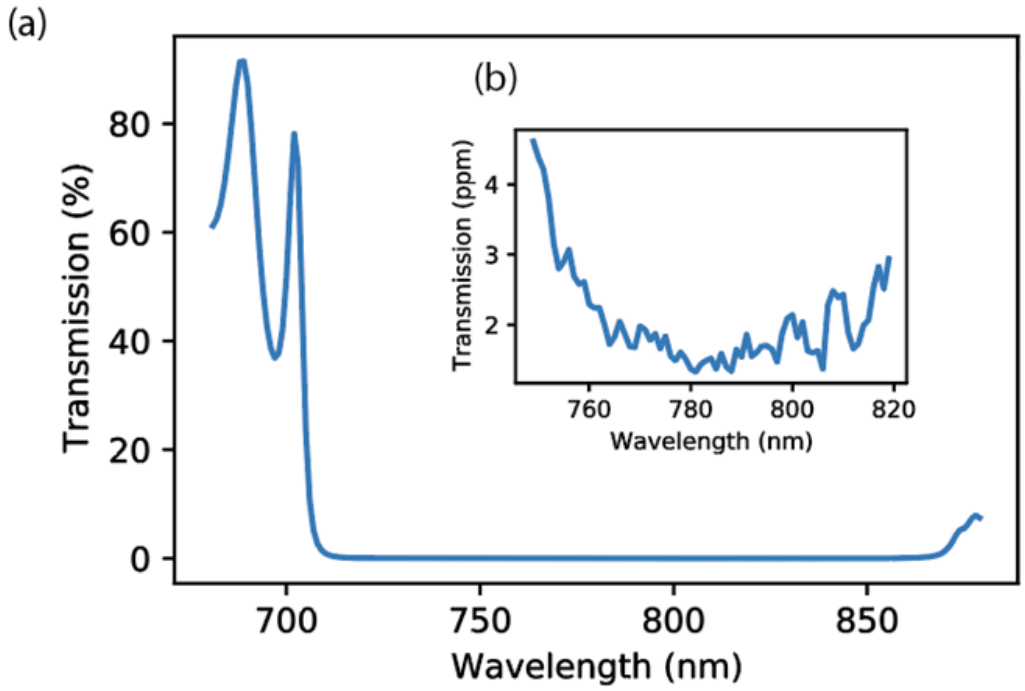


Figure D.1: (a) Reflectivity spectrum of the coating from FiveNine Optics (b) The reflectivity spectrum for the high reflectivity region of the coating from 750nm to 820nm showing a minimum transmission of 1.33ppm

(loss) is $T = 1.33$ ppm (Fig. SI. 1). This sets the lower limit of cavity loss to 2.66 ppm per round trip, which does not include the coating absorption loss. It is suggested that the coating absorption loss can be comparable to 1 ppm, where signal contrast issues can occur if the coating stack is too thick and when the stack transmission loss is designed to be ~ 1 ppm.

The shape of the mirror can be simulated almost perfectly by COMSOL, given the coating thickness and materials, where we treat the compressive strain as uniform and a parameter to adjust for. The estimated strain is 0.3%.

D.2 Cavity finesse measurement setup and method

The mirrors are mounted on six-axis translation stages, providing full degrees of freedom for alignment. One of the mirrors is attached to a piezoelectric transducer (Thorlabs PC4RG15M) to modulate the cavity length. The tip and tilt of the mirrors are initially aligned parallel to each other, and the mode matching to the TEM_{00} mode is optimized by adjusting the mirror positions.

To align the cavity, we first retroreflect a collimated beam from the back mirror. Next, we introduce the front mirror and retro-reflect from its polished silicon backside. Finally, we confirm proper alignment by sending white light through the back of the cavity and ensuring it passes through both mirror apertures without clipping. More optimal alignment can be found by minimizing the birefringence of the cavity or, similarly, the splitting between degenerate modes such as TEM_{01} and TEM_{01}.

When measuring finesse and quality factor (Q) as a function of cavity length, we observe that changes in mode waist affect mode matching. In addition, reducing the finesse decreases transmission and weakens the signal. To compensate, we realign the mode-matching lens and increase the optical power to maintain a similar level of transmitted light.

As the cavity length increases, the swept-ring-down spectroscopy method becomes less sensitive. The free spectral range (FSR) decreases with increasing length, causing the resonance frequency to vary more slowly at a given piezo sweep speed. To maintain a robust swept-ring-down signal, the frequency sweep must exceed the ring-down time of the cavity; however, increasing the sweep speed is limited by the loaded bandwidth of the piezo when the cavity is attached.

For our measurements, we use an Eagleyard 780 nm mini-ECL laser (EYP-ECL-0780-00080-1500-BFW01-0005), frequency-locked to a rubidium reference via modulation transfer spectroscopy. As the piezo transducer modulates the cavity length, the resonance sweeps through the laser frequency, and the resulting ringdown can be observed in the time domain when the cavity

shifts off resonance and the light decays. Fringes appear in the ringdown due to the high finesse/Q, where light circulates in the cavity on a timescale comparable to the length sweep.

$$I \propto e^{-\kappa t} \left| \operatorname{erfc}\left(\frac{(i+1)}{2} \frac{\kappa/2 - i\alpha\,(t - t_0)}{i\sqrt{\alpha}} \right) \right|^2$$

By fitting these fringes, we can extract the rate of frequency change across the resonance, α. With this measurement, in addition to a measurement of the amount of time required to travel a full FSR, Δt_{FSR}, we can extract the length of the cavity and the finesse.

$$\alpha = \frac{\nu_{\mathrm{FSR}}}{\Delta t_{\mathrm{FSR}}} = \frac{c}{2L\,\Delta t_{\mathrm{FSR}}}$$

$$L = \frac{c}{2\alpha\,\Delta t_{\mathrm{FSR}}}, \quad F = \frac{2\pi\,(\alpha\,\Delta t_{\mathrm{FSR}})}{\kappa}$$

Overall, this configuration enables accurate measurement of finesse and quality factors across a range of cavity lengths, even very short ones. To corroborate this measurement, we can also calculate the length of the cavity by measuring the relative spacing of the TEM modes. The resonance of a given TEM$_{mnq}$, where q denotes the longitudinal mode and m and n denote the transverse mode indexes, is given by:

$$\nu_{mnq} = \frac{c}{2L}\left(q + \frac{1}{\pi}(m + n + 1)\arccos\left(\pm\sqrt{g_1 g_2}\right) \right)$$

Where g_i is the stability parameter given by $g_i = 1 - \frac{L}{\mathrm{ROC}_i}$. By measuring the spacing of these modes in time, we can get a direct translation between time and frequency.

$$\nu_{00q} - \nu_{00(q+1)} = \frac{c}{2L}$$

$$\nu_{01q} - \nu_{00q} = \frac{c}{2\pi L} \arccos\left(\pm\sqrt{g_1 g_2}\right)$$

$$\frac{\nu_{01q} - \nu_{00q}}{\nu_{00q} - \nu_{00(q+1)}} = \frac{1}{\pi} \arccos\left(\pm\sqrt{g_1 g_2}\right)$$

If we assume symmetric mirrors, this equation then simplifies:

$$L = \mathrm{ROC}\left(1 - \pi \frac{\nu_{01q} - \nu_{00q}}{\nu_{00q} - \nu_{00(q+1)}}\right)$$

We can then utilize the information from the profile measurements to extract a length from the measurements of the mode spacing.

We also observe slight birefringence in the cavity, manifested by low-frequency beating in the transmission signal. This birefringence is typically on the order of the cavity line width, indicating a minor deviation from perfect symmetry that could arise from imperfect alignment. To mitigate its effects, we align the input polarization with one of the two polarization modes of the cavity.

Because the glued microcavity samples cannot be measured by sweeping their length, we perform swept-ring down spectroscopy by modulating the laser current. For the short glued microcavity, we use a Velocity™ TLB-6700 Widely Tunable Laser; Rapid current modulation combined with piezo modulation allows us to sweep across the resonance quickly enough to observe the ring down. We also leverage the wide range of laser tuning to measure a full FSR of the short glued microcavity, confirming its length and finesse. The accuracy of this FSR measurement depends on the internal calibration of the Velocity 6700.

For the longer glued microcavity, its narrow resonance allows us to use the same Eagleyard 780 nm mini-ECL employed for unglued samples. Because the laser current can be swept sufficiently fast relative to the cavity line width, swept ring-down spectroscopy remains feasible with this setup.

D.3 FEM simulation of the buckling mode

COMSOL is used to simulate the shape of the resulting mirror coatings, when subjected to compressive stress from the deposition process. This allows us to accurately predict their form, in addition to characterization of fabricated devices. Since all mirrors have spherical shapes, we apply the axial-symmetry condition to speed up the simulation, and model a disk shape that is hard-clamped at the perimeter boundary. The disk consists of 21 alternating layers of SiO_2 and Ta_2O_5 along the axial direction, with SiO_2 at 134 nm thickness, Ta_2O_5 at 94 nm thickness for each layer and a disk radius of varying sizes.

We begin with an uniaxial compressive strain of $\varepsilon = 5 \times 10^{-4}$ across the material stack and perform a Linear Buckling study to determine the critical load factor, which provides the threshold compressive strain required for buckling. Using the buckling profile from this study as an initial condition, we then conduct a stationary study that sweeps through a range of strains where buckling occurs. This stationary study generates multiple buckling profiles corresponding to different strain levels.

To anchor the strain in our device, we match the maximum displacement in the simulation with measurement results from an optical profiler. With the strain $\varepsilon = 3 \times 10^{-3}$ obtained this way, we find that the simulated buckling profiles closely match the measured data from the fabricated devices.

D.4 Simulation of the diffractive loss of the mirror

We can simulate the expected diffraction losses of the particular shape of the mirror using the techniques outlined in [9,87]. With these techniques, the deviation from spherical results in mixing between different eigenmodes of the cavity, resulting in mixing of the larger more lossy higher order modes with the TEM_{00} mode.

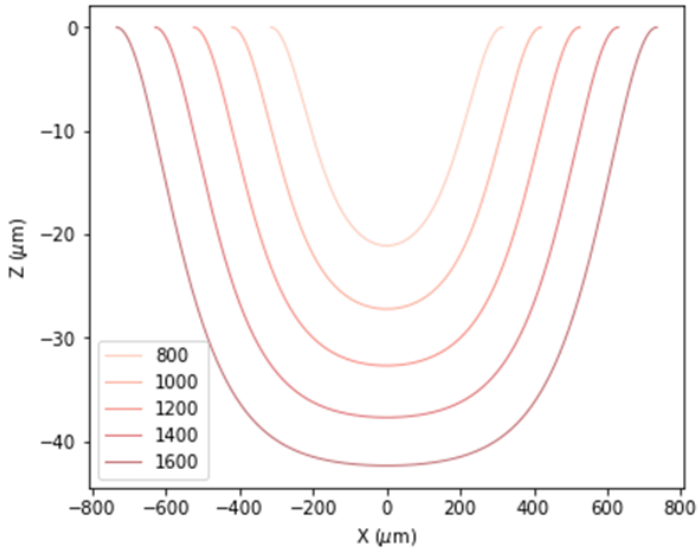


Figure D.2: Comsol simulations of the profile of the buckled mirror

D.5 Fabrication pitfall

The range of the ROC and depth of the mirror are limited by the method and materials. From fabrication trials, we observe that smaller diameters lead to buckling upwards, and larger diameters lead to dramatic drops in yield where the membrane starts to break.

References

[1] Aeppli, A., Kim, K., Warfield, W., Safronova, M. S., & Ye, J. (2024). Clock with $8\times$ 10-19 systematic uncertainty. *Physical Review Letters*, 133(2), 023401.

[2] Alt, W., Schrader, D., Kuhr, S., Müller, M., Gomer, V., & Meschede, D. (2003). Single atoms in a standing-wave dipole trap. *Physical Review A*, 67(3), 033403.

[3] Baranes, G., Cain, M., Ataides, J., Bluvstein, D., Sinclair, J., Vuletic, V., Zhou, H., & Lukin, M. D. (2025). Leveraging atom loss errors in fault tolerant quantum algorithms. *arXiv preprint arXiv:2502.20558*.

[4] Barontini, G., Hohmann, L., Haas, F., Esteve, J., & Reichel, J. (2015). Deterministic generation of multiparticle entanglement by quantum zeno dynamics. *Science*, 349(6254), 1317–1321.

[5] Barredo, D., De Léséleuc, S., Lienhard, V., Lahaye, T., & Browaeys, A. (2016a). An atom-by-atom assembler of defect-free arbitrary two-dimensional atomic arrays. *Science*, 354(6315), 1021–1023.

[6] Barredo, D., de Léséleuc, S., Lienhard, V., Lahaye, T., & Browaeys, A. (2016b). An atom-by-atom assembler of defect-free arbitrary two-dimensional atomic arrays. *Science*, 354(6315), 1021–1023.

[7] Barredo, D., Labuhn, H., Ravets, S., Lahaye, T., Browaeys, A., & Adams, C. S. (2015). Coherent excitation transfer in a spin chain of three rydberg atoms. *Physical review letters*, 114(11), 113002.

[8] Barredo, D., Lienhard, V., De Leseleuc, S., Lahaye, T., & Browaeys, A. (2018). Synthetic three-dimensional atomic structures assembled atom by atom. *Nature*, 561(7721), 79–82.

[9] Benedikter, J., Hümmer, T., Mader, M., Schlederer, B., Reichel, J., Hänsch, T. W., & Hunger, D. (2015). Transverse-mode coupling and diffraction loss in tunable fabry–pérot microcavities. *New Journal of Physics*, 17(5), 053051.

[10] Bennett, C. H., Brassard, G., Crépeau, C., Jozsa, R., Peres, A., & Wootters, W. K. (1993). Teleporting an unknown quantum state via dual classical and Einstein-Podolsky-Rosen channels. *Phys. Rev. Lett.*, 70, 1895–1899.

[11] Bennett, H. E. & Porteus, J. (1961). Relation between surface roughness and specular reflectance at normal incidence. *Journal of the optical society of America*, 51(2), 123–129.

[12] Berden, G. & Engeln, R. (2009). *Cavity ring-down spectroscopy: techniques and applications*. John Wiley & Sons.

[13] Bernien, H., Hensen, B., Pfaff, W., et al. (2013). Heralded entanglement between solid-state qubits separated by three metres. *Nature*, 497, 86–90.

[14] Beugnon, J., Tuchendler, C., Marion, H., et al. (2007a). Two-dimensional transport and transfer of a single atomic qubit in optical tweezers. *Nature Physics*, 3, 696–699.

[15] Beugnon, J., Tuchendler, C., Marion, H., Gaëtan, A., Miroshnychenko, Y., Sortais, Y. R., Lance, A. M., Jones, M. P., Messin, G., Browaeys, A., et al. (2007b). Two-dimensional transport and transfer of a single atomic qubit in optical tweezers. *Nature Physics*, 3(10), 696–699.

[16] Bluvstein, D., Evered, S. J., Geim, A. A., Li, S. H., Zhou, H., Manovitz, T., Ebadi, S., Cain, M., Kalinowski, M., Hangleiter, D., et al. (2024). Logical quantum processor based on reconfigurable atom arrays. *Nature*, 626(7997), 58–65.

[17] Bluvstein, D., Levine, H., Semeghini, G., Wang, T. T., Ebadi, S., Kalinowski, M., Keesling, A., Maskara, N., Pichler, H., Greiner, M., Vuletić, V., & Lukin, M. D. (2022). A quantum processor based on coherent transport of entangled atom arrays. *Nature*, 604(7906), 451–456.

[18] Bochmann, J., Mücke, M., Guhl, C., Ritter, S., Rempe, G., & Moehring, D. L. (2010). Lossless state detection of single neutral atoms. *Physical review letters*, 104(20), 203601.

[19] Borish, V., Marković, O., Hines, J. A., Rajagopal, S. V., & Schleier-Smith, M. (2020). Transverse-field ising dynamics in a rydberg-dressed atomic gas. *Physical review letters*, 124(6), 063601.

[20] Borregaard, J., Komar, P., Kessler, E., Sørensen, A. S., & Lukin, M. D. (2015). Heralded quantum gates with integrated error detection in optical cavities. *Physical Review Letters*, 114(11), 110502.

[21] Borregaard, J., Pichler, H., Schröder, T., Lukin, M. D., Lodahl, P., & Sørensen, A. S. (2020). One-way quantum repeater based on near-deterministic photon-emitter interfaces. *Phys. Rev. X*, 10, 021071.

[22] Browaeys, A., Barredo, D., & Lahaye, T. (2016). Experimental investigations of dipole–dipole interactions between a few rydberg atoms. *Journal of Physics B: Atomic, Molecular and Optical Physics*, 49(15), 152001.

[23] Browaeys, A. & Lahaye, T. (2020). Many-body physics with individually controlled Rydberg atoms. *Nat. Physics*, 16(2), 132–142.

[24] Brown, M., Thiele, T., Kiehl, C., Hsu, T.-W., & Regal, C. (2019). Gray-molasses optical-tweezer loading: controlling collisions for scaling atom-array assembly. *Physical Review X*, 9(1), 011057.

[25] Cao, A., Eckner, W. J., Yelin, T. L., Young, A. W., Jandura, S., Yan, L., Kim, K., Pupillo, G., Ye, J., Oppong, N. D., et al. (2024). Multi-qubit gates and 'schrödinger cat' states in an optical clock. *arXiv preprint arXiv:2402.16289*.

[26] Carr, H. Y. & Purcell, E. M. (1954). Effects of diffusion on free precession in nuclear magnetic resonance experiments. *Phys. Rev.*, 94, 630–638.

[27] Carter, J. D. & Martin, J. D. D. (2013). Coherent manipulation of cold Rydberg atoms near the surface of an atom chip. *Phys. Rev. A*, 88, 043429.

[28] Chang, D. E., Douglas, J. S., González-Tudela, A., Hung, C.-L., & Kimble, H. J. (2018). Colloquium: Quantum matter built from nanoscopic lattices of atoms and photons. *Rev. Mod. Phys.*, 90, 031002.

[29] Chang, T.-H., Zhou, X., Tamura, H., & Hung, C.-L. (2022). Realization of efficient 3d tapered waveguide-to-fiber couplers on a nanophotonic circuit. *Optics Express*, 30(18), 31643–31652.

[30] Chen, W., Hu, J., Duan, Y., Braverman, B., Zhang, H., & Vuletić, V. (2015). Carving complex many-atom entangled states by single-photon detection. *Phys. Rev. Lett.*, 115, 250502.

[31] Choi, H., Pant, M., Guha, S., et al. (2019). Percolation-based architecture for cluster state creation using photon-mediated entanglement between atomic memories. *npj Quantum Inf*, 5, 104.

[32] Cong, I., Levine, H., Keesling, A., Bluvstein, D., Wang, S.-T., & Lukin, M. D. (2022). Hardware-efficient, fault-tolerant quantum computation with Rydberg atoms. *Phys. Rev. X*, 12, 021049.

[33] Cooper, A., Sun, W. K. C., Jaskula, J.-C., & Cappellaro, P. (2019). Environment-assisted quantum-enhanced sensing with electronic spins in diamond. *Phys. Rev. Appl.*, 12, 044047.

[34] Covey, J. P., Sipahigil, A., Szoke, S., Sinclair, N., Endres, M., & Painter, O. (2019). Telecom-band quantum optics with ytterbium atoms and silicon nanophotonics. *Phys. Rev. Appl.*, 11, 034044.

[35] Covey, J. P., Weinfurter, H., & Bernien, H. (2023). Quantum networks with neutral atom processing nodes. *npj Quantum Information*, 9(1), 90.

[36] Cox, K. C., Greve, G. P., Weiner, J. M., & Thompson, J. K. (2016). Deterministic squeezed states with collective measurements and feedback. *Physical review letters*, 116(9), 093602.

[37] Cripe, J., Aggarwal, N., Lanza, R., Libson, A., Singh, R., Heu, P., Follman, D., Cole, G. D., Mavalvala, N., & Corbitt, T. (2019). Measurement of quantum back action in the audio band at room temperature. *Nature*, 568(7752), 364–367.

[38] Daiss, S., Langenfeld, S., Welte, S., Distante, E., Thomas, P., Hartung, L., Morin, O., & Rempe, G. (2021). A quantum-logic gate between distant quantum-network modules. *Science*, 371(6529), 614–617.

[39] Davis, E. J., Wang, Z., Safavi-Naeini, A. H., & Schleier-Smith, M. H. (2018). Painting nonclassical states of spin or motion with shaped single photons. *Phys. Rev. Lett.*, 121, 123602.

[40] Davtyan, D., Machluf, S., Soudijn, M. L., Naber, J. B., van Druten, N. J., van Linden van den Heuvell, H. B., & Spreeuw, R. J. C. (2018). Controlling stray electric fields on an atom chip for experiments on Rydberg atoms. *Phys. Rev. A*, 97, 023418.

[41] de Hond, J., van Bijnen, R., Kokkelmans, S. J. J. M. F., Spreeuw, R. J. C., van den Heuvell, H. B. v. L., & van Druten, N. J. (2018). From coherent collective excitation to Rydberg blockade on an atom chip. *Phys. Rev. A*, 98, 062714.

[42] de Leon, N. P., Itoh, K. M., Kim, D., Mehta, K. K., Northup, T. E., Paik, H., Palmer, B., Samarth, N., Sangtawesin, S., & Steuerman, D. (2021). Materials challenges and opportunities for quantum computing hardware. *Science*, 372(6539), eabb2823.

[43] De Léséleuc, S., Barredo, D., Lienhard, V., Browaeys, A., & Lahaye, T. (2018). Analysis of imperfections in the coherent optical excitation of single atoms to rydberg states. *Physical Review A*, 97(5), 053803.

[44] Deist, E., Lu, Y.-H., Ho, J., Pasha, M. K., Zeiher, J., Yan, Z., & Stamper-Kurn, D. M. (2022). Mid-circuit cavity measurement in a neutral atom array. *Physical Review Letters*, 129(20), 203602.

[45] Dibos, A. M., Raha, M., Phenicie, C. M., & Thompson, J. D. (2018). Atomic source of single photons in the telecom band. *Phys. Rev. Lett.*, 120, 243601.

[46] Ding, S. W., Grinkemeyer, B., Jiang, R., Mandopoulou, G. E., Zibrov, A. S., Yang, K. Y., Lukin, M. D., & Lončar, M. (2025). Near a million finesse near-infrared microcavity. in preparation.

[47] Duan, L.-M. & Kimble, H. J. (2004). Scalable photonic quantum computation through cavity-assisted interactions. *Phys. Rev. Lett.*, 92, 127902.

[48] Ebadi, S., Keesling, A., Cain, M., Wang, T. T., Levine, H., Bluvstein, D., Semeghini, G., Omran, A., Liu, J.-G., Samajdar, R., Luo, X.-Z., Nash, B., Gao, X., Barak, B., Farhi, E., Sachdev, S., Gemelke, N., Zhou, L., Choi, S., Pichler, H., Wang, S.-T., Greiner, M., Vuletić, V., & Lukin, M. D. (2022). Quantum optimization of maximum independent set using rydberg atom arrays. *Science*, 376(6598), 1209–1215.

[49] Ebadi, S., Wang, T. T., Levine, H., Keesling, A., Semeghini, G., Omran, A., Bluvstein, D., Samajdar, R., Pichler, H., Ho, W. W., Choi, S., Sachdev, S., Greiner, M., Vuletić, V., & Lukin, M. D. (2021a). Quantum phases of matter on a 256-atom programmable quantum simulator. *Nature*, 595(7866), 227–232.

[50] Ebadi, S., Wang, T. T., Levine, H., Keesling, A., Semeghini, G., Omran, A., Bluvstein, D., Samajdar, R., Pichler, H., Ho, W. W., et al. (2021b). Quantum phases of matter on a 256-atom programmable quantum simulator. *Nature*, 595(7866), 227–232.

[51] Endres, M., Bernien, H., Keesling, A., Levine, H., Anschuetz, E. R., Krajenbrink, A., Senko, C., Vuletic, V., Greiner, M., & Lukin, M. D. (2016a). Atom-by-atom assembly of defect-free one-dimensional cold atom arrays. *Science*, 354(6315), 1024–1027.

[52] Endres, M., Bernien, H., Keesling, A., Levine, H., Anschuetz, E. R., Krajenbrink, A., Senko, C., Vuletic, V., Greiner, M., & Lukin, M. D. (2016b). Atom-by-atom assembly of defect-free one-dimensional cold atom arrays. *Science*, 354(6315), 1024–1027.

[53] Epple, G., Kleinbach, K. S., Euser, T. G., Joly, N. Y., Pfau, T., Russell, P. S. J., & Löw, R. (2014). Rydberg atoms in hollow-core photonic crystal fibres. *Nat. Commun.*, 5(1), 4132.

[54] Evered, S. J., Bluvstein, D., Kalinowski, M., Ebadi, S., Manovitz, T., Zhou, H., Li, S. H., Geim, A. A., Wang, T. T., Maskara, N., et al. (2023). High-fidelity parallel entangling gates on a neutral-atom quantum computer. *Nature*, 622(7982), 268–272.

[55] Gallagher, T. F. (1994). Rydberg atoms. In *Springer Handbook of Atomic, Molecular, and Optical Physics* (pp. 231–240). Springer.

[56] Gallego, J., Ghosh, S., Alavi, S. K., Alt, W., Martinez-Dorantes, M., Meschede, D., & Ratschbacher, L. (2016). High-finesse fiber fabry–perot cavities: stabilization and mode matching analysis. *Applied Physics B*, 122, 1–14.

[57] Gehr, R., Volz, J., Dubois, G., Steinmetz, T., Colombe, Y., Lev, B. L., Long, R., Esteve, J., & Reichel, J. (2010). Cavity-based single atom preparation and high-fidelity hyperfine state readout. *Physical review letters*, 104(20), 203602.

[58] Goban, A., Hung, C.-L., Hood, J. D., Yu, S.-P., Muniz, J. A., Painter, O., & Kimble, H. J. (2015). Superradiance for atoms trapped along a photonic crystal waveguide. *Phys. Rev. Lett.*, 115, 063601.

[59] Graham, T., Kwon, M., Grinkemeyer, B., Marra, Z., Jiang, X., Lichtman, M., Sun, Y., Ebert, M., & Saffman, M. (2019). Rydberg-mediated entanglement in a two-dimensional neutral atom qubit array. *Physical review letters*, 123(23), 230501.

[60] Grimm, R., Weidemuller, M., & Ovchinnikov, Y. (2000). Optical dipole traps for neutral atoms. *Advances in Atomic, Molecular and Optical Physics*, 42, 95–170.

[61] Grinkemeyer, B., Guardado-Sanchez, E., Dimitrova, I., Shchepanovich, D., Mandopoulou, G. E., Borregaard, J., Vuletić, V., & Lukin, M. D. (2025). Error-detected quantum operations with neutral atoms mediated by an optical cavity. *Science*, 387(6740), 1301–1305.

[62] Guardado-Sanchez, E., Spar, B. M., Schauss, P., Belyansky, R., Young, J. T., Bienias, P., Gorshkov, A. V., Iadecola, T., & Bakr, W. S. (2021). Quench dynamics of a fermi gas with strong nonlocal interactions. *Physical Review X*, 11(2), 021036.

[63] Hartung, L., Seubert, M., Welte, S., Distante, E., & Rempe, G. (2024). A quantum-network register assembled with optical tweezers in an optical cavity. *Science*, 385(6705), 179–183.

[64] Hermann-Avigliano, C., Teixeira, R. C., Nguyen, T. L., Cantat-Moltrecht, T., Nogues, G., Dotsenko, I., Gleyzes, S., Raimond, J. M., Haroche, S., & Brune, M. (2014). Long coherence times for Rydberg qubits on a superconducting atom chip. *Phys. Rev. A*, 90, 040502(R).

[65] Hood, J. D., Goban, A., Asenjo-Garcia, A., Lu, M., Yu, S.-P., Chang, D. E., & Kimble, H. J. (2016). Atom–atom interactions around the band edge of a photonic crystal waveguide. *Proceedings of the National Academy of Sciences*, 113(38), 10507–10512.

[66] Huft, P., Song, Y., Graham, T. M., Jooya, K., Deshpande, S., Fang, C., Kats, M., & Saffman, M. (2022). Simple, passive design for large optical trap arrays for single atoms. *Phys. Rev. A*, 105, 063111.

[67] Huie, W., Menon, S. G., Bernien, H., & Covey, J. P. (2021). Multiplexed telecommunication-band quantum networking with atom arrays in optical cavities. *Physical Review Research*, 3(4), 043154.

[68] Hümmer, D., Schneeweiss, P., Rauschenbeutel, A., & Romero-Isart, O. (2019). Heating in nanophotonic traps for cold atoms. *Phys. Rev. X*, 9, 041034.

[69] Hung, C.-L., González-Tudela, A., Cirac, J. I., & Kimble, H. (2016). Quantum spin dynamics with pairwise-tunable, long-range interactions. *Proceedings of the National Academy of Sciences*, 113(34), E4946–E4955.

[70] Hunger, D., Steinmetz, T., Colombe, Y., Deutsch, C., Hänsch, T. W., & Reichel, J. (2010). A fiber fabry–perot cavity with high finesse. *New Journal of Physics*, 12(6), 065038.

[71] Isenhower, L., Urban, E., Zhang, X., Gill, A., Henage, T., Johnson, T. A., Walker, T., & Saffman, M. (2010). Demonstration of a neutral atom controlled-not quantum gate. *Physical review letters*, 104(1), 010503.

[72] Isichenko, A., Hunter, A. S., Bose, D., Chauhan, N., Song, M., Liu, K., Harrington, M. W., & Blumenthal, D. J. (2024). Sub-hz fundamental, sub-khz integral linewidth self-injection locked 780 nm hybrid integrated laser. *Scientific Reports*, 14(1), 27015.

[73] Jaksch, D., Cirac, J. I., Zoller, P., Rolston, S. L., Côté, R., & Lukin, M. D. (2000). Fast quantum gates for neutral atoms. *Physical Review Letters*, 85(10), 2208.

[74] Jandura, S. & Pupillo, G. (2022). Time-optimal two-and three-qubit gates for rydberg atoms. *Quantum*, 6, 712.

[75] Jandura, S., Srivastava, V., Pecorari, L., Brennen, G., & Pupillo, G. (2023a). Non-local multi-qubit quantum gates via a driven cavity. *arXiv preprint arXiv:2303.13127*.

[76] Jandura, S., Thompson, J. D., & Pupillo, G. (2023b). Optimizing rydberg gates for logical-qubit performance. *PRX Quantum*, 4(2), 020336.

[77] Jau, Y.-Y., Hankin, A., Keating, T., Deutsch, I. H., & Biedermann, G. (2016). Entangling atomic spins with a rydberg-dressed spin-flip blockade. *Nature Physics*, 12(1), 71–74.

[78] Jenkins, A., Lis, J. W., Senoo, A., McGrew, W. F., & Kaufman, A. M. (2022). Ytterbium nuclear-spin qubits in an optical tweezer array. *Physical Review X*, 12(2), 021027.

[79] Jiang, L., Brennen, G. K., Gorshkov, A. V., Hammerer, K., Hafezi, M., Demler, E., Lukin, M. D., & Zoller, P. (2008). Anyonic interferometry and protected memories in atomic spin lattices. *Nature Physics*, 4(6), 482–488.

[80] Jin, N., McLemore, C. A., Mason, D., Hendrie, J. P., Luo, Y., Kelleher, M. L., Kharel, P., Quinlan, F., Diddams, S. A., & Rakich, P. T. (2022). Micro-fabricated mirrors with finesse exceeding one million. *Optica*, 9(9), 965–970.

[81] Jones, M. P., Beugnon, J., Gaëtan, A., Zhang, J., Messin, G., Browaeys, A., & Grangier, P. (2007). Fast quantum state control of a single trapped neutral atom. *Physical Review A—Atomic, Molecular, and Optical Physics*, 75(4), 040301.

[82] Kaiser, M., Glaser, C., Ley, L. Y., Grimmel, J., Hattermann, H., Bothner, D., Koelle, D., Kleiner, R., Petrosyan, D., Günther, A., & Fortágh, J. (2022). Cavity-driven Rabi oscillations between Rydberg states of atoms trapped on a superconducting atom chip. *Phys. Rev. Res.*, 4, 013207.

[83] Kaufman, A. M., Lester, B. J., & Regal, C. A. (2012). Cooling a single atom in an optical tweezer to its quantum ground state. *Physical Review X*, 2(4), 041014.

[84] Kaufman, A. M., Lester, B. J., Reynolds, C. M., Wall, M. L., Foss-Feig, M., Hazzard, K. R. A., Rey, A. M., & Regal, C. A. (2014). Two-particle quantum interference in tunnel-coupled optical tweezers. *Science*, 345(6194), 306–309.

[85] Kim, M. E., Chang, T.-H., Fields, B. M., Chen, C.-A., & Hung, C.-L. (2019). Trapping single atoms on a nanophotonic circuit with configurable tweezer lattices. *Nature Communications*, 10(1), 1647.

[86] Kimble, H. J. (2008). The quantum internet. *Nature*, 453(7198), 1023–1030.

[87] Kleckner, D., Irvine, W. T., Oemrawsingh, S. S., & Bouwmeester, D. (2010). Diffraction-limited high-finesse optical cavities. *Physical Review A—Atomic, Molecular, and Optical Physics*, 81(4), 043814.

[88] Knaut, C. M., Suleymanzade, A., Wei, Y.-C., Assumpcao, D. R., Stas, P.-J., Huan, Y. Q., Machielse, B., Knall, E. N., Sutula, M., Baranes, G., et al. (2024). Entanglement of nanophotonic quantum memory nodes in a telecom network. *Nature*, 629(8012), 573–578.

[89] Kroeze, R. M., Marsh, B. P., Lin, K.-Y., Keeling, J., & Lev, B. L. (2023). High cooperativity using a confocal-cavity–qed microscope. *PRX Quantum*, 4(2), 020326.

[90] Kübler, H., Shaffer, J. P., Baluktsian, T., Löw, R., & Pfau, T. (2010). Coherent excitation of Rydberg atoms in micrometre-sized atomic vapour cells. *Nature Photonics*, 4(2), 112–116.

[91] Kudelin, I., Groman, W., Ji, Q.-X., Guo, J., Kelleher, M. L., Lee, D., Nakamura, T., McLemore, C. A., Shirmohammadi, P., Hanifi, S., et al. (2024). Photonic chip-based low-noise microwave oscillator. *Nature*, 627(8004), 534–539.

[92] Kuhr, S., Alt, W., Schrader, D., Dotsenko, I., Miroshnychenko, Y., Rauschenbeutel, A., & Meschede, D. (2005). Analysis of dephasing mechanisms in a standing-wave dipole trap. *Phys. Rev. A*, 72, 023406.

[93] Langenfeld, S., Thomas, P., Morin, O., & Rempe, G. (2021). Quantum repeater node demonstrating unconditionally secure key distribution. *Physical review letters*, 126(23), 230506.

[94] Lee, H., Suh, M.-G., Chen, T., Li, J., Diddams, S. A., & Vahala, K. J. (2013). Spiral resonators for on-chip laser frequency stabilization. *Nature communications*, 4(1), 2468.

[95] Lengwenus, A., Kruse, J., Schlosser, M., Tichelmann, S., & Birkl, G. (2010). Coherent transport of atomic quantum states in a scalable shift register. *Phys. Rev. Lett.*, 105, 170502.

[96] Leroux, I. D., Schleier-Smith, M. H., & Vuletić, V. (2010). Implementation of cavity squeezing of a collective atomic spin. *Physical Review Letters*, 104(7), 073602.

[97] Levine, H., Bluvstein, D., Keesling, A., Wang, T. T., Ebadi, S., Semeghini, G., Omran, A., Greiner, M., Vuletić, V., & Lukin, M. D. (2022). Dispersive optical systems for scalable raman driving of hyperfine qubits. *Physical Review A*, 105(3), 032618.

[98] Levine, H., Keesling, A., Omran, A., Bernien, H., Schwartz, S., Zibrov, A. S., Endres, M., Greiner, M., Vuletić, V., & Lukin, M. D. (2018a). High-fidelity control and entanglement of rydberg-atom qubits. *Physical review letters*, 121(12), 123603.

[99] Levine, H., Keesling, A., Omran, A., Bernien, H., Schwartz, S., Zibrov, A. S., Endres, M., Greiner, M., Vuletić, V., & Lukin, M. D. (2018b). High-fidelity control and entanglement of Rydberg-atom qubits. *Phys. Rev. Lett.*, 121, 123603.

[100] Levine, H., Keesling, A., Semeghini, G., Omran, A., Wang, T. T., Ebadi, S., Bernien, H., Greiner, M., Vuletić, V., Pichler, H., & Lukin, M. D. (2019). Parallel implementation of high-fidelity multiqubit gates with neutral atoms. *Phys. Rev. Lett.*, 123, 170503.

[101] Li, B., Jin, W., Wu, L., Chang, L., Wang, H., Shen, B., Yuan, Z., Feshali, A., Paniccia, M., Vahala, K. J., et al. (2021). Reaching fiber-laser coherence in integrated photonics. *Optics Letters*, 46(20), 5201–5204.

[102] Li, L., Hu, X., Jia, Z., Huie, W., Sun, W. K. C., Dong, Y., Covey, J. P., et al. (2025). Parallelized telecom quantum networking with a ytterbium-171 atom array. *arXiv preprint arXiv:2502.17406*.

[103] Li, Y. & Thompson, J. D. (2024). High-rate and high-fidelity modular interconnects between neutral atom quantum processors. *PRX Quantum*, 5, 020363.

[104] Liang, Q., Bisht, A., Scheck, A., Schunemann, P. G., & Ye, J. (2025). Modulated ringdown comb interferometry for sensing of highly complex gases. *Nature*, (pp. 1–8).

[105] Liang, W., Ilchenko, V., Savchenkov, A., Matsko, A., Seidel, D., & Maleki, L. (2010). Whispering-gallery-mode-resonator-based ultranarrow linewidth external-cavity semiconductor laser. *Optics letters*, 35(16), 2822–2824.

[106] Liu, G.-Q., Zhang, Y.-R., Chang, Y.-C., Yue, J.-D., Fan, H., & Pan, X.-Y. (2015). Demonstration of entanglement-enhanced phase estimation in solid. *Nature Communications*, 6(1), 6726.

[107] Liu, Y., Li, L., & Ma, Y. (2022). Hybrid Rydberg quantum gate for quantum network. *Phys. Rev. Res.*, 4, 013008.

[108] Liu, Y., Wang, Z., Yang, P., Wang, Q., Fan, Q., Guan, S., Li, G., Zhang, P., & Zhang, T. (2023). Realization of strong coupling between deterministic single-atom arrays and a high-finesse miniature optical cavity. *Phys. Rev. Lett.*, 130, 173601.

[109] Ludlow, A. D., Boyd, M. M., Ye, J., Peik, E., & Schmidt, P. O. (2015). Optical atomic clocks. *Reviews of Modern Physics*, 87(2), 637–701.

[110] Ma, L., Paradis, E., & Raithel, G. (2020). DC electric fields in electrode-free glass vapor cell by photoillumination. *Opt. Express*, 28(3), 3676–3685.

[111] Ma, S., Liu, G., Peng, P., Zhang, B., Jandura, S., Claes, J., Burgers, A. P., Pupillo, G., Puri, S., & Thompson, J. D. (2023). High-fidelity gates and mid-circuit erasure conversion in an atomic qubit. *Nature*, 622(7982), 279–284.

[112] Madjarov, I. S., Cooper, A., Shaw, A. L., Covey, J. P., Schkolnik, V., Yoon, T. H., Williams, J. R., & Endres, M. (2019). An atomic-array optical clock with single-atom readout. *Physical Review X*, 9(4), 041052.

[113] Madjarov, I. S., Covey, J. P., Shaw, A. L., Choi, J., Kale, A., Cooper, A., Pichler, H., Schkolnik, V., Williams, J. R., & Endres, M. (2020). High-fidelity entanglement and detection of alkaline-earth Rydberg atoms. *Nat. Phys.*, 16(8), 857–861.

[114] Maller, K., Lichtman, M., Xia, T., Sun, Y., Piotrowicz, M., Carr, A., Isenhower, L., & Saffman, M. (2015). Rydberg-blockade controlled-not gate and entanglement in a two-dimensional array of neutral-atom qubits. *Physical Review A*, 92(2), 022336.

[115] Manetsch, H. J., Nomura, G., Bataille, E., Leung, K. H., Lv, X., & Endres, M. (2024). A tweezer array with 6100 highly coherent atomic qubits. *arXiv preprint arXiv:2403.12021*.

[116] Manovitz, T., Shaniv, R., Shapira, Y., Ozeri, R., & Akerman, N. (2019). Precision measurement of atomic isotope shifts using a two-isotope entangled state. *Phys. Rev. Lett.*, 123, 203001.

[117] Martinez-Dorantes, M., Alt, W., Gallego, J., Ghosh, S., Ratschbacher, L., Völzke, Y., & Meschede, D. (2017). Fast nondestructive parallel readout of neutral atom registers in optical potentials. *Phys. Rev. Lett.*, 119, 180503.

[118] McLemore, C. A., Jin, N., Kelleher, M. L., Luo, Y., Lee, D., Liu, Y., Nakamura, T., Mason, D., Rakich, P., Diddams, S. A., et al. (2024). Fiber-coupled 2 ml vacuum-gap fabry–perot reference cavity for portable laser stabilization. *Optics Letters*, 49(16), 4737–4740.

[119] Meade, R. D. V., Johnson, S. G., & Winn, J. N. (2008). Photonic crystals: Molding the flow of light.

[120] Meng, Y., Liedl, C., Pucher, S., Rauschenbeutel, A., & Schneeweiss, P. (2020). Imaging and localizing individual atoms interfaced with a nanophotonic waveguide. *Phys. Rev. Lett.*, 125, 053603.

[121] Menon, S. G., Singh, K., Borregaard, J., & Bernien, H. (2020). Nanophotonic quantum network node with neutral atoms and an integrated telecom interface. *New J. Phys.*, 22(7), 073033.

[122] Meyer, V., Rowe, M. A., Kielpinski, D., Sackett, C. A., Itano, W. M., Monroe, C., & Wineland, D. J. (2001). Experimental demonstration of entanglement-enhanced rotation angle estimation using trapped ions. *Phys. Rev. Lett.*, 86, 5870–5873.

[123] Monroe, C. & Kim, J. (2013). Scaling the ion trap quantum processor. *Science*, 339(6124), 1164–1169.

[124] Monroe, C., Raussendorf, R., Ruthven, A., Brown, K. R., Maunz, P., Duan, L.-M., & Kim, J. (2014). Large-scale modular quantum-computer architecture with atomic memory and photonic interconnects. *Phys. Rev. A*, 89, 022317.

[125] Moon, H. S., Lee, L., & Kim, J. B. (2007). Double-resonance optical pumping of rb atoms. *Journal of the Optical Society of America B*, 24(9), 2157–2164.

[126] Needham, L.-M., Saavedra, C., Rasch, J. K., Sole-Barber, D., Schweitzer, B. S., Fairhall, A. J., Vollbrecht, C. H., Wan, S., Podorova, Y., Bergsten, A. J., et al. (2024). Label-free detection and profiling of individual solution-phase molecules. *Nature*, 629(8014), 1062–1068.

[127] Neuzner, A., Körber, M., Morin, O., Ritter, S., & Rempe, G. (2016). Interference and dynamics of light from a distance-controlled atom pair in an optical cavity. *Nature Photonics*, 10(5), 303–306.

[128] Nguyen, C. T., Sukachev, D. D., Bhaskar, M. K., Machielse, B., Levonian, D. S., Knall, E. N., Stroganov, P., Chia, C., Burek, M. J., Riedinger, R., Park, H., Lončar, M., & Lukin, M. D. (2019). An integrated nanophotonic quantum register based on silicon-vacancy spins in diamond. *Phys. Rev. B*, 100, 165428.

[129] Nichol, B. C., Srinivas, R., Nadlinger, D. P., Drmota, P., Main, D., Araneda, G., Ballance, C. J., & Lucas, D. M. (2022). An elementary quantum network of entangled optical atomic clocks. *Nature*, 609(7928), 689–694.

[130] Nickerson, N. H., Li, Y., & Benjamin, S. C. (2013). Topological quantum computing with a very noisy network and local error rates approaching one percent. *Nature Communications*, 4, 1756 EP –.

[131] Norcia, M. A., Lewis-Swan, R. J., Cline, J. R., Zhu, B., Rey, A. M., & Thompson, J. K. (2018). Cavity-mediated collective spin-exchange interactions in a strontium superradiant laser. *Science*, 361(6399), 259–262.

[132] Northup, T. & Blatt, R. (2014). Quantum information transfer using photons. *Nature Photonics*, 8, 356–363.

[133] Ocola, P. L., Dimitrova, I., Grinkemeyer, B., Guardado-Sanchez, E., Đorđević, T., Samutpraphoot, P., Vuletić, V., & Lukin, M. D. (2024). Control and entanglement of individual rydberg atoms near a nanoscale device. *Phys. Rev. Lett.*, 132, 113601.

[134] Đorđević, T., Samutpraphoot, P., Ocola, P. L., Bernien, H., Grinkemeyer, B., Dimitrova, I., Vuletić, V., & Lukin, M. D. (2021). Entanglement transport and a nanophotonic interface for atoms in optical tweezers. *Science*, 373(6562), 1511–1514.

[135] Orr, B. J. & He, Y. (2011). Rapidly swept continuous-wave cavity-ringdown spectroscopy. *Chemical Physics Letters*, 512(1-3), 1–20.

[136] O'Sullivan, M. S. & Stoicheff, B. P. (1985). Scalar polarizabilities and avoided crossings of high Rydberg states in Rb. *Phys. Rev. A*, 31, 2718–2720.

[137] Ott, K., Garcia, S., Kohlhaas, R., Schüppert, K., Rosenbusch, P., Long, R., & Reichel, J. (2016). Millimeter-long fiber fabry-perot cavities. *Optics express*, 24(9), 9839–9853.

[138] Pandey, D. (2024). *Fiber-Based Optical Resonators: Cavity QED, Resonator Design and Technological Applications*. Walter de Gruyter GmbH & Co KG.

[139] Paulisch, V., Perarnau-Llobet, M., González-Tudela, A., & Cirac, J. I. (2019). Quantum metrology with one-dimensional superradiant photonic states. *Phys. Rev. A*, 99, 043807.

[140] Peper, M., Li, Y., Knapp, D. Y., Bileska, M., Ma, S., Liu, G., Peng, P., Zhang, B., Horvath, S. P., Burgers, A. P., et al. (2024). Spectroscopy and modeling of ^{171}yb rydberg states for high-fidelity two-qubit gates. *arXiv preprint arXiv:2406.01482*.

[141] Periwal, A., Cooper, E. S., Kunkel, P., Wienand, J. F., Davis, E. J., & Schleier-Smith, M. (2021). Programmable interactions and emergent geometry in an array of atom clouds. *Nature*, 600(7890), 630–635.

[142] Petrosyan, D., Bensky, G., Kurizki, G., Mazets, I., Majer, J., & Schmiedmayer, J. (2009). Reversible state transfer between superconducting qubits and atomic ensembles. *Phys. Rev. A*, 79, 040304(R).

[143] Pezze, L., Smerzi, A., Oberthaler, M. K., Schmied, R., & Treutlein, P. (2018). Quantum metrology with nonclassical states of atomic ensembles. *Rev. Mod. Phys.*, 90, 035005.

[144] Phillips, W. D. (1998). Nobel lecture: Laser cooling and trapping of neutral atoms. *Reviews of Modern Physics*, 70(3), 721.

[145] Pino, J. M., Dreiling, J. M., Figgatt, C., Gaebler, J. P., Moses, S. A., Allman, M. S., Baldwin, C. H., Foss-Feig, M., Hayes, D., Mayer, K., Ryan-Anderson, C., & Neyenhuis, B. (2021). Demonstration of the trapped-ion quantum CCD computer architecture. *Nature*, 592(7853), 209–213.

[146] Poirson, J., Bretenaker, F., Vallet, M., & Le Floch, A. (1997). Analytical and experimental study of ringing effects in a fabry–perot cavity. application to the measurement of high finesses. *Journal of the Optical Society of America B*, 14(11), 2811–2817.

[147] Pritchard, J. D., Isaacs, J. A., Beck, M. A., McDermott, R., & Saffman, M. (2014). Hybrid atom-photon quantum gate in a superconducting microwave resonator. *Phys. Rev. A*, 89, 010301(R).

[148] Qiu, Z., Vool, U., Hamo, A., & Yacoby, A. (2021). Nuclear spin assisted magnetic field angle sensing. *npj Quantum Information*, 7(1), 39.

[149] Rajasree, K. S., Ray, T., Karlsson, K., Everett, J. L., & Nic Chormaic, S. (2020). Generation of cold Rydberg atoms at submicron distances from an optical nanofiber. *Phys. Rev. Res.*, 2, 012038(R).

[150] Ramette, J., Sinclair, J., Breuckmann, N. P., & Vuletić, V. (2023). Fault-tolerant connection of error-corrected qubits with noisy links.

[151] Ramette, J., Sinclair, J., & Vuletić, V. (2024). Counter-factual carving exponentially improves entangled-state fidelity. *arXiv preprint arXiv:2401.11407*.

[152] Reiserer, A., Kalb, N., Rempe, G., & Ritter, S. (2014). A quantum gate between a flying optical photon and a single trapped atom. *Nature*, 508(7495), 237–240.

[153] Reiserer, A. & Rempe, G. (2015). Cavity-based quantum networks with single atoms and optical photons. *Rev. Mod. Phys.*, 87, 1379–1418.

[154] Reitz, D., Sayrin, C., Mitsch, R., Schneeweiss, P., & Rauschenbeutel, A. (2013). Coherence properties of nanofiber-trapped cesium atoms. *Phys. Rev. Lett.*, 110, 243603.

[155] Rempe, G., Thompson, R., Kimble, H. J., & Lalezari, R. (1992). Measurement of ultralow losses in an optical interferometer. *Optics letters*, 17(5), 363–365.

[156] Riera Sabat, F. & Duer, W. (2024). A modular entanglement-based quantum computer architecture. *New Journal of Physics*.

[157] Ritter, S., Nölleke, C., Hahn, C., Reiserer, A., Neuzner, A., Uphoff, M., Mücke, M., Figueroa, E., Bochmann, J., & Rempe, G. (2012a). An elementary quantum network of single atoms in optical cavities. *Nature*, 484(7393), 195–200.

[158] Ritter, S., Nölleke, C., Hahn, C., et al. (2012b). An elementary quantum network of single atoms in optical cavities. *Nature*, 484, 195–200.

[159] Robinson, J. M., Oelker, E., Milner, W. R., Zhang, W., Legero, T., Matei, D. G., Riehle, F., Sterr, U., & Ye, J. (2019). Crystalline optical cavity at 4 k with thermal-noise-limited instability and ultralow drift. *Optica*, 6(2), 240–243.

[160] Roos, C. F., Chwalla, M., Kim, K., Riebe, M., & Blatt, R. (2006). Designer atoms'for quantum metrology. *Nature*, 443(7109), 316–319.

[161] Rovny, J., Yuan, Z., Fitzpatrick, M., Abdalla, A. I., Futamura, L., Fox, C., Cambria, M. C., Kolkowitz, S., & de Leon, N. P. (2022). Nanoscale covariance magnetometry with diamond quantum sensors. *Science*, 378(6626), 1301–1305.

[162] Roy, R., Condylis, P. C., Johnathan, Y. J., & Hessmo, B. (2017). Atomic frequency reference at 1033 nm for ytterbium (yb)-doped fiber lasers and applications exploiting a rubidium (rb) 5 s 1/2 to 4 d 5/2 one-colour two-photon transition. *Optics Express*, 25(7), 7960–7969.

[163] Rudelis, A., Hu, B., Sinclair, J., Bytyqi, E., Schwartzman, A., Brenes, R., Zhitomirsky, T. K., Schleier-Smith, M., & Vuletić, V. (2023). Degradation of ta205 / sio2 dielectric cavity mirrors in ultra-high vacuum. *Opt. Express*, 31(24), 39670–39680.

[164] Ruf, M., Weaver, M. J., van Dam, S. B., & Hanson, R. (2021). Resonant excitation and purcell enhancement of coherent nitrogen-vacancy centers coupled to a fabry-perot microcavity. *Physical Review Applied*, 15(2), 024049.

[165] Ruster, T., Kaufmann, H., Luda, M. A., Kaushal, V., Schmiegelow, C. T., Schmidt-Kaler, F., & Poschinger, U. G. (2017). Entanglement-based dc magnetometry with separated ions. *Phys. Rev. X*, 7, 031050.

[166] Saavedra, C., Pandey, D., Alt, W., Pfeifer, H., & Meschede, D. (2021). Tunable fiber fabry-perot cavities with high passive stability. *Optics Express*, 29(2), 974–982.

[167] Sackett, C., Kielpinski, D., King, B., et al. (2000). Experimental entanglement of four particles. *Nature*, 404(6775), 256–259.

[168] Saffman, M., Walker, T. G., & Mølmer, K. (2010). Quantum information with Rydberg atoms. *Rev. Mod. Phys.*, 82(3), 2313.

[169] Sahay, K., Jin, J., Claes, J., Thompson, J. D., & Puri, S. (2023). High-threshold codes for neutral-atom qubits with biased erasure errors. *Physical Review X*, 13(4), 041013.

[170] Samutpraphoot, P., Đorđević, T., Ocola, P. L., Bernien, H., Senko, C., Vuletić, V., & Lukin, M. D. (2020). Strong coupling of two individually controlled atoms via a nanophotonic cavity. *Phys. Rev. Lett.*, 124, 063602.

[171] Santarelli, G., Laurent, P., Lemonde, P., Clairon, A., Mann, A. G., Chang, S., Luiten, A. N., & Salomon, C. (1999). Quantum projection noise in an atomic fountain: A high stability cesium frequency standard. *Physical Review Letters*, 82(23), 4619.

[172] Savard, T., O'hara, K., & Thomas, J. (1997). Laser-noise-induced heating in far-off resonance optical traps. *Physical Review A*, 56(2), R1095.

[173] Schlosser, N., Reymond, G., Protsenko, I., & Grangier, P. (2001). Sub-poissonian loading of single atoms in a microscopic dipole trap. *Nature*, 411(6841), 1024–1027.

[174] Scholl, P., Schuler, M., Williams, H. J., Eberharter, A. A., Barredo, D., Schymik, K.-N., Lienhard, V., Henry, L.-P., Lang, T. C., Lahaye, T., Läuchli, A. M., & Browaeys, A. (2021). Quantum simulation of 2d antiferromagnets with hundreds of Rydberg atoms. *Nature*, 595(7866), 233–238.

[175] Scholl, P., Shaw, A. L., Tsai, R. B.-S., Finkelstein, R., Choi, J., & Endres, M. (2023). Erasure conversion in a high-fidelity rydberg quantum simulator. *Nature*, 622(7982), 273–278.

[176] Schymik, K.-N., Pancaldi, S., Nogrette, F., Barredo, D., Paris, J., Browaeys, A., & Lahaye, T. (2021). Single atoms with 6000-second trapping lifetimes in optical-tweezer arrays at cryogenic temperatures. *Physical Review Applied*, 16(3), 034013.

[177] Sedlacek, J. A., Kim, E., Rittenhouse, S. T., Weck, P. F., Sadeghpour, H. R., & Shaffer, J. P. (2016). Electric field cancellation on quartz by Rb adsorbate-induced negative electron affinity. *Phys. Rev. Lett.*, 116, 133201.

[178] Shaw, A. L., Finkelstein, R., Tsai, R. B.-S., Scholl, P., Yoon, T. H., Choi, J., & Endres, M. (2024). Multi-ensemble metrology by programming local rotations with atom movements. *Nature Physics*, 20(2), 195–201.

[179] Shaw, A. L., Scholl, P., Finklestein, R., Madjarov, I. S., Grinkemeyer, B., & Endres, M. (2023). Dark-state enhanced loading of an optical tweezer array. *Physical Review Letters*, 130(19), 193402.

[180] Sheng, C., He, X., Xu, P., Guo, R., Wang, K., Xiong, Z., Liu, M., Wang, J., & Zhan, M. (2018). High-fidelity single-qubit gates on neutral atoms in a two-dimensional magic-intensity optical dipole trap array. *Physical review letters*, 121(24), 240501.

[181] Shin, D. K., Ross, J. A., Henson, B. M., Hodgman, S. S., & Truscott, A. G. (2020). Entanglement-based 3d magnetic gradiometry with an ultracold atomic scattering halo. *New Journal of Physics*, 22(1), 013002.

[182] Sinclair, J., Ramette, J., Grinkemeyer, B., Bluvstein, D., Lukin, M., & Vuletić, V. (2024). Fault-tolerant optical interconnects for neutral-atom arrays. *arXiv preprint arXiv:2408.08955*.

[183] Singh, S., Gu, F., de Bone, S., Villaseñor, E., Elkouss, D., & Borregaard, J. (2024). Modular architectures and entanglement schemes for error-corrected distributed quantum computation. *arXiv preprint arXiv:2408.02837*.

[184] Sipahigil, A., Evans, R. E., Sukachev, D. D., Burek, M. J., Borregaard, J., Bhaskar, M. K., Nguyen, C. T., Pacheco, J. L., Atikian, H. A., Meuwly, C., Camacho, R. M., Jelezko, F.,

Bielejec, E., Park, H., Lončar, M., & Lukin, M. D. (2016). An integrated diamond nanophotonics platform for quantum-optical networks. *Science*, 354(6314), 847–850.

[185] Sørensen, A. S. & Mølmer, K. (2003). Probabilistic generation of entanglement in optical cavities. *Phys. Rev. Lett.*, 90, 127903.

[186] Sørensen, A. S., van der Wal, C. H., Childress, L. I., & Lukin, M. D. (2004). Capacitive coupling of atomic systems to mesoscopic conductors. *Phys. Rev. Lett.*, 92(6), 063601.

[187] Sortais, Y. R., Marion, H., Tuchendler, C., Lance, A., Lamare, M., Fournet, P., Armellin, C., Mercier, R., Messin, G., Browaeys, A., et al. (2007). Diffraction-limited optics for single-atom manipulation. *Physical Review A—Atomic, Molecular, and Optical Physics*, 75(1), 013406.

[188] Sunami, S., Tamiya, S., Inoue, R., Yamasaki, H., & Goban, A. (2024). Scalable networking of neutral-atom qubits: Nanofiber-based approach for multiprocessor fault-tolerant quantum computer. *arXiv preprint arXiv:2407.11111*.

[189] Teller, M., Fioretto, D. A., Holz, P. C., Schindler, P., Messerer, V., Schüppert, K., Zou, Y., Blatt, R., Chiaverini, J., Sage, J., et al. (2021). Heating of a trapped ion induced by dielectric materials. *Physical Review Letters*, 126(23), 230505.

[190] Thiele, T., Filipp, S., Agner, J. A., Schmutz, H., Deiglmayr, J., Stammeier, M., Allmendinger, P., Merkt, F., & Wallraff, A. (2014). Manipulating rydberg atoms close to surfaces at cryogenic temperatures. *Phys. Rev. A*, 90, 013414.

[191] Thomas, P., Ruscio, L., Morin, O., & Rempe, G. (2024). Fusion of deterministically generated photonic graph states. *Nature*, (pp. 1–6).

[192] Thompson, J. D., Tiecke, T., Zibrov, A. S., Vuletić, V., & Lukin, M. D. (2013a). Coherence and raman sideband cooling of a single atom in an optical tweezer. *Physical review letters*, 110(13), 133001.

[193] Thompson, J. D., Tiecke, T. G., de Leon, N. P., Feist, J., Akimov, A. V., Gullans, M., Zibrov, A. S., Vuletić, V., & Lukin, M. D. (2013b). Coupling a single trapped atom to a nanoscale optical cavity. *Science*, 340(6137), 1202–1205.

[194] Thompson, J. D., Tiecke, T. G., Zibrov, A. S., Vuletić, V., & Lukin, M. D. (2013c). Coherence and raman sideband cooling of a single atom in an optical tweezer. *Phys. Rev. Lett.*, 110, 133001.

[195] Tiecke, T. G., Nayak, K. P., Thompson, J. D., Peyronel, T., de Leon, N. P., Vuletić, V., & Lukin, M. D. (2015). Efficient fiber-optical interface for nanophotonic devices. *Optica*, 2(2), 70–75.

[196] Tiecke, T. G., Thompson, J. D., de Leon, N. P., Liu, L. R., Vuletić, V., & Lukin, M. D. (2014). Nanophotonic quantum phase switch with a single atom. *Nature*, 508(7495), 241–244.

[197] Tsai, R. B.-S., Sun, X., Shaw, A. L., Finkelstein, R., & Endres, M. (2024). Benchmarking and linear response modeling of high-fidelity rydberg gates. *arXiv preprint arXiv:2407.20184*.

[198] Tuchendler, C., Lance, A. M., Browaeys, A., Sortais, Y. R. P., & Grangier, P. (2008). Energy distribution and cooling of a single atom in an optical tweezer. *Phys. Rev. A*, 78, 033425.

[199] Uphoff, M., Brekenfeld, M., Rempe, G., & Ritter, S. (2016). An integrated quantum repeater at telecom wavelength with single atoms in optical fiber cavities. *Applied Physics B*, 122, 1–15.

[200] van Leent, T., Bock, M., Fertig, F., Garthoff, R., Eppelt, S., Zhou, Y., Malik, P., Seubert, M., Bauer, T., Rosenfeld, W., et al. (2022). Entangling single atoms over 33 km telecom fibre. *Nature*, 607(7917), 69–73.

[201] Volz, J., Weber, M., Schlenk, D., Rosenfeld, W., Vrana, J., Saucke, K., Kurtsiefer, C., & Weinfurter, H. (2006). Observation of entanglement of a single photon with a trapped atom. *Physical review letters*, 96(3), 030404.

[202] Wachter, G., Kuhn, S., Minniberger, S., Salter, C., Asenbaum, P., Millen, J., Schneider, M., Schalko, J., Schmid, U., Felgner, A., Hüser, D., Arndt, M., & Trupke, M. (2019). Silicon microcavity arrays with open access and a finesse of half a million. *Light: Science & Applications*, 8(1), 37.

[203] Weber, S., Tresp, C., Menke, H., Urvoy, A., Firstenberg, O., Büchler, H. P., & Hofferberth, S. (2017). Tutorial: Calculation of Rydberg interaction potentials. *J. Phys. B: At. Mol. Opt. Phys.*, 50(13), 133001.

[204] Welte, S., Hacker, B., Daiss, S., Ritter, S., & Rempe, G. (2017). Cavity carving of atomic bell states. *Phys. Rev. Lett.*, 118, 210503.

[205] Welte, S., Hacker, B., Daiss, S., Ritter, S., & Rempe, G. (2018). Photon-mediated quantum gate between two neutral atoms in an optical cavity. *Phys. Rev. X*, 8, 011018.

[206] Wilk, T., Gaëtan, A., Evellin, C., Wolters, J., Miroshnychenko, Y., Grangier, P., & Browaeys, A. (2010). Entanglement of two individual neutral atoms using rydberg blockade. *Physical review letters*, 104(1), 010502.

[207] Wilson, J. T., Saskin, S., Meng, Y., Ma, S., Dilip, R., Burgers, A. P., & Thompson, J. D. (2022). Trapping alkaline earth Rydberg atoms optical tweezer arrays. *Phys. Rev. Lett.*, 128, 033201.

[208] Wootters, W. K. (2001). Entanglement of formation and concurrence. *Quantum Inf. Comput.*, 1(1), 27–44.

[209] Wu, Y., Kolkowitz, S., Puri, S., & Thompson, J. D. (2022). Erasure conversion for fault-tolerant quantum computing in alkaline earth Rydberg atom arrays. *Nat. Commun.*, 13(1), 4657.

[210] Xia, T., Lichtman, M., Maller, K., Carr, A., Piotrowicz, M., Isenhower, L., & Saffman, M. (2015). Randomized benchmarking of single-qubit gates in a 2d array of neutral-atom qubits. *Physical review letters*, 114(10), 100503.

[211] Yan, Z., Ho, J., Lu, Y.-H., Masson, S. J., Asenjo-Garcia, A., & Stamper-Kurn, D. M. (2023). Superradiant and subradiant cavity scattering by atom arrays. *Phys. Rev. Lett.*, 131, 253603.

[212] Young, A. W., Eckner, W. J., Milner, W. R., Kedar, D., Norcia, M. A., Oelker, E., Schine, N., Ye, J., & Kaufman, A. M. (2020). Half-minute-scale atomic coherence and high relative stability in a tweezer clock. *Nature*, 588(7838), 408–413.

[213] Young, C. B., Safari, A., Huft, P., Zhang, J., Oh, E., Chinnarasu, R., & Saffman, M. (2022). An architecture for quantum networking of neutral atom processors. *Appl. Phys. B*, 128(8), 151.

[214] Zhou, H., Zhao, C., Cain, M., Bluvstein, D., Duckering, C., Hu, H.-Y., Wang, S.-T., Kubica, A., & Lukin, M. D. (2024). Algorithmic fault tolerance for fast quantum computing. *arXiv preprint arXiv:2406.17653*.

[215] Đorđević, T., Samutpraphoot, P., Ocola, P. L., Bernien, H., Grinkemeyer, B., Dimitrova, I., Vuletić, V., & Lukin, M. D. (2021). Entanglement transport and a nanophotonic interface for atoms in optical tweezers. *Science*, 373(6562), 1511–1514.

[216] Šibalić, N., Pritchard, J., Adams, C., & Weatherill, K. (2017). Arc: An open-source library for calculating properties of alkali rydberg atoms. *Computer Physics Communications*, 220, 319–331.